Recirculating Planar Crossed-Field Amplifiers

by

Steven Christopher Exelby Jr.

A dissertation submitted in partial fulfillment
of the requirements for the degree of
Doctor of Philosophy
(Nuclear Engineering and Radiological Sciences)
in the University of Michigan
2019

Doctoral Committee:

Professor Ronald M. Gilgenbach, Chair
Assistant Research Scientist Nicholas Jordan
Professor Yue Ying Lau
Associate Professor Ryan McBride
Assistant Professor Louise Willingale

© Steven C. Exelby Jr.

scexlb@umich.edu

ORCID ID: 0000-0001-7441-5944

2019

ACKNOWLEDGEMENTS

I would like to express my gratitude to my advisor and committee chair, Professor Ronald Gilgenbach, for the work he has done advising me over the past 7 years, 6 as a graduate student. Professor Gilgenbach created an environment where I felt I was free to experiment and learn. He allowed me to struggle at times, and build machines that failed, an unpleasant experience at the time, but one that I believe ultimately improved my abilities as a scientist and an engineer. When I truly needed help, he provided excellent advice and connected me, on numerous occasions, with experts in the field. His most defining quality as an advisor is the care and attention that he gives his students, both toward their graduate progress and career development, and for that I am grateful I could have the experience working in his lab.

I would also like to thank my committee: Professors Y.Y. Lau, Ryan McBride, Nicholas Jordan, and Louise Willingale. This thesis would not be nearly the quality it is without their careful proofreading and insightful edits. Additionally, I would like to thank Y.Y. Lau for his theoretical contributions to this project throughout its development. He is an exceptional lecturer and helped me understand, and appreciate the complexity of, the problems I encountered. Nick Jordan also deserves recognition for his role as lab manager. I am extremely appreciative of the time and effort Nick invested in helping me with my extensive technical difficulties. Though not listed as an official committee member, Dr. Brad Hoff also provided his valuable technical expertise toward the improvement of this thesis and the research project as a whole.

I joined the Plasma, Pulsed Power, and Microwave Laboratory as an undergrad in the summer of 2012. Hired to work primarily on the LTD, I met the graduate students from the LTD side of the lab, Sonal Patel, Adam Steiner, and David Yager-Elorriaga. I would like to thank the three of them for making me feel welcome in the lab, while also introducing me to graduate level research. My decision to stay in this research group for my own graduate career was heavily influenced by the friendships I made as an undergrad. I would like to thank Geoff Greening for being my first mentor on HPM and teaching me the ways of being a beer snob and complaining about Michigan football. I would like to thank Drew Packard for helping me set up my experiments and collecting data. I would also like to thank the other graduate students, Paul Campbell, Jeff Woolstrum, Nick Ramey, Stephanie Miller, Akash Shah, Trevor Smith, Brendan Sporer and Stephen Langelotti, for their assistance and for maintaining the friendly work environment.

I would like to thank Mark Perrault for his help fabricating components, fixing those same components after I broke them, and ensuring the lab was set up to run our experiments. I would like to thank the professionals at L-3 Communications, Carter Armstrong and Mike Worthington for their generous support, and expert technical advice. The assistance provided by John Cipolla in conditioning and running the MG5193 magnetrons is appreciated immensely, and the project likely would not have reached the conclusion it did without his help. Finally, I would like to acknowledge the support provided by my family. Without the emotional support of my wife, Luka, the difficulties of grad school would have been unbearable. I would like to thank my parents, Shirley and Steve Sr., and my sister, Marissa, for raising me with the drive to succeed academically, and providing reassurance that the work I was doing was meaningful.

This work was funded by the Air Force Office of Scientific Research Grant FA9550-15-1-0097. Additional support was provided by the Directed Energy Professional Society through the Directed Energy Professional Society Graduate Scholarship.

TABLE OF CONTENTS

ACKNOWLEDGEMENTS ii
LIST OF FIGURES vii
LIST OF TABLES xvi
LSIT OF APPENDICES xvii
LIST OF SYMBOLS xviii
ABSTRACT xx
CHAPTER 1. Introduction 1
CHAPTER 2. Theory and Simulation 8
2.1. Single Particle Motion 8
2.2. Brillouin Flow 11
2.3. Amplification in CFAs 12
2.4. Dispersion in the RPCFA 15
2.5. Designing the Slow Wave Structure 25
2.6. Particle-in-Cell Simulations 30
CHAPTER 3. Experimental Configuration 37
3.1. Microwave Circuit Overview 37
3.2. The RPCFA Anode 42
3.3. The RPCFA Cathode 52
3.4. MELBA 54
3.5. Microwave Sources 58
3.5.1 MG5223F Magnetron 58
3.5.2 4J32 Magnetron 60
3.5.3 EPSCO PG5KB Signal Source 62
3.5.4 MG5193 Magnetron 64
CHAPTER 4. Experimental Results 68

4.1. RPCFA Fundamental Operation and Moderate Power Amplification 68
4.2. Phase Analysis 76
4.3. Parametric Characterization of the RPCFA 81
4.4. Consistency Analysis 86
4.5. Cathode Optimization 91
4.6. High Power Amplification 96
4.7. Phase Analysis at High Power RF Drive 102
CHAPTER 5. Summary and Conclusions 106
5.1. Summary of Results 106
5.2. Comparison to existing CFAs 108
5.3. Recommendations for Future Work 110
APPENDICES 113
BIBLIOGRAPHY 195

LIST OF FIGURES

Figure 1.1: Fundamental schematic diagram of a distributed emission CFA.[20,4] 3

Figure 1.2: Comparison of cylindrical and recirculating planar geometries for magnetrons and CFAs. 6

Figure 2.1: Example of anode circuit and cathode. The circuit mode illustrated is the "pi-mode", where there is a phase shift of π between adjacent anode cavities. The dash lines show the RF electric fields which are assumed to co-move to the right at the $E \times B$ drift velocity, so that this circuit mode may synchronously interact with the electrons. The magnetic field points out of plane of the paper..... 10

Figure 2.2: Lumped circuit element model for a section of a magnetron. Y_Q is the admittance of cavity Q. 16

Figure 2.3: Circuit diagram for a magnetron around cavity Q. 16

Figure 2.4: Expected dispersion relation for a magnetron with N = 12 cavities. The n = 6 mode is the π -mode. 18

Figure 2.5: Circuit model for general CFA SWS. 19

Figure 2.6: Dispersion relation for various values of *C'* and *L'*. The forward wave solution is in blue and the backward wave solution is in red, both for the fundamental mode, $\beta/\pi < 1$. A zero group velocity mode is shown in yellow.. 20

Figure 2.7a (left): Unit cell with the current paths for measuring L_q and L_A. The lower boundary is a grounded conducting plane.. Figure 2.7b (right): Magnetic field generated by current flowing on the L_q path. 22

Figure 2.8: Electric fields generated from a 3 GHz excitation from the waveport at the left side of the cell to the highlighted waveport at the lower boundary. 23

Figure 2.9: Dispersion relation from equation 2.47 with lumped circuit element values calculated from ANSYS HFSS and MAXWELL. 24

Figure 2.10: Figure 2.10: MAGIC dispersion relation. Discrete mode numbers are given due to discrete spatial sampling. A mode number of 3 corresponds to a π/2 phase shift per cell on this 12 cell RPCFA. 24

Figure 2.11a (top): Isometric view of 8-cell SWS with coaxial input and output ports generated in HFSS. Figure 2.11b (bottom): Top view of same SWS with the meander line highlighted. 26

Figure 2.12a (top): S_{11} for the RPCFA SWS around the 3.0 GHz design frequency. The trace is identical to S_{22}. Figure 2.12b (bottom): S_{21} for the RPCFA SWS. The trace is identical to S_{12}. 27

Figure 2.13: Electric field when the structure is excited by a 3 GHz RF signal. Lighter colors indicate a more intense field. Generated in HFSS. 29

Figure 2.14: Figure 2.14: RF fields when the RPCFA is injected with a 3 GHz signal in MAGIC simulation. Blue indicates the field points toward the right and red indicates the field points toward the left. Brighter colors indicate a stronger field. The snap shot is taken along the centerline of the SWS, which is the x-axis in Figure 2.19b, so the coaxial ports are not seen. 30

Figure 2.15: MAGIC simulation showing spoke formation as the injected signal and particles move from the input (left) to the output (right). The color scale is consistent with Figure 2.14..... 31

Figure 2.16: Injected power, output power, and diode voltage for the RPCFA zero-drive MAGIC simulation. 32

Figure 2.17: FFT traces for the simulated voltage across a single cell of the RPCFA during steady amplification (blue) and after RF injection had been terminated (red). 33

Figure 2.18: RPCFA gain versus injected RF frequency. 34

Figure 2.19: Simulated gain and output power as a function of the injected 3.0 GHz RF power. 35

Figure 2.20: Simulated gain versus the applied axial magnetic field and the pulsed DC voltage. For variations in the magnetic field, the voltage was held constant at 330 KV. For variations in the voltage, the magnetic field was held constant at 0.23 T. 35

Figure 3.1: Figure 3.1: Experimental block diagram generalized for moderate power RPCFA experiments. The positions of the circulator and directional coupler were reversed for high power (>150 kW) experiments. 38

Figure 3.2: Photograph of the fully assembled microwave circuit with the MG5223F magnetron as the RF source. The pulsed power driver for this magnetron is not pictured. 39

Figure 3.3: Map of positions in the RPCFA at which magnetic field was measured for calibration..... 40

Figure 3.4a (top): Magnetic field for the 9 marked locations over time with a 5 kV charge on the capacitor bank that drives the Helmholtz coils. Figure 3.4b (bottom): Zoomed in plot near peak of magnetic fields showing differences in the traces. Locations in the bends (4 and 8) are distinguished from locations in the gap. 41

Figure 3.5: Additively manufactured copper SWS. 43

Figure 3.6: Original SWS designed in HFSS on the left compared to the rounded structure designed to reduce field enhancement. The copper surface shows the effects of operation in the RPCFA. The rounded structure is unused at the time the picture is taken. 44

Figure 3.7: Coaxial wave ports for injecting and extracting power from the RPCFA. Copper mesh is fastened to the inner coaxial conductor to improve electrical/RF contact with the puck couplers. 45

Figure 3.8: RPCFA SWS and inner housing with the upper backwall excluded for clarity. 46

Figure 3.9: RPCFA inner housing with puck couplers attached, mounted inside WR-284 waveguide. The inner conductors which extend into the puck couplers are wrapped in copper mesh to improve electrical/RF contact with the pucks. 47

Figure 3.10: S_{21} for a single puck coupler calculated in HFSS simulation. 47

Figure 3.11: HFSS simulation and electric field magnitude overlay of a puck coupler at 3 GHz. 48

Figure 3.12: Experimentally measured S_{21} through two puck couplers connected by a short inner conductor. 49

Figure 3.13: Inner housing mounted to the inner wheel. The steel braid fastened to the wheel ensures good electrical contact with the vacuum chamber. 50

Figure 3.14: Endplate, magnetic field coils, and vacuum window. The access panel is open during assembly. 51

Figure 3.15a (top, left): Glyptal Cathode: Bare aluminum emitter with Glyptal to inhibit emission at other locations. Figure 3.15b (top, right): Cathode A: Steel cathode brazed to coarse carbon fiber emitter. Photo taken of new cathode, still in plastic bag. Figure 3.15c (bottom, left): Cathode B: Steel cathode brazed to fine carbon fiber emitter. Photo taken after 40 shots. Figure 3.15d (bottom, right): Cathode A with Endhat: AFRL cathode A modified to include aluminum endhat. 53

Figure 3.16a (top): MELBA spark gap switch and resistors prior to rebuild. Oil can be seen to have permeated the resistors, and the switch body has become opaque from interaction with SF_6 breakdown products. Deposition of electrode material can also be seen inside the switch. Figure 3.16b (bottom): MELBA suspended over the oil tank after a completed rebuild. 56

Figure 3.17: MELBA Ceramic insulator. Scale measures from the leftmost surface of the cathode endplate to where the insulator intersects with the oil tank. 57

Figure 3.18: MG5223F magnetron. The green lead (marked "H," not shown) connects to the filament heater and the yellow lead (marked "K") connects to the high voltage output of the driver. 59

Figure 3.19: Unattenuated output microwave pulse for the MG5223F magnetron. 60

Figure 3.20: Raytheon 4J32 magnetron. The coaxial RF output is adapted to WR-284 waveguide using a scaled puck coupler shown here. 61

Figure 3.21: Unattenuated output microwave pulse from the 4J32 magnetron driven by the Stanford Modulator. 61

Figure 3.22: EPSCO model PG5KB pulse signal source. For scale, the source is fits into standard 19-inch rack mount. 62

Figure 3.23: Pulse-wait triggering scheme used for experiments driven by the EPSCO Source or magnetrons driven by the Stanford Modulator (MG5223F and 4J32). Programmed channel delay may vary slightly due to the RF source or to investigate the RPCFA's response to variation in timings. Figure is not to scale. 63

Figure 3.24: MG5193 magnetron with L-3 solenoid. Approximately 18 A were transmitted to this 1-Ω solenoid during operation. Water lines connect the magnetron and the solenoid. An E2V adaptor on the left converts the output of the magnetron from cylindrical to WR-284 waveguide. 65

Figure 3.25: Unattenuated output microwave pulse from the MG5193 magnetron driven by the XLB PFN. Low power is generated early in the pulse (600 to 1000 ns), though still at the pi-mode frequency, prior to high power output. 65

Figure 3.26: Voltage, current and RF power output from the MG5193 magnetron driven by the XLB PFN 66

Figure 3.27: Triggering scheme for experiments that utilized the single shot XLB PFN and the MG5193 magnetron. Figure not to scale. 67

Figure 4.1: RPCFA connected to the network analyzer for cold tube transmission measurement. 69

Figure 4.2: Measured and simulated S_{21} for the RPCFA 69

Figure 4.3: Zero RF drive, MELBA voltage and current profile with the output RF power measurement overlaid. 71

Figure 4.4a (top): MAGIC simulated spectrum of zero drive output signal. Figure 4.4b (bottom): measured output spectrum from zero drive experiment. The range of calibrated frequencies is marked by the red lines. Both spectra are on linear scales. 72

Figure 4.5: Shot 15316. MELBA current and voltage overlaid with the injected 8 kW at 3.05 GHz and 117 kW amplified power. 73

Figure 4.6a (top): Output power spectrum for shot 15316 driven at 3.05 GHz. Figure 4.6b (bottom): Output power spectrum for shot 15534 driven at 2.84 GHz. Both spectra show small peaks at exact multiples of 1/8 GHz. These peaks are exactly 1 frequency bin wide and presumed to be artifacts of sampling and not representative of the frequency content of the measured signals. 75

Figure 4.7: Phase shift between the input and output signal measured in MAGIC simulation. The erratic phase difference early in time is due to the RF signal not yet reaching the output coaxial line. .. 76

Figure 4.8a (top): MELBA current and voltage with RF output power during the time phase difference measurements are calculated (shot #15570). Figure 4.8b (bottom): Phase difference over time with moving average overlaid. 77

Figure 4.9a (top): MELBA current and voltage with RF output power for a shot that displays both amplifying and oscillatory behavior (shot #15567). Input microwave power is constant at around 15 kW over the plotted time scale. Figure 4.9b (bottom): Phase difference over time showing a trend similar to Figure 4.8b until around 1100 ns, when transmission terminates. 79

Figure 4.10: Time frequency analysis of the output signal for shot #15567, which displays amplification followed by oscillation. 80

Figure 4.11: Measured RPCFA output power versus the input power supplied by the two magnetrons tested. Lines are drawn showing gain values of 3, 10, 13, and 16 dB for reference. Power measurements have an uncertainty of 0.3 dB. 81

Figure 4.12: Measured RPCFA gain versus the applied axial magnetic field. The vertical lines indicate the values selected for the input power sweep: 2.03 kG for 2.84 GHz drive, and 2.26 kG for 3.05 GHz drive. An uncertainty of 0.3 dB is present. 82

Figure 4.13: Measured RPCFA gain versus frequency with moving averages and local standard deviation overlaid. 83

Figure 4.14: Photograph of the SWS after 564 shots. Figure 3.5 shows the same structure before any shots had been taken. The copper has been lightly sanded to remove some of the aluminum deposition. The effect of the beam impacting the SWS is most significant at the vane tips. 85

Figure 4.15: Transmission rates for a new SWS versus the same SWS after 564 shots taken during the final shot series using the EPSCO generator. 85

Figure 4.16: Peak gain for shots 15682 – 15761 plotted against the voltage and current when peak gain is achieved. Instances of shots with a failed crowbar and shots that display oscillation are omitted. Input microwave power is 30 kW. 86

Figure 4.17: Peak output power for shots 15682 – 15761 plotted against current at the time of peak power. A linear (constant efficiency) trendline with R^2 = 0.246 indicates the weak correlation. Input microwave power is 30 kW. 87

Figure 4.18: Overlaid current and voltage for the 9 optimal MELBA pulses. All show excellent consistency in voltage and acceptable consistency in current. 88

Figure 4.19: Output power as a function of the time difference between the beginning of the MELBA pulse and the onset of RF. Negative values indicate the MELBA pulse begins prior to the RF injection. 89

Figure 4.20: Shot 16237. MELBA current and voltage overlaid with RF traces. MELBA is fired and reaches near full voltage before the RF begins. 90

Figure 4.21: Shot 16242. MELBA current and voltage overlaid with RF traces. The rise of the RF and MELBA voltage occur concurrently. 91

Figure 4.22a (top left): Shot #15704. Ideal, high current, type 1 pulse. Figure 4.22b (top right): Shot #15738. Low current, type 2 pulse. Figure 4.22c (bottom left): Shot #15722. Short, low current, type 3 pulse. Figure 4.22d (bottom right): Shot #15734. Failed crowbar, arc, type 4 pulse. The current in these pulses typically reaches 30 kA. 93

Figure 4.23: Peak gain and standard deviation compared for different shot types using the Glyptal cathode and other experimental parameters held constant. 94

Figure 4.24: Percentage of shots of a given shot type for the consistency analyses for each cathode. 95

Figure 4.25: Peak gain and instantaneous current at the time of peak gain for each of the four cathodes. 95

Figure 4.26: Shot 16817. MELBA current and voltage overlaid with the injected 633 kW at 3.0 GHz and 5.86 MW amplified power. Input power cuts off after amplified output breaks down the RPCFA. 97

Figure 4.27: Shot 16829. MELBA current and voltage overlaid with the injected 340 kW at 3.0 GHz and 3.06 MW amplified power. Input power continues through the end of amplification. 98

Figure 4.28: Shot 16829. Peak output power is reached during the rise of the MELBA pulse then decays rapidly. Slow, constantly decreasing gain is observed for much of the pulse. 99

Figure 4.29: Peak output microwave power versus the simultaneous input power over the range of powers tested on the RPCFA. 100

Figure 4.30: Peak output microwave power versus simultaneous input power plotted on a log scale. The transition to consistent amplification as the input power is increased to around 150 kW is apparent. 100

Figure 4.31: Peak microwave output power versus cumulative the number of times RF breakdown was induced for the 32 shots in which this occurred..... 101

Figure 4.32: Phase shift over the transmission of 30 kW of RF input at 3.05 GHz with no MELBA beam. The microwave pulse begins around 200 ns. 102

Figure 4.33: Phase shift over the transmission of approximately 700 kW of RF input at 3.0 GHz with no MELBA beam..... 103

Figure 4.34a (top): Log plot of the integrated spectrum for the MG5223F magnetron driven by the Stanford Modulator. Figure 4.34b (bottom): Log plot of the integrated spectrum for the MG5193 magnetron driven by the XLB PFN. 104

Figure 4.35: Histogram comparing the phase shift for 54 shots. The centroid is given by the red line, calculated by identifying phase shift values of zero with phase shift values of π to obtain a continuous distribution. 105

Figure 5.1: Comparison of the RPCFA, operated safely below RF breakdown (shot 16829) and at mean RF breakdown levels, with existing commercial CFAs. 109

Figure A.1: Geometry over two SWS periods used in this estimation of RPCFA performance. 114

Figure A.2: Cyclotron orbit. Particle position in (x,y) space is traced over time for the case with no electric potential. 115

Figure A.3a (left): Cycloidal path traced by a particle in a static electric and magnetic field. In this figure, the cathode surface is located at y = 0.0125 m and the top of the single particle cycloidal orbit is at y = 0.008 m. Figure A.3b (right): Normalized momentum trace for the same particle. 115

Figure A.4a: A section of an arbitrary SWS with the RF field drawn. For the 180° phase shift in RF field as shown this represents 2 cells of the RPCFA SWS. In this figure, the cathode is located at y = 15 mm and the anode vane tip is located at y = 0 mm. The x-coordinate at the middle of the cavity is x = 7.5 mm. Figure A.4b: The RF potential in the interaction space in V for a 1.3 MW RF excitation.

The x, y coordinates of this figure illustrate the numerical grid. Each cell represents a square in physical space with a side length of 15/16 mm. 117

Figure A1.5: Sample trajectory of a particle (in the Lagrangian frame) initiated at the center of the focusing field frame and the edge of the Brillouin hub. This particle's trajectory ends at the anode. In this figure, the initial y-coordinate (tip of Brillouin hub) is 12 mm from the anode. 118

Figure A.6: Each of 320 components individual contribution to RF gain in units of 10 kW. 119

Figure A.7: Map of the end conditions for components of the Brillouin hub. Blue indicates the particle is drawn to the anode; green indicates it remains in the interaction space after a time of 3 RF periods. Yellow indicates the particle is returned to the cathode and does not contribute to the overall current draw. 119

Figure A.8: Output Power and gain from the RPCFA for various levels of input drive. 120

Figure B.1: Stanford Modulator Model No. 344M. 122

Figure B.2: XLB PFN with XLBox trigger amplifier and Pulspak 10A trigger generator. 123

Figure B.3: XLB PFN with interior circuitry extracted. 2 additional capacitor stages are mounted below the breadboard and are not visible. 124

Figure B.4: Circuit diagram generated in LT SPICE for the XLB PFN with charging, triggering, and load architecture included. 125

Figure B.5: Voltage trace of the XLB PFN at 70 kV charge firing into a resistive 400 Ω load. 126

Figure C.1a: RPCFA Slow wave structure, page 1. 128

Figure C.1b: RPCFA slow wave structure, page 2. 129

Figure C.1c: Inner conducting pin, connects the SWS into the puck couplers. Two of these plus the SWS form the assembly that was additively manufactured for the prototype RPCFA. 130

Figure C.2a: The RPCFA slow wave structure substrate, page 1. 131

Figure C.2b: The RPCFA slow wave structure substrate, page 2. 132

Figure C.2c: The RPCFA slow wave structure substrate, page 3. 133

Figure C.2d: The RPCFA slow wave structure substrate, page 4. 134

Figure C.3a: Cylindrical side pieces of the RPCFA inner housing, page 1. 135

Figure C.3b: Cylindrical side pieces of the RPCFA inner housing, page 2. 136

Figure C.3c: Cylindrical side pieces of the RPCFA inner housing, page 3. 137

Figure C.3d: Cylindrical side pieces of the RPCFA inner housing, page 4. 138

Figure C.4a: Smooth bore planar section of RPCFA inner housing, page 1. 139

Figure C.4b: Smooth bore planar section of RPCFA inner housing, page 2. 140

Figure C.5a: Center piece of the back wheel that locks the inner housing into position, page 1. 141

Figure C.5b: Center piece of the back wheel that locks the inner housing into position, page 2. 142

Figure C.6: Outer piece of the back wheel. Four of these surround the center piece on threaded ¼" rods lock the RPCFA into position. 143

Figure C.7a: Input side waveguide to RPCFA adaptor. A puck coupler is bolted through the small hole in the bottom, page 1. 144

Figure C.7b: Input side waveguide to RPCFA adaptor. A puck coupler is bolted through the small hole in the bottom, page 2. 145

Figure C.8a: Output side waveguide to RPCFA adaptor. A puck coupler is bolted through the small hole in the bottom, page 1. 146

Figure C.8b: Input side waveguide to RPCFA adaptor. A puck coupler is bolted through the small hole in the bottom, page 2. 147

Figure C.9a: Input side waveguide (WR-284) with customized compact flange, page 1. 148

Figure C.9b: Input side waveguide (WR-284) with customized compact flange, page 2. 149

Figure C.10a: Output side waveguide (WR-284) with customized compact flange, page 1. 150

Figure C.10b: Output side waveguide (WR-284) with customized compact flange, page 2. 151

Figure C.11: Puck coupler. 152

Figure C.12: Cathode stalk adaptor. Connects the MELBA cathode stalk to a ½" rod for mounting a cathode with variable z-axis positioning. 153

Figure C.13: Planar cathode. Fundamental shape used for all experiments. 154

Figure C.14: Cathode endhat, mounted to front of planar cathode. 155

Figure C.15a: Endplate. Connects the interior vacuum waveguide to the exterior RF circuitry, page 1. 156

Figure C.15b: Endplate. Connects the interior vacuum waveguide to the exterior RF circuitry, page 2. 157

Figure C.15c: Endplate. Connects the interior vacuum waveguide to the exterior RF circuitry, page 3. 158

Figure C.16a: Vacuum interface, a 2mm thick lexan window is mounted between this piece and the endplate to make the vacuum window. Page 1. 159

Figure C.16b: Vacuum interface, a 2mm thick lexan window is mounted between this piece and the endplate to make the vacuum window. Page 2. 160

Figure C.16c: Vacuum interface, a 2mm thick lexan window is mounted between this piece and the endplate to make the vacuum window. Page 3. 161

Figure C.16d: Vacuum interface, a 2mm thick lexan window is mounted between this piece and the endplate to make the vacuum window. Page 4. 162

Figure C.16e: Vacuum interface, a 2mm thick lexan window is mounted between this piece and the endplate to make the vacuum window. Page 5. 163

Figure C.17: Coupler puck used to extract power from the Raytheon 4J32 magnetron. 164

Figure D.1: Current measuring loops with surfaces perpendicular to x, the direction of $E_{rf} \times B$ drift. Electrons recirculate counter-clockwise in this figure. Location 1 measures the current flowing into the SWS, location 2 measures the current leaving the SWS, and location 2 measures current in the center of the planar drift region. 166

Figure D.2a (top): Current passing through loop 1, approaching the SWS. Figure D.2b (middle): Current passing through loop 2, in the planar drift region. Unlike the other two locations, current is positive as electrons are travelling in the -x direction at this point. Figure D.2c (bottom): Current passing through loop 3, leaving the SWS. 167

Figure D.3a (top): Frequency spectrum of the current passing through the loop at location 1. Peaks at the RF drive frequency and first harmonic can be observed. Figure D.3b (middle): Frequency spectrum of current passing through the loop at location 2. Small peaks at the RF drive frequency and first harmonic can be observed. Figure D.3c (bottom): Frequency spectrum of the current passing through the loop at location 3. The peaks at the fundamental RF frequency as well as the first and second harmonic are observed. 168

Figure E.1: Data processing software flowchart 172

Figure F.1: Shot #16868, showing high power amplification sufficient to cause both RF breakdown in the SWS, and again when the reflected amplified signal reaches the circulator, terminating the input pulse. 183

Figure F.2: Shot #16819, showing high power amplification sufficient to cause RF breakdown in the SWS, but insufficient to induce breakdown when the reflected amplified signal reaches the circulator, not terminating the input pulse. 184

Figure F.3: Shot #16834, showing high power amplification insufficient to cause RF breakdown in the SWS. Amplified output power decays gradually as the wave desynchronizes from the beam. . 184

Figure G.1: Cross section of MAGIC simulation showing cathode with large endhats and a reduced A-K gap spacing that effectively inhibits endloss current. 186

Figure G.2: Realistic simulation of RPCFA in MELBA chamber with modest endhats and increased A-K gap spacing. Significant endloss is apparent. 186

Figure G.3: Collected currents from a realistic simulation of the RPCFA. 187

Figure H.1: XPS spectrum from the unperturbed patch of the SWS. Copper is the dominant element, as expected, but oxygen and carbon can be seen in small amounts 190

Figure H.2: XPS spectrum from the exposed section of the SWS vane tip. Addition elements not seen in the unperturbed spectrum include sodium calcium and silicon 191

LIST OF TABLES

Table 1.1: Comparison of amplification with primed oscillators of both soft and hard excitation. Green check marks indicate a feature confirmed on the RPCFA. Red x-marks indicate a feature not observed. 7

Table 3.1: Summary of microwave input power sources used in this dissertation. 58

Table 5.1: Summary of RPCFA response to various levels of injected RF power. 108

Table D.1: Frequency content of the Brillouin hub at three marked locations for two different magnitudes of input RF drive power. 170

Table I.1: List of commercially available crossed-field amplifiers at the time of publication [52]. 193

LIST OF APPENDICES

Appendix A: Estimating the Performance if the RPCFA. 113

Appendix B: A Description of Devices used to Drive RF Sources. 121

Appendix C: Detail Drawings. 127

Appendix D: Analysis of Demodulation and Harmonic Beam Content 165

Appendix E: Matlab Post-Processing Software 171

Appendix F: Determination of RF Breakdown 183

Appendix G: Discussion of Endloss and Electronic Efficiency 185

Appendix H: X-ray Photoelectron Spectroscopy 189

Appendix I: Table of Commercially Available Crossed-Field Amplifiers 193

LIST OF SYMBOLS

Q	Quality Factor
E	Electric Field
B	Vacuum Magnetic Field
$\boldsymbol{E_{RF}}$	RF Electric Field
N	Number of Cavities/Resonators
m	Mass
$\vec{v}$	Velocity
e	Electronic Unit Charge
Ω_c	Electron Cyclotron Frequency
t	Time
T	Cyclotron Period
D	A-K gap
B_H	Hull Cutoff Magnetic Field
ϕ	Electric Potential
n	Particle Number Density
ε_0	Permittivity of Free Space
ω_p	Plasma Frequency
x_b	Brillouin Hub Height
ω	Frequency in rad/s
k	Propagation Constant
μ_0	Magnetic Permeability of Free Space
H	Magnetic Field
J	Current Density
c	Speed of Light in Vacuum
I	Current

C	Pierce Gain Parameter, Capacitance
v_{phase}	RF Phase Velocity
Y_Q	Cavity Admittance
L	Inductance
γ	Phase Shift per Cell in Magnetron
P	Normalized Capacitance
Z	Impedance
β	Phase Shift Per Cell in CFA
C’	Normalized Capacitance
L’	Normalized Inductance
f	Frequency in Hz
P	Power

ABSTRACT

The Recirculating Planar Crossed-Field Amplifier (RPCFA) is an adaptation of the Recirculating Planar Magnetron (RPM) that has been the focus of research at the University of Michigan's Plasma, Pulsed Power and Microwave Laboratory for nearly a decade. The RPM is a high power microwave (HPM) source that utilizes an innovative geometry to overcome some of the power generation limitations of existing magnetrons while maintaining the characteristic high efficiencies of these devices. The large planar cathode emits higher currents, leading to higher power, than a rod cathode at space charge limited densities due to its increased emitting surface area. The recirculating interaction space effectively recycles the electron beam, which preserves the electronic efficiency of the device. The RPCFA utilizes a geometry similar to the RPM and is likewise expected to hold the same advantages over traditional CFAs that the RPM holds over traditional magnetrons. Additionally, the planar amplifying structure permits the injection and extraction ports be placed physically far away from each other. This allows the Brillouin hub to demodulate over a long distance which minimizes feedback, a primary power limiting mechanism in cylindrical CFAs. The focus of this thesis is to design and test a prototype RPCFA which demonstrates these features.

The slow wave structure (SWS) is the key component to a magnetron and CFA which is responsible for promoting the synchronous interaction between the RF wave and the Brillouin hub. The SWS in a CFA is designed with the following criteria: First, the SWS must act as a transmission line over the band of frequencies the device is expected to amplify (typically with about 10% bandwidth). The transmission should minimize radiative and resistive losses and minimize reflection at any point in the RF circuit. Thus, the SWS should have an inherently low quality factor, Q. Second, the SWS must generate periodic fringing RF fields in response to an excitation in the amplification band. Finally, the phase velocity of these fringing

fields must be slowed to the speed of the Brillouin hub, which (in this device) will be 20 – 30% of the speed of light. Using Ansys HFSS driven modal simulation, a SWS was designed that satisfied the criteria listed. This SWS was reproduced using the particle-in-cell code, MAGIC, to simulate operation. MAGIC simulations, with pulsed 330 kV and 540 A, suggested that the device could amplify a 1.3 MW signal at 3 GHz to a steady state output power of 29 MW, a gain of nearly 13.5 dB. MAGIC simulation also predicted approximately 13% bandwidth, zero-drive stability (meaning output power was linearly dependent on the presence of an input signal), and nearly linear amplification in the range of testable input powers.

The RPCFA was then prototyped, employing the "lost wax" technique with an additively manufactured wax casting form to build the intricate SWS, and traditional machining techniques to fabricate the supporting components. The RPCFA was tested experimentally to test the predictions of MAGIC simulations. Zero-Drive stability was observed and a minimum amplifiable power was established to be around 100 W. Moderate power (10's of kW) input signals showed moderate levels of amplification, 7.87 dB with high levels of variability, $\sigma = 2.74$ dB. At moderate power, the bandwidth was measured to be 15%, slightly exceeding the bandwidth predicted by simulation. At high-power input drive (150 kW and above), the RPCFA demonstrated much more consistent amplification and an increased mean gain of 8.71 dB, with $\sigma = 0.63$ dB. The RPCFA consistently reached peak output powers around 5 MW before exhibiting RF breakdown of the RF circuit. This RF breakdown is characterized by the abrupt termination of the transmitted RF signal. This RF breakdown represents the existing limit for output power from the RPCFA. Future experiments will make attempts to remove this limitation, redesigning the S-band structure to accommodate high RF fields or moving to lower frequencies where features will be inherently larger.

CHAPTER 1

Introduction

High Power Microwaves (HPM) have applications critical to the fields of science, industry and defense [1 - 4]. Prominent scientific applications include use in particle accelerators and plasma heating [5]. In industry, HPM are used in medical accelerators and processing of food and other materials. In national defense, HPM play a crucial role in RADAR and active denial systems [6]. The development of devices that can improve upon some aspects of HPM generation or amplification, such as peak power, efficiency, or phase control, is therefore of great interest. The focus of this dissertation is the design, fabrication, and demonstration of a novel HPM amplifier: The Recirculating Planar Crossed-Field Amplifier (RPCFA). This device employs a novel geometry to achieve exceptionally high peak powers while maintaining the efficiency, phase control, and stability that is characteristic of crossed-field amplifiers (CFAs) [7 – 8]. The prototype tested in this investigation demonstrated high peak output powers, although efficient operation could not be achieved with the available experimental equipment. The device demonstrated a limited level of phase stability.

The CFA is an HPM device designed to utilize the crossed-field geometry, originally developed in magnetrons, to amplify an injected RF signal rather than oscillate [9 – 10]. The development of the magnetron began in 1910 when German physicist Hans Gerdien of the Siemens corporation invented a device that featured a rod-shaped cathode surrounded by a cylindrical anode with an axially oriented magnetic field throughout the A-K gap [13]. A similar device which featured a cylindrical anode with a single split was investigated by Albert Hull of the General Electric Co. in the United States [11]. Hull's device was designed to operate as a magnetic switch, insulating above a threshold magnetic field, called

the “Hull cutoff field,” and conducting below that threshold. The first dedicated magnetron oscillator was introduced by Erich Habban which featured a cylindrical anode split into 2 separate components [12]. In the 1930’s, interest arose in shorter wavelengths (1 – 0.1 m) for application in wireless telephone links and radar [13].

From 1938 to 1940, in the United Kingdom, there was a push to improve the angular resolution of existing airborne and surface radar systems using a device capable of generating at least 1 kW at a frequency of approximately 3 GHz [14]. At Birmingham University, J. Randall and H. Boot introduced a cavity magnetron that generated 400 W of RF power at a wavelength of 9.8 cm (3.06 GHz) which was quickly improved up to 1 MW over the next year. On August 9, 1940, Winston Churchill approved the “Tizard mission” [15 - 16] which brought the cavity magnetron to the United States for mass production and implementation into radar systems. These powerful and compact magnetron-based radar systems were a significant advantage for the Allies, as compared to the German klystron powered systems [17]. Following WWII, and up until the early 1950’s, there was interest in extending the magnetron’s crossed-field interaction to an amplifier. Early devices were similar to travelling wave tubes and featured an electron emitter, separate from the cathode, called a sole. In 1953, William Brown introduced the modern CFA to enhance the capabilities of radar systems [18]. The Platinotron is synonymous with the CFA. When used to amplify high peak or average power levels, it can be referred to as an Amplitron; when used as an oscillator in conjunction with a stabilizing high-quality factor (high-Q) cavity, the assembly is referred to as a Stabilotron [19].

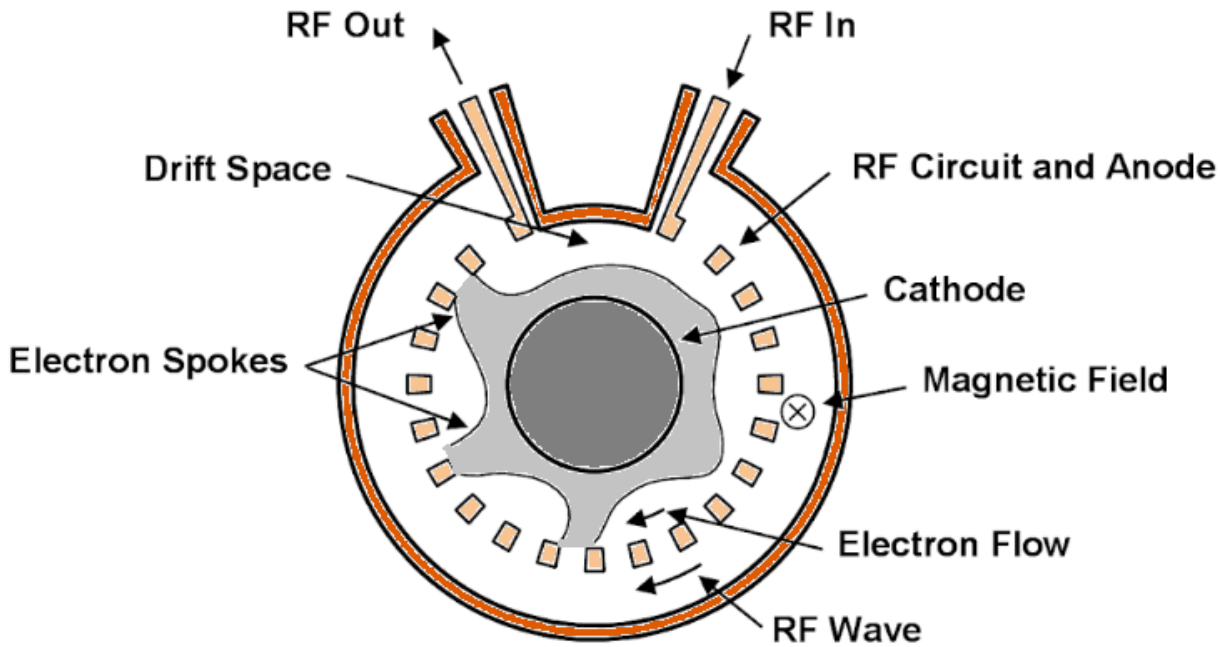

Figure 1.1: Fundamental schematic diagram of a distributed emission CFA.[20,4]

A diagram of the distributed emission CFA is shown in Figure 1.1. The cathode, anode, and magnetic field form a magnetically insulated diode. CFAs typically employ thermionic cathodes, so the cathode is usually heated and sufficient voltage is supplied to emit electrons via thermionic emission. These emitted electrons form a Brillouin hub [21 - 23] due to the $\boldsymbol{E} \times \boldsymbol{B}$ drift which orbits the cathode. The anode or RF circuit is typically low Q so electronic noise that is generated on the anode in response to the Brillouin hub propagates out of the interaction space through either the RF input or output port. This is in contrast to the magnetron, where electronic noise drives the oscillation of the high-Q anode. Thus, a CFA without RF drive is a magnetically insulated diode [24] that does not draw current and generates no RF power.

For RF excitation, an external RF electric field is applied with a component perpendicular to both the DC electric field and the magnetic field and parallel to the direction of travel of the Brillouin hub. This component of the RF field permits an $\boldsymbol{E_{RF}} \times \boldsymbol{B}$ drift that either pulls electrons toward the anode or returns them to the cathode depending on the phase. When the phase velocity of the RF excitation matches the speed of the Brillouin hub, this interaction becomes resonant, allowing energy to transfer from the potential

of the electron to the RF wave. This synchronism condition is known as the Buneman-Hartree condition [25 – 27]. Further explanation of this process is given in the following chapter.

Compared to other vacuum tube amplifiers, such as the klystron, the travelling wave tube (TWT), and their fast-wave counterparts including gyrotron travelling wave amplifiers, the CFA finds application for its combination of high power at modest voltage, high efficiency, moderate bandwidth (5 – 15%), and compact frame. Gain in CFAs is typically modest (5 – 20 dB) compared to linear beam tubes like helix TWTs, which may exceed 40 dB [28 – 29]. Helix TWTs also possess the highest bandwidth of any vacuum tube, often significantly beyond an octave, though they are typically limited by their low peak output power. Efficiencies in excess of 60% have been demonstrated on helix TWTs, though typical values are low (20%). Klystrons have demonstrated higher powers than are obtainable with either helix TWTs or CFAs [30], with efficiencies and bandwidths lower than CFAs. These linear beam devices tend to be large and heavy in comparison to CFAs [31], making CFAs more appropriate in mobile and airborne applications. Fast-wave, gyro-devices, such as the gyro-TWT and the gyro-klystron, dominate the market at high frequencies, where 100s of kW of peak power can be generated at frequencies up to 100s of GHz [32]; typically, these require superconducting magnets.

The design of the RPCFA is based on by the Recirculating Planar Magnetron (RPM) [33 - 35], which has been patented and is a focus of research at the University of Michigan. The RPM employs a recirculating planar geometry that provides a number of advantages. The planar cathode has an extended emitting surface area, allowing for significantly increased current at space-charge limited current densities. This increased current permits an increase in the RF power generating capabilities of the device. The increased surface area of both electrodes also helps dissipate heat generated in high power and potentially high duty cycle devices. The recirculating cylindrical bends recycle the electron beam, maintaining higher efficiency than devices that feature beam dumps or collectors. The planar geometry also admits favorable scaling of the magnetic field volume. For a number of cavities (N), which is proportional to the total output power of the device, the magnetic field volume required to insulate the diode scales linearly, whereas it

scales with N^2 in a cylindrical device. Reducing the magnetic field volume decreases both the weight and energy consumption of the system.

The RPCFA is expected to maintain the same advantages over traditional cylindrical CFAs that the RPM held over cylindrical magnetrons. Additionally, the amplifying circuit of the RPCFA can be easily made longer or shorter depending on the application, with the same favorable scaling of the magnetic field volume. Furthermore, the input and output ports of the RPCFA are placed far apart, limiting feedback. Feedback is a gain-limiting phenomenon in amplifiers, where the output signal, contained within the modulation of the Brillouin hub in the case of CFAs, couples to the input, and the RF drive signal becomes insufficiently powerful to lock the CFA in the amplifying mode. In this case the device becomes oscillatory. Existing devices, such as the Dematron [36], have used collectors and RF attenuators to eliminate feedback at the expense of efficiency. By providing two recirculating bends and an upper drift space region for effective demodulation of the Brillouin hub, the RPCFA is less prone to feedback; and it may be driven to higher output powers and gain without losing efficiency. A comparison of cylindrical versus recirculating planar geometry for magnetrons and CFAs is given in Figure 1.2.

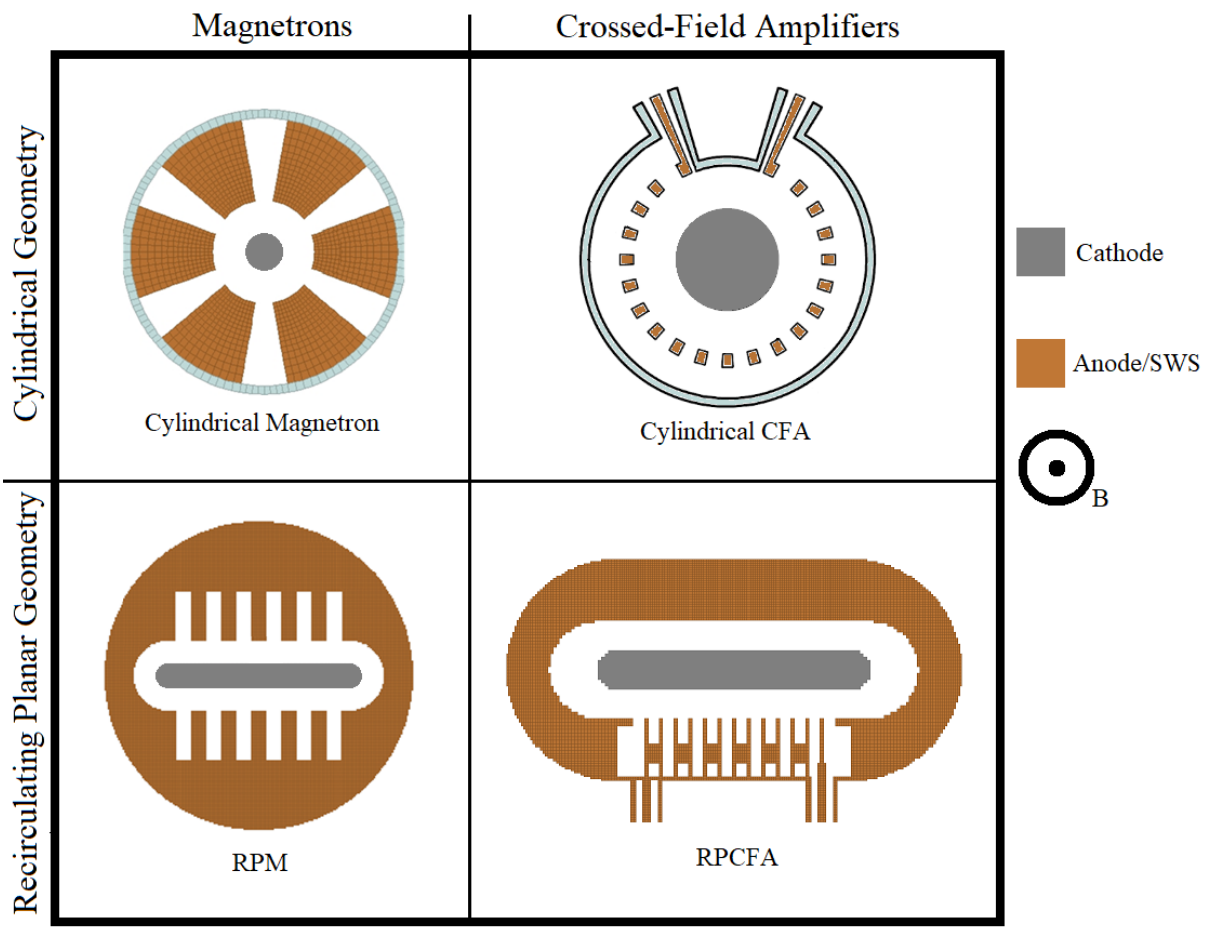

Figure 1.2: Comparison of cylindrical and recirculating planar geometries for magnetrons and CFAs.

The identification of amplified output power is a nuanced topic which requires detailed observation of the device in order to differentiate it from primed oscillators [37]. The criteria that must be satisfied for an amplifier is compared in Table 1.1, with related forms of RF signal generation from primed oscillators which may be confused with amplification: soft excitation, and hard excitation. In the absence on an injected RF signal ($P_{in} = 0$), both the amplifier and a device operating in the hard excitation regime generate no output signal, while a device undergoing soft excitation oscillates at its free running frequency. If the power of an injected RF signal is reduced to zero (P_{in} is reduced to 0) after initially driving the device, the amplifier ceases to produce an output signal whereas the hard excitation will continue to oscillate. The amplifier is the only device compared here for which the output power is a function of the power of the injected signal ($P_{out} = P_{out}(P_{in})$), although it may not necessarily be a linear correlation. All three devices can display

frequency locking, where the output frequency is locked to the drive frequency ($f_d = f_0$), and phase locking, where the phase of the device measured at a given location is locked to a known phase shift of the input signal ($\phi_{out} = \phi_{out}(\phi_{in})$). For an amplifier this is always the case. However, with sufficient injected drive power and frequency near enough to the free-running frequency of the excited oscillator, both hard and soft excitation can display these phenomena. The requirements for power and frequency are given by Adler's condition [38]:

$$\frac{P_{in}}{P_{out}} = Q^2 \left[\frac{(f_d - f_0)}{f_0}\right]^2, \tag{1.1}$$

where P_{in} is the injected power, P_{out} is the power of the primed oscillator, Q is the quality factor of the primed oscillator, f_0 is the free running frequency of the primed oscillator, and f_d is the drive frequency.

	Soft Excitation	Hard Excitation	Amplification
$P_{in} = 0$	Free Oscillation ✗	$P_{out} = 0$ ✓	$P_{out} = 0$ ✓
P_{in} is reduced to 0	Free Oscillation ✗	$P_{out} \neq 0$ ✗	$P_{out} = 0$ ✓
Is $P_{out} = P_{out}(P_{in})$?	No ✗	No ✗	Yes ✓
$f_d = f_0$?	Yes, for sufficiently high P_{in} and f_d near f_0	Yes, for sufficiently high P_{in} and f_d near f_0	Yes ✓
$\phi_{out} = \phi_{out}(\phi_d)$?	Yes, for sufficiently high P_{in} and f_d near f_0	Yes, for sufficiently high P_{in} and f_d near f_0	Yes ✓

Table 1.1: Comparison of amplification with primed oscillators of both soft and hard excitation. Green check marks indicate a feature confirmed on the RPCFA. Red x-marks indicate a feature not observed.

This dissertation will detail the development of the RPCFA. Chapter 2 will present the theoretical principles behind the design of the slow wave structure and surrounding components. Cold-tube and hot-tube simulations will be used to predict the performance of the device. Chapter 3 will discuss the fabrication of the prototype and the hardware used for experimentation. Chapter 4 will present the results of those experiments and discuss the implications of these results including their agreement or disagreement with simulated results. Chapter 5 will summarize the progress of this investigation and highlight key results. Recommendation for future study will also be provided.

CHAPTER 2

Theory and Simulation

This chapter provides the theoretical framework regarding the operation of the RPCFA as well as its design. Cold tube dispersion characteristics are predicted and verified in simulation. Cold tube simulations, involving calculation of scattering parameters and RF electric fields, are used to optimize the slow wave structure (SWS). The results of cold tube simulation, performed in Ansys HFSS, are verified using a particle-in-cell (PIC) code which is also employed to perform hot tube simulations. The results of these simulations are tested experimentally in chapter 4.

2.1 Single Particle Motion

The operation of the Crossed-Field Amplifier (CFA) is very similar to its close relative, the magnetron. For both devices, an insulating magnetic field is applied perpendicular to the DC electric field. Electrons emitted from the cathode are governed by the Lorentz force and deflected by this magnetic field. They undergo cycloidal motion, propagating in the direction perpendicular to both the electric and magnetic field, according to the $E \times B$ drift [39]. For simplicity, we consider a nonrelativistic, planar, crossed-field diode, and ignore the self-fields of the electrons. The Lorentz force equation,

$$m\frac{d\vec{v}}{dt} = e(\vec{E} + \vec{v} \times \vec{B}), \tag{2.1}$$

subject to the external DC electric and magnetic fields, $\vec{E} = \hat{x}E_0$ and $\vec{B} = \hat{z}B_0$, may be written in component form,

$$m\frac{dv_y}{dt} = e(v_x B_0) \tag{2.2}$$

$$m\frac{dv_x}{dt} = -e(E_0 + v_y B_0) \tag{2.3}$$

For cases involving anode-cathode gap voltages exceeding 1 kV, it may be assumed that electrons are emitted from the cathode with zero initial velocity. An electron emitted from the cathode at time $t = 0$ at position $(x, y) = (0,0)$ follows these orbital equations:

$$y(t) = \frac{1}{\Omega_c}\frac{E_0}{B_0}(\sin(\Omega_c t) - \Omega_c t) \tag{2.4}$$

$$x(t) = \frac{1}{\Omega_c}\frac{E_0}{B_0}(\cos(\Omega_c t) - 1) \tag{2.5}$$

where $\Omega_c = |eB|/m$ is the electron cyclotron frequency. Averaging these equations over the period of one cyclotron period, $T = 2\pi/\Omega_c$ and dividing by the period gives the average drift velocity, $(\langle v_x \rangle, \langle v_y \rangle) = (0, E_0/B_0)$, which is the $E \times B$ drift. This electron, which is at a distance D from the cathode, will not reach the anode if $D > 2E_0/\Omega_c B_0$ according to Eq. (2.5). This is the condition for "magnetic insulation", $B_0 > B_H$, where B_H is the Hull cutoff magnetic field,

$$B_H = \sqrt{\frac{2mV_0}{eD^2}} \tag{2.6}$$

Most crossed-field devices operate with an external magnetic field between 1.5 to 3 times the Hull cutoff value [40].

In the absence of other fields, this magnetically insulated diode generates no RF power. However, once an RF signal is present, either self-excited in an oscillator or externally provided in an amplifier, electron current can be drawn across this magnetically insulated gap. The electric potential energy gained from the electron motion then leads to growth of this RF signal. This is illustrated in Figure 2.1.

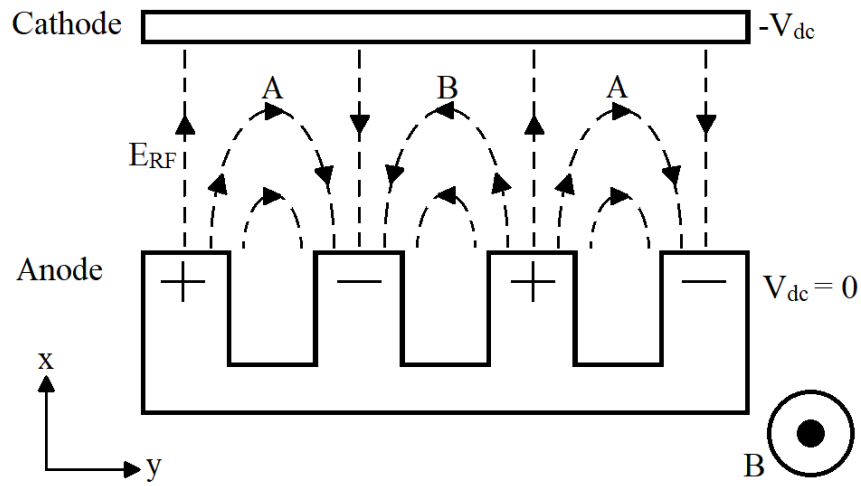

Figure 2.1: Example of anode circuit and cathode. The circuit mode illustrated is the "pi-mode", where there is a phase shift of π between adjacent anode cavities. The dash lines show the RF electric fields which are assumed to co-move to the right at the $E \times B$ drift velocity, so that this circuit mode may synchronously interact with the electrons. The magnetic field, B, points out of plane of the paper.

Consider now the action of the RF electric field on an electron positioned at point A in Figure 2.1. The $E_{rf} \times B$ drift brings electron A toward the anode without much change of its kinetic energy. By energy conservation, electron A instead yields its potential energy to the RF electric field. Conversely, an electron at point B experiences an $E_{rf} \times B$ drift that accelerates it towards the cathode, and in so doing, electron B absorbs energy from the RF electric field. Thus, the A-electrons lead to wave energy gain while the B-electrons lead to wave energy loss. However, examining the $E_{rf} \times B$ drift on the vertical lines midway between A and B, one readily sees that the B-electrons tend to drift towards the A-electrons. That is, the B-electrons are depleted and they are turned into the A-electrons. This is why electron current spokes are generated from the A-electrons and there are very few B-electrons in between. This is also the reason why crossed-field devices are very efficient, because virtually all of the potential energy carried by the A-electrons is converted to RF energy, with few B-electrons left behind. This explains why formation of electron spokes is so important for the functioning of RF crossed-field devices [27].

2.2 Brillouin Flow

While imagining the motion of a single particle is useful in understanding the fundamental operation of crossed-field devices, an alternate description is the Brillouin flow model [22 – 27]. The Brillouin flow is a laminar flow extending from the cathode to a specific distance into the A-K gap called the "hub height", and it has been shown to be the dominant flow pattern in crossed-field devices. Electrons in this "Brillouin hub" travel parallel to the surface of the cathode in the direction of $E \times B$ drift.

We again assume a nonrelativistic treatment of the Brillouin flow. Electrons are assumed to be emitted from the cathode with zero energy and the electric field at the surface of the cathode is taken to be zero due to the space charge of the Brillouin hub. Thus, the self electric field is important while the self magnetic field is not. For the equilibrium steady state flow, we set the net force on a particle to zero, equation 2.3 gives

$$v_y(x) = -E_0(x)/B_0. \tag{2.7}$$

Conservation of energy gives

$$\frac{1}{2}mv_y^2 = e\phi(x), \tag{2.8}$$

where $\phi(x)$ is the electric potential. Gauss's law relates the electric field to the charge density in this 1D diode,

$$\frac{\partial E_0(x)}{\partial x} = en_0/\varepsilon_0. \tag{2.9}$$

Equations 2.7, 2.8, and 2.9 may easily be shown to admit solutions that are linear in x for E_0 and v_y, and a constant for the density n_0. The electron density of the hub satisfies

$$\omega_p^2 = \Omega_c^2 \tag{2.10}$$

where $\omega_p = \sqrt{\frac{e^2 n_0}{m\epsilon_0}}$ is the electron plasma frequency. The velocity of particles in the Brillouin hub is given by

$$v_y(x) = \Omega_c x, \tag{2.11}$$

and the hub height, x_b, is given by

$$x_b = D\left(1 - \sqrt{1 - 2V_0/\Omega_c B_0 D^2}\right) = D\left(1 - \sqrt{1 - (\frac{\boldsymbol{B}_H}{B_0})^2}\right), \tag{2.12}$$

where D is the A-K gap spacing and $\boldsymbol{B}_H$ is the Hull cutoff magnetic field given in equation 2.6. Thus, given a DC potential, V_0, a magnetic field, $B_0 > B_H$, and an A-K gap spacing, D, the properties of the Brillouin hub are completely described by Eqs. (2.10), (2.11), and (2.12).

2.3 Amplification in CFAs

The nature of amplification in crossed-field amplifiers can be qualitatively understood by applying Maxwell's equations to a resonant structure as shown in Figure 2.1 and assuming solutions of the form $X(x,t) = X_0 + X_1 e^{i\omega t - i\vec{k}\cdot\vec{x}}$ where the subscript 0 (1) denotes the DC (perturbation) quantity. The Maxwell equations govern the perturbation (or RF) quantities:

$$\nabla \times \overrightarrow{E_1} = -\mu_0 \frac{\partial \overrightarrow{H_1}}{\partial t} = -i\mu_0 \omega \overrightarrow{H_1}. \tag{2.13}$$

$$\nabla \times \overrightarrow{H_1} = \overrightarrow{J_1} + i\varepsilon_0 \omega \overrightarrow{E_1}. \tag{2.14}$$

Taking the curl of equation 2.14 and applying Gauss's law, $\nabla \cdot \vec{H} = 0$, yields

$$\frac{\omega^2}{c^2}\overrightarrow{H_1} + \nabla^2 \overrightarrow{H_1} = -\nabla \times \overrightarrow{J_1}. \tag{2.15}$$

From equation 2.15 may be solved for the cold tube dispersion relation, $\omega = \omega_c(k)$, by setting $\overrightarrow{J_1} = 0$, and by solving the eigenvalue equation,

$$\frac{\omega_c^2(k)}{c^2}\overrightarrow{H_{1V}} + \nabla^2\overrightarrow{H_{1V}} = 0. \tag{2.16}$$

The approximation is then made that the introduction of current does not substantially alter $\overrightarrow{H_1}$ from the cold tube solution, that is, $\overrightarrow{H_1} \approx \overrightarrow{H_{1V}}$. Combining this approximation with equations 2.15 and 2.16 gives

$$\left(\frac{\omega^2}{c^2} - \frac{\omega_c^2(k)}{c^2}\right)\overrightarrow{H_{1V}} \approx -\nabla \times \overrightarrow{J_1}. \tag{2.17}$$

Multiplying equation 2.17 with $\vec{H}_{1V}^*$ and integrating over the volume of the A-K gap, gives

$$\left(\frac{\omega^2}{c^2} - \frac{\omega_c^2(k)}{c^2}\right)\iiint |H_{1V}|^2\, d^3V \approx \iiint -(\nabla \times \overrightarrow{J_1}) \cdot \vec{H}_{1V}^* d^3V. \tag{2.18}$$

Performing an integration by parts on the RHS, applying the Maxwell equation (2.14) in the absence of current, and rearranging gives:

$$\frac{\omega^2}{c^2} - \frac{\omega_c^2(k)}{c^2} \approx \frac{\iiint \overrightarrow{J_1} \cdot i\omega_c \varepsilon_0 \vec{E}_{1V}^* d^3V}{\iiint |H_{1V}|^2\, d^3V}. \tag{2.19}$$

Equation 2.19 gives insight into the nature of gain in all amplifiers, including the crossed-field amplifiers. It says that there could be change in the real part of the frequency (detune) and in the imaginary part of the frequency (gain) by the action of the AC current on the cold-tube circuit mode, through the product $\overrightarrow{J_1} \cdot \vec{E}_{1V}^*$ that appears in the RHS of Eq. (2.19). While the DC fields are necessary for current emission and synchronism between the electron flow and the circuit wave, amplification is due to the RF current and the RF field. We shall now use Eq. (2.19) to illustrate qualitatively why a linear tube such as TWT has a higher gain than a crossed-field tube such as a CFA.

In a TWT, a strong magnetic field is applied in the direction of the beam motion which constrains the motion of particles along the magnetic field. The orbit of an electron is defined by, $\vec{x}(t) = \hat{y}v_0 t +$

$\vec{x}_1(t)$, with $\vec{x}_1 = \hat{y}y_1$, where v_0 is the DC beam velocity, and the electron's perturbation displacement, due to an AC electric field along the beam, E_{1y}, is governed by,

$$\ddot{y}_1 = eE_{1y}/m. \tag{2.20}$$

The AC current density on the beam of the TWT, $\overrightarrow{J_1} = en_0 \frac{\partial \vec{x}_1}{\partial t}$, for a traveling wave solution, may then be computed,

$$\overrightarrow{J_1} = \hat{y} i\omega \frac{e^2 n_0}{m} \frac{E_{1y}}{(\omega - k_y v_0)^2}. \qquad \text{(TWT)} \tag{2.21}$$

For a CFA, the perturbed motion is due to the $E \times B$ drift, whose perturbation displacement becomes

$$\overrightarrow{x_1} = (x_1, y_1) = \frac{1}{i(\omega - k_y v_0)} \left(\frac{-E_{1y}}{B_0}, \frac{E_{1x}}{B_0} \right). \tag{2.22}$$

So the AC current density in a CFA may be approximately written as

$$\overrightarrow{J_1} = \frac{\omega e n_0}{(\omega - k_y v_0)} \left(\frac{-E_{1y}}{B_0}, \frac{E_{1x}}{B_0} \right). \qquad \text{(CFA)} \tag{2.23}$$

In the present linear theory, the AC current is assumed to only slightly perturb the vacuum mode, $\omega \approx \omega_c(k)$, thus we may approximate the LHS of Eq. (2.19) as

$$\omega^2 - \omega_c^2(k) \approx (\omega - \omega_c(k))(2\omega). \tag{2.24}$$

Applying this approximation to equation 2.19 and the derived current densities for the TWT and CFA in equations 2.21 and 2.23 respectively gives

$$\omega - \omega_c(k) \propto \frac{I}{(\omega - k_y v_0)^2} \qquad \text{(TWT)} \tag{2.25}$$

$$\omega - \omega_c(k) \propto \frac{I}{(\omega - k_y v_0)} \qquad \text{(CFA)} \tag{2.26}$$

where I is the DC current, which is directly proportional to the DC electron density, n_0, that appears in both Eqs. (2.21) and (2.23). Next, for both TWT and CFA, we require operation close to the synchronism

condition, which can be defined as, $\omega_c(k) = k_y v_{phase} = k_y v_0$. In terms of the dimensionless gain parameter, C, that was introduced by Pierce, where $C^3 \propto$ I, Eq. (2.25) then yields the following growth rate for a linear tube,

$$\omega_i/\omega \propto C. \qquad \text{(TWT)} \tag{2.26}$$

Likewise, for the CFA, Eq. (2.26) gives,

$$\omega_i/\omega \propto C^{3/2}. \qquad \text{(CFA)} \tag{2.27}$$

Note that the exponentiation rate in a CFA is less than the exponentiation rate for a TWT by a factor of $C^{1/2}$, by comparing Eq. (2.26) and (2.27). Since the typical values for *C* range between 0.01 and 0.1, the exponentiation rate in a CFA is only about 1/10 to 1/3 of a TWT for similar frequency, beam voltage, and beam current. This qualitatively explains why CFA is a lower gain device (typically 13 dB), but operates at a higher power and efficiency because virtually all of the potential energy in the DC state may be utilized for RF generation or amplification.

2.4 Dispersion in the RPCFA

The vacuum mode solution is governed by equation 2.16, and this cold-tube mode is critical to the operation of the amplifier. The cold tube dispersion relation can be derived approximately using the same lumped circuit element analysis used to model magnetrons. The electrical functions in a CFA SWS are very different from magnetrons as they serve nearly opposite purposes, the magnetron is composed of high quality factor resonators while the CFA is essentially a low quality factor transmission line; however, the topology of the circuit is nearly identical. A section of a cylindrical magnetron can be modelled as the circuit shown in Figure 2.2.

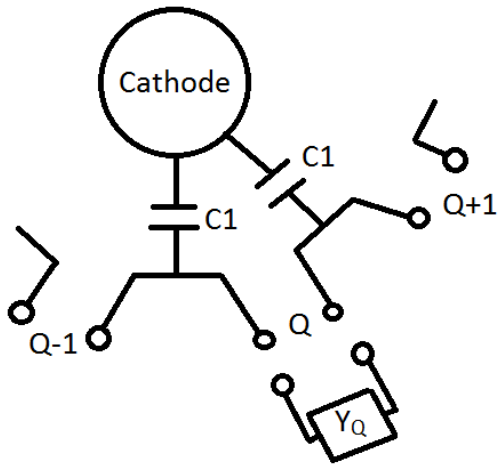

Figure 2.2: Lumped circuit element model for a section of a magnetron. Y_Q is the admittance of cavity Q [41].

The cylindrical geometry is irrelevant as the circuit topology remains the same for a planar magnetron or planar CFA. In order for resonance to occur, the admittance looking out from the cavity must be equal to the admittance looking into the interaction space [41]. The admittance of cavity Q is simply given by

$$Y_Q = -i\left(\omega C - \frac{1}{\omega L}\right), \tag{2.30}$$

where C and L are the capacitances and inductances of cavity Q respectively. To obtain the admittance looking into the interaction space we can analyze the circuit around the cavity as shown in Figure 2.3.

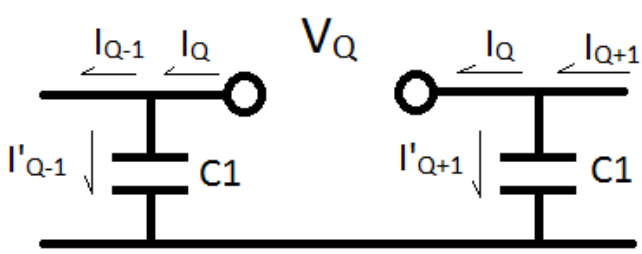

Figure 2.3: Circuit diagram for a magnetron around cavity Q.

From the diagram it is apparent that

$$I'_{Q-1} = I_Q - I_{Q-1} \tag{2.31a}$$

$$I'_{Q+1} = I_{Q+1} - I_Q. \tag{2.31b}$$

The voltage across the capacitors, in general, is given by

$$V = I/i\omega C1. \tag{2.32}$$

V_Q is the difference between the voltages across the two capacitors and is thus given by

$$V_Q = (1/i\omega C1)[I'_{Q-1} - I'_{Q+1}]. \tag{2.33}$$

Applying equations 2.31a and 2.31b yields

$$V_Q = (1/i\omega C1)[2I_Q - I_{Q-1} - I_{Q+1}]. \tag{2.34}$$

It is assumed that between adjacent resonators, the voltage and current vary only a constant phase factor, γ. Thus, V_Q can be written entirely in terms of I_Q, as

$$V_Q = (I_Q/i\omega C1)[2 - e^{-i\gamma} - e^{+i\gamma}] = (2I_Q/i\omega C1)[1 - \cos(\gamma)] \tag{2.35}$$

Taking the definition of admittance Y = I/V gives the admittance looking into the interaction space around cavity Q

$$Y_Q = \frac{i\omega C1}{2(1-\cos(\gamma))}. \tag{2.36}$$

Combining equations 2.36 and 2.30 gives

$$\frac{1}{\omega L} - \omega C = \frac{\omega C1}{2(1-\cos(\gamma))} \tag{2.37}$$

Letting $\omega_0 = 1/\sqrt{LC}$ and $P = C1/C$ and rearranging, taking only the positive value for the frequency gives the expected dispersion relation

$$\frac{\omega}{\omega_0} = 1/\sqrt{1 + \frac{P}{2(1-\cos(\gamma))}}. \tag{2.38}$$

For magnetrons, the resonators form a complete loop, creating the condition that the total phase shift around all the resonators is an integer multiple of 2π. It follows that Nγ = 2πn where N is the total number of resonators and n is an integer. Applying this to equation 2.38 gives the dispersion relation, as the guided wavenumber is directly proportional to γ and the physical dimensions of the slow wave structure. Writing equation 9 in terms of n gives

$$\frac{\omega}{\omega_0} = 1\Big/\sqrt{1 + \frac{P}{2(1-\cos(2\pi n/N))}}. \tag{2.39}$$

Equation 10 is plotted for P = 1 and N = 12 in Figure 2.4.

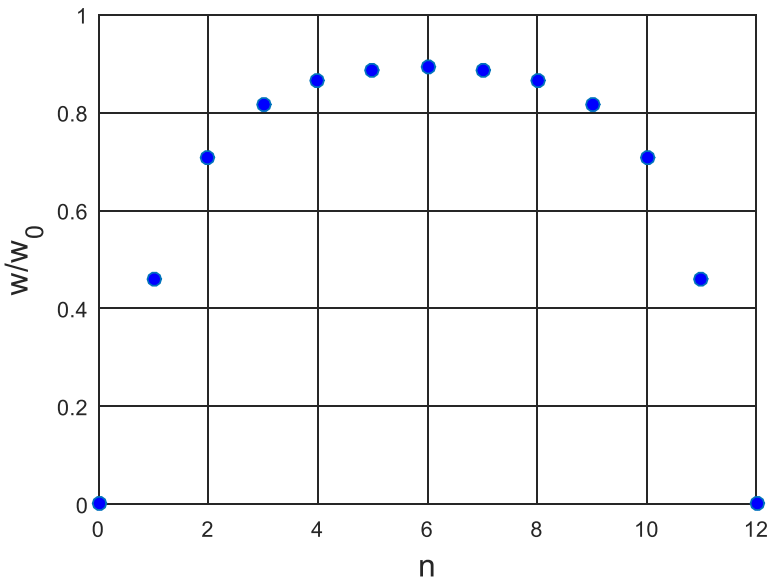

Figure 2.4: Expected dispersion relation for a magnetron with N = 12 cavities. The n = 6 mode is the π -mode.

A common operating mode, known as the π-mode, occurs when the AC voltage across each cavity is exactly 180 degrees out of phase with adjacent cavities. In this case n = N/2 = 6 and the argument in the cosine in equation 2.39 is π. At this mode the group velocity, $\Delta\omega/\Delta n$, is equal to zero indicating RF power is held stationary of the SWS. While the beam and the phase velocity of the circuit wave move forward, there is no energy propagation of the wave. This is opposite the desired behavior for the operating mode for a CFA.

For a CFA, the circuit can be modeled as a series of identical "cells" with some general impedance, Z_q, arranged in series and connected to a grounded substrate through another impedance, Z_A. This is depicted in Figure 2.5. The circuit is distinct from the magnetron circuit as the CFA SWS does not strongly capacitively couple to the cathode. While the magnetron identified resonances by matching admittances into the cavity with those into the interaction space, the CFA SWS is a transmission line where the signal carrying electrode couples both inductively and capacitively primarily to the grounded substrate, though

the cathode may contribute to the total capacitance within Z_A. In the transmission line model of Figure 2.5, Z_q represents the unit cell impedance, and Z_A represents the parasitic impedance.

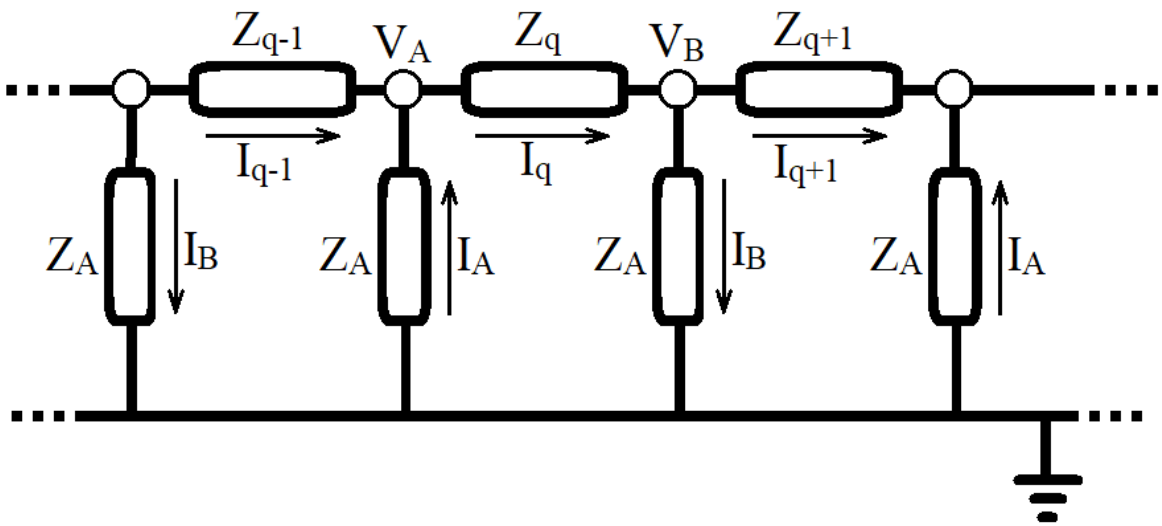

Figure 2.5: Circuit model for general CFA SWS.

It is apparent from Figure 2.13 that:

$V_A = -I_A Z_A$ (2.40a) $V_B = I_B Z_A$ (2.40b)

$I_{q-1} = I_q - I_A$ (2.40c) $I_{q+1} = I_q - I_B$ (2.40d)

Defining the voltage across cell q, $V_q = I_q Z_q$ gives,

$$V_q = V_B - V_A = (I_A + I_B)Z_A \tag{2.41}$$

Combining equations 2.40c and 2.40d gives

$$I_A + I_B = 2I_q - I_{q+1} - I_{q-1} \tag{2.42}$$

As in the analysis for the magnetron, it is assumed the quantities, V_q and I_q vary only by a phase shift, β such that $X_{q\pm1} = X_q e^{\pm i\beta}$. Equation 2.42 can then be rewritten

$$I_A + I_B = 2I_q(1 - \cos(\beta)) \tag{2.43}$$

Substituting this into equation 2.41 gives

$$I_q Z_q = 2I_q Z_A(1 - \cos(\beta)) \tag{2.44}$$

Assuming the impedance is purely reactive, and defining $Z_q = i\omega L - i(1/\omega C)$, and $Z_A = i\omega L_A - i(1/\omega C_A)$, equation 2.44 becomes

$$\omega L - \frac{1}{\omega C} = (2 - 2\cos(\beta))\left(\omega L_A - \frac{1}{\omega C_A}\right) \tag{2.45}$$

Defining $\omega_0 = 1/\sqrt{LC}$, $L' = L/L_A$, and $C' = C/C_A$, then multiplying equation 2.45 by ωC, gives

$$\left(\frac{\omega}{\omega_0}\right)^2 - 1 = (2 - 2\cos(\beta))\left(\frac{\omega^2}{\omega_0^2}\frac{1}{L'} - C'\right). \tag{2.46}$$

Solving for ω/ω_0,

$$\frac{\omega}{\omega_0} = \left[\frac{1+(2\cos(\beta)-2)C'}{1+(2\cos(\beta)-2)(1/L')}\right]^{1/2} \tag{2.47}$$

gives the cold tube dispersion relation for the CFA. The quantities *C'* and *L'* are properties of the SWS cell. *C'* is taken to be small (~ 0.1) so that ω remains real and lossless. *L'* is assumed large for the same reason though this could be inferred as the long circuitous current path of a SWS is likely a higher inductance than the stubs which connect it to the substrate. Equation 2.47 is plotted in Figure 2.6 for various values of *C'* and *L'*. The forward wave and backward wave dispersion relations can both be recovered by selecting the appropriate values of *C'* and *L'*. As could be inferred from Figure 2.6, for the fundamental mode, $\beta/\pi < 1$, the forward wave occurs when $C' * L' < 1$, the and the backward wave occurs when $C' * L' > 1$.

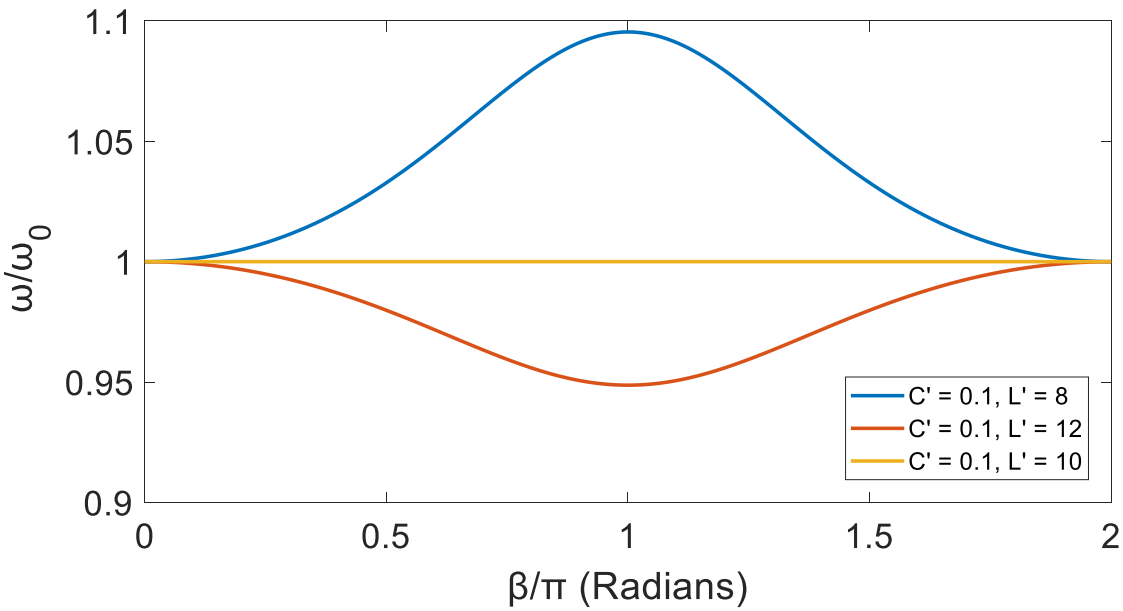

Figure 2.6: Dispersion relation for various values of *C'* and *L'*. The forward wave solution is in blue and the backward wave solution is in red, both for the fundamental mode, $\beta/\pi < 1$. A zero group velocity mode is shown in yellow.

This method can be applied to the RPCFA SWS if the unit cell impedance, Z_q, and parasitic impedance, Z_A, are calculated. The inductances can be evaluated by generating a unit cell in ANSYS MAXWELL [42] and applying a current source at one terminal and moving the sink to the other terminals. The inductances can be evaluated from the magnetic fields generated by each conduction path. A unit cell, to be used in the RPCFA, with current paths for L_q and L_A is shown in Figure 2.7a. Figure C.1a details the dimensions of the RPCFA unit cell.

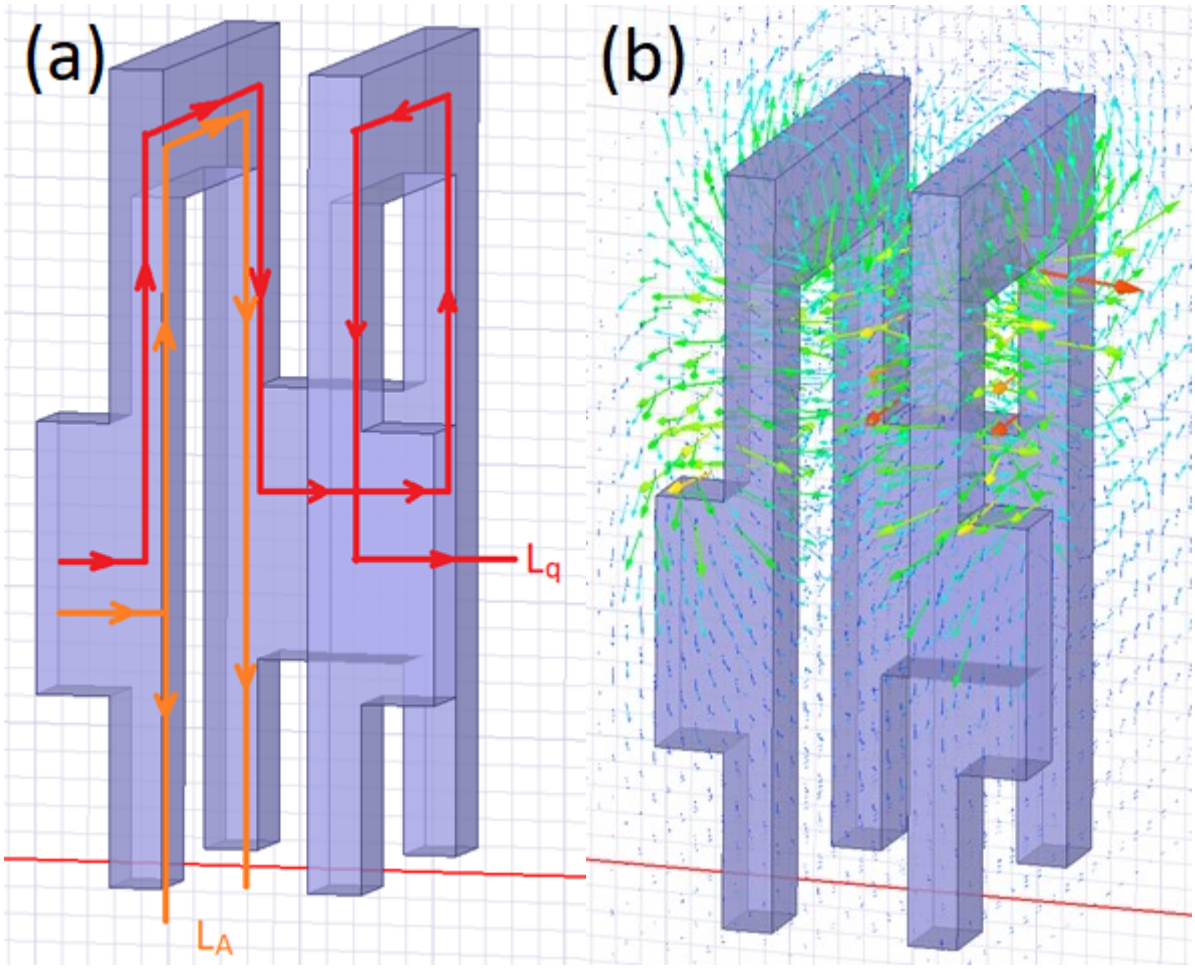

Figure 2.7a (left): Unit cell with the current paths for measuring L_q and L_A. The lower boundary is a grounded conducting plane.
Figure 2.7b (right): Magnetic field generated by current flowing on the L_q path.

The current source is placed at the left end of the cell as shown in Figure 2.7a, and the sink is moved to the ends of the current paths as drawn. The current generates a magnetic field, from which the inductance is calculated. The magnetic field generated from current flowing across the structure is shown in Figure 2.7b. The inductance for this path is $L_q = 21.65$ nH. For the shorter of the two paths to the ground plane the inductance is 3.64 nH and the longer is 15.89 nH. This gives an equivalent inductance $L_A = 2.96$ nH.

Capacitances are measured in a similar manner. In ANSYS HFSS [43], a 3 GHz excitation is launched from the input side of a unit cell. To measure the parasitic capacitance, C_A, the output side of the cell is modelled as a perfectly matched load and half of the lower boundary is assigned to be a second waveport, the other half is the conducting ground plane as shown in Figure 2.8. To calculate the cell

capacitance C_q, the lower boundary is entirely set to a conducting ground plane and the output side of the cell is the second waveport. The capacitances are calculated from the formula $C = (-1/2\pi f) * (1/im\{Z_{21}\})$. HFSS gives these values C_q = 15.3 pF and C_A = 129.4 pF. With these parameters calculated, equation 2.47 can be applied to get the RPCFA dispersion relation, plotted in Figure 2.9.

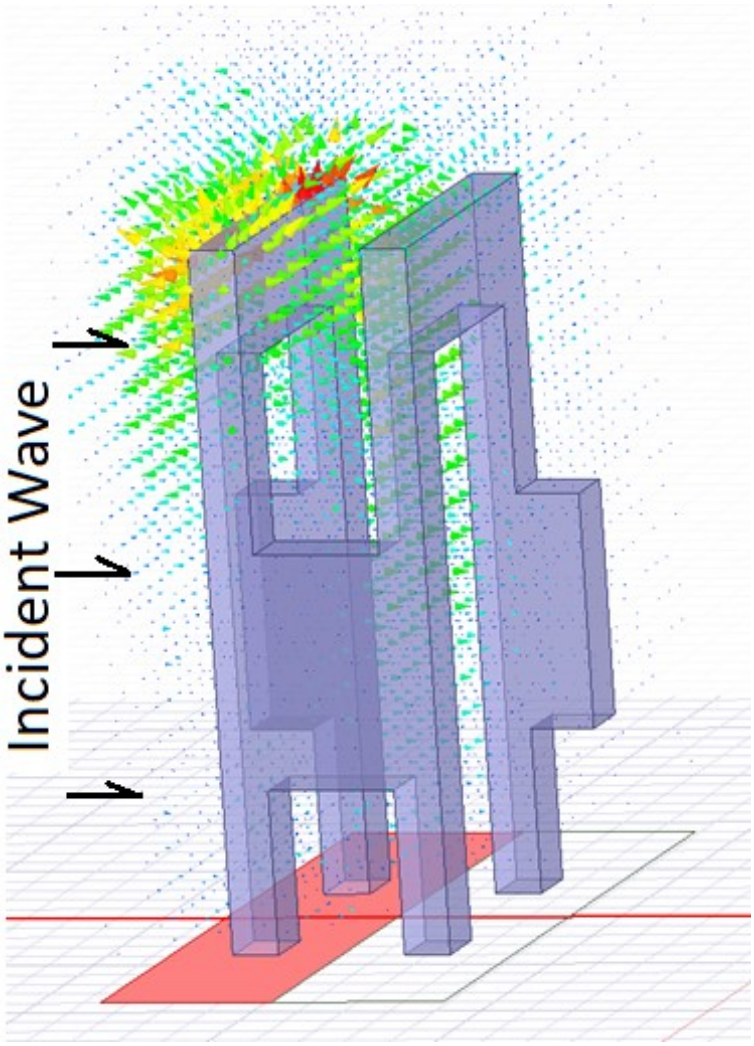

Figure 2.8: Electric fields generated from a 3 GHz excitation from the waveport at the left side of the cell to the highlighted waveport at the lower boundary.

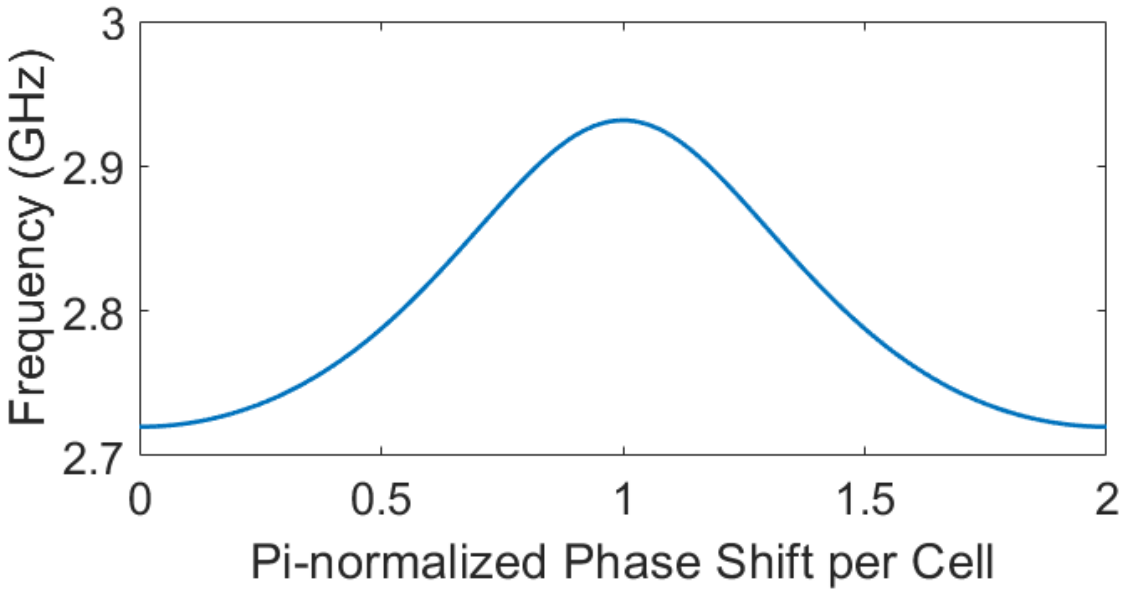

Figure 2.9: Dispersion relation from equation 2.47 with lumped circuit element values calculated from ANSYS HFSS and MAXWELL.

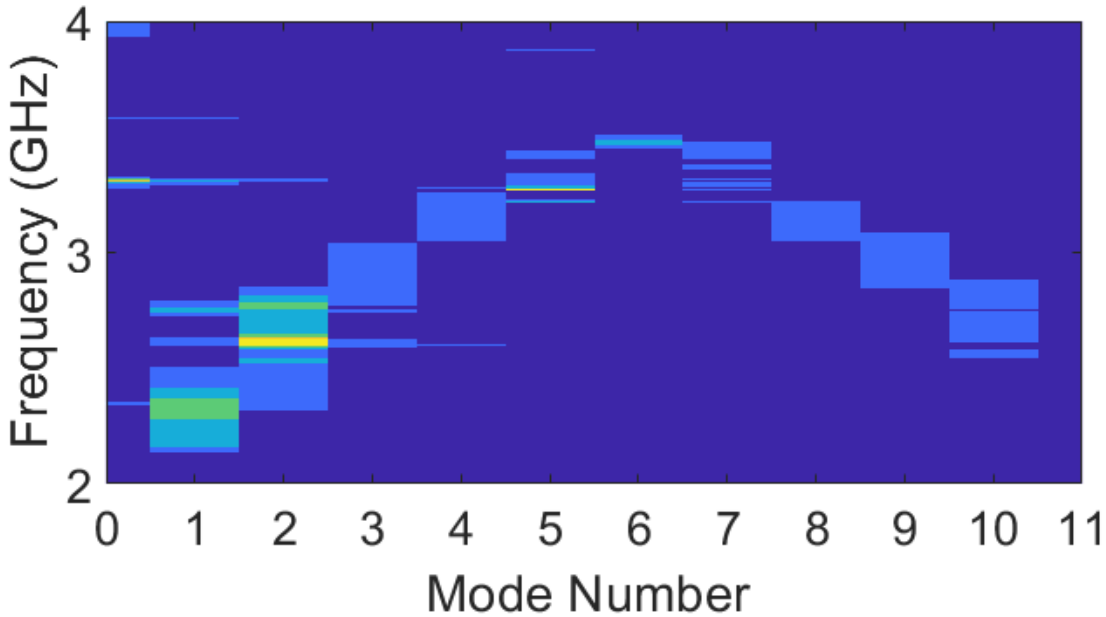

Figure 2.10: MAGIC dispersion relation. Discrete mode numbers are given due to discrete spatial sampling. A mode number of 3 corresponds to a $\pi/2$ phase shift per cell on this 12 cell RPCFA.

This dispersion relation can be compared with the same quantity generated in MAGIC [44]. To generate the MAGIC dispersion relation the full RPCFA was modeled and excited using a loop antenna placed on the surface of the cathode, across the A-K gap from the center of the SWS. The RF electric field

was recorded over time for 24 locations (2 per cell) position along the center of the A-K gap in a line parallel to the direction of RF propagation. A 2-D FFT can be applied to this matrix of electric field over time and position, *E(x,t)*, to get the dispersion relation $\hat{E}(\omega, \beta)$. This dispersion relation is plotted in Figure 2.10.

The MAGIC dispersion relation shows operation at higher frequencies with greater variation due to phase shift compared to the theoretical prediction. This can be attributed to the approximations made regarding the boundary conditions in the ANSYS simulations. The position of conducting boundaries adds an additional parasitic capacitance that is unaccounted for in the above analysis. Regardless, the analytic theory correctly predicts the forward wave interaction and gets within 10% of the design frequency.

2.5 Designing the Slow Wave Structure

The slow wave structure is responsible for ensuring the correct interaction between the electron beam and the RF excitation [45]. In general, the SWS for an amplifier should behave as a transmission line when the device is off, allowing an injected RF wave to pass from the input to the output port without attenuation or distortion [18]. In terms of scattering parameters, this means high S_{12} and low S_{11}, over the range of frequencies the device will amplify. The SWS was designed using ANSYS Electronic Desktop, HFSS driven model solutions. A coaxial transmission line connected to the first cell forms the input waveport and an identical transmission line connected to the eighth and final cell forms the output waveport. The scattering parameters listed above are measured as the dimensions of the cell is varied to find the optimal geometry. The shape of the cell draws inspiration from the planar cavity arrays used on magnetrons in previous experiments [34, 46] and the meander-line circuits of existing CFAs. A planar structure array ensures the transverse RF fringing fields needed for drawing current. The vanes are carved out and connected by straps to form the transmission line which carries RF current from the input to output port. The cell array developed in HFSS is shown in Figures 2.11a and b.

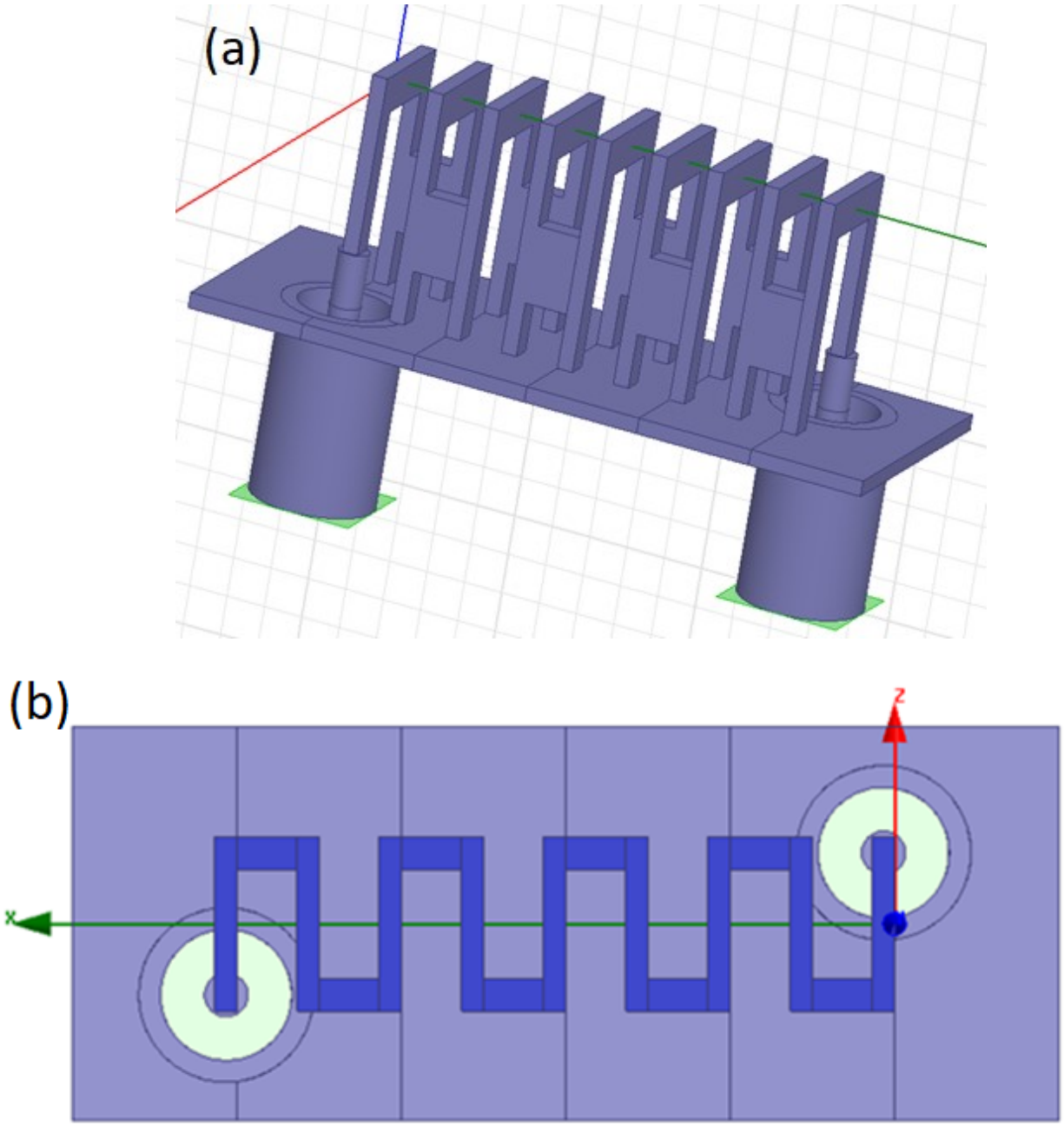

Figure 2.11a (top): Isometric view of an 8-cell SWS with coaxial input and output ports generated in HFSS.
Figure 2.11b (bottom): Top view of same SWS with the meander-line highlighted.

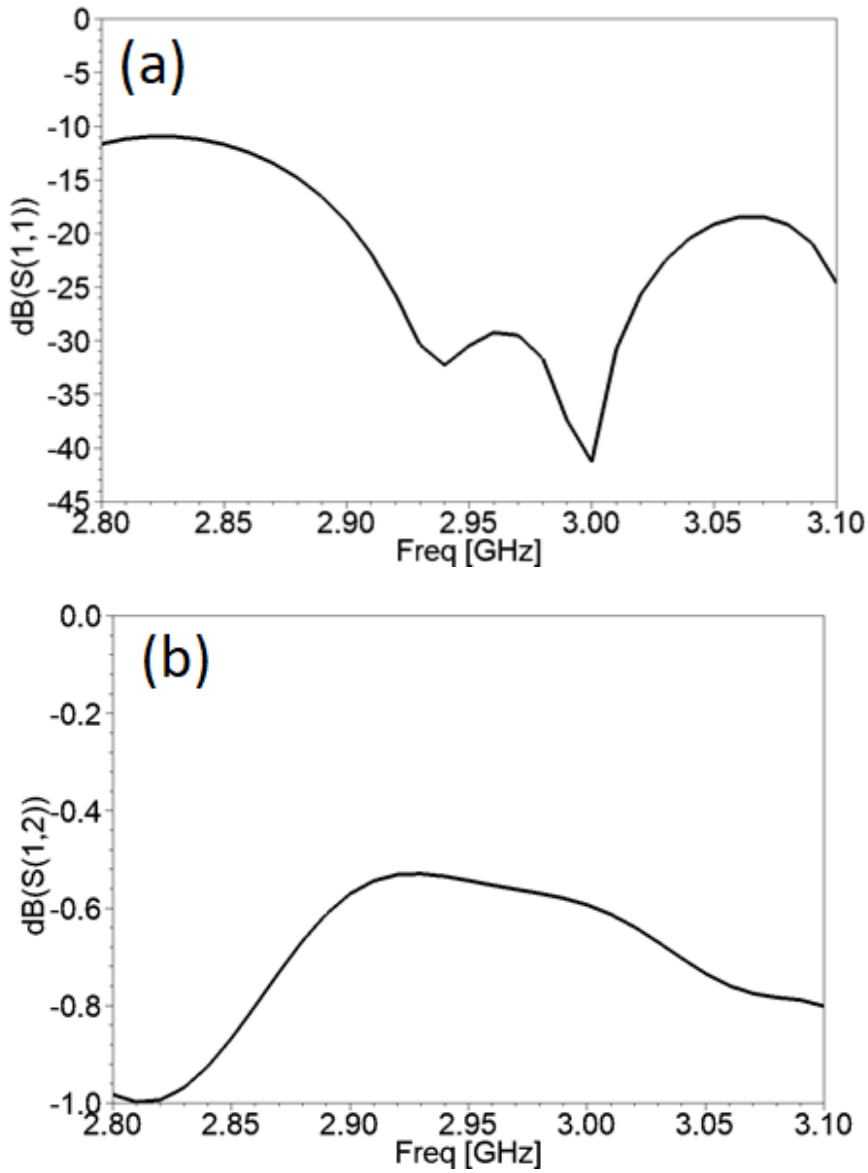

Figure 2.12a (top): S_{11} for the RPCFA SWS around the 3.0 GHz design frequency. The trace is identical to S_{22}.
Figure 2.12b (bottom): S_{21} for the RPCFA SWS. The trace is identical to S_{12}.

The S-parameters for the SWS are shown in Figure 2.12a and b. At the design frequency (3 GHz), the value of S_{11} is -40 dB, indicating that the slow wave structure will reflect 0.01% of the injected power back to the source. This level is low enough to ensure the source is protected from reflected power. At the same frequency, the value of S_{21} is approximately -0.6 dB indicating approximately 98.6% of RF power will be transmitted. This is an excellent transmission rate, though it is unlikely that this quality of transmission will be reproduced in a prototype due to manufacturing imperfections.

The quality factor, or Q, of the SWS can be calculated from the measurement of S_{21} using the formula [47]

$$Q = \frac{f_0}{f_2 - f_1} \tag{2.48}$$

where f_0 is the central transmitting frequency, f_1 is the greatest frequency less than f_0 where $S_{21} < -3$ dB and f_2 is the lowest frequency greater than f_0 where $S_{21} < -3$ dB, after subtracting transmission losses at the central frequency. Equation 2.48 is an accurate approximation for devices with bandwidths of one octave or less. Though not shown on Figure 2.12b, f_1 occurs at 2.4 GHz and f_2 occurs at 3.2 GHz giving a Q of approximately 3.7. This low Q is expected for a device that is designed to passively transmit power in a cold tube. For reference, a magnetron typically has Q in the 100's [48] and the MG5223F magnetron used to drive some of the RPCFA experiments had a Q measured at 308. In the case of the magnetron, the Q was measured by how rapidly power (P) was dissipated from the structure when the driver was turned off according to the formula

$$P(t) = P_0 \exp(-t\omega/2Q). \tag{2.49}$$

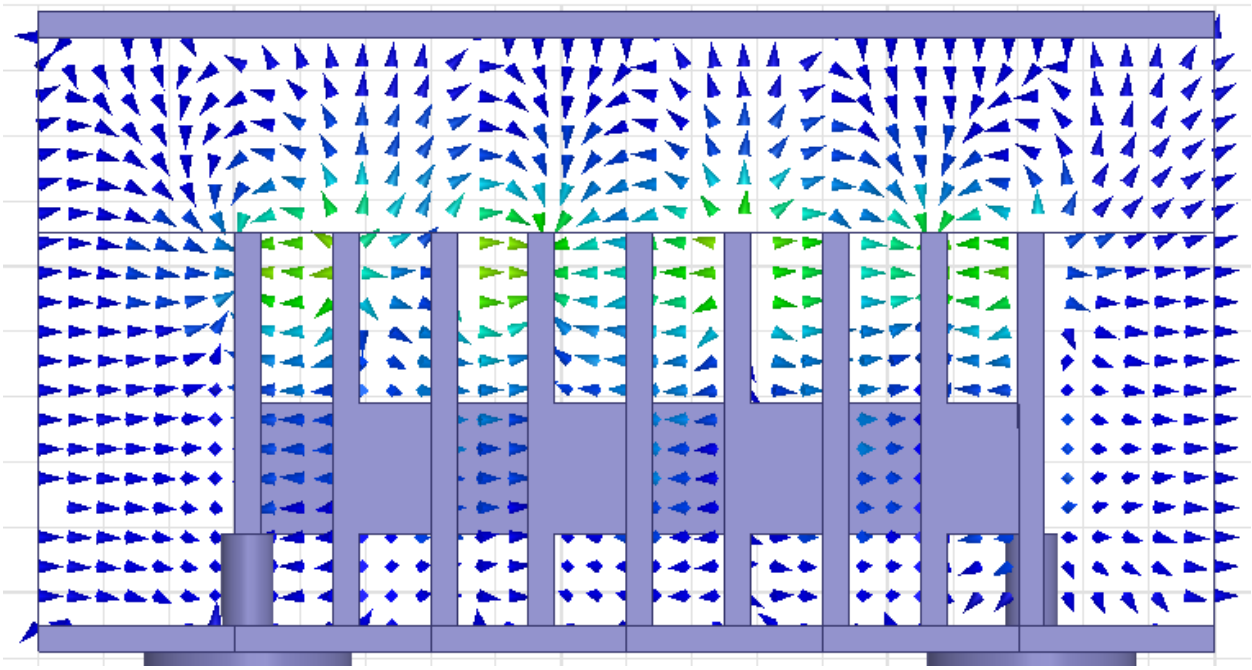

Figure 2.13: Electric field when the structure is excited by a 3 GHz RF signal. Lighter colors indicate a more intense field. Generated in HFSS.

This structure's response to a 3 GHz excitation can be viewed in Figure 2.13. From Figure 2.13 it is apparent that the phase shift of the electric field over a single cell is approximately $\pi/2$. This, combined with a SWS cell length of 7.5 mm gives a phase velocity of 0.3c which is slow enough to interact with the electrons in the Brillouin hub. When animated, it can be seen that this excitation moves smoothly from input to output, with minimal modulation, indicating this SWS is operating via a forward wave interaction. The boundaries around the simulation space shown in Figure 2.13 are a mix of conducting and radiative boundaries, though neither has a significant effect on the transmission of RF power across the SWS as the majority of the electric field power is carried close to the SWS.

2.6 Particle-in-Cell Simulations

To verify the results of the HFSS simulation, a 12-cell SWS was modeled using the electromagnetic particle in cell code, MAGIC. For this simulation, the interaction space is fully recirculating to efficiently recycle the beam as it would in experiment. The cathode is connected axially to a large waveport from which the pulsed excitation can be initiated to generate the DC electric field. The fields generated by the injection of 3 GHz RF into the RPCFA modelled in MAGIC are shown in Figure 2.14. The field pattern in Figure 2.14 also shows an approximately π/2 phase shift per cell, agreeing with the HFSS simulation, and verifying both simulations. In addition, minimal losses in RF power are measured across the length of the 12-cell SWS.

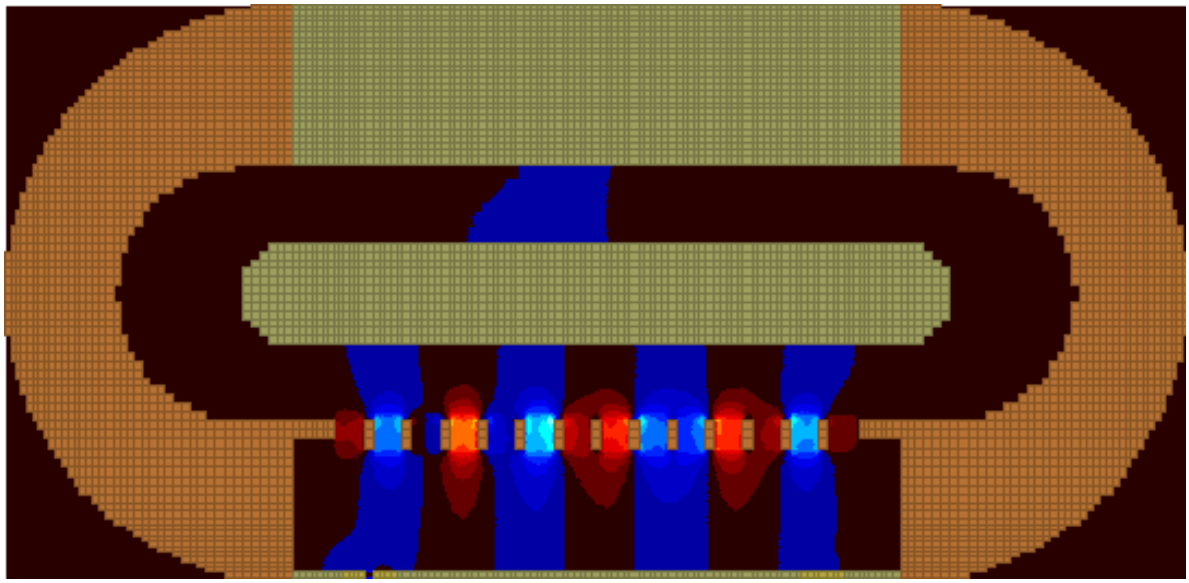

Figure 2.14: RF fields when the RPCFA is injected with a 3 GHz signal in MAGIC simulation. Blue indicates the field points toward the right and red indicates the field points toward the left. Brighter colors indicate a stronger field. The snap shot is taken along the centerline of the SWS, which is the x-axis in Figure 2.11b, so the coaxial ports are not seen.

A pulsed voltage of −330 kV and RF power of 1.3 MW were supplied to the RPCFA in MAGIC simulation with a 0.23-T magnetic field. These parameters are nominal values obtainable in the laboratory. Steady-state amplification of the injected signal was achieved on the order of 10 ns following the application of pulsed power. Spoke formation, indicating the transfer of power from the Brillouin hub electrons to the wave [49], can be seen in Figure 2.15.

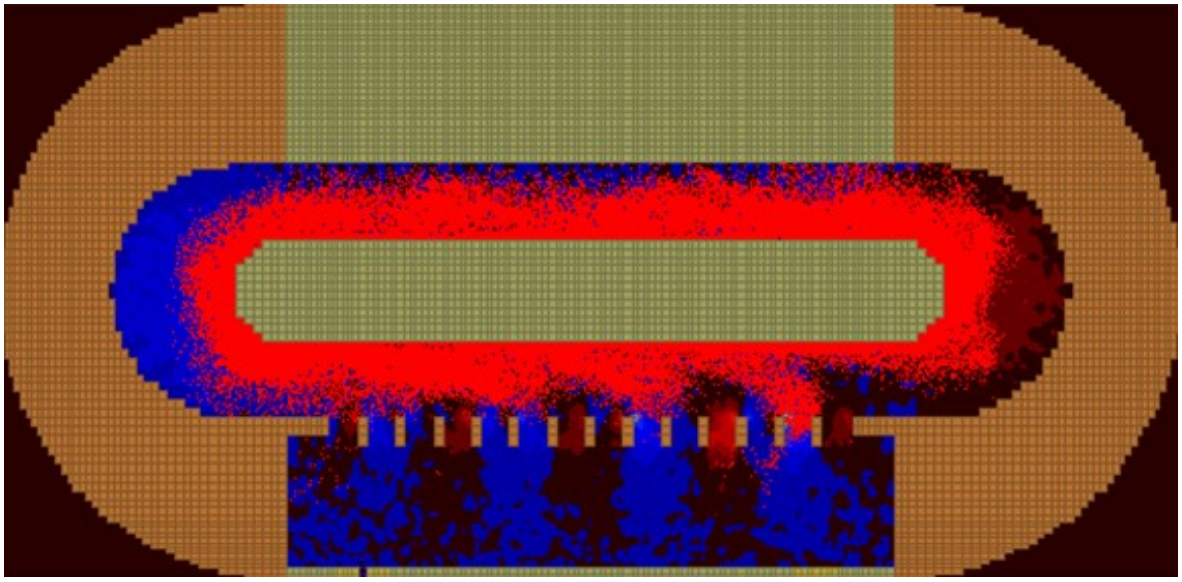

Figure 2.15: MAGIC simulation showing spoke formation as the injected signal and particles move from the input (left) to the output (right). The color scale is consistent with Figure 2.14.

A net current of 540 A was emitted from the cathode of which 160 A was collected on the SWS. Axial losses were small, generally less than 10 A, with most of the remaining current being collected in the recirculating bends or in the planar drift space opposite the SWS. A mean peak microwave power of 29 MW was measured at the output coaxial port of the RPCFA giving a gain of approximately 13.5 dB. The total efficiency is thus 15.5% and the electronic efficiency, which considers only the current drawn to the SWS, is 52%. Though greater efficiencies have been achieved [50] this is acceptable for high-power crossed-field devices.

From this simulation, the level of demodulation due to the recirculating planar geometry can be estimated by measuring the hub current, current travelling perpendicular to the DC electric field due to the $E \times B$ drift. By evaluating the AC component of the hub current as it exits the amplification region and comparing it to the hub current passing the center of the planar drift region, it is observed that the AC modulation is reduced by approximately 15 dB. The full drift region demodulates the signal further though it is significantly below the amplification level at this point and thus oscillation is eliminated. This suggests that the recirculating planar geometry is indeed an effective means of increasing demodulation and minimizing feedback. This measurement of hub current also showed evidence of significant harmonic

content in the Brillouin hub at frequencies of one and two octaves above the RF drive frequency. These frequencies are beyond the bandwidth of the waveports and are thus not extracted from the RPCFA. Details on this subject can be found in Appendix D.

Zero-drive stability was investigated to confirm the RPCFA indeed amplified the injected signal rather than oscillated at a primed frequency [51]. The RF signal was injected into the RPCFA model and allowed to reach steady state propagating along the SWS. Pulsed DC was then applied to initiate amplification which too was then allowed to reach a steady state. After steady amplification was achieved, the RF injected power was smoothly turned off. This simulation is summarized in Figure 2.16.

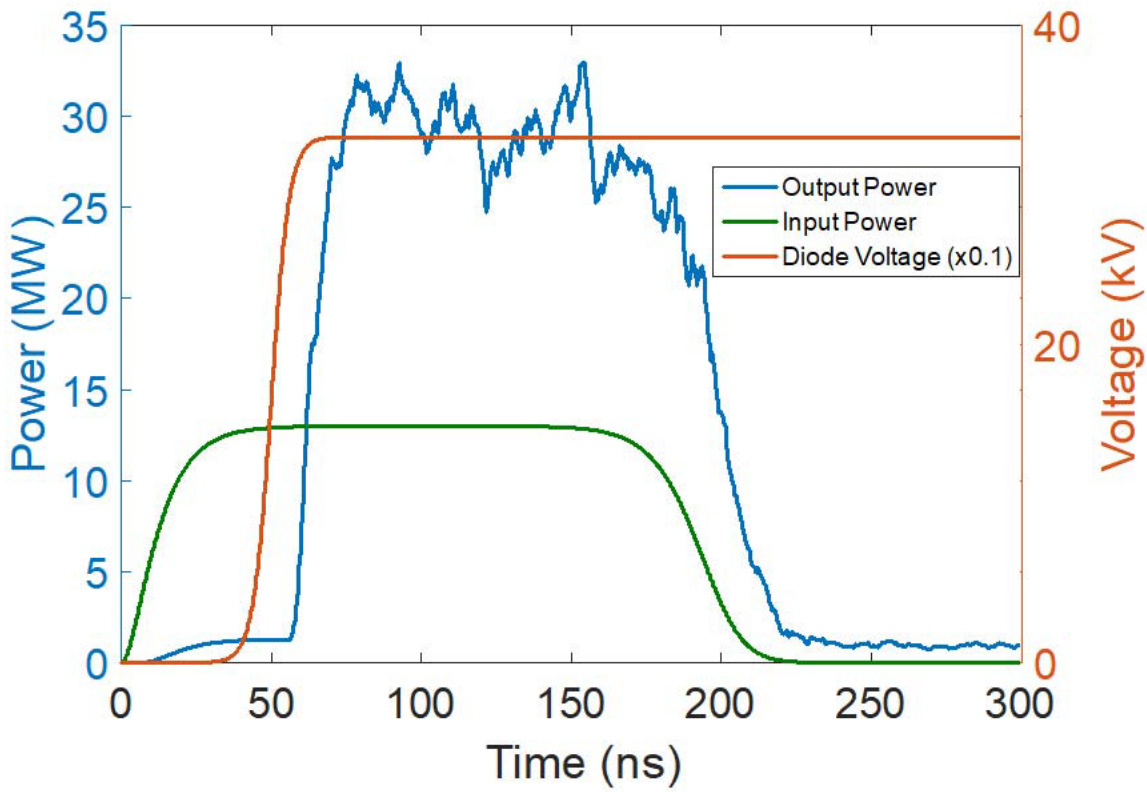

Figure 2.16: Injected power, output power, and diode voltage for the RPCFA zero-drive MAGIC simulation.

When RF power is turned off, the output power follows, suggesting the device is indeed amplifying. However, non-drive frequency signals may exist in the RPCFA that are not extracted from the coaxial ports due to their limited bandwidth. In order to confirm the presence of these signals, or lack thereof, the voltage across a cell of the RPCFA was measured and an FFT was taken to observe the frequency content. The

FFTs were taken when RF injection was present and amplification was in steady state, as well as after it was turned off. The FFTs are plotted in Figure 2.17.

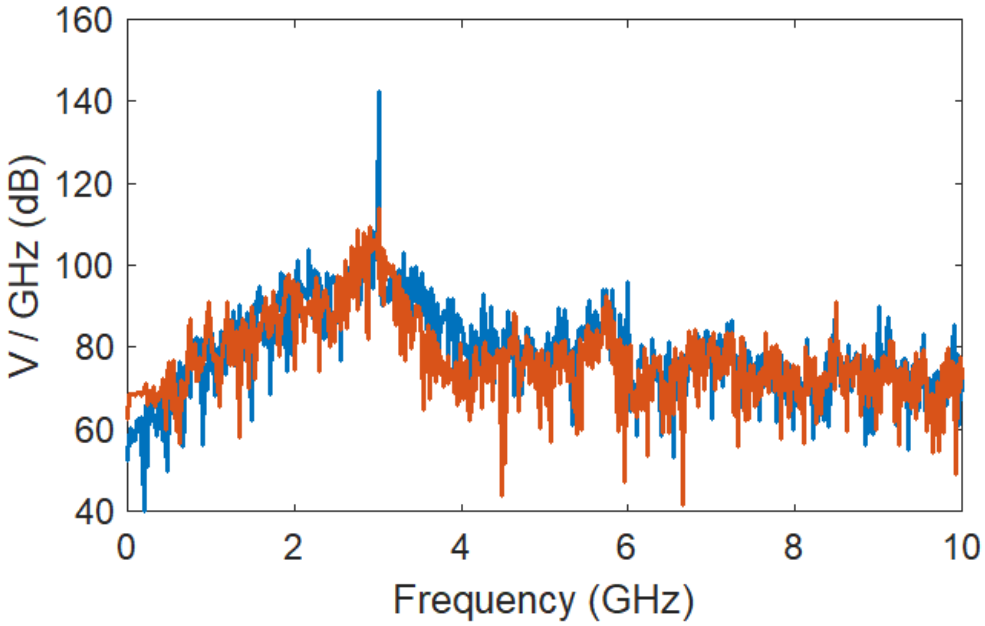

Figure 2.17: FFT traces for the simulated voltage across a single cell of the RPCFA during steady amplification (blue) and after RF injection had been terminated (red).

The spectra presented in Figure 2.17 confirm zero drive stability. No frequency is amplified other than the 3 GHz drive signal. Once the injected signal is terminated, the spectrum shows no other frequency component persisting significantly above the noise floor. With zero-drive stability and the amplifying nature of the output power confirmed, various parameters of RPCFA operation were varied to determine its characteristics.

The bandwidth of the RPCFA was estimated in MAGIC simulation by varying the injected frequency and measuring the output power. These data are presented in Figure 2.18.

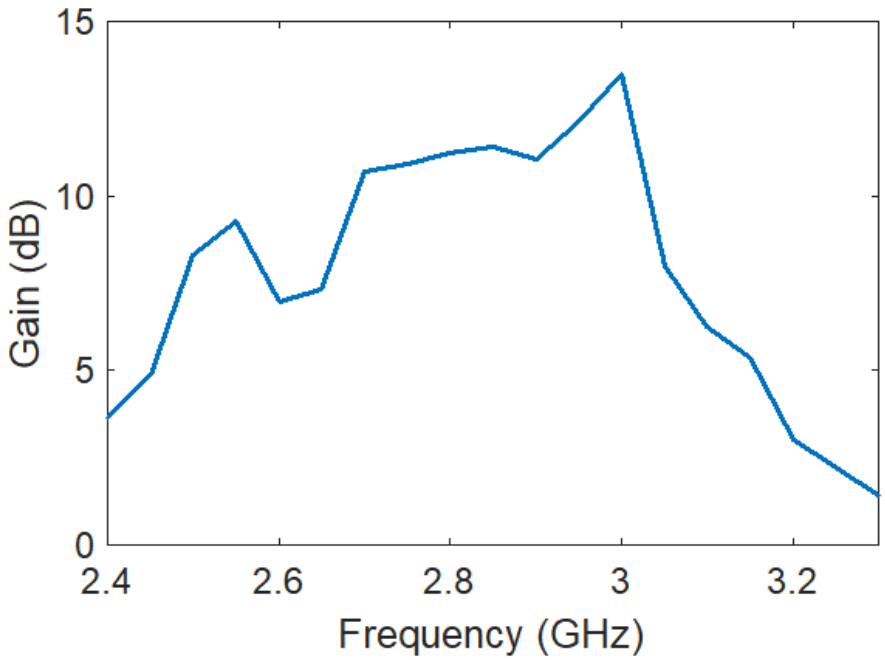

Figure 2.18: Simulated RPCFA gain versus injected RF frequency.

Peak gain occurs at the design frequency of 3.0 GHz. This gain decreases rapidly as the frequency increases and more slowly as frequency decreases. A continuous band from approximately 2.7 to 3.0 GHz shows gain greater than the peak gain minus 3 dB which is taken to be the bandwidth. This gives a bandwidth of 10.5% which is comparable to commercial CFAs [52]. It is observed that significantly powerful non-drive frequency oscillations arise when the RPCFA is driven at frequencies lower than the design at 2.7 GHz.

The power of the inject RF signal was varied to determine the relationship between RF drive and gain, as shown in Figure 2.19. Nearly 45 MW of RF power was extracted at the highest drive power simulated in MAGIC, at the cost of gain and efficiency. This compression curve shows diminishing gain at increased input RF drive powers, typical for CFAs. Insight into the cause of this diminishing gain is provided in Appendix D.

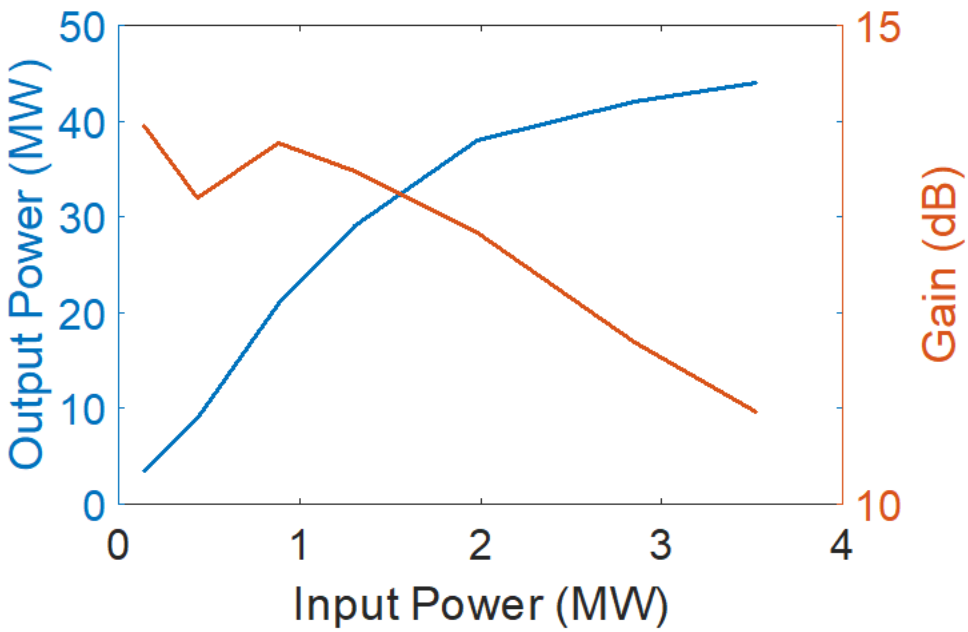

Figure 2.19: Simulated gain and output power as a function of the injected 3.0 GHz RF power.

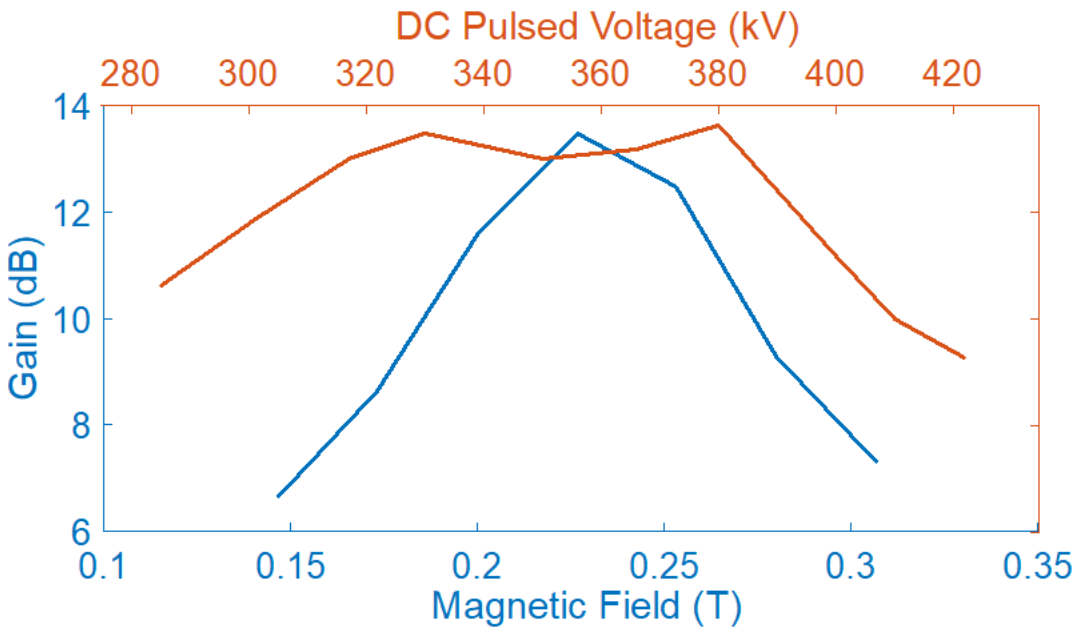

Figure 2.20: Simulated gain versus the applied axial magnetic field and the pulsed DC voltage. For variations in the magnetic field, the voltage was held constant at 330 KV. For variations in the voltage, the magnetic field was held constant at 0.23 T.

The RPCFA's response to a suboptimal DC electric, and axial magnetic field was also simulated. The data of gain versus magnetic field and DC voltage are shown in Figure 2.20. The simulated magnetic field magnitude for previous simulations, 0.23T, was determined from the Buneman-Hartree condition, a

pulsed DC voltage of 330 KV (determined by experimental constraints), and a planar A-K gap spacing of 1.5 cm. The optimal magnetic field strength is indeed the value predicted by Buneman-Hartree. The RPCFA was able to accommodate increased electric fields, at the cost of efficiency. Lower voltages showed uniformly inferior performance. Gain in excess of 10 dB was observed for voltages ranging from 285 to 400 kV.

CHAPTER 3

Experimental Configuration

This chapter discusses the configuration of equipment used in RPCFA experiments for this dissertation. An overview of the microwave circuitry is provided, detailing methods of data acquisition. The fabrication and assembly of the RPCFA prototype is discussed (and detailed drawings for the device are available in Appendix C). The pulsed driver and RF sources used for testing the RPCFA are detailed in this section and additional information regarding RF source drivers can be found in Appendix B.

3.1 Microwave Circuit Overview

The general configuration for all experiments conducted using the RPCFA is outlined in Figure 3.1. WR-284 waveguide is used to transport microwaves between components of the experiment. Microwave power is generated by a source, discussed in Section 3.4 and usually a magnetron, which is powered by a pulsed driver, discussed in Section 3.5. The RF signal is first passed through a variable attenuator to vary the power injected into the RPCFA. This injected power is then measured by a directional coupler which samples the forward and reverse powers at -40 and -35 dB, respectively, and sends the signal to the screen room. In the screen room (not pictured) the signal is split, with one half power sent to a HP 8472B Low Barrier Schottky Diode to make calibrated power measurements with 0.3 dB precision. The other half-power is sent to a 20 GS/s Agilent 54855A oscilloscope, capable of resolving frequencies up to 6 GHz, for extracting time-resolved frequency information. Calibration of all RF components, such as the

directional couplers, attenuators and type-N cables, was performed using a Hewlett-Packard 8772D network analyzer.

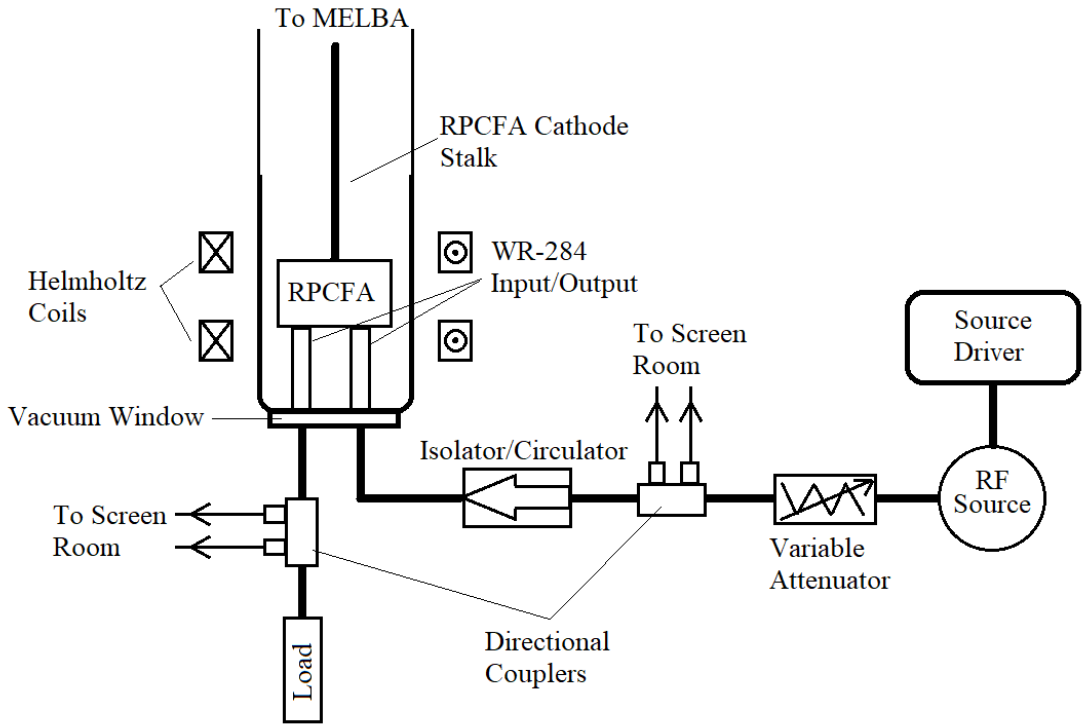

Figure 3.1: Experimental block diagram generalized for moderate power RPCFA experiments. The positions of the circulator and directional coupler were reversed for high power (>150 kW) experiments.

After passing through the directional coupler, the RF signal is passed through an isolator (for input powers less than 100 kW) or a high-power circulator (for input powers in excess of 100 kW). These components protect the source from backward power generated in the RPCFA. For high power amplification experiments, the order of the directional coupler and the circulator were reversed to measure reflected power, and because the single-pulsed microwave source was thought to not be in danger of single-pulse reflected power. The RF signal is then passed through a vacuum window into the RPCFA. The RPCFA pulsed power is provided to the amplifier by the Michigan Electron Long Beam Accelerator with Ceramic stack, MELBA-C, discussed in section 3.3. An axial magnetic field is provided by a pair of pulsed Helmholtz coils. The amplified microwave power is extracted from the RPCFA back through the vacuum window and passed through a second directional coupler which samples the amplified output RF power in

the same manner that input RF power is measured at the first directional coupler. The output power is absorbed by a solid-state resistive load calibrated to absorb at least 99% of the RF power in the frequencies of interest. Since the RF sources are low average power, solid-state absorbers can be used in both the load and the variable attenuator. A photograph of the fully assembled microwave circuit is shown in Figure 3.2.

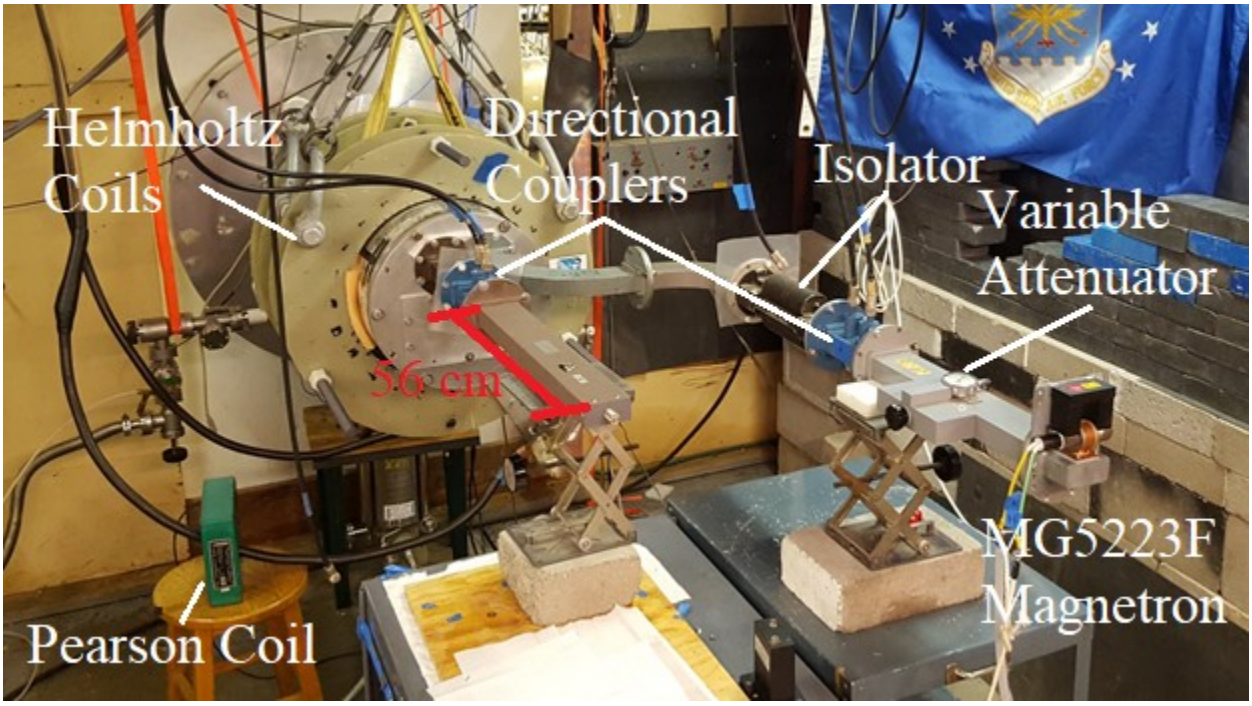

Figure 3.2: Photograph of the fully assembled microwave circuit with the MG5223F magnetron as the RF source. The pulsed power driver for this magnetron is not pictured.

The lower left of Figure 3.2 shows the Pearson coil [53] which measures the current flowing into the Helmholtz coils [54]. Prior to running the experiment, the current through the coils is correlated to the magnetic field in the A-K gap measured by a Lakeshore 475 gaussmeter with HMNA-1908-VR probe. The gaussmeter is able to resolve the temporal evolution of the magnetic field at various positions in the A-K gap. Due to the relatively long time during which the magnetic field diffuses into the RPCFA it is important to calculate an appropriate delay between the firing of the Helmholtz coils and the firing of the RF source and MELBA. The magnetic field was measured at 8 locations around the RPCFA as shown in Figure 3.3. For each of these positions the magnetic field was measured over time at 5 different charge voltages of the

capacitor bank which drives the Helmholtz coils. The magnetic field at each of these locations is plotted in Figures 3.4a and 3.4b.

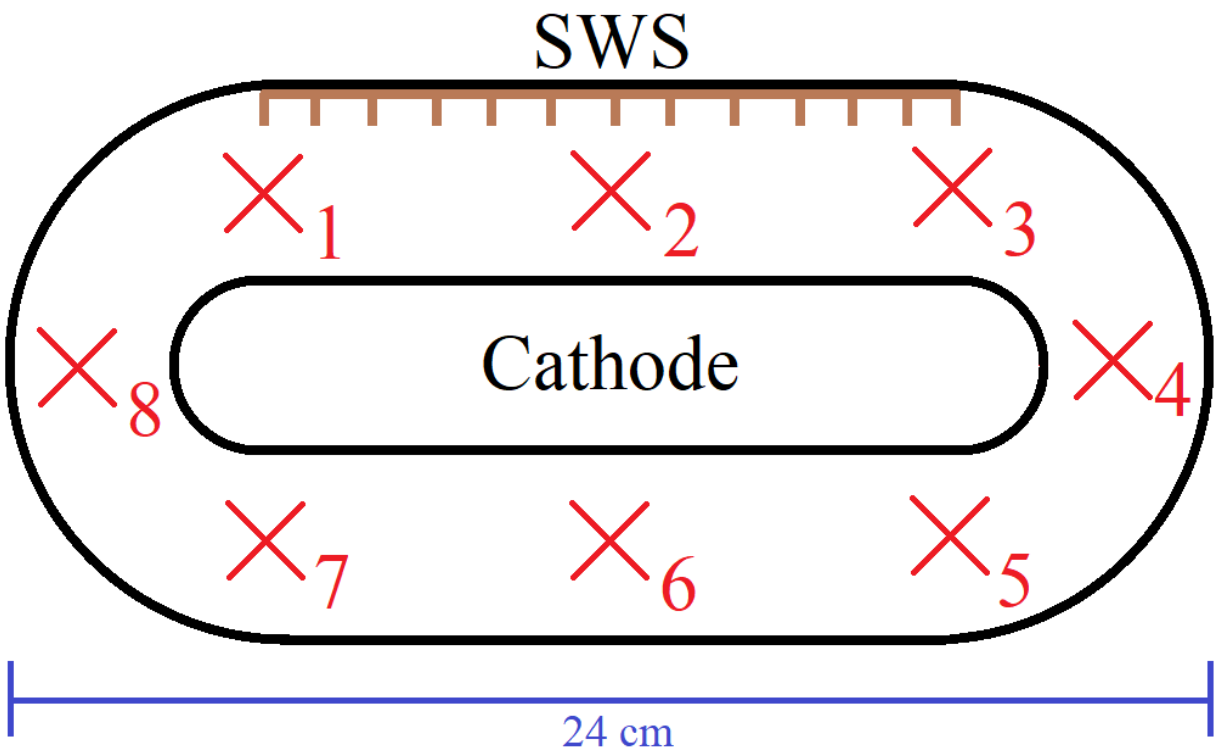

Figure 3.3: Map of positions in the RPCFA at which magnetic field was measured for calibration.

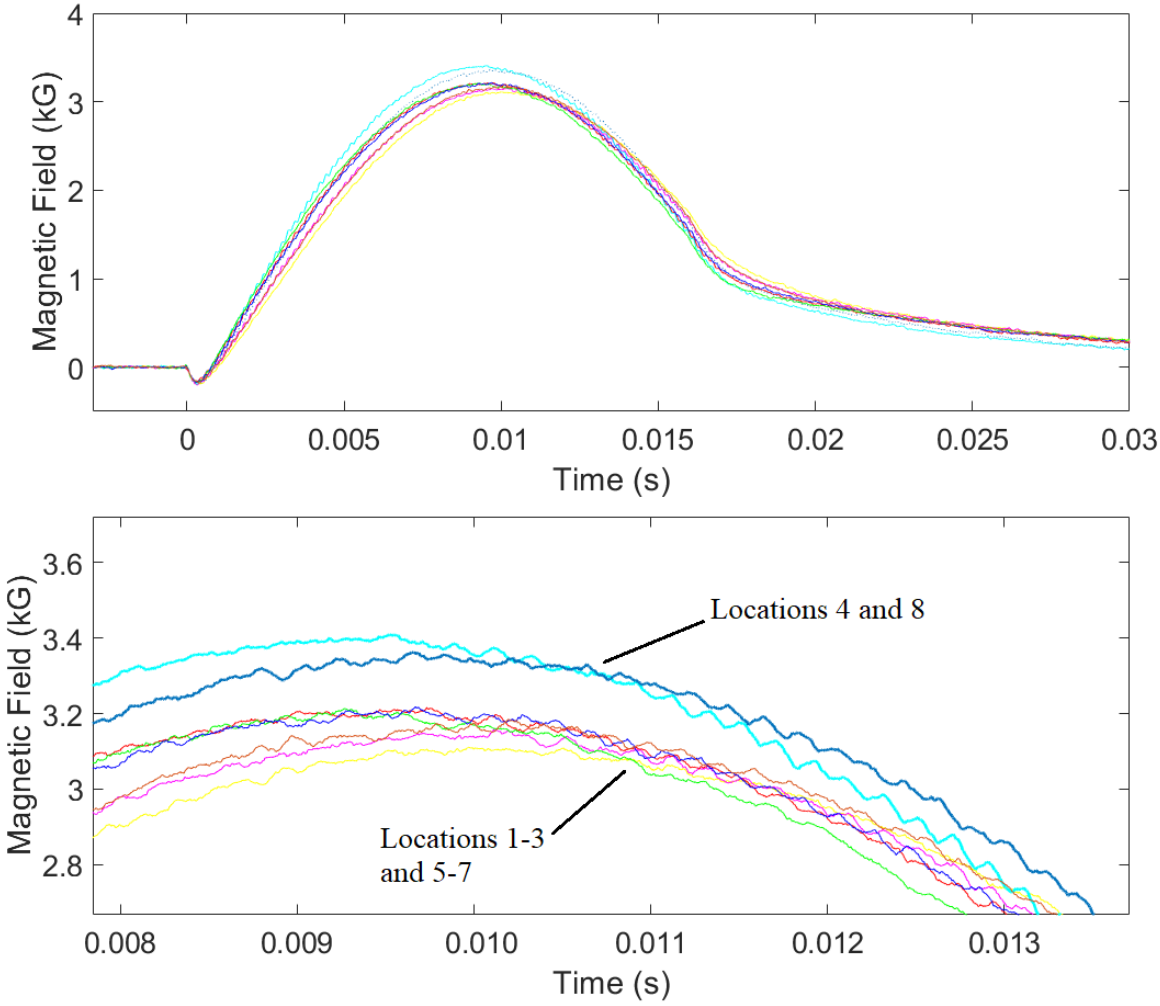

Figure 3.4a (top): Magnetic field for the 9 marked locations over time with a 5 kV charge on the capacitor bank that drives the Helmholtz coils.

Figure 3.4b (bottom): Zoomed in plot near peak of magnetic fields showing differences in the traces. Locations in the bends (4 and 8) are distinguished from locations in the gap.

The locations in the bends show higher peak field than those in the planar regions. This is due to their location further from the center of the experiment and thus closer to the coils. The optimal field delay was 10.9 ms, chosen by taking the time at which the variance between the fields in the planar region was minimized. The average field in the planar region at this time was then correlated to a current measured by the Pearson coil, and a charge on the capacitor bank. As no experiment significantly modifies hardware

located further from the center of the coils than the interaction space, this timing and correlation were assumed valid for all RPCFA experiments.

3.2 The RPCFA Anode

The RPCFA is a diode with a cathode connected to the negatively charged MELBA-C and an anode connected to ground. This anode is composed of the slow-wave structure (SWS), the inner housing which secures the SWS, the vacuum chamber and the RF circuit system responsible for injecting and extracting RF power. The SWS was fabricated using the manufacturing technique known as the “lost wax” method [55]. A ceramic negative is additively manufactured, then liquid copper is introduced. Removing the negative leaves behind a solid copper SWS. Semi-pure (99.9%), and non-oxygen free high thermal conductivity copper was chosen for the SWS due to the ease (and low expense) at which this method is performed for copper structures. Since the SWS is relatively easily produced and receives significant damage during operation, multiple SWS were produced and utilized over the course of the RPCFA experiments. A photograph of an unused SWS is shown in Figure 3.5.

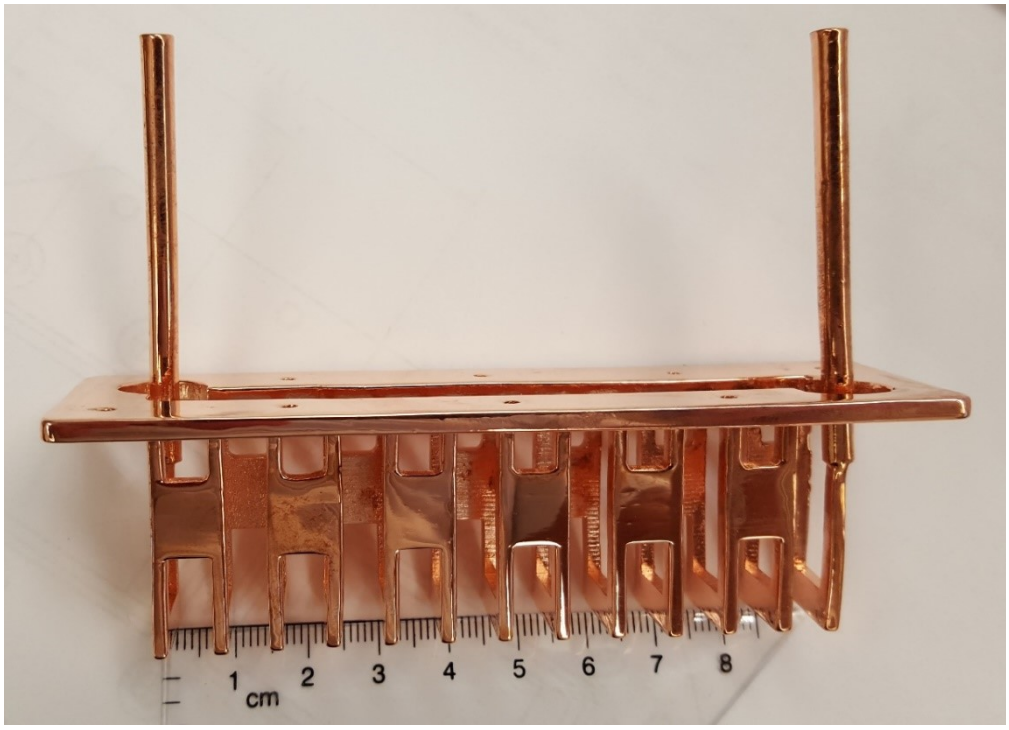

Figure 3.5: Additively manufactured copper SWS.

Two types of SWS were fabricated. The original is shown in Figure 3.5, as well as a structure with rounded corners to minimize field enhancement with the intention of increasing the RF breakdown threshold. A comparison of the two structures is presented in Figure 3.6. The structures show essentially identical operation characteristics within the margin of variation for individual structures.

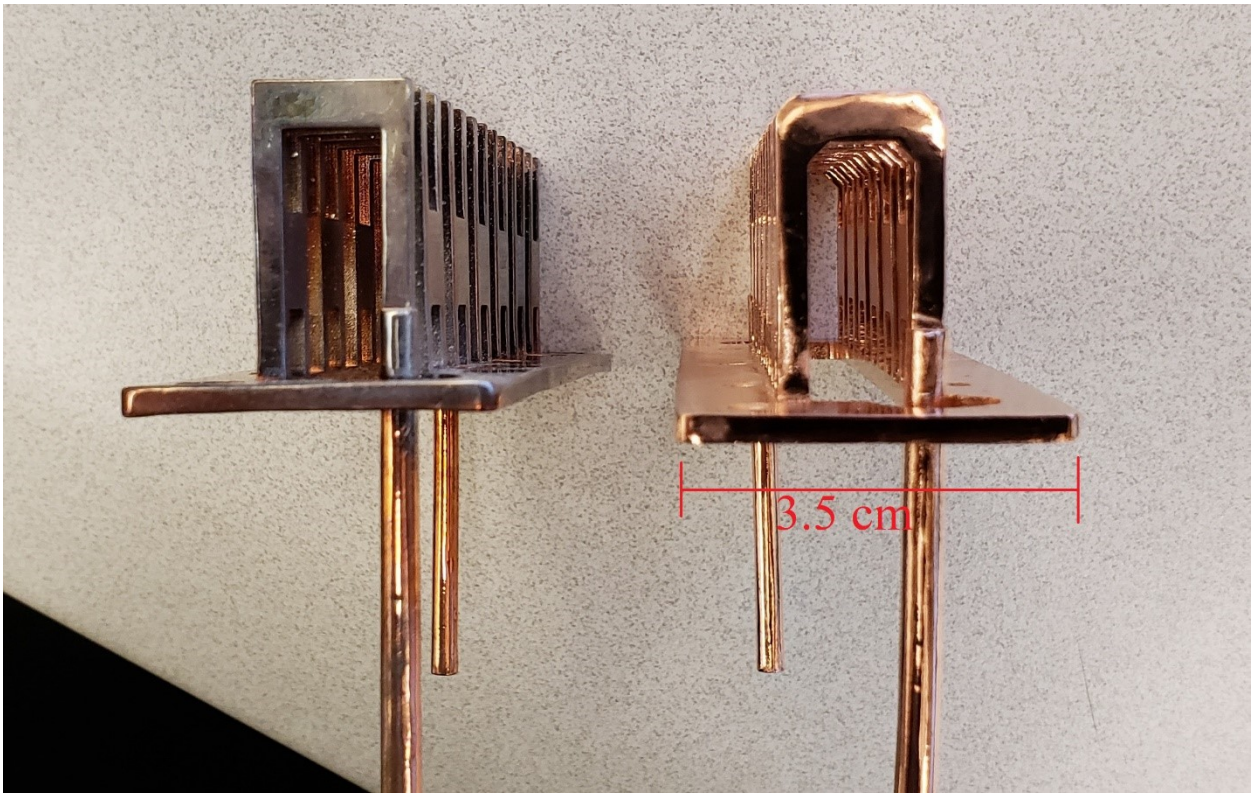

Figure 3.6: Original SWS designed in HFSS on the left compared to the rounded structure designed to reduce field enhancement. The copper surface on the left shows the effects of operation in the RPCFA. The rounded structure is unused at the time the picture is taken.

The SWS is mounted into the inner housing. This inner housing defines the interaction space around the cathode and features 3 components in addition to the SWS. The substrate holds the SWS in place and provides the outer conductor for the RPCFA's coaxial ports; the inner conductor is the long cylinder protruding from the base of the SWS. The coaxial ports are detailed in Figure 3.7. The recirculating bends recycle the beam around the cathode and demodulate the Brillouin hub. The bends feature spherical voids which form the corners of the inner housing, pictured in Figure 3.8. In HFSS simulation, these voids appeared to reduce the propensity for oscillation within the inner housing, eliminating the need for mode attenuators/severs. The SWS, substrate and recirculating bends are pictured in Figure 3.8. For clarity, the upper wall is not shown, which connects the recirculating bends and is located opposite the SWS. It is a smooth-bore planar section which serves to close the inner housing around the cathode.

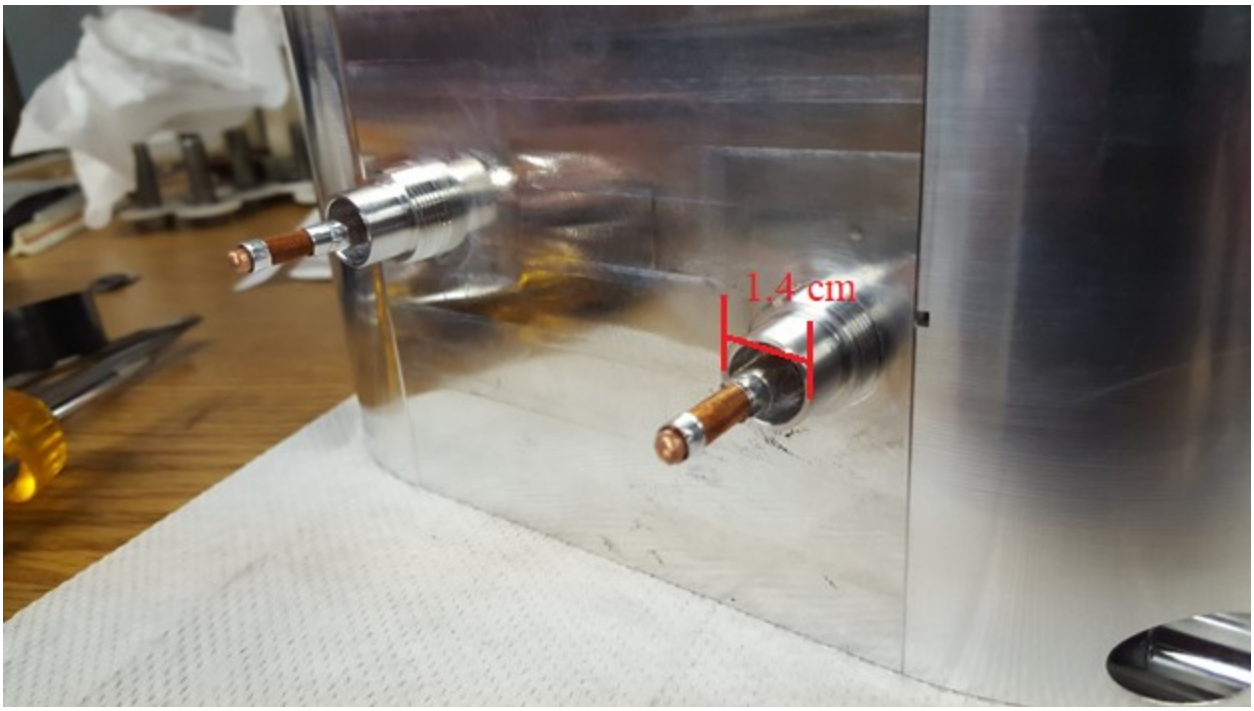

Figure 3.7: Coaxial wave ports for injecting and extracting power from the RPCFA. Copper mesh is fastened to the inner coaxial conductor to improve electrical/RF contact with the puck couplers.

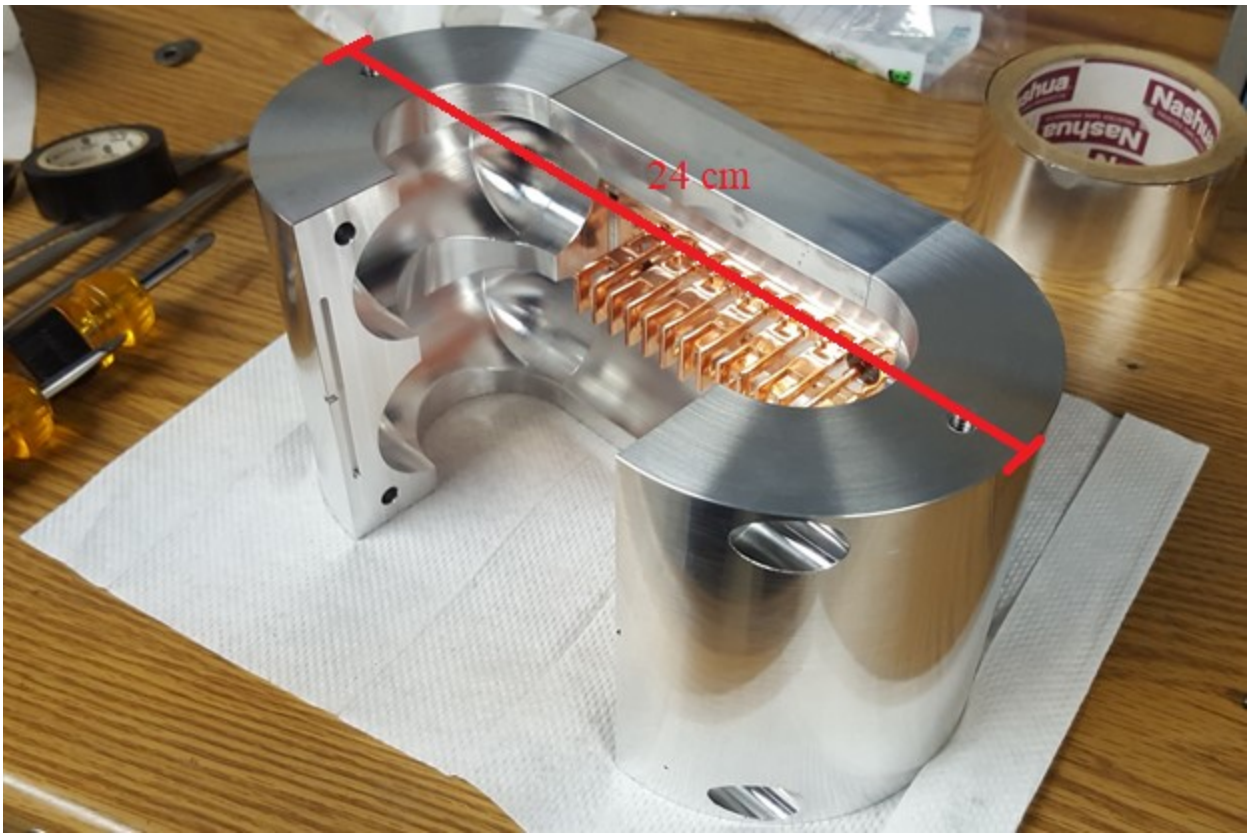

Figure 3.8: RPCFA SWS and inner housing with the upper backwall excluded for clarity.

To connect the RPCFA to the rest of the RF circuit, a pair of "puck" couplers were designed. The puck couplers are mounted into WR-284 waveguide and attach to the inner conductor of the RPCFA coaxial wave ports as shown in Figure 3.9. These puck couplers are designed to provide broadband transmission with minimal loss. The simulated S_{21} for an individual puck coupler is given in Figure 3.10. An HFSS simulation of the fields generated at 3 GHz is shown in Figure 3.11.

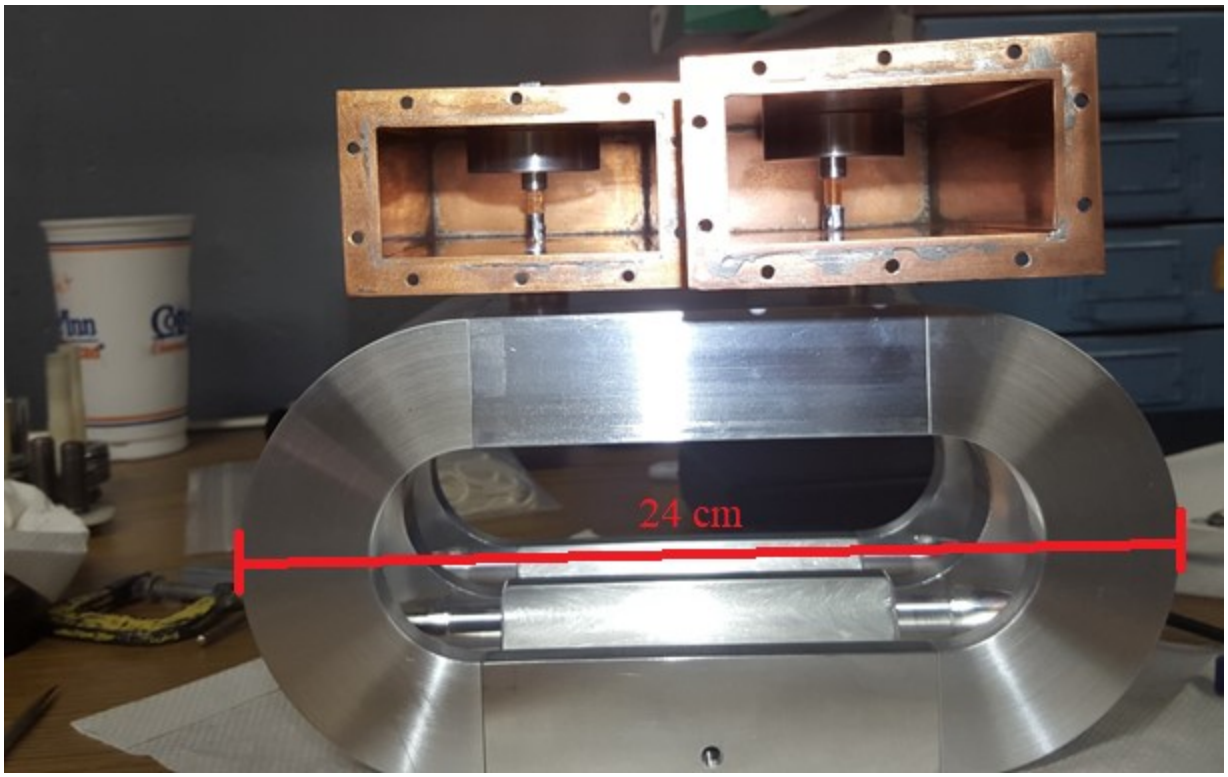

Figure 3.9: RPCFA inner housing with puck couplers attached, mounted inside WR-284 waveguide. The inner conductors which extend into the puck couplers are wrapped in copper mesh to improve electrical/RF contact with the pucks.

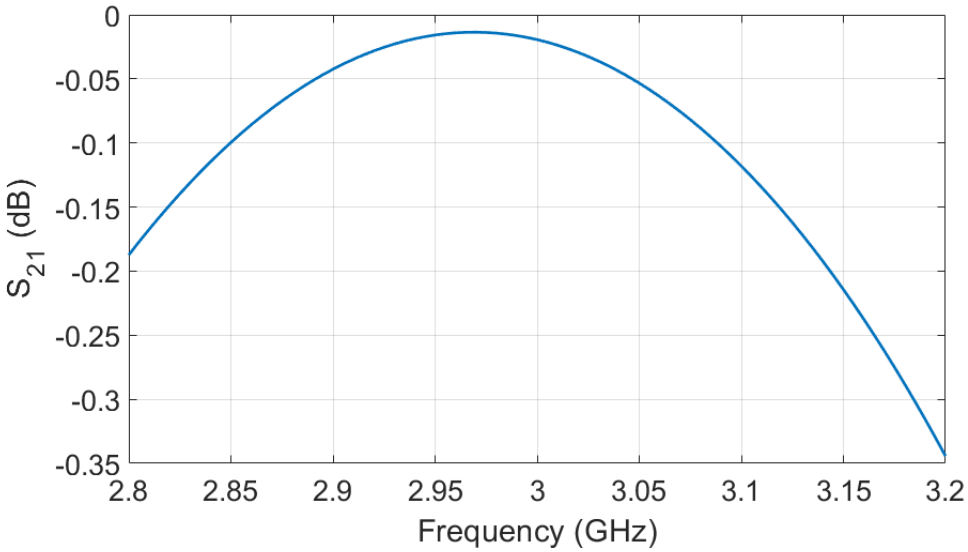

Figure 3.10: S_{21} for a single puck coupler calculated in HFSS simulation.

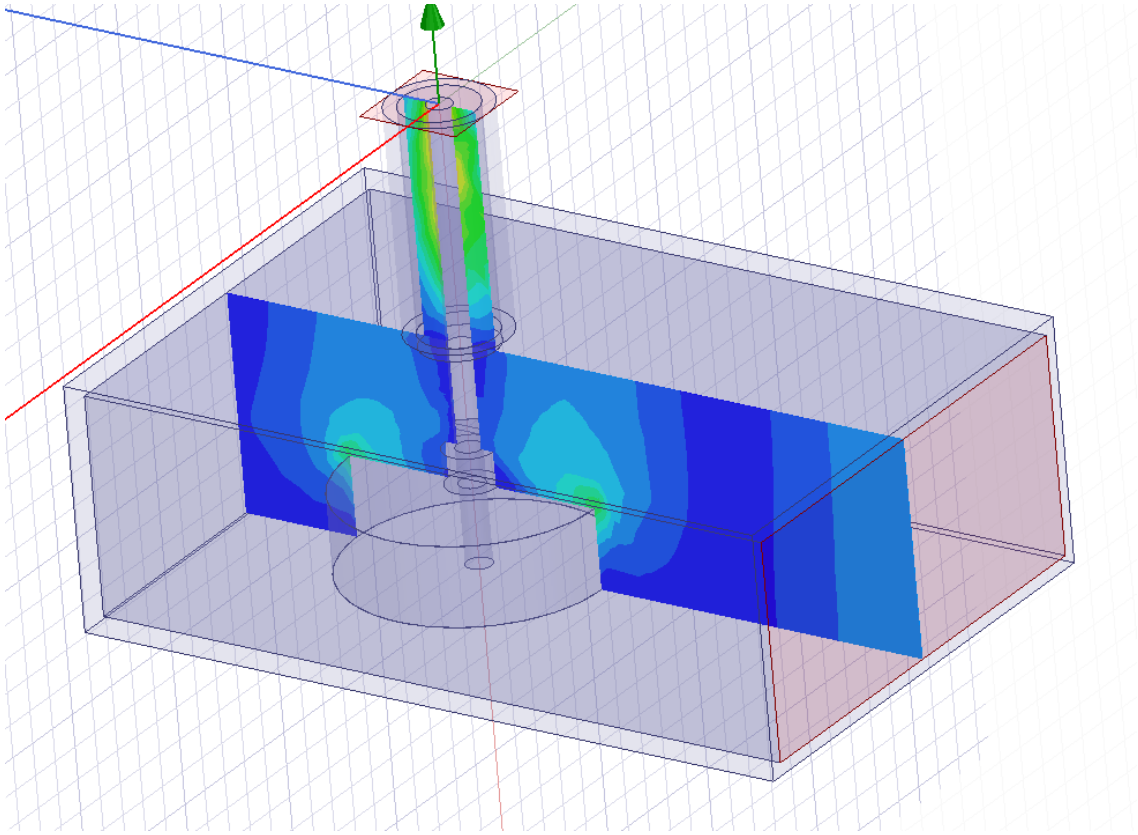

Figure 3.11: HFSS simulation and electric field magnitude overlay of a puck coupler at 3 GHz.

The puck couplers are a point of significant transmission loss in the RPCFA, presumably due to the poor quality of electrical contact [56 - 58], the primary difference between the HFSS model and the prototype. The loss in the two puck couplers was measured by connecting the two coaxial ends together with a short copper rod serving as the inner conductor. The network analyzer was connected to the waveguide ends. The measured S_{21} for transmission across the two couplers, after subtracting other sources of loss in the system, is given in Figure 3.12. Transmission losses in the waveguide and vacuum windows were small compared to the puck couplers and SWS.

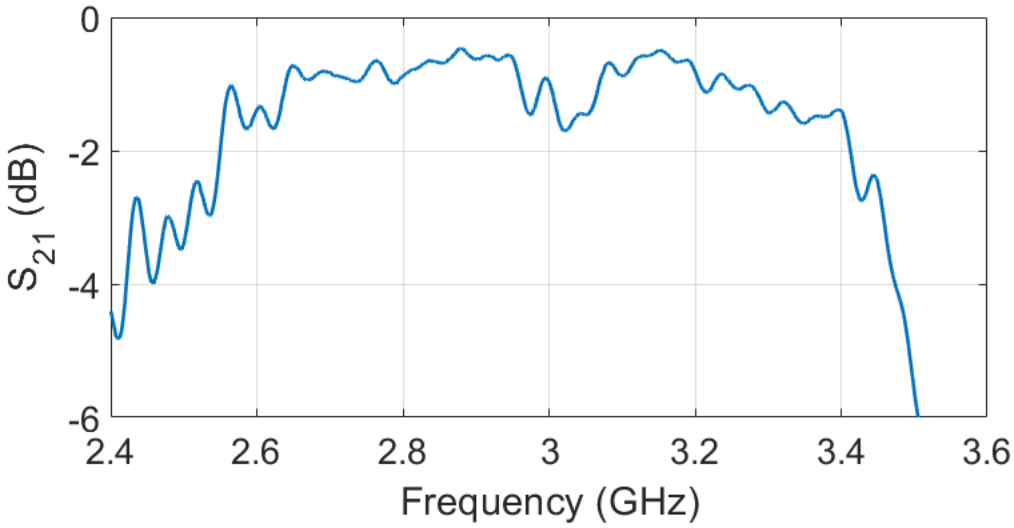

Figure 3.12: Experimentally measured S_{21} through two puck couplers connected by a short inner conductor.

The inner housing is held in place in the cylindrical vacuum chamber by means of an adjustable inner wheel. This inner wheel allows for slight manipulation of the RPCFA in the chamber in the directions perpendicular to the axis of the cylindrical chamber, to offset any sag or deflection of the cathode stalk, ensuring the cathode is properly centered relative to the anode. Once placed, the inner wheel expands to lock the anode in position. The inner housing mounted to the inner wheel is shown in Figure 3.13.

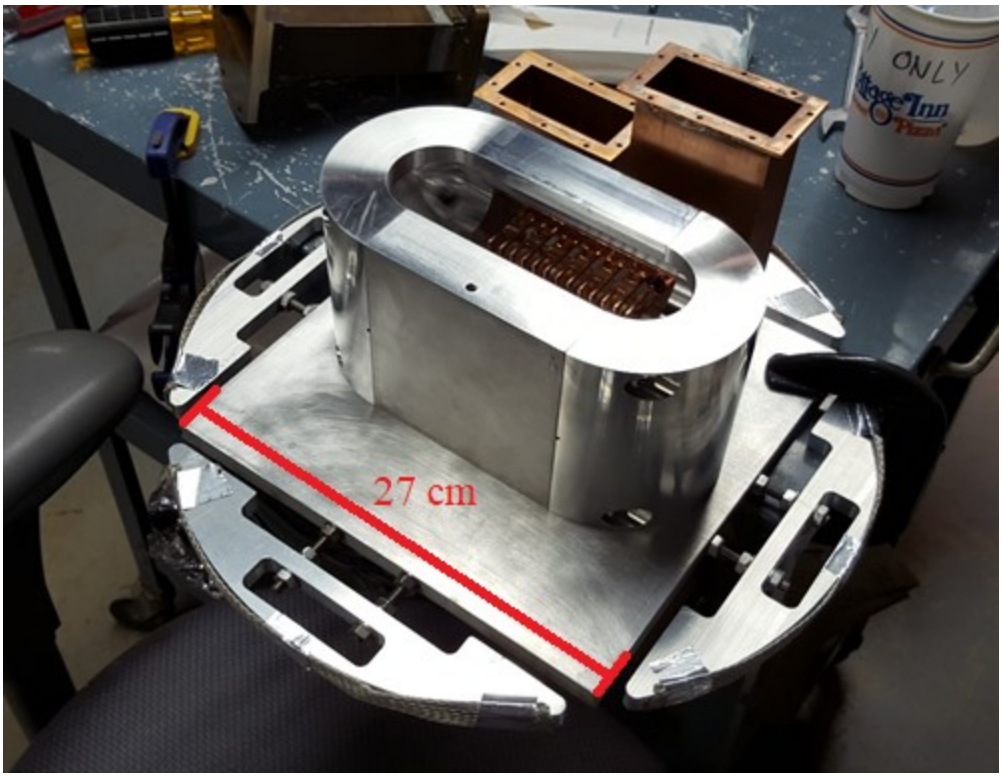

Figure 3.13: Inner housing mounted to the inner wheel. The steel braid fastened to the wheel ensures good electrical contact with the vacuum chamber.

WR-284 waveguide is used to connect the fastened puck couplers to the vacuum window located at the front of the vacuum chamber. The vacuum windows are 2-mm thick Lexan, which is thin enough to not interact with the RF signals and thick enough to withstand the force of the pressure differential between the vacuum chamber and the lab atmosphere. An iris is cut into the vacuum plate to maximize transmission through the Lexan window. The vacuum plate is connected to the endplate, which closes the vacuum chamber. The endplate also features an access panel to view the experiment in place and assist with the assembly and disassembly. The endplate mounted on the chamber with the vacuum window attached is shown in Figure 3.14. The vacuum window connects to the non-vacuum rated waveguide and the rest of the RF circuit.

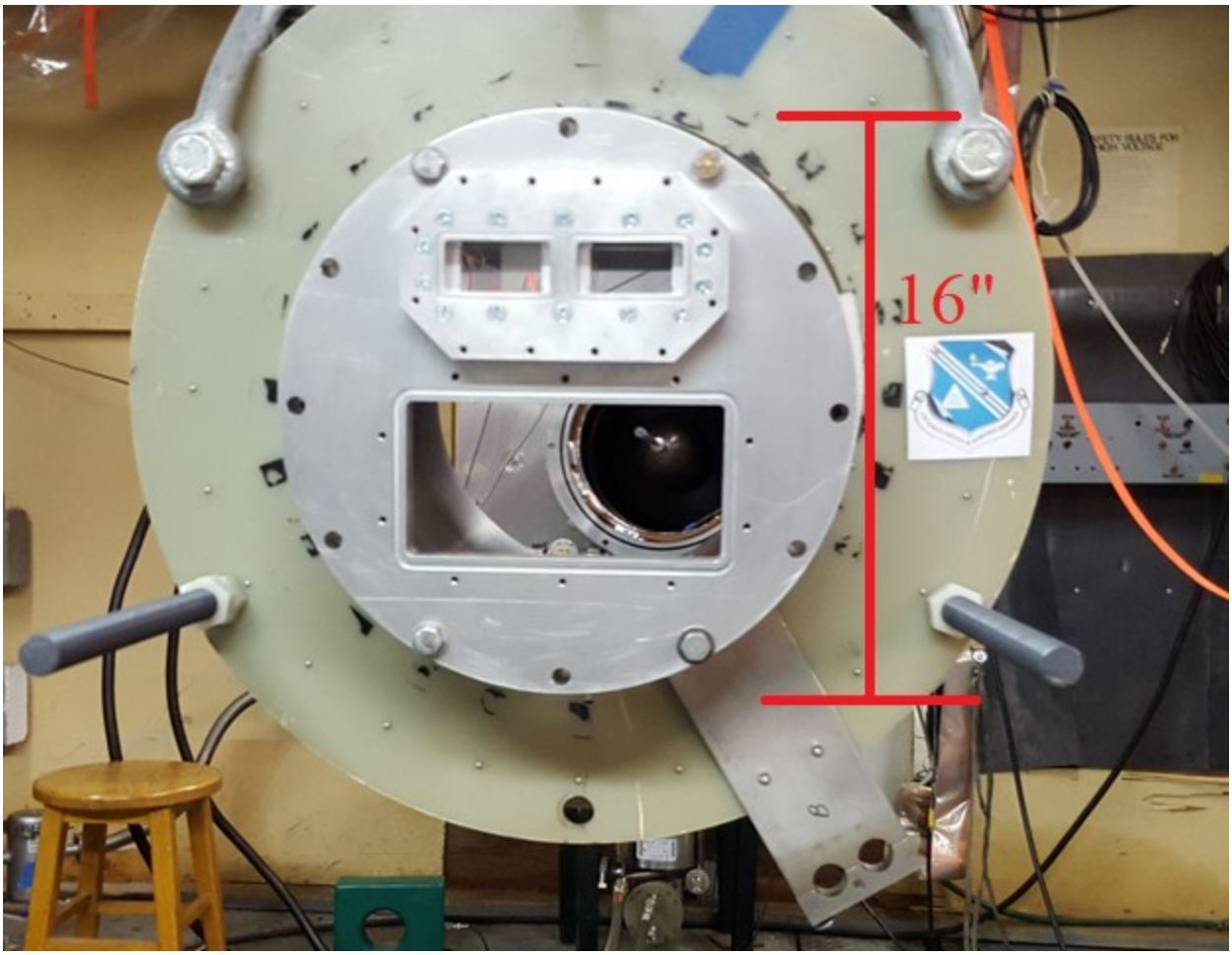

Figure 3.14: Endplate, magnetic field coils, and vacuum window. The access panel is open during assembly.

3.3 The RPCFA Cathode

Four different cathodes were used over the course of the RPCFA experiments. The four cathodes are shown in Figures 3.15a through 3.15d. The first was the Glyptal cathode. This cathode was a rounded block made from aluminum and coated in an emission-limiting enamel called Glyptal. A patch, approximately the area of the top surface of the SWS, was left bare to create an electron emission site. The emission site faced the SWS during operation. A new layer of Glyptal was applied between every shot series (typically ~70 shots) to maintain the integrity of the emission blocking layer. The Glyptal cathode was employed for 8 shot series, a total of 562 shots, numbered 15236-15598 and 15682-15880.

The Air Force Research Laboratory provided 2 cathodes, denoted Cathode A and Cathode B. Both cathodes were built to the same physical dimensions as the Glyptal cathode. The bodies of these cathodes were made of stainless steel and featured carbon fiber emitters brazed onto a patch of similar dimensions to the emission region on the Glyptal cathode [77]. The emitter was placed over the SWS during operation. Cathode A featured a coarser carbon fiber emitter than Cathode B. Cathode A was employed for 3 shot series, a total of 131 shots. Between series, the cathode was refurbished by lightly sanding out imperfections and material deposited on the cathode, taking care not to perturb the emitter. Cathode B was employed for a single shot series, 40 shots due to its dramatically inferior performance (see chapter 4, section 6) compared to cathode A.

The final cathode tested was Cathode A, modified to include a single endhat on its downstream end [59 - 61]. MAGIC simulation predicted a significant reduction in endloss current with the inclusion of even a modest endhat. While a significant reduction in mean current draw was not observed, Cathode A with endhat showed the lowest variation in gain at moderate input power drive. For this reason, Cathode A-with-endhat was used for the final 194 shots, including all shots driven with high microwave power (>100 kW).

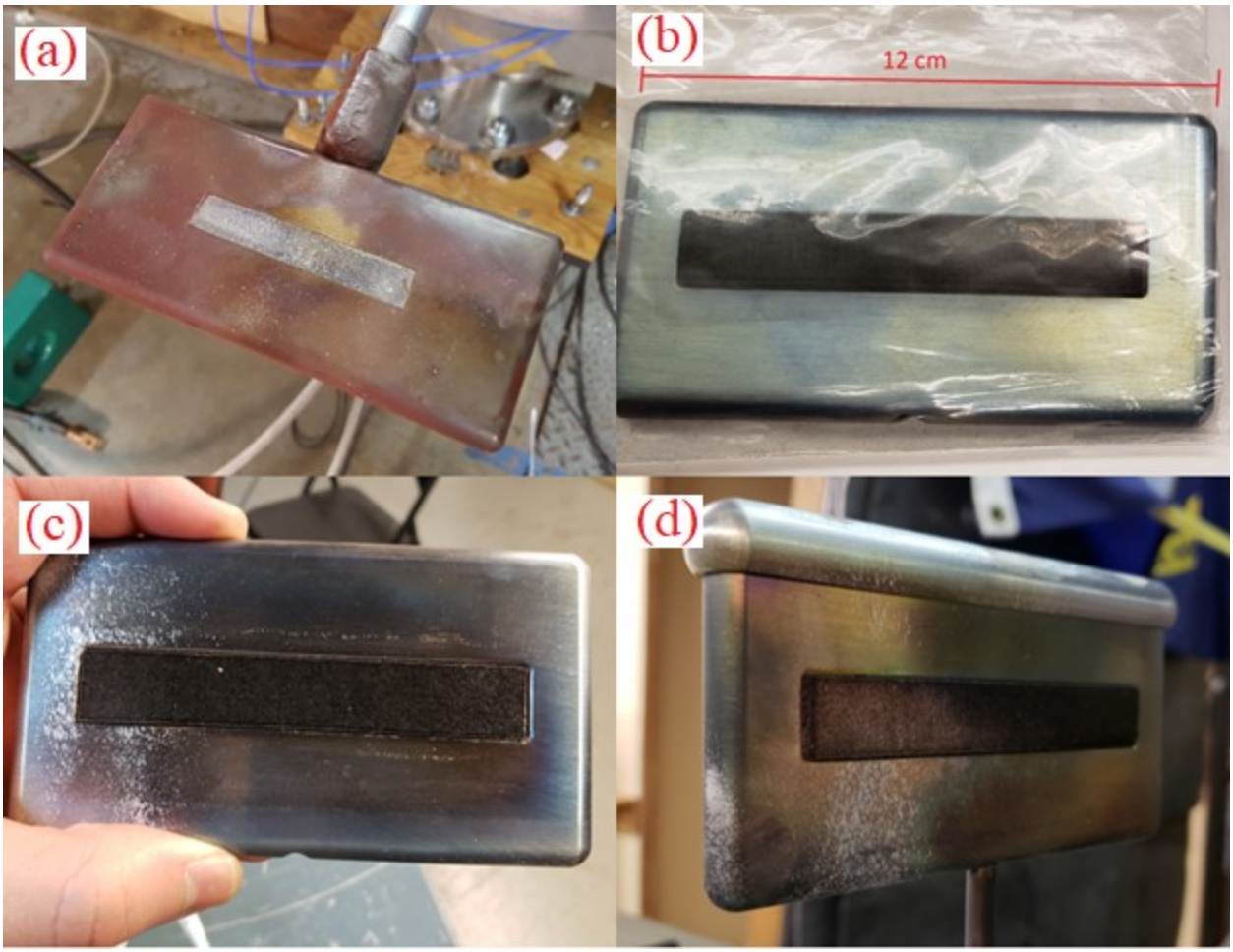

Figure 3.15a (top, left): Glyptal Cathode: Bare aluminum emitter with Glyptal to inhibit emission at other locations.

Figure 3.15b (top, right): Cathode A: Steel cathode brazed to coarse carbon fiber emitter. Photo taken of new cathode, still in plastic bag.

Figure 3.15c (bottom, left): Cathode B: Steel cathode brazed to fine carbon fiber emitter. Photo taken after 40 shots.

Figure 3.15d (bottom, right): Cathode A with Endhat: AFRL cathode A modified to include aluminum endhat.

3.4 MELBA

The Michigan Electron Long Beam Accelerator with Ceramic Insulator (MELBA-C) is an Abramyan Marx [62 – 64] bank consisting of 16 capacitors, each rated for 100 kV with a capacitance of 1 μF. Fourteen of these capacitors comprise the main Marx circuit while the remaining 2 form the Abramyan circuit. At full charge, MELBA is capable of delivering -1 MV, 10 kA pulses of up to 1 μs in length. The rise time for these pulses is typically around 100 to 200 ns, depending on the load. For these RPCFA experiments, MELBA is charged to -30 kV, thus delivering pulses of -300 kV. The measured current is load dependent but typically reaches 6 kA before the pulse is crowbarred. To protect both MELBA and the load from excessive currents in the event of diode closure and impedance collapse, a crowbar switch is triggered to shunt power to ground through a ~3Ω set of large series resistors. The crowbar is typically triggered around 500 ns after the main Marx is fired.

With ceramic stack and the vacuum system present, the MELBA vacuum chamber is able to achieve pressures on the order of 1 μtorr. A scroll pump is used to reach pressures in the range of 50 mTorr. Once this pressure is reached the chamber is crossed over to a cryopump which brings the pressure down to micro-Torr range. To bring the chamber back up to atmospheric pressures, both pumps are gated off and the chamber is backfilled with dry nitrogen. This dry nitrogen prevents water from adsorbing on the interior of the chamber and ceramic insulator, reducing the effects of oxidation and allowing for faster pump down for subsequent experiments.

Operation of a Marx bank requires charging a capacitor bank in parallel at some moderate voltage. Once the capacitors are charged, the power supply disconnects and the circuit topology is quickly switched to discharge the capacitors in series, adding their voltages. In order to trigger MELBA, a delay generator sends a +5 V pulse to a trigger amplifier that amplifies it to +300 V. This pulse is sent to trigger a PT-55 pulse generator that generates a +40 kV pulse which in turn breaks down a PT-70 pulse generator. The PT-70 generates a -85 kV pulse that directly breaks down two of MELBA's spark gap switches, including the

switch located in the Abramyan circuit. The resulting voltage swings breakdown the remaining switches in the main circuit, firing MELBA. The -85 kV charge on the PT-70 is near the breakdown threshold for its insulator and coaxial capacitor, so caution must be exercised not to exceed this charge value.

MELBA requires approximately 60s to charge, which limits the rate at which shots can be fired. Thus, no repetitively pulsed experiments can be run using MELBA as the source of pulsed power. MELBA uses seven spark gap switches to erect the Marx. This erection time is generally on the order of 400 ns and must be accounted for when devising a triggering scheme. The timing jitter on these switches can be significant as well. The precise firing time of each of switch is recorded by pointing a fiber-optic cable at the switch and connecting it to a photo-multiplier tube. In extreme cases, switches may fire 100s of ns late. This can have a significant impact on the timing and shape of the MELBA voltage pulse.

MELBA is charged and triggered through a series of resistors made using copper sulfate solution. Failure of these resistors can introduce contaminants that can dissolve into the insulating oil, reducing its electrical hold off. The resistance and physical dimensions of the resistors can be manipulated by altering the concentration of the copper sulfate solution. Exchanging the copper electrodes of these resistors with stainless steel electrodes appears to improve the longevity of the resistor. A photograph of MELBA's capacitors, switches, charging and triggering resistors is shown in Figure 3.16. The ceramic insulating stack is shown in Figure 3.17.

The MELBA voltage is measured by a large $CuSO_4$ resistive voltage divider [65]. The voltage divider is embedded directly into MELBA's high voltage cathode plate under oil. The divider was calibrated using a Northstar high voltage probe and a pair of Febetron modules. The Febetron modules delivered 30-80 kV to the un-shorted high voltage cathode plate. A linear calibration was determined over the voltages tested and extrapolated to MELBA voltages. The MELBA current is measured by a Rogowski coil embedded in the large flange of the MELBA oil tank. This Rogowski coil was made from a 259 cm RG-58 coaxial cable with the outer conducting braid removed and replaced with a 1 turn-per-inch helix of 20 AWG

stranded wire, soldered to the end of the inner conductor. The assembly is held together using heat-shrink wrap. The Rogowski coil was calibrated using a Pearson coil and a pulser.

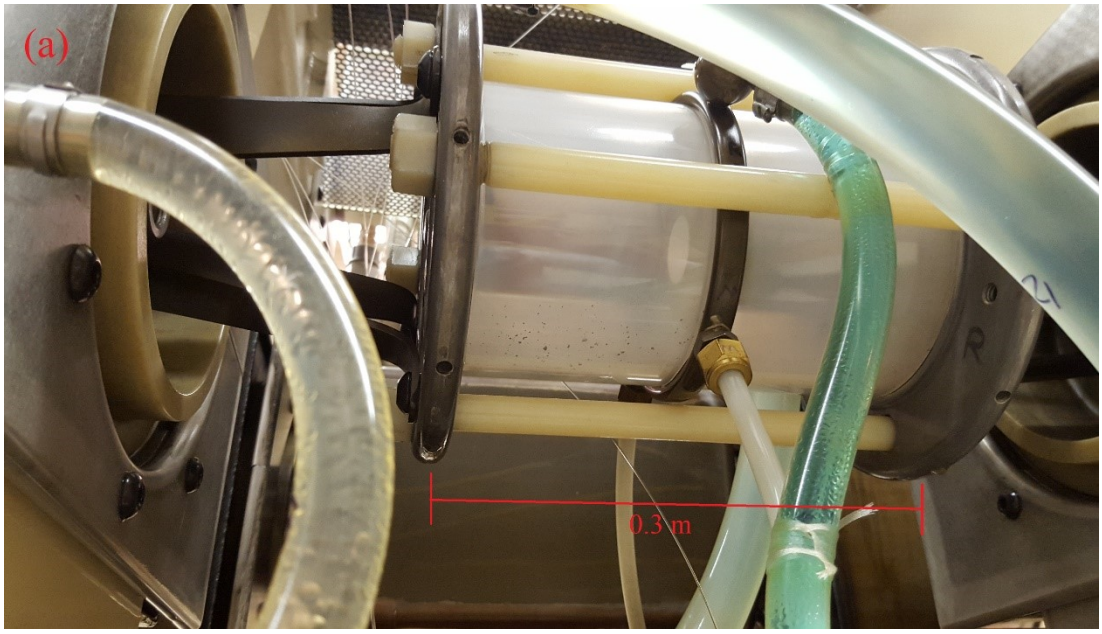

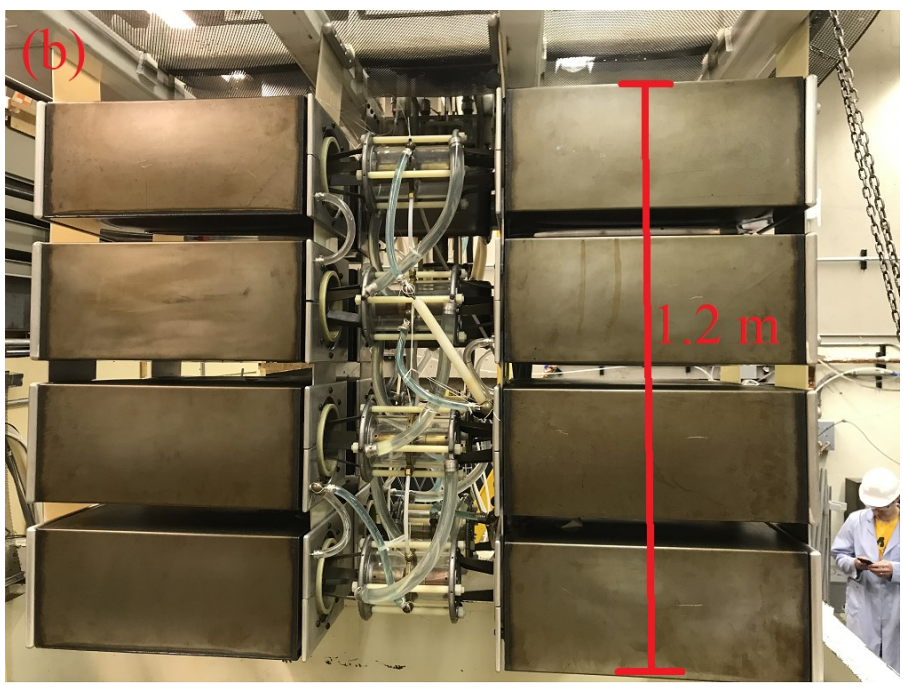

Figure 3.16a (top): MELBA spark gap switch and resistors prior to rebuild. Oil can be seen to have permeated the resistors, and the switch body has become opaque from interaction with SF_6 breakdown products. Deposition of electrode material can also be seen inside the switch.

Figure 3.16b (bottom): MELBA suspended over the oil tank after a completed rebuild.

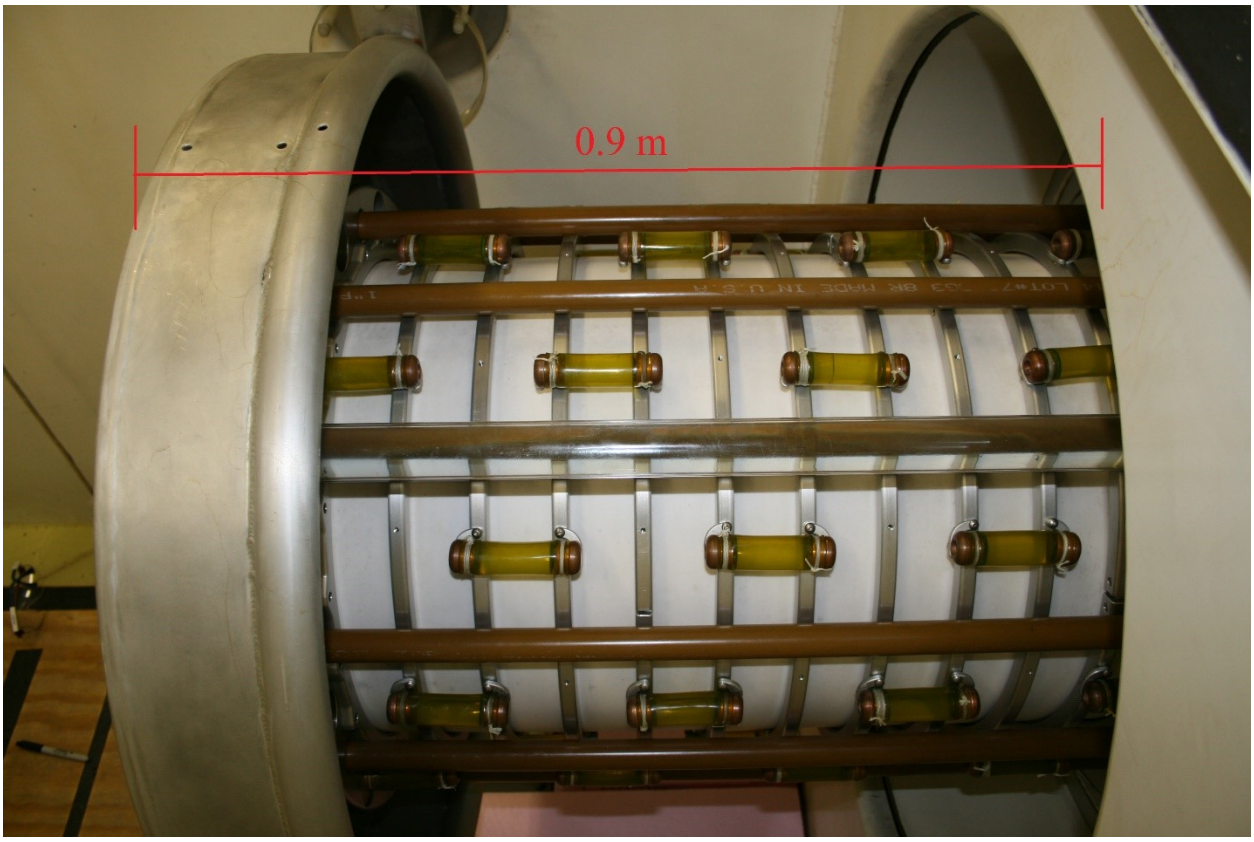

Figure 3.17: MELBA Ceramic insulator. Scale measures from the leftmost surface of the cathode endplate to where the insulator intersects with the oil tank.

3.5 Microwave Sources

A summary of the microwave sources used to generate input power in all RPCFA experiments is presented in Table 3.1. This section gives additional details regarding these sources.

Source	Specifications	Purpose	Driver
MG5223F Magnetron	3.05 GHz, 40kW	Baseline performance	Stanford Modulator (40 kV, 30 A)
4J32 Magnetron	2.84 GHz, 30 kW	~150 MHz off design frequency, still within expected amplification range	Stanford Modulator (40 kV, 30 A)
EPSCO PG5KB signal source	2.4-2.7 GHz continuously adjustable, ~1KW	Small signal response to frequencies outside of the expected amplification range	Internal (5 kV)
MG5193 Magnetron	3.00 GHz, ~ 1 MW	Amplification of high power drive	XLB PFN (40 kV, 100A)

Table 3.1: Summary of microwave input power sources used in this dissertation.

3.5.1 MG5223F Magnetron

The MG5223F magnetron, shown in Figure 3.18, was the first RF source used to drive the RPCFA. The MG5223F is a 3.05 ± 0.05 GHz magnetron rated for 30 kW peak output power and 16 W mean output power. Based on these parameters, this RF source was used to obtain the baseline performance for the RPCFA, at the design frequency and moderate input power levels. The cathode requires 6.3 V, 1.25 A for heating. High voltage pulses of 8.5 kV and peak currents of 12 A were used to operate the magnetron. The maximum recommended pulse length is 1.2 μs and the duty cycle is 0.001. The magnetic field for the MG5223F is provided by a built-in permanent magnet and the magnetron outputs power directly into WR-284 waveguide. No cooling beyond natural air convection was required. The Stanford Modulator (see

Appendix B) is an ideal driver for this magnetron. A typical microwave pulse from the MG5223F is shown in Figure 3.19. The magnetron was repetitively pulsed at 182 Hz and synchronized with the MELBA pulse.

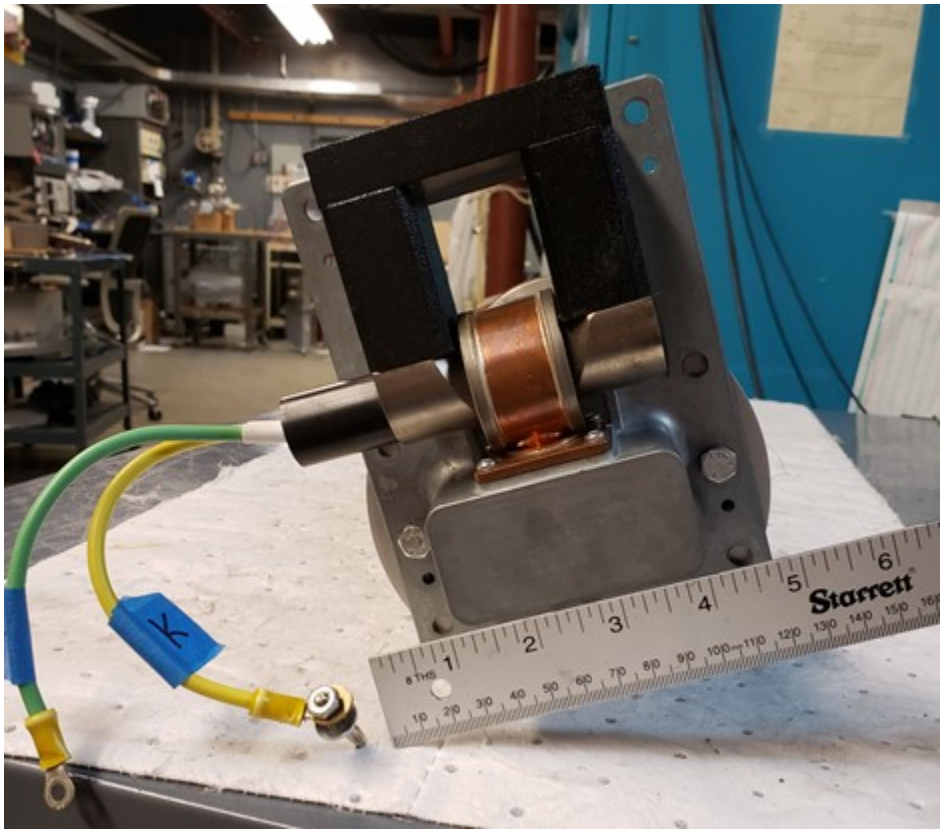

Figure 3.18: MG5223F magnetron. The green lead connects to the filament heater and the yellow lead (marked "K") connects to the high voltage output of the driver.

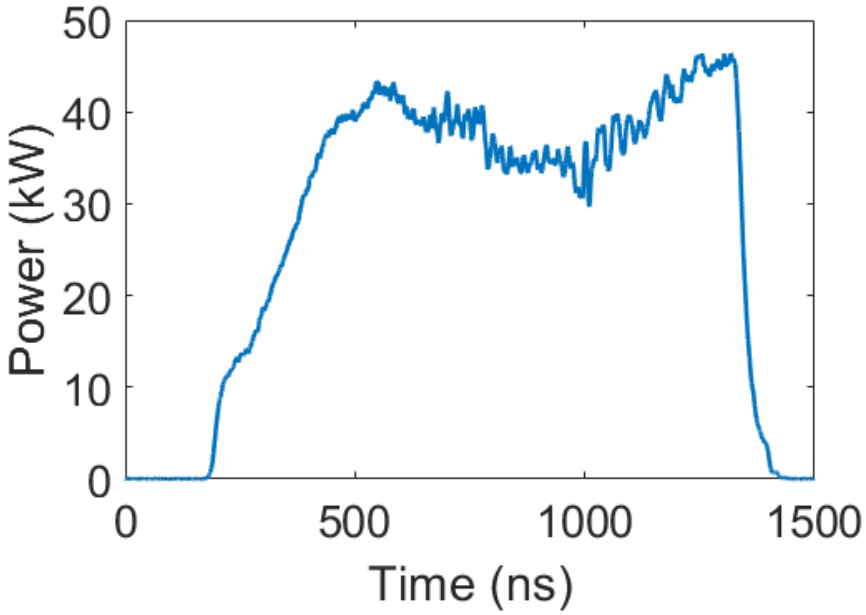

Figure 3.19: Unattenuated output microwave pulse for the MG5223F magnetron.

3.5.2 4J32 Magnetron

The second microwave source used in the RPCFA experiments was the Raytheon 4J32 magnetron shown in Figure 3.20. This RF source was used to test the performance of the RPCFA at frequencies off the design frequency but still within the expected amplification band and delivered at moderate power. The 4J32 is a 2.82 to 2.86 GHz magnetron with a listed peak output of 1 MW and mean output of 500 W. Like the MG5223F, this RF source was driven by the Stanford Modulator. The cathode is heated with 16 V and 3 A. High voltage pulses of up to 30 kV and 70 A are recommended for ideal operation. The Stanford Modulator is incapable of providing these parameters so this magnetron was run at considerably lower power, the peak power obtainable from this magnetron was around 20 kW. The maximum recommended pulse length is 2.5 μs and the duty cycle is 0.001. The magnetic field of 2150 Gauss was provided by an external permanent magnet. The 4J32 magnetron does not require cooling beyond natural air convection. The magnetron features a coaxial output which was adapted to WR-284 using a puck coupler similar to those used in the RPCFA. A typical output pulse for the 4J32 magnetron is shown in Figure 3.21. Again, this magnetron was repetitively pulsed at 182 Hz and synchronized with the MELBA pulse.

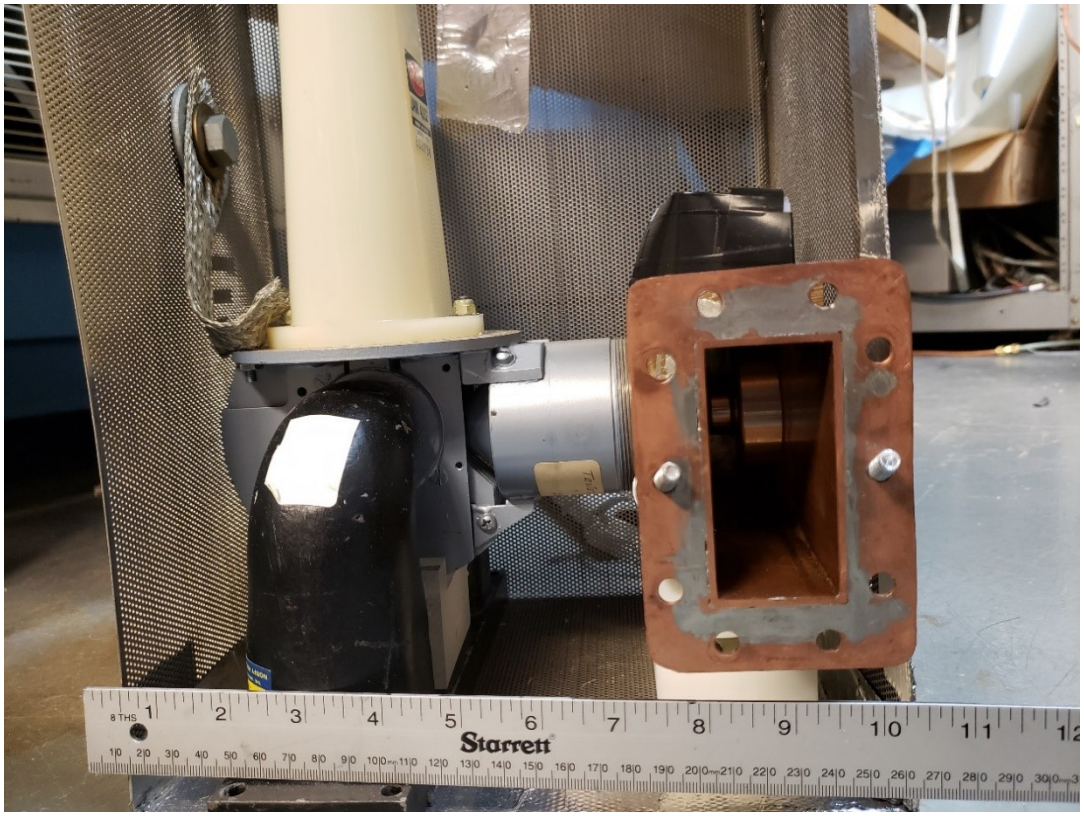

Figure 3.20: Raytheon 4J32 magnetron. The coaxial RF output is adapted to WR-284 waveguide using a scaled puck coupler shown here.

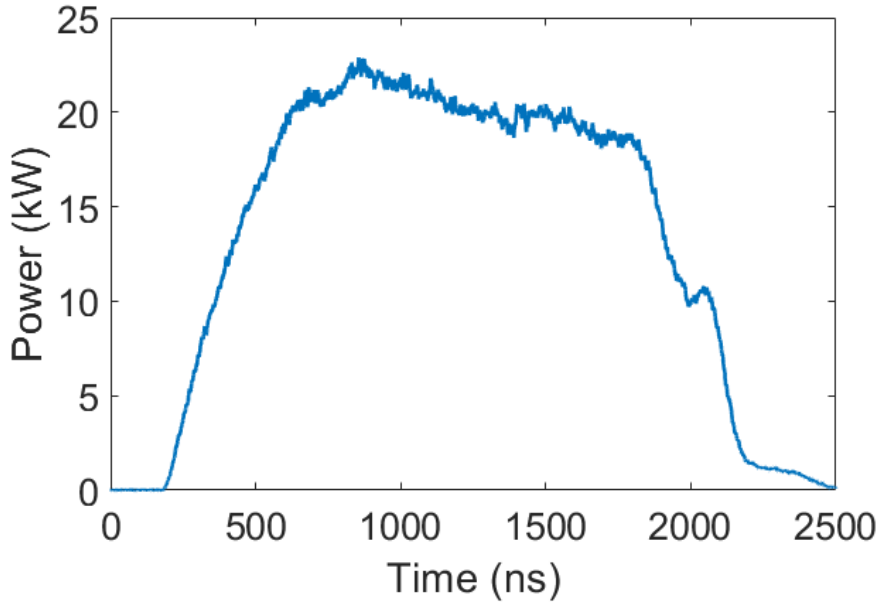

Figure 3.21: Unattenuated output microwave pulse from the 4J32 magnetron driven by the Stanford Modulator.

3.5.3 EPSCO PG5KB Signal Source

The third microwave source used to drive the RPCFA experiments was the EPSCO PG5KB Signal Source, pictured in Figure 3.22. The EPSCO Source is rated for 5 kW output power at frequencies ranging continuously from 2.4 to 2.7 GHz. It was determined experimentally that only around 1 kW could be generated over the listed frequency range. This RF source was used to observe the performance of the RPCFA when driven at frequencies beyond its expected amplification band. The EPSCO Source generates microwave pulses ranging from 0.3 to 50 μs in length at a continuously-variable repetition frequency up to 25 kHz and a maximum duty cycle of 0.003. The EPSCO Source requires only 120 V AC wall power and no external driver. It has a synch-out port which is used to synchronize with other components of the experiment.

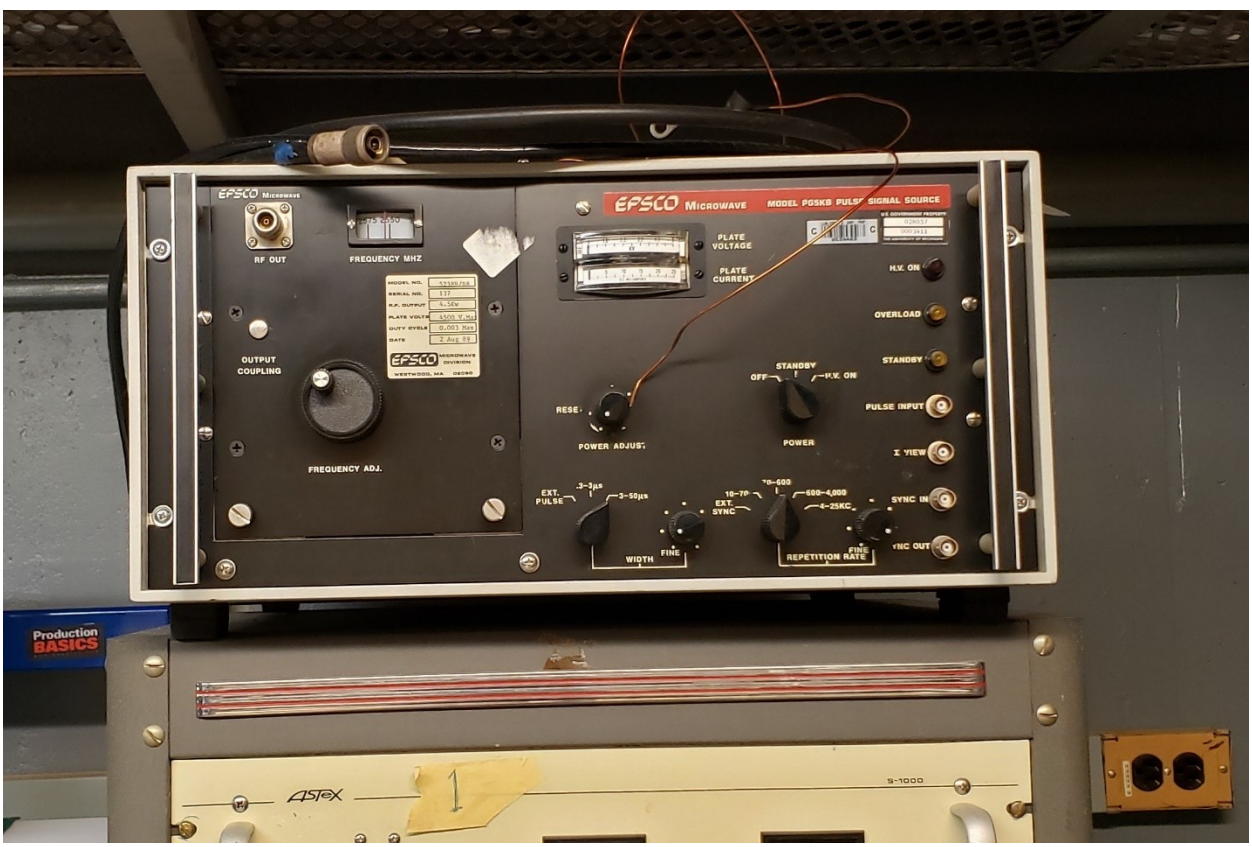

Figure 3.22: EPSCO model PG5KB pulse signal source. For scale, the source is fits into standard 19-inch rack mount.

The pulse-waiting method is used to permit the comparatively slow diffusion of the magnetic field from the Helmholtz coils, while minimizing the effect of jitter from the RF source driver, delay generator, and MELBA triggering. In this method, the RF source driver (the Stanford Modulator or EPSCO Source) is set to fire repetitively at a repetition rate of 182 Hz, or one shot every 5.5 ms. After charging MELBA, the run-stop button of the BNC delay generator is pressed. The delay generator then waits for a synch-out pulse from the RF source driver. Once this pulse is received, the delay generator triggers the Helmholtz coil. The delay generator then waits for two subsequent synch-out pulses, firing MELBA and triggering the oscilloscopes for data collection on the third, giving the magnetic field 11 ms to diffuse into the experiment and synchronizing faster components onto a single trigger. A triggering sequence diagram for this pulse-waiting method is presented in Figure 3.23.

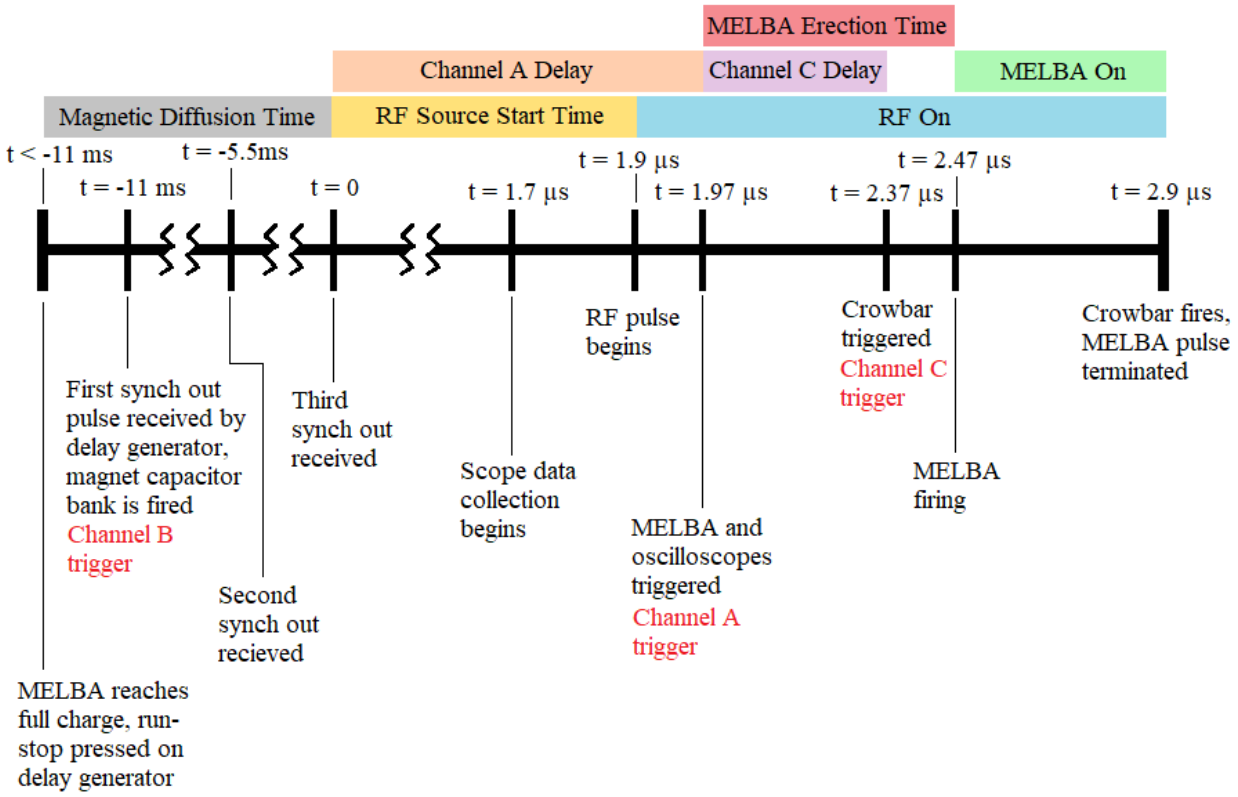

Figure 3.23: Pulse-wait triggering scheme used for experiments driven by the EPSCO Source or magnetrons driven by the Stanford Modulator (MG5223F and 4J32). Programmed channel delay may vary slightly due to the RF source or to investigate the RPCFA's response to variation in timings. Figure is not to scale.

3.5.4 MG5193 Magnetron

The fourth microwave source used to drive RPCFA experiments was the E2V MG5193 magnetron, pictured in Figure 3.24. This magnetron is rated for up to 2.5 MW of peak RF power at frequencies ranging from 2.993 to 3.002 GHz. The performance of the RPCFA at high power RF drive was investigated using this magnetron. The cathode is heated with 8.5 V, 9 A which was provided by the Stanford Modulator. The 45 kV, 100 A pulses required to operate this magnetron were not obtainable using the Stanford modulator so the XLB PFN (see appendix B) was designed and used to drive the MG5193. The MG5193 is capable of pulse lengths up to 5.0 μs and a maximum duty cycle of 0.001. The magnetic field for the magnetron is provided by an electromagnet, also shown in Figure 3.24. The magnetron and electromagnet are both cooled by flowing water. Power is output into cylindrical waveguide and the converted to WR-284 waveguide through an adapter built by E2V. A typical microwave pulse from the MG5193 magnetron is shown in Figure 3.25.

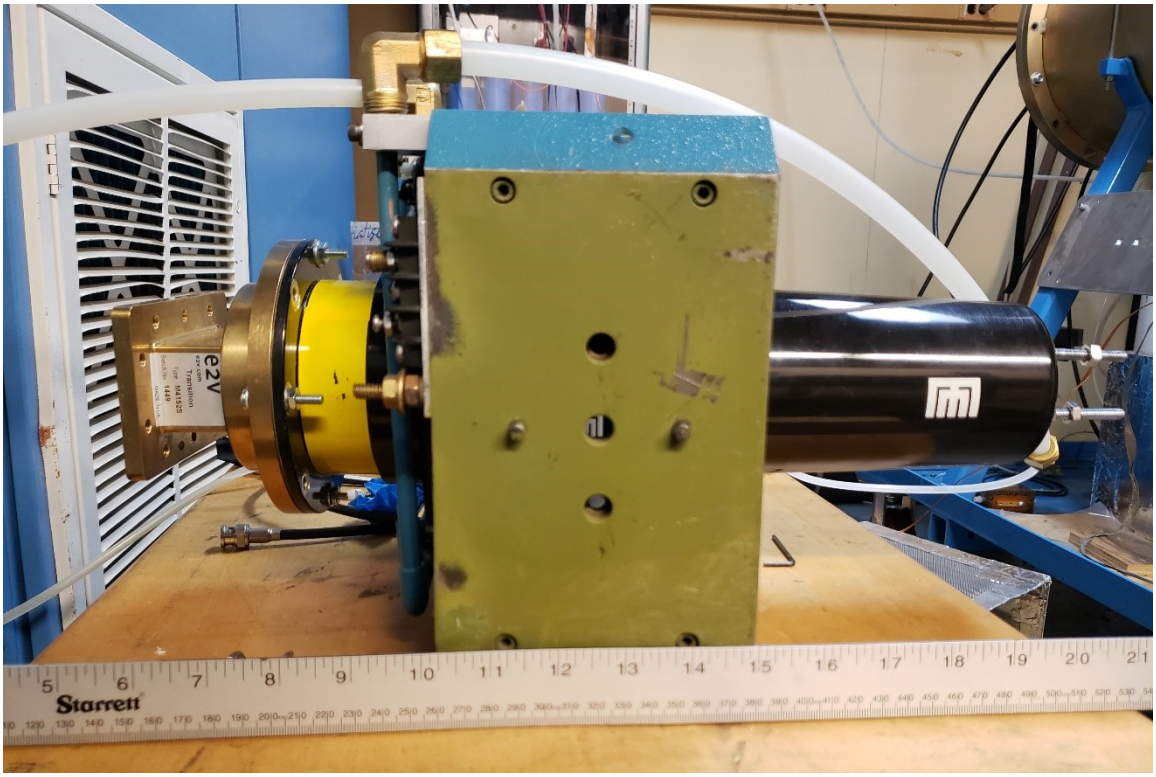

Figure 3.24: MG5193 magnetron with L-3 solenoid. Approximately 18 A were transmitted to this 1-Ω solenoid during operation. Water lines connect the magnetron and the solenoid. An E2V adaptor on the left converts the output of the magnetron from cylindrical to WR-284 waveguide.

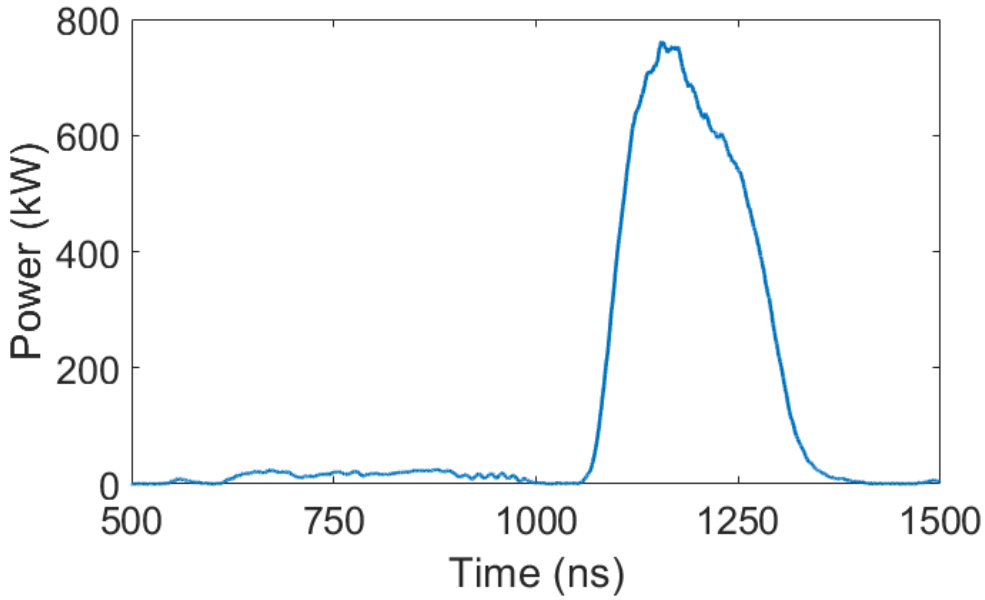

Figure 3.25: Unattenuated output microwave pulse from the MG5193 magnetron driven by the XLB PFN. Low power is generated early in the pulse (600 to 1000 ns), though still at the pi-mode frequency, prior to high power output.

A Pearson coil (0.1 V/A) was used to measure the current entering the magnetron. The anode current, voltage, and microwave power are plotted in Figure 3.26. The high voltage and currents seen early in the pulse are due to signals from the PT-55. The RF power begins late in the pulse and is only at high power for a relatively short time, despite the current and voltage remaining at apparently sufficient levels after the RF pulse ends. This may be due to the temperature of the cathode. While the current supplied by the Stanford Modulator's filament heater is sufficient for maintaining the stand-by temperature of the cathode, the MG5193 is typically operated with significantly higher repetition rates and duty cycles where the back bombardment of electrons heats the cathode far beyond the stand-by temperature. In this single shot mode, the cathode may be too cold for the magnetron to start up quickly and produce stable RF pulses. Since the XLB PFN is single-shot which can be triggered externally, the pulse-waiting method is not required. The triggering scheme diagram is presented in Figure 3.27.

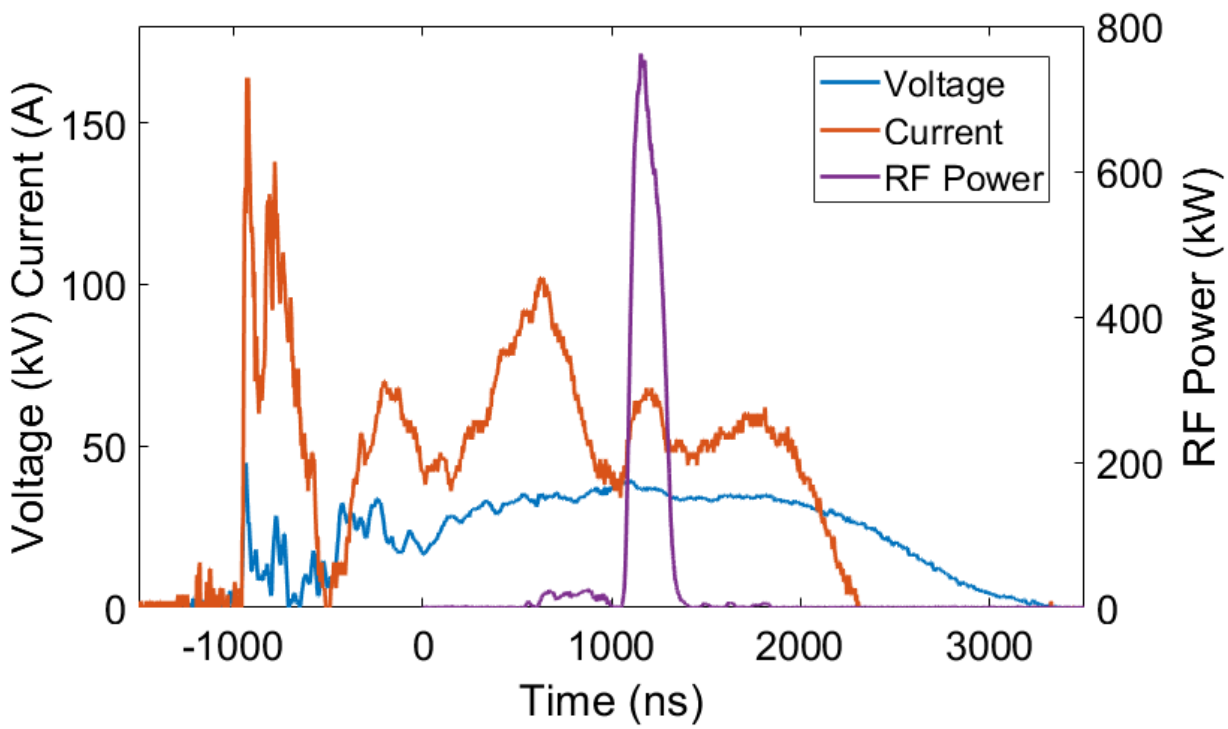

Figure 3.26: Voltage, current and RF power output from the MG5193 magnetron driven by the XLB PFN

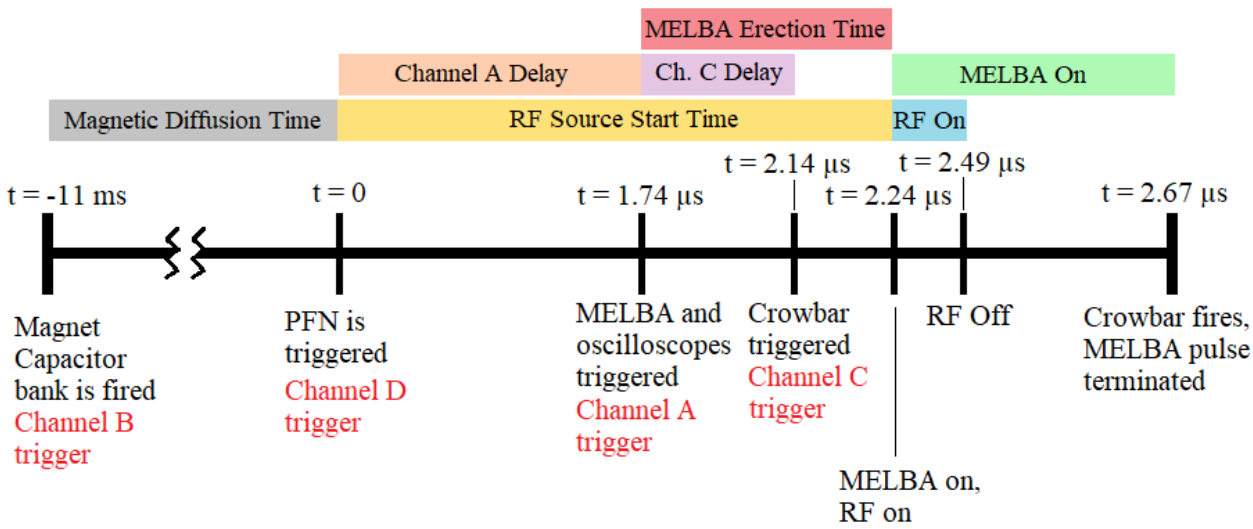

Figure 3.27: Triggering scheme for experiments that utilized the single shot XLB PFN and the MG5193 magnetron. Figure not to scale.

CHAPTER 4

Experimental Results

This chapter presents and discusses the results of experiments performed using the RPCFA prototype. In the first section, amplification of moderate-power RF input drive is demonstrated at frequencies within the simulated amplification band. Zero-drive stability is demonstrated as is verification of simulated cold tube scattering parameters. The relative phase of the output signal is analyzed in the second section. In section 3, the RPCFA response to variation in the magnitude of the input microwave drive power, frequency, and applied magnetic field is presented. Section 4 discusses the sources of variation in the observed amplification. The different cathodes used in the RPCFA experiments and their effects are presented in section 5. Amplification of high power (100's of kW) input microwave drive and an analysis of the relative phase is presented in the sections 6 and 7 respectively.

4.1 RPCFA Fundamental Operation and Moderate Power Amplification

The first aspect of the RPCFA to be tested experimentally was proper transmission over the range of frequencies predicted in simulation. The RPCFA was installed into the MELBA vacuum chamber and the WR-284 wave ports were connected to a Hewlett-Packard 8772D network analyzer as shown in Figure 4.1. The measured S_{21} is plotted over the S_{21} simulated in HFSS in Figure 4.2.

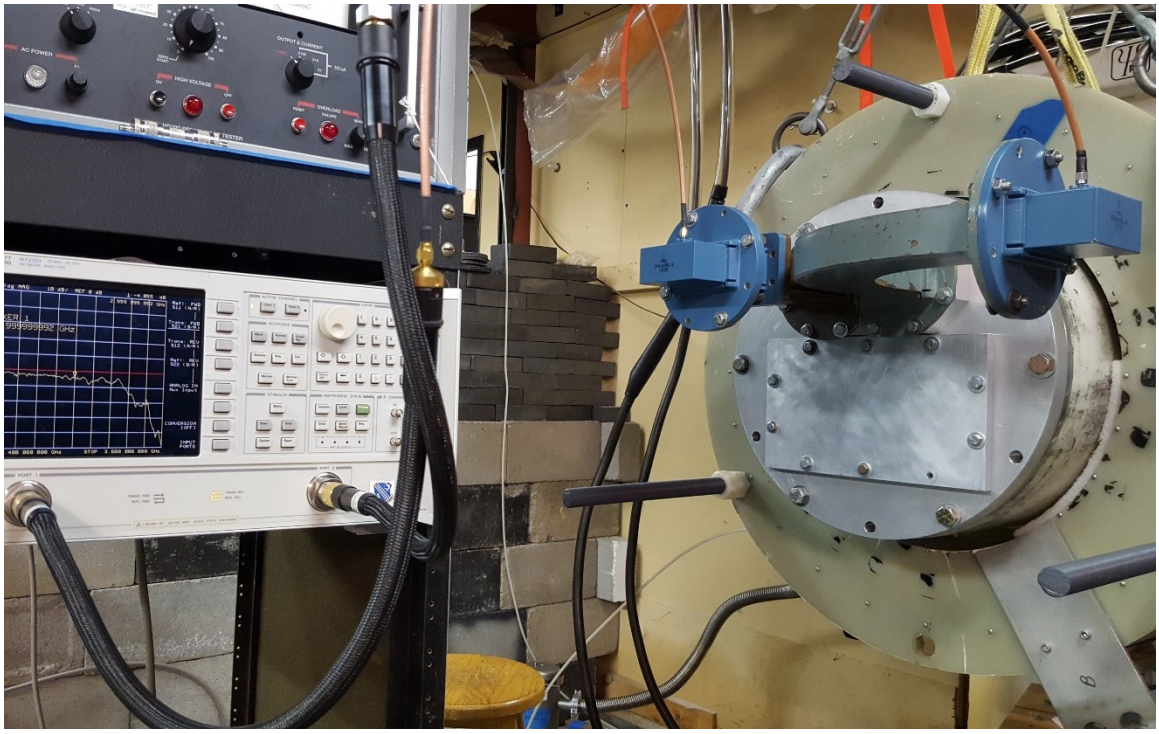

Figure 4.1: RPCFA connected to the network analyzer for cold tube transmission measurement.

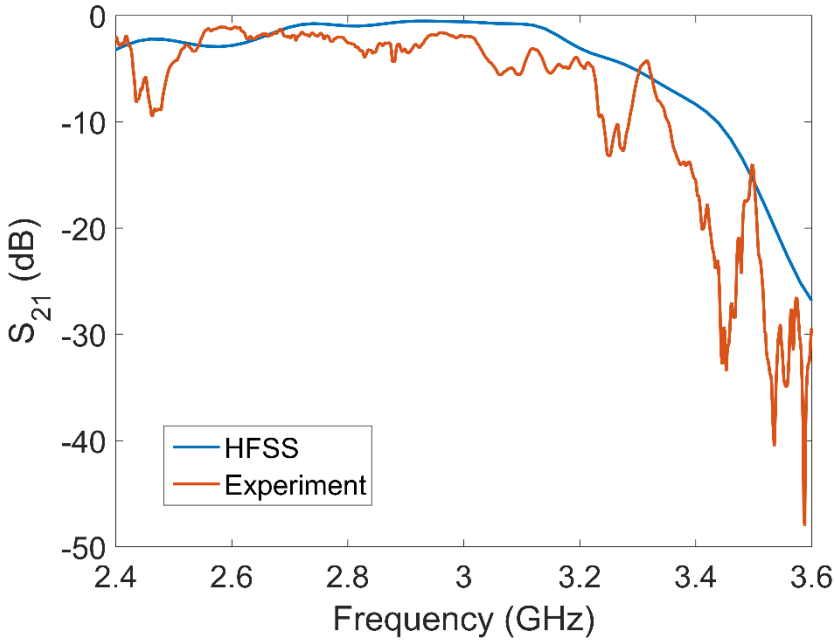

Figure 4.2: Measured and simulated S_{21} for the RPCFA.

Qualitatively, the traces show acceptable agreement, displaying a broad passband from approximately 2.6 to 3.1 GHz. Within this passband, no high Q resonances are observed. The S_{21} values at the design frequency are -0.6 dB in simulation and -1.9 dB experimentally. The measured S_{21} features a sharp drop in transmission at 2.45 GHz as well as generally worse transmission for much of the band. This is likely due to two factors; In simulation all conducting elements are perfect conductors and connections between components have zero contact resistance. The prototype RPCFA is composed of several components bolted (not brazed) together. These interfaces, especially near the waveguide to coaxial adaptors introduce RF contact resistances, that reduce the rate of power transmission [79]. The number of components and joints in the experimental measurement is also greater than in simulation. In simulation, the measurement ports are located directly on the ends of the coaxial input and output lines. Components were optimized in simulation individually to reduce the run time of simulations. The standardized ports of the network analyzer required the experimental measurements be taken outside of the vacuum chamber. Thus, the simulated S_{21} measures the transmission across the SWS, whereas the experimental S_{21} measures transmission across the SWS and two passes through the vacuum window, the coaxial-to-waveguide adaptors, and the WR-284 waveguide inside and outside the vacuum chamber. Each of these locations represent a potential loss in transmission. The most significant losses in transmission occur at the puck couplers, (see Figure 3.12), across the SWS, and at the points of contact between these, and other components where RF contact resistance is significant.

Tuning stubs were included in the RF circuit in an attempt to mitigate any impedance mismatches that may have been a source of transmission loss. The measured S_{21} with tuning stubs was lower for all frequencies of interest and all configurations of the stubs. This indicates that the nature of transmission loss is not reflective, due to an impedance mismatch, and confirms that the losses are resistive or radiative. In either of these scenarios, no significant backward wave is present, meaning the phase velocity of RF is unperturbed. The consequence of these losses should reduce the gain of the RPCFA but not alter the propagation of the RF excitation nor its interaction with the Brillouin hub.

Zero-drive stability was confirmed by firing MELBA into the RPFCA without microwave injection. The zero-drive pulsed current, voltage and measured RF power were recorded and plotted in Figure 4.3.

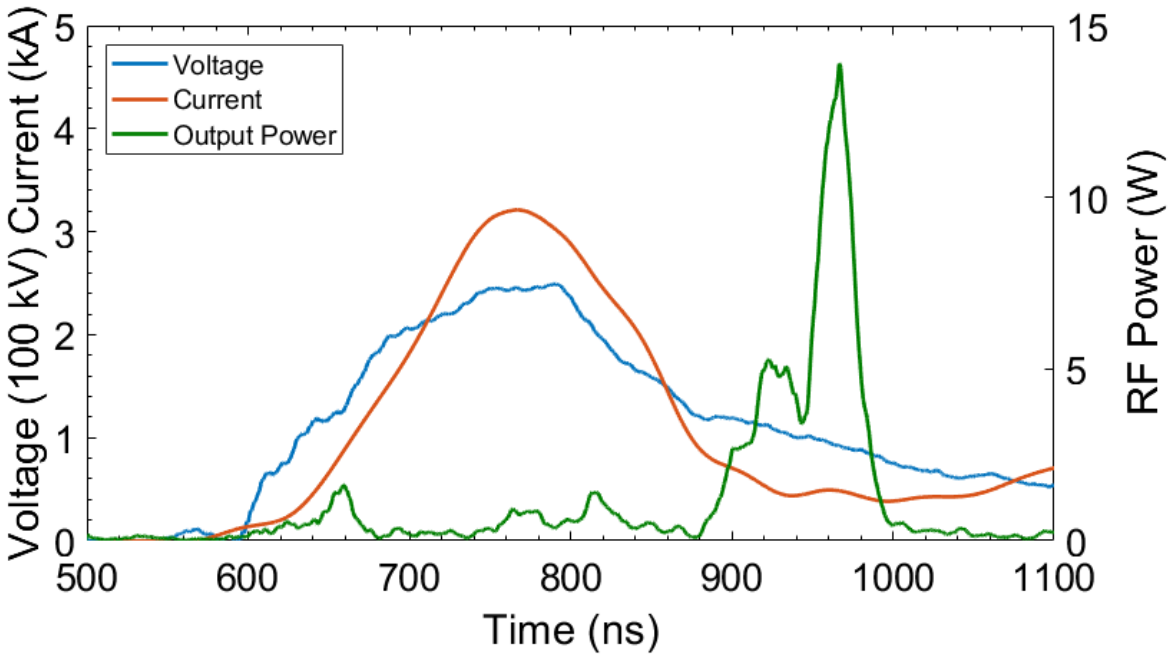

Figure 4.3: Zero RF drive, MELBA voltage and current profile with the output RF power measurement overlaid.

Multiple shots were taken, each displaying consistent behavior. Inline attenuation was removed until RF power was measurable and within the calibrated range on the diode. From nearly 770 MW of peak pulsed power, a peak output power of less than 15 W was measured. Furthermore, this peak occurs long after the MELBA voltage pulse is crowbarred. This experiment suggests zero-drive stability is achieved at operating conditions. It is possible however, that oscillatory modes may exist inside the RPCFA at frequencies that cannot be extracted through the coaxial waveports. No such oscillations were observed in simulation.

The spectrum of this extracted microwave power can be compared with the same result obtained from MAGIC simulation. These spectra are plotted in Figures 4.4a and 4.4b.

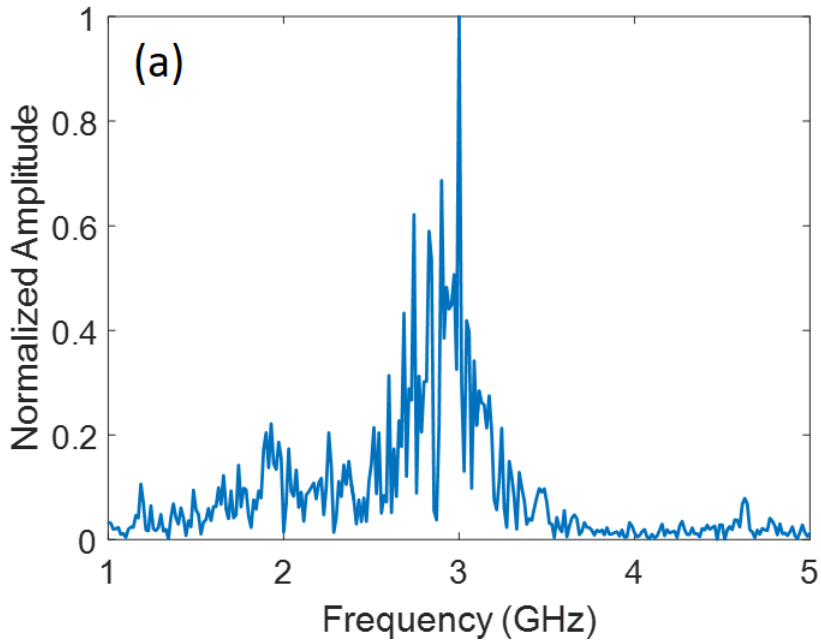

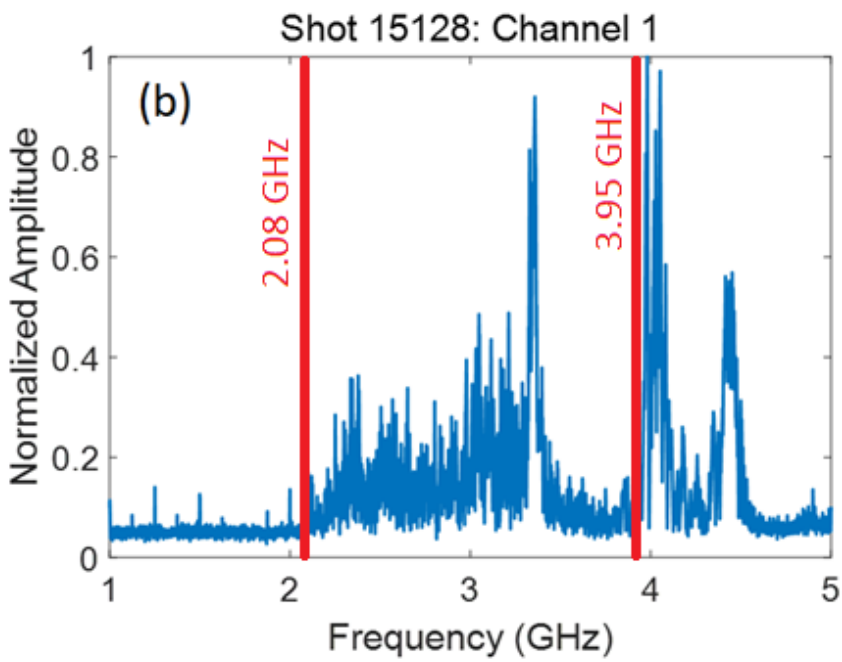

Figure 4.4a (top): MAGIC simulated spectrum of zero-drive output signal.

Figure 4.4b (bottom): Measured output spectrum from zero-drive experiment. The range of calibrated frequencies is marked by the red lines. Both spectra are on linear scales.

Both spectra show broadband radiation from approximately 2 to 3 GHz. Neither are indicative of a well-defined oscillating mode. At frequencies greater than 3.95 GHz, WR-284 waveguide becomes overmoded and the diodes used to measure RF power are uncalibrated. It is expected that the power at the high frequencies suggested by Figure 4.4b are not representative of the frequency content of the output spectrum. Regardless, an oscillatory mode would be expected to have a narrower peak and normalized amplitude orders of magnitude greater than the surrounding broadband noise. The observed spectrum suggests zero-drive stability in the RPCFA as predicted by MAGIC simulation.

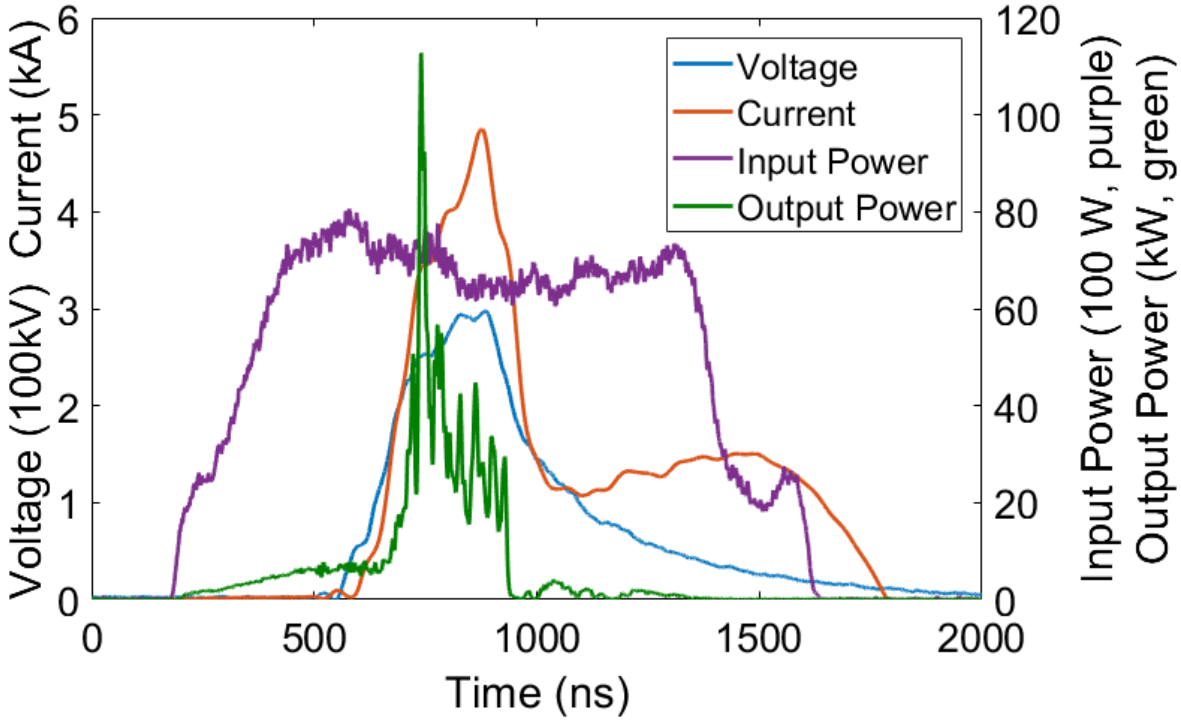

Figure 4.5: Shot 15316. MELBA current and voltage overlaid with the injected 8 kW at 3.05 GHz and 117 kW amplified power.

Both pulsed DC and microwave power were applied to the RPCFA and amplification was observed. The current and voltage traces, as well as the injected 8 kW and amplified RF power, are presented in Figure 4.5. RF power was initiated 400ns prior to the onset of the MELBA pulse. The output power before the application of pulsed power matches the transmission (and loss) predicted by the experimental cold test. Amplification begins during the rise of the MELBA pulse and peaks before the voltage reaches the targeted

flat-top value of -300 kV. Peak microwave amplification lasts for approximately 20 ns FWHM and reaches 117 kW, a peak gain of 11.4 dB. This amplification drops to much more modest values after the peak, though gain remains in the 5 – 6 dB range for the length of the MELBA pulse, approximately 260 ns.

The output microwave power spectrum was measured for amplifying shots. Spectra of a shot driven at 3.05 GHz is shown in Figure 4.6a and a shot driven at 2.84 GHz is shown in 4.6b. Both spectra show the dominance of the drive frequency and the absence of any other significant frequencies. These spectra are integrated over the length of the observation, 4000 ns, much longer than both the RF drive and the MELBA pulse. This confirms that even for suboptimal and transient conditions, such as during the rise and fall of the pulsed voltage, the RPCFA is not prone to oscillation for the majority (> 90%) of moderate input drive power shots.

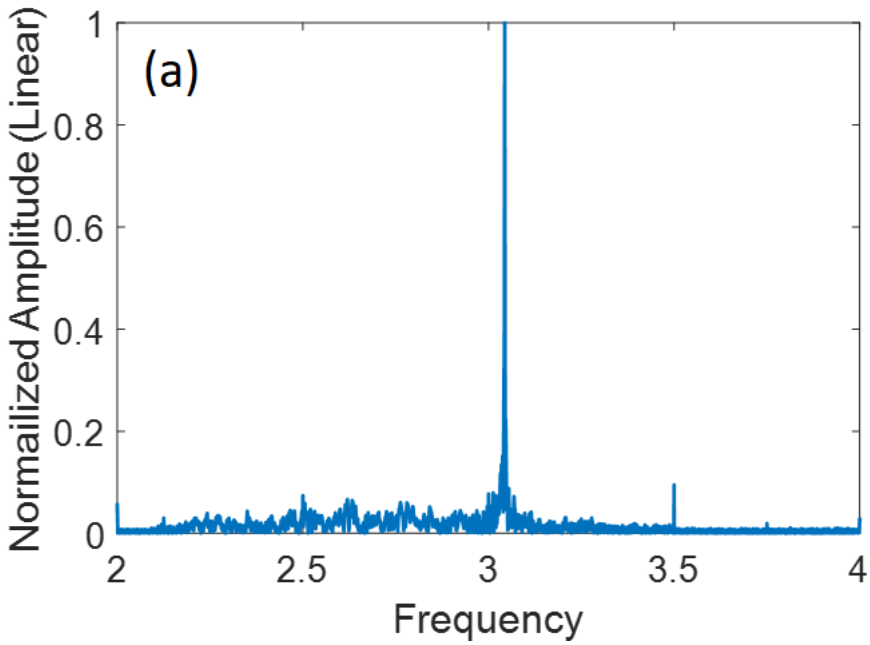

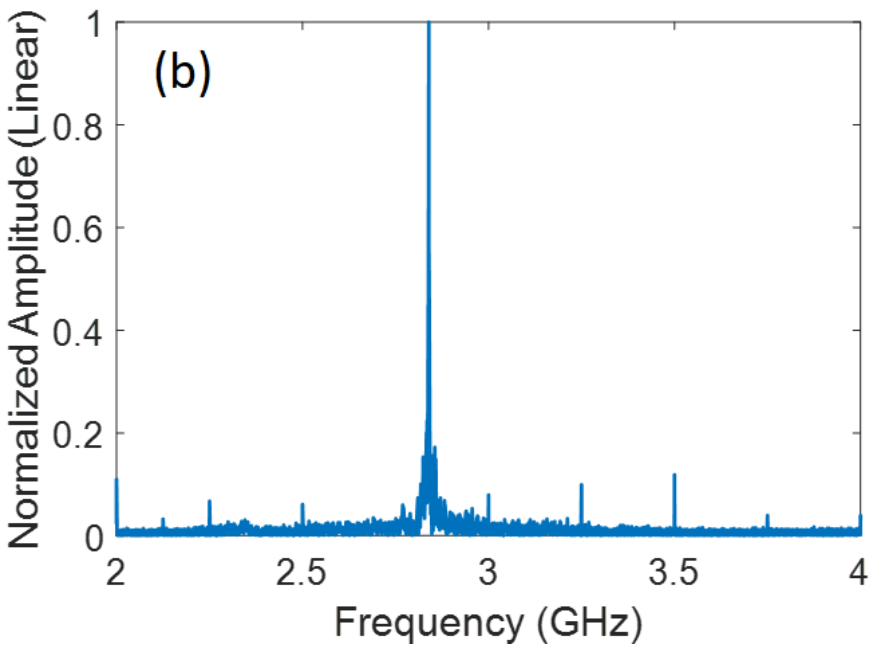

Figure 4.6a (top): Output microwave power spectrum for shot 15316 driven at 3.05 GHz.

Figure 4.6b (bottom): Output microwave power spectrum for shot 15534 driven at 2.84 GHz. Both spectra show small peaks at exact multiples of 1/8 GHz. These peaks are exactly 1 frequency bin wide and presumed to be artifacts of sampling and not representative of the frequency content of the measured signals.

4.2 Phase Analysis

A feature of amplifiers in general is the preservation of phase information. The phase of the output signal must be a predictable function of the input signal. This is a major distinction between a primed oscillator and an amplifier [37]. It is possible to show the RPCFA retains phase information in MAGIC simulation by measuring the voltage over time at a given point in the input coaxial line and another point in the output coaxial line. The phase difference between the two signals is given in Figure 4.7

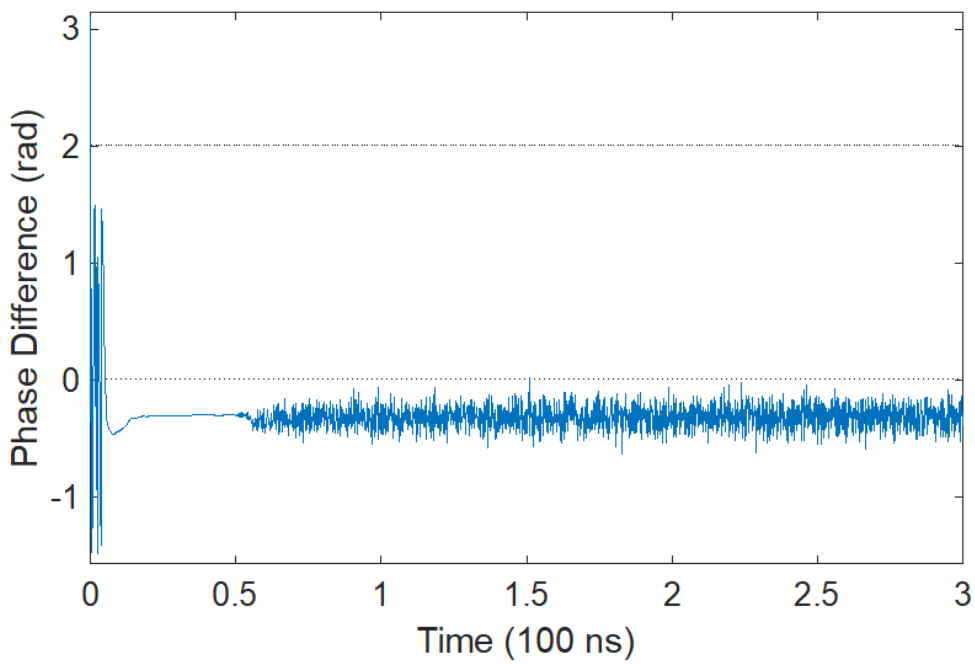

Figure 4.7: Phase shift between the input and output signal measured in MAGIC simulation. The erratic phase difference early in time is due to the RF signal not yet reaching the output coaxial line.

MAGIC simulation shows excellent phase stability in the RPCFA. At steady-state and even during the rise of the DC voltage, the phase difference between the input and output signal is essentially constant. This process can be repeated for the RPCFA experimentally by measuring the phase shift between the forward input and forward output power from the directional couplers. An example plot of phase shift over time is given in Figure 4.8a and 4.8b.

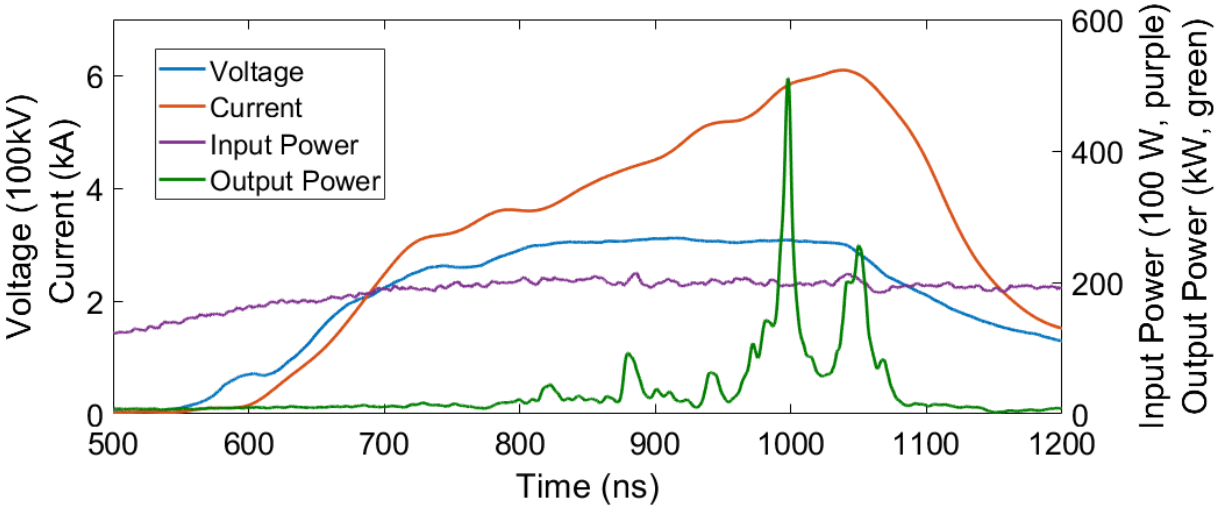

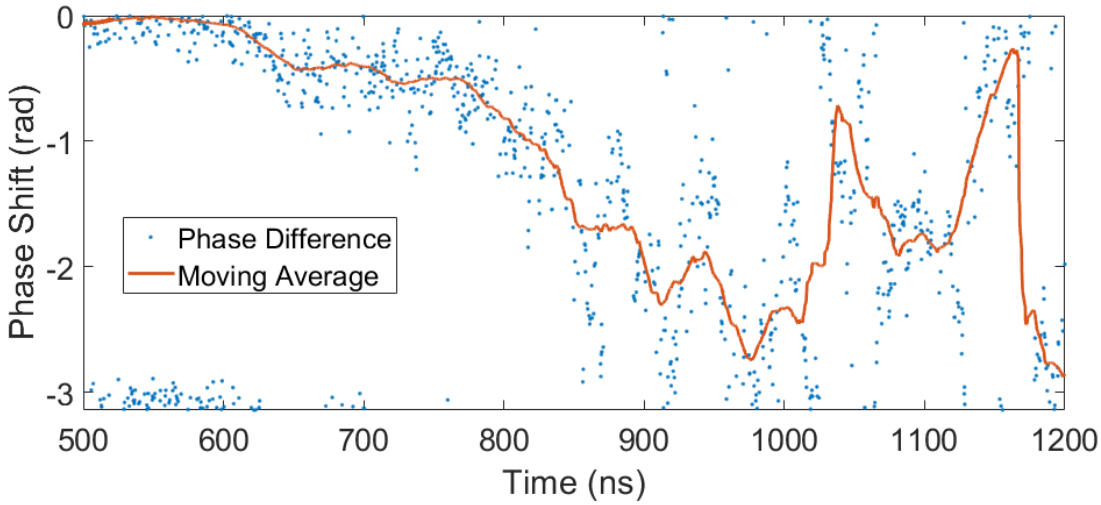

Figure 4.8a (top): MELBA current and voltage with RF output power during the time phase difference measurements are calculated (shot #15570).

Figure 4.8b (bottom): Phase difference over time with moving average overlaid.

The measured phase difference drifts at a roughly constant rate in the early stages of the MELBA pulse. The source of this drift is likely due to the changing pulsed current and the expansion of the Brillouin hub and the creation of a conducting plasma layer that expands from the cathode into the interaction space [66 - 69], which alters the electrical characteristics of unit cells in the SWS (see section 2.5). A change in the phase shift per cell is magnified by a factor of 12 due to the length of the 12-cell SWS. As greater currents are present later in the pulse, the phase shift drifts further and becomes more erratic. Precise phase difference measurements are not repeatable in experiments at moderate (< 150 kW) input RF power due to

the inconsistencies discussed in section 4.4. At these moderate RF drive levels, the RF signals may additionally be altered by electrical noise generated in the experiment. This noise can significantly impact the sensitive phase measurements shown in Figure 4.8b leading to the high variation in phase shift observed at a given instant. This electrical noise should not have a significant impact of the measurement of RF power as the Low Barrier Schottky Diode's response is relatively slow. Continuity of the phase difference over time is observed, indicating the information is preserved. Therefore, the phase shift is not random, giving evidence that the RPCFA is amplifying microwave power.

The measurement of phase over time can also be used to identify shots which generate non-amplifying RF power. A small fraction (< 10%) of shots display significant levels of non-amplifying power, an example of which is presented in Figure 4.9a and 4.9b.

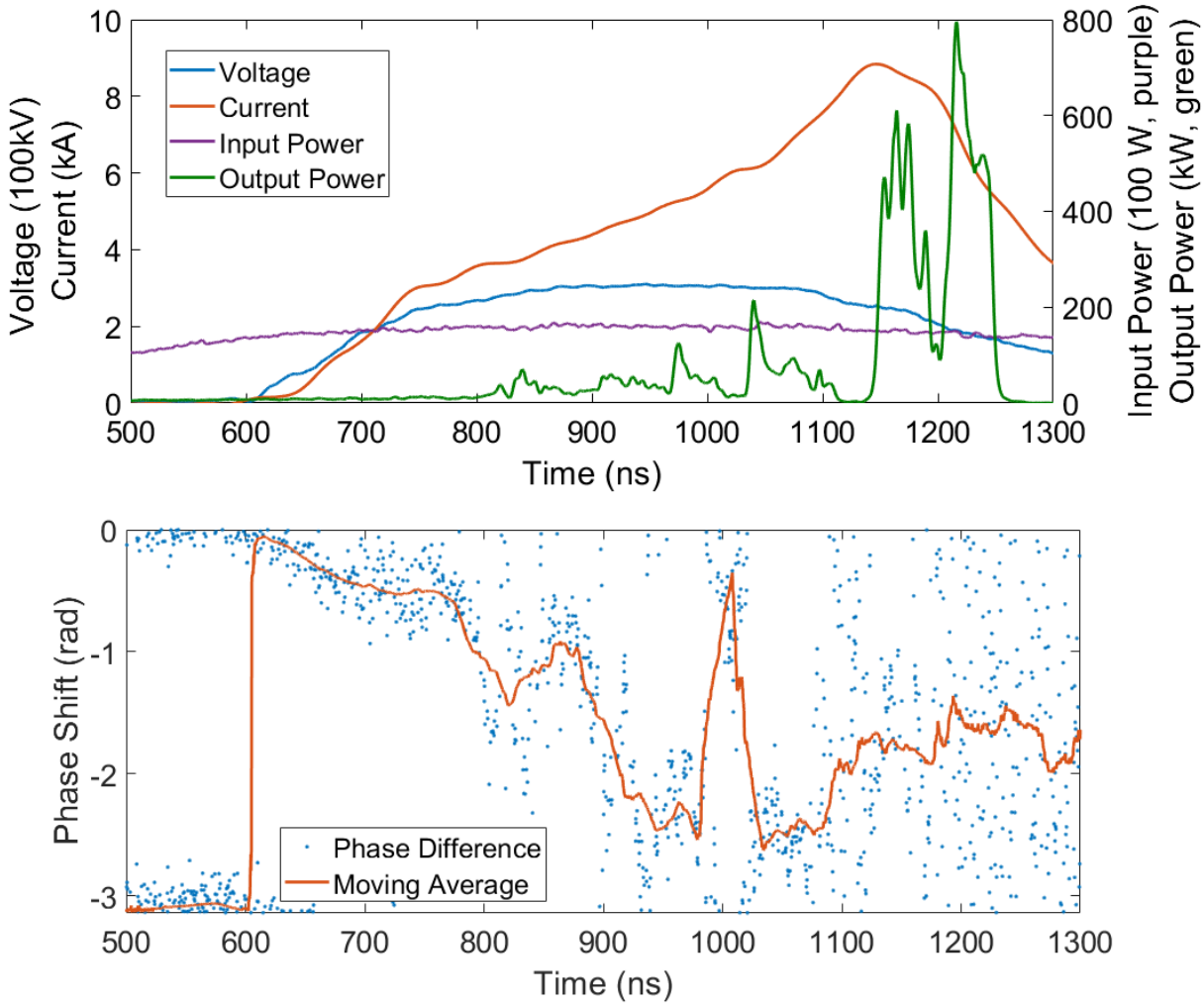

Figure 4.9a (top): MELBA current and voltage with RF output power for a shot that displays both amplifying and oscillatory behavior (shot #15567). Input microwave power is constant at around 15 kW over the plotted time scale.

Figure 4.9b (bottom): Phase difference over time showing a trend similar to Figure 4.8b until around 1100 ns, when transmission terminates.

A peak microwave power of 796 kW is measured from an input drive of 14.9 kW, an apparent gain of 17.3 dB. It is seen from Figure 4.9b that the phase difference over time drifts continuously until approximately 1120 ns. At this point the phase difference becomes randomized and the output power drops to levels significantly below transmission. This demonstrates that the impact of plasma in the interaction space has affected the SWS so greatly that it is no longer transmitting the input signal. This non-transmitting

SWS no longer carries information about the phase of the input signal and can support oscillatory modes. The peak power for the shot occurs during this time when the output signal does not contain phase information from the input and is in fact oscillating at a frequency different from the injected RF. This is verified by a time-frequency analysis (TFA) shown in Figure 4.10.

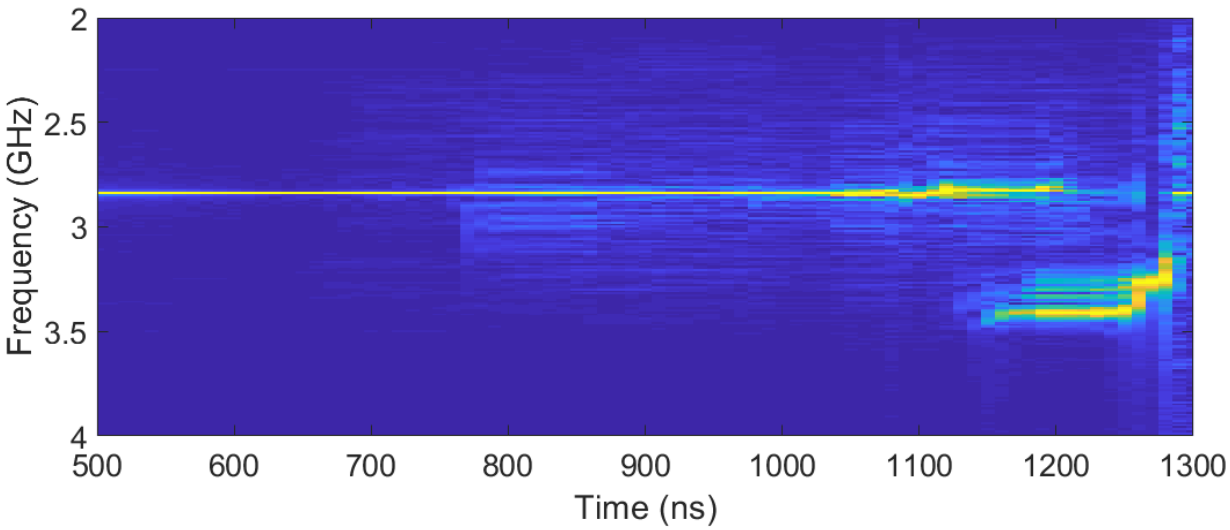

Figure 4.10: Time frequency analysis of the output signal for shot #15567, which displays amplification followed by oscillation.

The analysis of phase difference over time verifies the RPCFA generally operates as an amplifier though under certain conditions, oscillation can occur. Oscillating power such as the peak power in shot 15567 is removed from data sets where quantities such as mean gain and output power are analyzed.

4.3 Parametric Characterization of the RPCFA

The RPCFA's response to variation in input drive power was measured by varying the attenuation on a WR-284 variable attenuator. Two sources, the 2.84 GHz magnetron and the 3.05 GHz magnetron, were used to investigate the amplifier's performance to amplify frequencies well within the expected amplification band. The plot of output power versus moderate input power is displayed in Figure 4.11. The magnetic field used when driving at 2.84 GHz was 2.26 kG and the magnetic field when driving at 3.05 GHz was 2.03 kG. These fields were chosen as they minimized variation in output power.

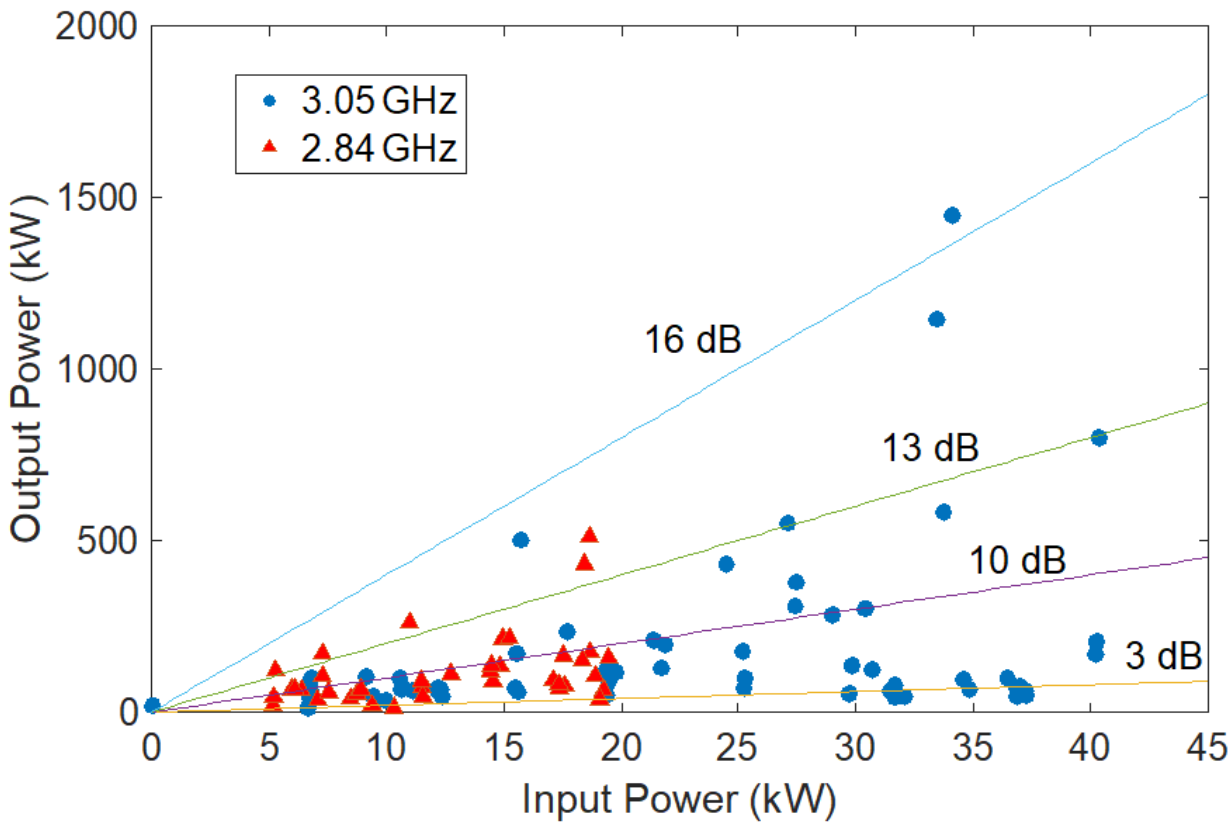

Figure 4.11: Measured RPCFA output power versus the input power supplied by the two magnetrons tested. Lines are drawn showing gain values of 3, 10, 13, and 16 dB for reference. Power measurements have an uncertainty of 0.3 dB.

While the data show a large amount of variation and inconsistency, the highest output powers are generated from high input powers. This is evidence that at these modest input drive levels, the RPCFA is

unsaturated. The mean amplification over all shots in Figure 4.11 is 7.2 dB. The amplifier operates similarly at moderate input powers, for the two frequencies tested within the expected amplification band.

The strength of the axial magnetic field was varied to determine the RPCFA's response. The plot of gain versus magnetic field, for the same 2.84 and 3.05 GHz input drive sources, is given in Figure 4.12. Variation in gain is again a major issue in this dataset. For this reason, the magnetic fields chosen for future experiments are based primarily on minimizing the variation in gain at a given field. The highest gain, 19.6 dB corresponding to 1.5 MW of peak output power, is achieved at the highest field. However, the greatest variation in output power also occurs at this setting.

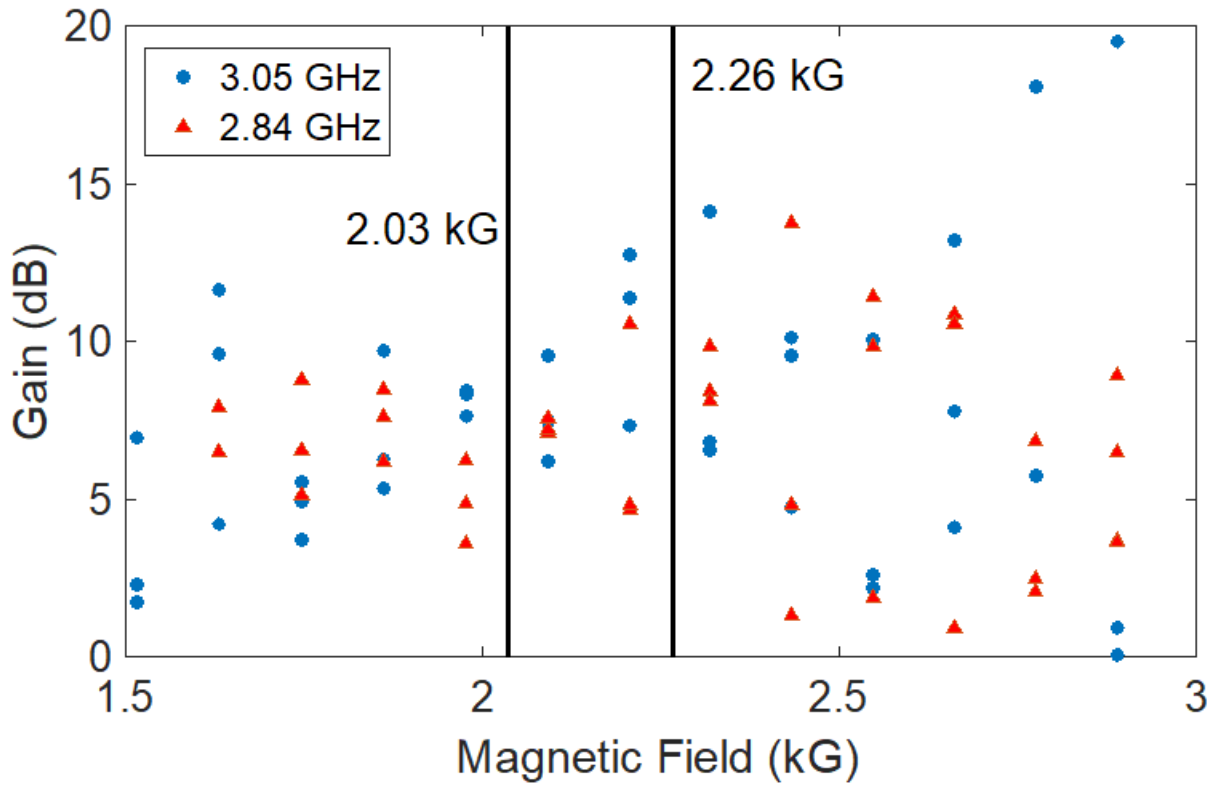

Figure 4.12: Measured RPCFA gain versus the applied axial magnetic field. The vertical lines indicate the values selected for the input power sweep: 2.03 kG for 2.84 GHz drive, and 2.26 kG for 3.05 GHz drive. An uncertainty of 0.3 dB is present.

Figure 4.12 indicates that the RPCFA is much less sensitive to the magnetic field strength in experiment than simulation would indicate. Again, the cause of this is likely the expansion of the cathode

plasma. As the effective cathode expands, the electric field in the interaction space increases and the velocity of particles increases proportionally according to the $E \times B$ drift. Since slow electrons are always present near the surface of the cathode, and electrons significantly faster than the initial $E \times B$ drift are present late in time, at some point during the shot there are electrons present which interact resonantly with the RF wave, allowing a peak output microwave power to occur at some point during the pulse. This contrasts with MAGIC simulation where plasma is not generated, steady state operation is achieved, and electrons not synchronized with the RF signal can not interact to produce amplification, making the simulated RPCFA more sensitive to changes in the magnetic field.

The small-signal bandwidth of the RPCFA was measured using a low power (~1 kW) RF source with a continuously variable frequency in the range of 2.4 to 2.7 GHz. The amplifier is assumed to operate over the range of frequencies between 2.7 and 3.05 GHz as predicted from simulation and cold test, though a source was not available to verify this. Gain as a function of frequency is plotted in Figure 4.13.

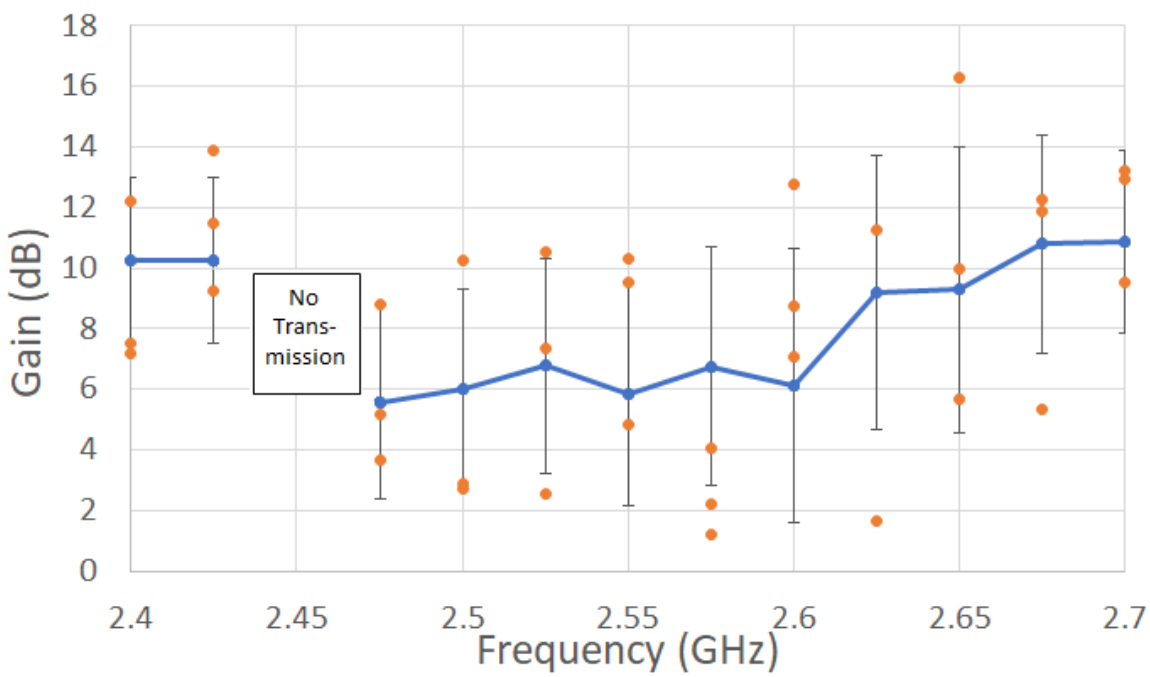

Figure 4.13: Measured RPCFA gain versus frequency with moving averages and local standard deviation overlaid.

Mean gain decreases as frequency decreases below 2.7 GHz, as expected. Non-drive frequency oscillations are not observed for these frequencies as they are in MAGIC simulation, though this is likely because they do not couple out of the RPCFA through the coaxial adaptors. The 11 dB maximum mean gain observed in this experiment is at 2.7 GHz and a drop of 3 dB below peak gain occurs around 2.63 GHz. This permits an estimate of the bandwidth of approximately 15%, slightly higher than the 10.5% predicted by MAGIC.

It was also observed that no amplified power was generated when the RPCFA was driven at 2.45 GHz. The output power spectrum for shots fired at this frequency appears similar to the spectrum generated at zero-drive. From Figure 4.2 it is apparent that 2.45 GHz corresponds to a sharp drop in the transmitted signal. With only 1 kW of input drive at this frequency and a transmission loss of greater than 10 dB, the transmitted power at this frequency would be under 100 W. This gives the lower bound for the injected power the RPCFA is capable of amplifying.

After 564 shots had been fired into the RPCFA, the degradation of the SWS was analyzed. Significant erosion of the vane tips was observed on the side facing the incoming beam, as expected. The thickness of the vane tips was initially 2.0 mm. At the most damaged locations, this was reduced to 1.3 mm. A photograph of the SWS after 564 shots is shown in Figure 4.14. The impact of this degradation is illustrated by a plot of the transmission as a function of frequency. Figure 4.15 shows S_{21} for the new SWS taken before any shots had been fired, compared to the final set of shots over a year later for this particular SWS, using an RF source with a continuously variable frequency. Figure 4.15 shows the sweep of S_{21} has undergone minor distortion and has decreased across the band by approximately 2 dB.

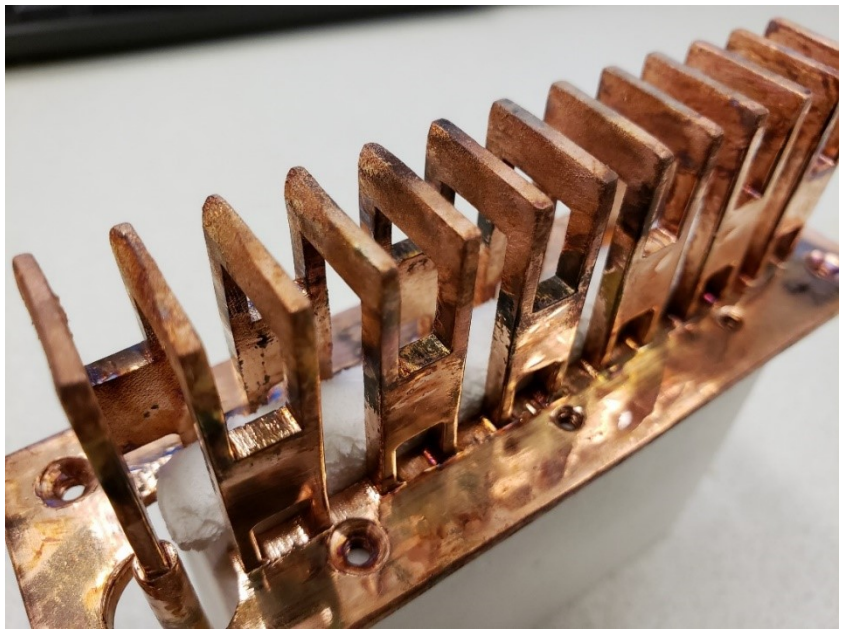

Figure 4.14: Photograph of the SWS after 564 shots. Figure 3.5 shows the same structure before any shots had been taken. The copper has been lightly sanded to remove some of the aluminum deposition. The effect of the beam impacting the SWS is most significant at the vane tips.

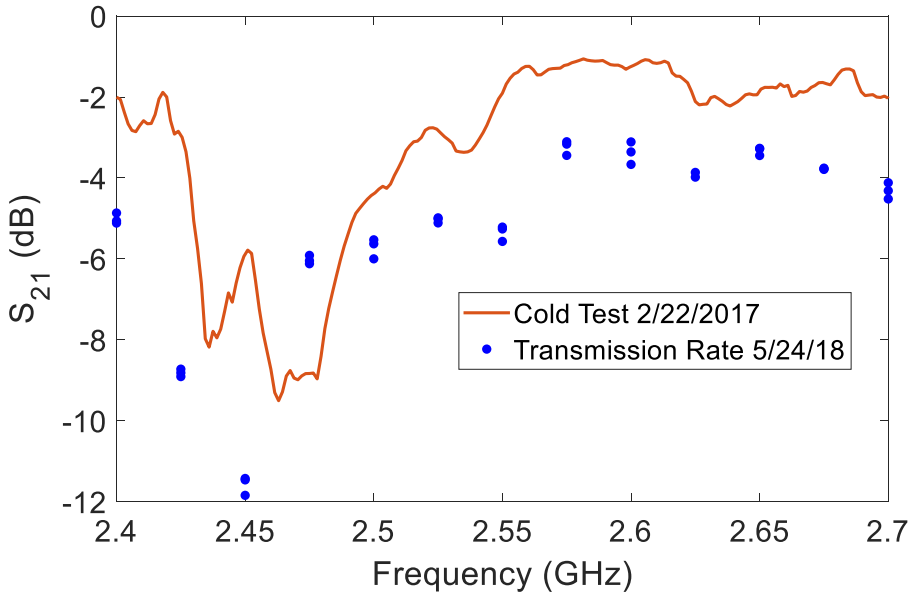

Figure 4.15: Transmission rates for a new SWS versus the same SWS after 564 shots taken during the final shot series using the EPSCO generator.

4.4 Consistency Analysis

Variation in performance at moderate input power levels (10's of kW) is a significant issue on the RPCFA and is readily apparent in Figures 4.11, 4.12, and 4.13. The underlying causes for this variation are investigated in this section. All RF sources used to drive the RPCFA were extremely consistent, leaving the source of variation to either the pulsed power drive or the RPCFA itself. The first source of variability to be analyzed is the MELBA pulsed current and voltage. To correlate gain with the instantaneous current and voltage, the peak gain is plotted in Figure 4.16 against the MELBA voltage and current at the time peak gain is achieved. For this dataset, 58 shots were taken at 3.05 GHz input drive and all quantities, such as input power (30 kW) and magnetic field, held constant. Mean gain over the full shot series is 6.21 ± 2.6 dB (mean ± 1 standard deviation). In general, high instantaneous current corresponds to higher peak gain, although high peak power was still observed at lower currents (~ 4 kA). A plot illustrating this is given in Figure 4.17. Instantaneous voltage shows a much weaker trend but neither quantity shows an especially strong correlation.

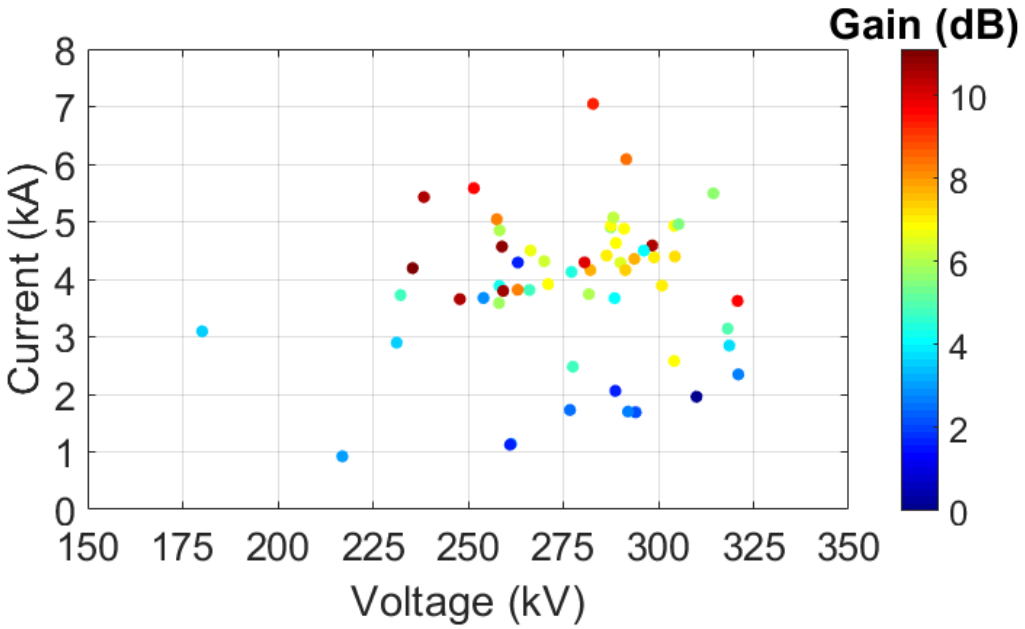

Figure 4.16: Peak gain for shots 15682 – 15761 plotted against the voltage and current when peak gain is achieved. Instances of shots with a failed crowbar and shots that display oscillation are omitted. Input microwave power is 30 kW.

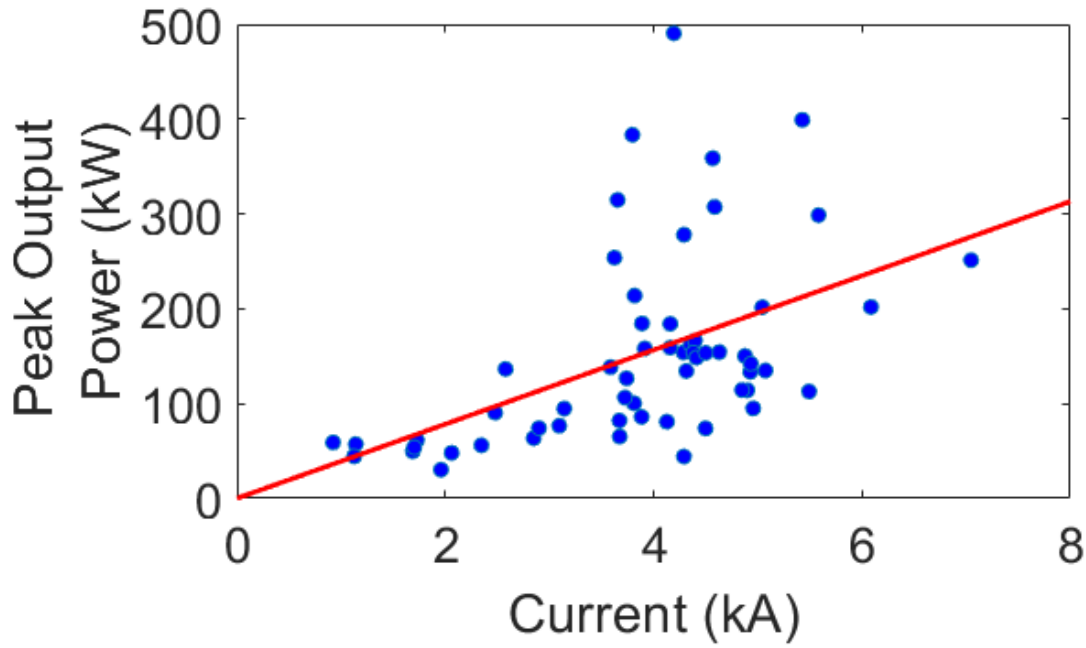

Figure 4.17: Peak output power for shots 15682 – 15761 plotted against current at the time of peak power. A linear (constant efficiency) trendline with $R^2 = 0.246$ indicates the weak correlation. Input microwave power is 30 kW.

Jitter in the switches which erect the MELBA Marx bank is significant and occasionally comparable to rise-time of a given shot. This leads to a significant variation in the shape of the current and voltage pulse. To eliminate this variation, the data can be filtered. For the shot series 15682 – 15761, optimal pulses were selected according to their current and voltage profile. Of these 58 (non-oscillating, successful crowbar) shots, only 9 were considered optimal (type 1, as explained further in section 4.6), having 200+ ns flat top voltages and drawing current in excess of 6 kA at the time of crowbar. The current and voltage up to the time of crowbar and synchronized according to start time for all 9 of these shots is overlaid in Figure 4.18. Pulse start time is determined by the onset of current.

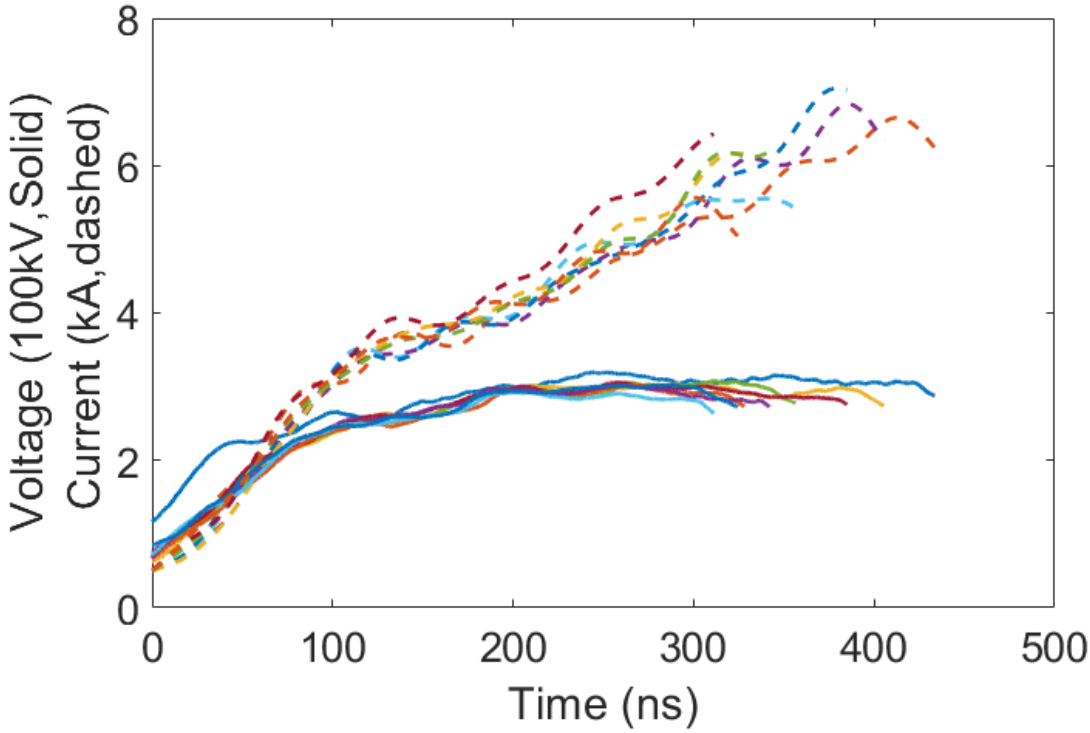

Figure 4.18: Overlaid current and voltage for the 9 optimal MELBA pulses. All show excellent consistency in voltage and acceptable consistency in current.

By reducing the dataset to only ideal MELBA pulses and then truncating each of these pulses according to the length of the shortest pulse, the remaining variation in RPCFA performance can be attributed to the RPCFA itself. The shortest of these pulses shown in Figure 4.18 is 376 ns, so for each pulse, the peak gain is only measured over the first 376 ns of the pulse. For the 9 optimal, truncated pulses, the mean gain is 6.63 ± 1.57 dB. This is an increase in the mean by 0.42 dB and a decrease in the standard deviation by 1.03 dB.

The relative timing of the pulsed power compared to the onset of RF was varied to investigate whether an optimal timing could be found to reduce variation in gain. A plot of this relative time difference (Δt) against gain is given in Figure 4.19. For other experiments, the RF was injected around 350 ns prior ($\Delta t = +350$ in Figure 4.19) to the MELBA pulse as shown in Figure 4.5. According to Figure 4.19, optimal results occur around $\Delta t = 400$ regarding both mean peak power and reproducibility, though the latter

quantity may simply be a result of the limited dataset. Regardless, analysis of the RPCFA response to variations in the relative timings of the RF and pulsed power yields insight on the dynamic behavior of the device.

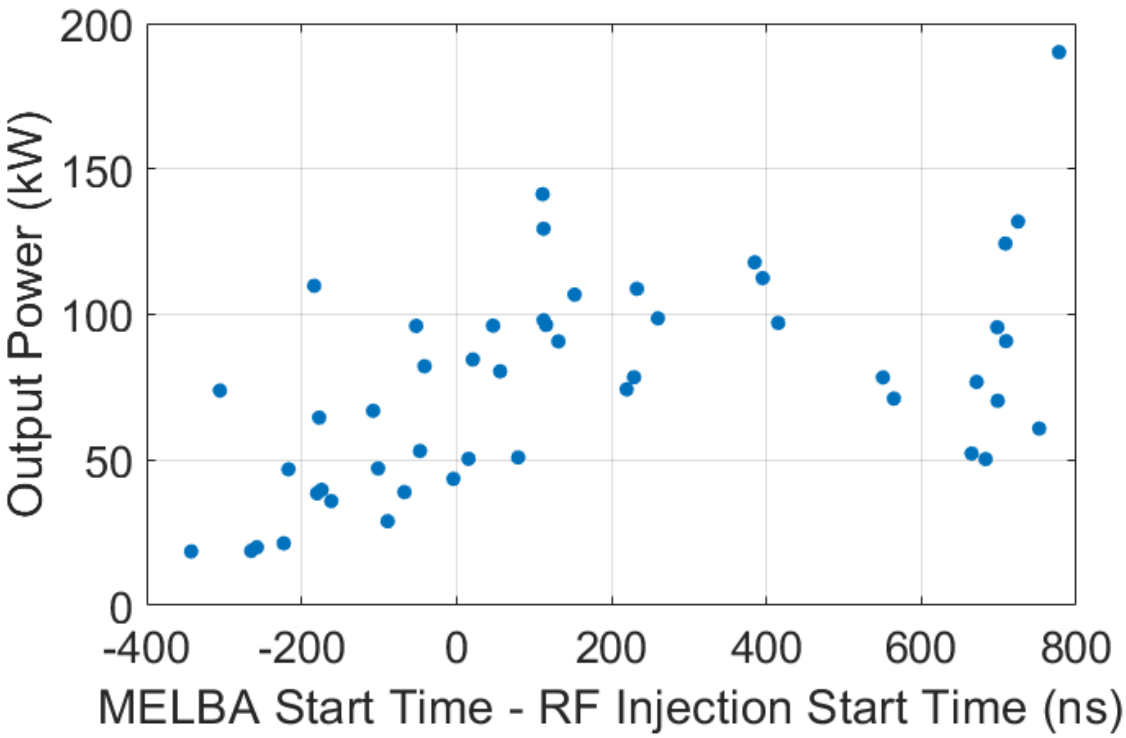

Figure 4.19: Output power as a function of the time difference between the beginning of the MELBA pulse and the onset of RF. Negative values indicate the MELBA pulse begins prior to the RF injection.

Peak output power tends to decrease as Δt becomes more negative. This is expected as the amplifier cannot operate without both RF and pulsed electron beam power present. For increasingly negative Δt, this implies the RPCFA has less time to achieve high gain as MELBA pulses are much shorter than the RF pulses. This is illustrated in Figure 4.20, MELBA fires before the RF begins (Δt = -177 ns) and no output power is detected until the input RF begins. Output power precisely tracks input power as it rises, then decays as the pulsed voltage and current terminate, the expected behavior for an amplifier.

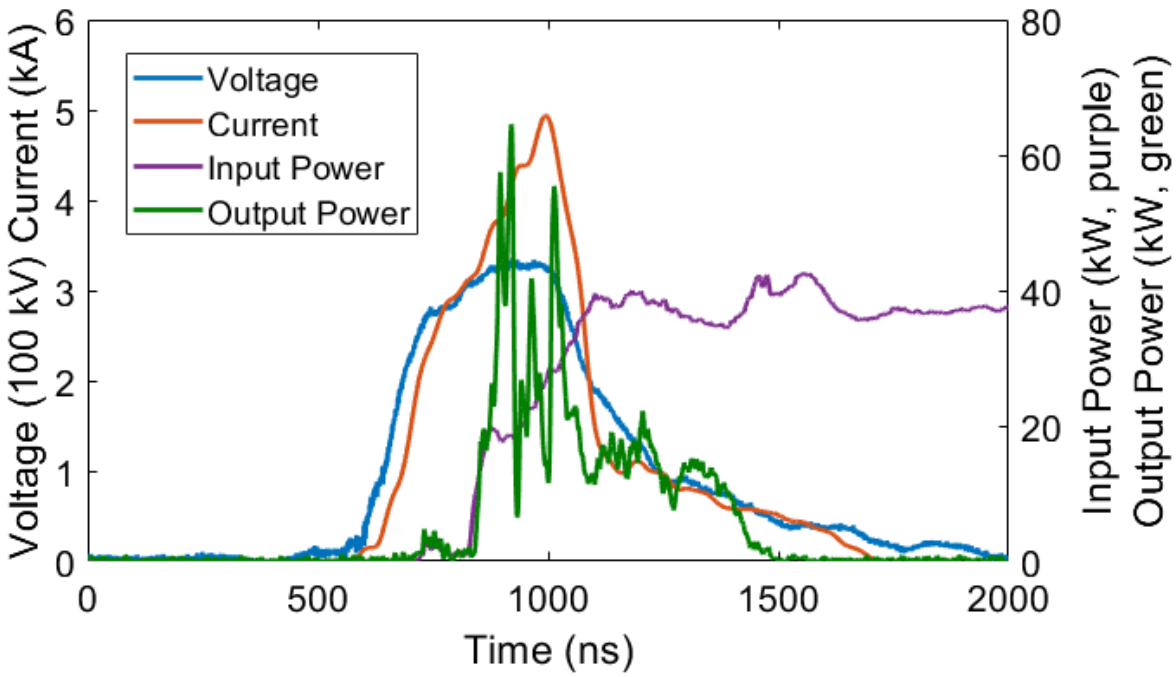

Figure 4.20: Shot 16237. MELBA current and voltage overlaid with RF traces. MELBA is fired and reaches near full voltage before the RF begins.

The dynamic behavior of the RPCFA can be illustrated in detail by examining Figure 4.21, a shot in which MELBA and the RF are initiated nearly simultaneously ($\Delta t = +47$ ns) such that the rise of the RF coincides with the rise of the voltage. As in Figure 4.20, the output RF power follows the input closely early in time. The delay between the two signals (~10 ns) corresponds to the time required for the RF to travel across the RPCFA. The output power does not exceed the input until late in the rise of the voltage pulse when the electric field is of sufficient strength to promote synchronism between the hub and the RF wave. Peak gain of 4.9 dB is achieved near peak current and the output decays as the pulsed power turns off, as in Figure 4.20.

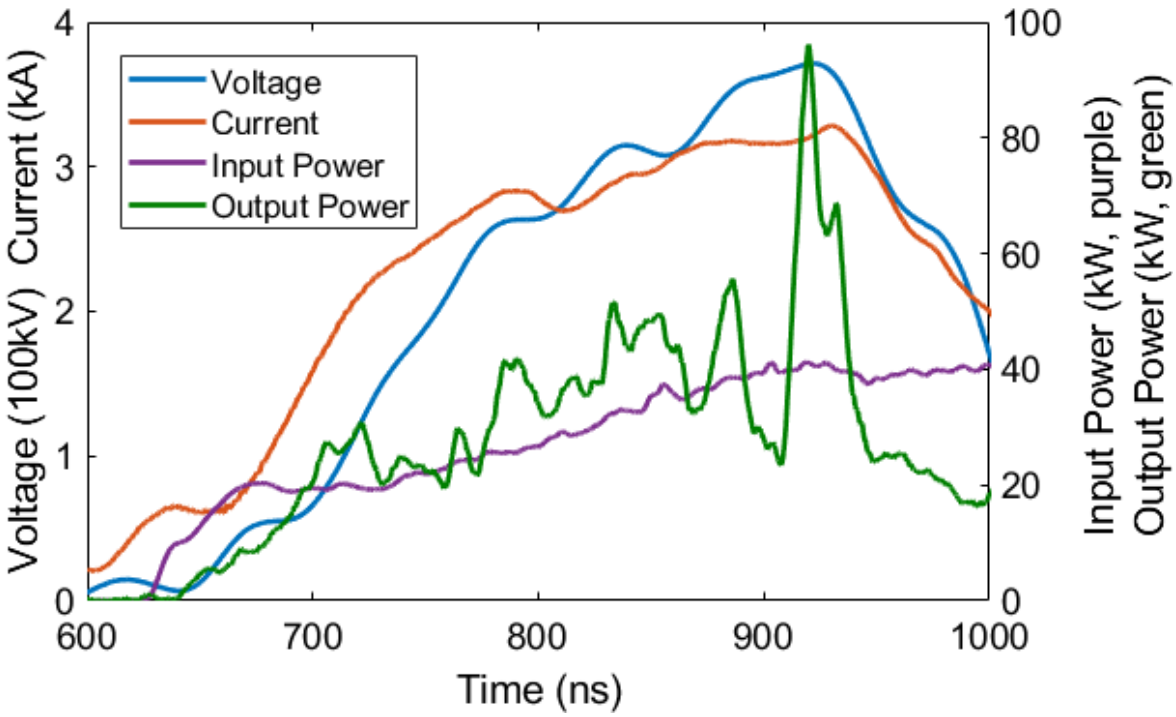

Figure 4.21: Shot 16242. MELBA current and voltage overlaid with RF traces. The rise of the RF and MELBA voltage occur concurrently.

4.5 Cathode Optimization

The effect of the cathode materials and geometry were investigated in order to improve gain and consistency. For all RPCFA shots numbered lower than 15881 (15236 – 15880) the Glyptal cathode was employed. Two additional cathodes, Cathode A and Cathode B (see chapter 3 section 3), were acquired from the Air Force Research Laboratory after the shot series ending in 15881. For each cathode a shot series was run with identical settings (input power, frequency, magnetic field) to isolate the effect of the cathode. Since the cathode serves primarily to interface the pulsed power from MELBA with the RPCFA and has minimal effect on the performance of the SWS, the determination of the optimal cathode is the cathode that yields the longest voltage pulses with high current and gain consistency to the RPCFA.

Pulse quality was determined subjectively from examination of only the voltage and current trace. Pulses were categorized into 4 classes: Type 1 shots: optimal pulses, with extended (200+ ns) flat-top voltages and peak current near 6 kA or greater. Type 2 shots: sub-optimal pulses, with usually shorter flat-top voltages and peak currents less than 6 kA. Type 3 shots: short pulses, generally the result of a premature crowbar, these shots usually reach peak voltage but do not maintain a flat-top for long and peak currents generally do not reach 4 kA. Type 4 shots: arcs, the result of a failed crowbar, display extremely high currents (often 20+ kA) and voltage which decays slowly due to the lack of crowbar. An example of each of these types of shots, taken from the shot series 15682 – 15761, performed using the glyptal cathode, is shown in Figures 4.22a through 4.22d.

The source of variation in each of these shots is the crowbar timing. While the crowbar command delay is set manually, the actual time of firing is variable due to jitter as well as spontaneous breakdown. The likelihood of spontaneous crowbar can be reduced by increasing the pressure of the crowbar switch. Increasing both the switch pressure and the crowbar fire command delay serve to increase the length of the pulse, which in general corresponds to higher current and gain, at the risk of producing an arc. The ideal crowbar delay and switch pressure, and thus average pulse quality, is strongly influenced by the cathode's emission properties and propensity to arc.

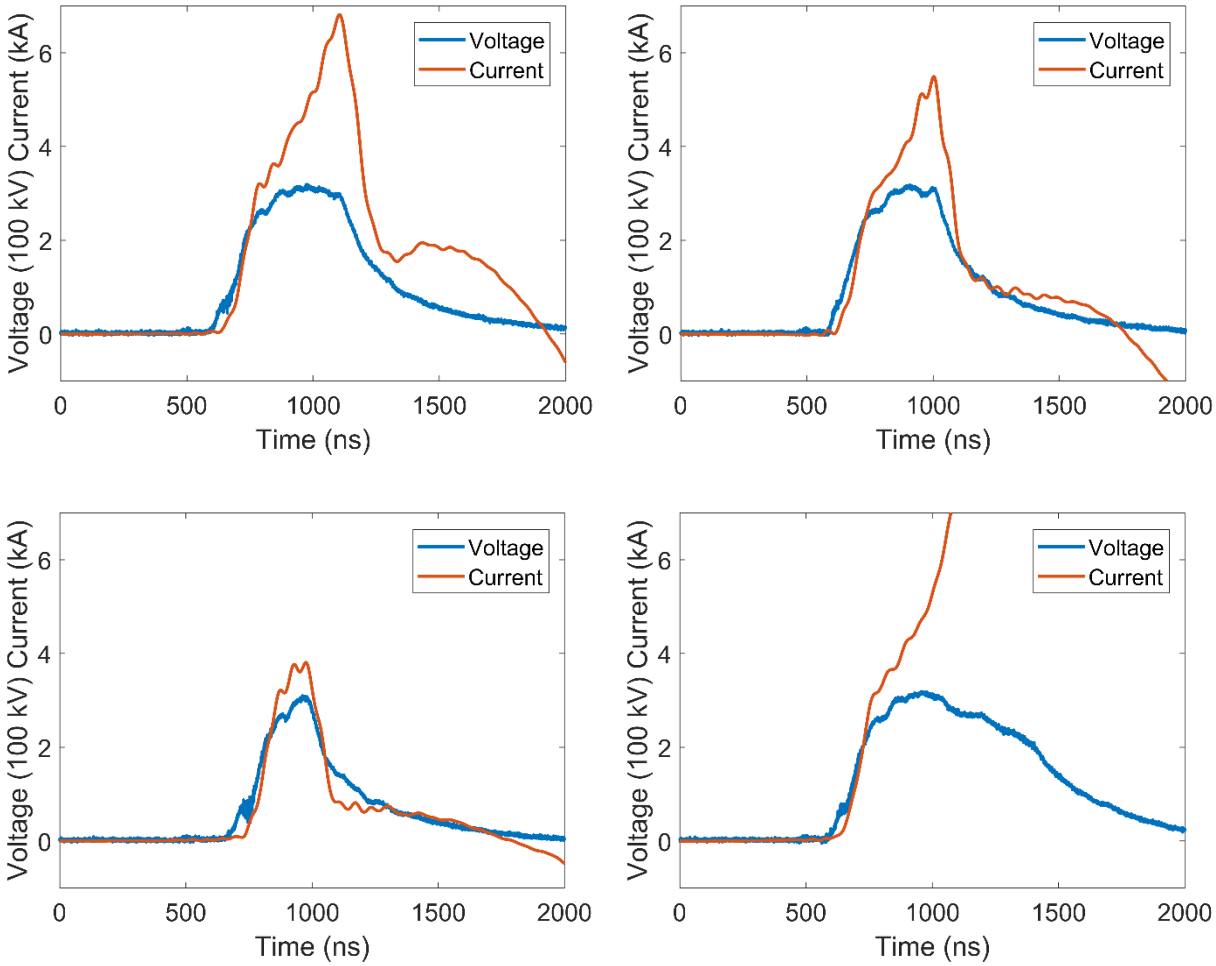

Figure 4.22a (top left): Shot #15704. Ideal, high current, type 1 pulse.

Figure 4.22b (top right): Shot #15738. Low current, type 2 pulse.

Figure 4.22c (bottom left): Shot #15722. Short, low current, type 3 pulse.

Figure 4.22d (bottom right): Shot #15734. Failed crowbar, arc, type 4 pulse. The current in these pulses typically reaches 30 kA.

Sorting the shot series 15682 – 15761 according to shot type gives insight on the effect of pulse quality on RPCFA performance with the Glyptal cathode. A histogram showing the peak gain with standard deviation for each shot type is shown in Figure 4.23. Type 1, 2 and arcs show above average peak gain with only type 3 below. Arcs are undesirable due to the damage they are capable of causing the experiment.

Type 2 shows comparable mean peak gain to type 1 at the cost of higher variation, though the difference is negligible considering the error bars. The higher variation is likely due to the limited size of the dataset.

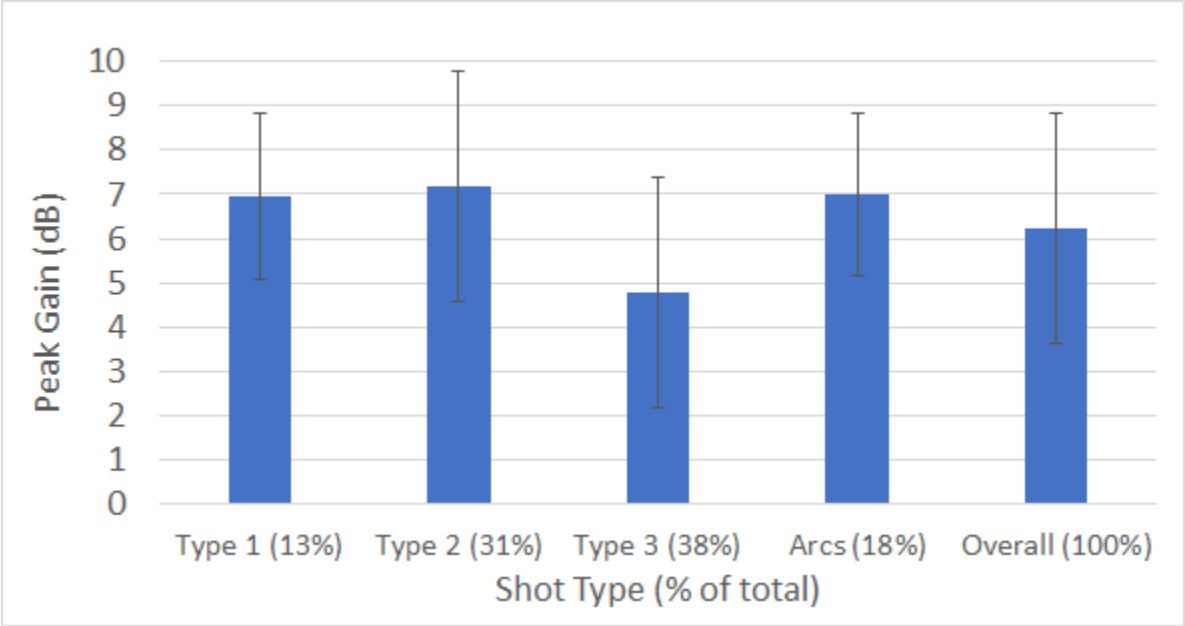

Figure 4.23: Peak gain and standard deviation compared for different shot types using the Glyptal cathode and other experimental parameters held constant.

A consistency analysis dataset was taken for each of the 3 other cathodes. For each of these, approximately 40 shots were taken at a constant magnetic field and input RF frequency and power, as was done for the Glyptal cathode. The fraction of the dataset that produced a given shot type for each cathode is given in Figure 4.24. The overall mean peak gain and instantaneous current at that peak gain for each of the different cathodes are shown in Figure 4.25.

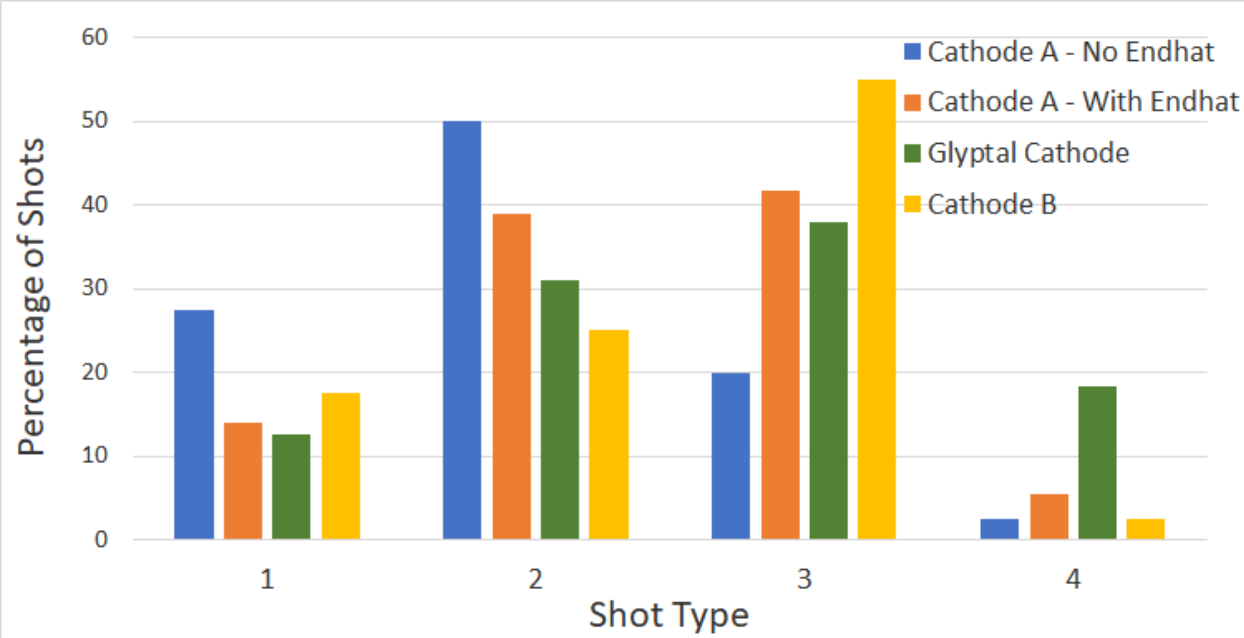

Figure 4.24: Percentage of shots of a given shot type for the consistency analyses for each cathode.

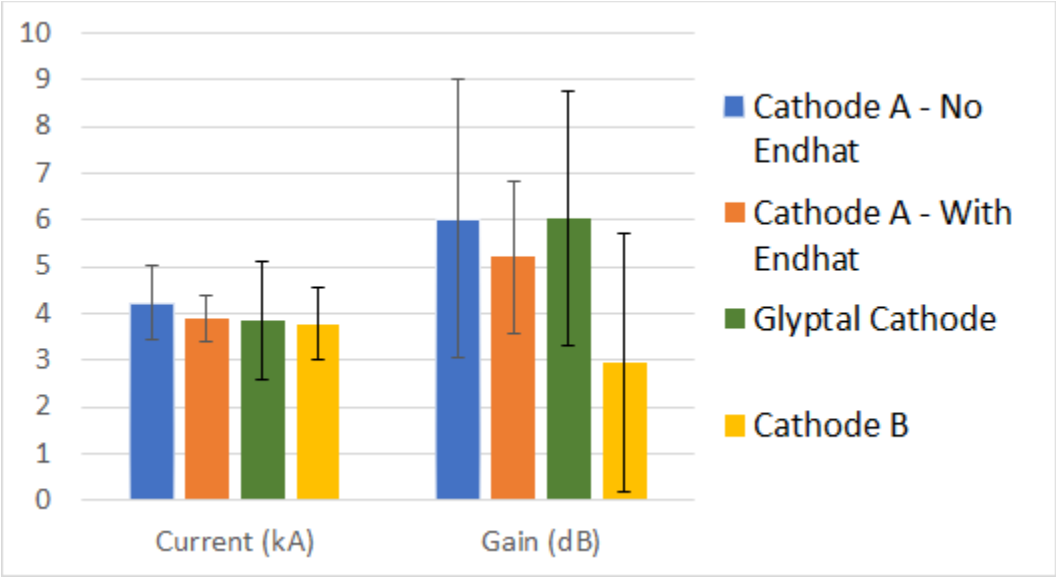

Figure 4.25: Peak gain and instantaneous current at the time of peak gain for each of the four cathodes.

Cathode A without the endhat showed the highest percentage of type 1 and type 2 shots. It also matched cathode B for the lowest rate of arcs among the 4 cathodes, and the Glyptal cathode for the highest mean peak gain of the four. It does, however, also possess the greatest variation in gain. The endhat reduces

this variation but at the cost of mean gain and current. With the endhat, cathode A shows an average decrease in shot quality and potentially a slightly increased risk of arc (2/36 versus 1/40 without the endhat). The Glyptal cathode shows a significantly increased arc rate (~18%) over the steel cathodes. A possible explanation is that the Glyptal coating generates a plasma which expands around the cathode and rapidly shorts the diode before the crowbar can terminate the pulse. Cathode B showed generally worse performance than the other cathodes, with the highest rate of type 3 shots leading to significantly reduced mean peak gain and very high variation in gain. The brazed carbon fiber emitter which differentiates it from cathode A is likely less effective as an emitter for this application. Cathode A with endhat was utilized for the following high-power amplification shots due to its lower variability.

4.6 High Power Amplification

The final experiment conducted using the RPCFA is the amplification of high power (100's of kW) input signals. The XLB PFN (see section 3.5) was used to drive an MG5193 magnetron and generate input signals in excess of 800 kW. For this experiment, 91 shots were taken at varying input powers. Of these, the PFN fired coincidently with MELBA 73 times. For these 73 shots, the input power ranged from 32.2 to 739 kW with peak amplified powers between 0.129 and 5.86 MW. Optimal performance was observed to occur when the input RF power and MELBA voltage rise occurred simultaneously or as near as possible considering the jitter in the devices. In the example shot (#16817) shown in Figure 4.26, the input microwave power of 630 kW is amplified to nearly 6 MW (9.2 dB) before abruptly cutting off, presumably due to RF breakdown of the SWS, terminating transmission of the input microwave signal as well. The introduction of RF breakdown sends a reflected amplified signal backwards toward the microwave source. This amplified signal is sufficiently powerful that it could induce RF breakdown in the circulator, terminating the input microwave pulse. The circulator is rated for only 25 kW of peak RF power. RF breakdown in the RPCFA provides a high-power limit for this prototype RPCFA. A lower power shot

shown in Figure 4.27 does not display this termination of the input signal though amplification is still terminated by RF breakdown. In this case, the reflected signal is not sufficiently powerful to induce breakdown of the circulator, so the injected microwave power persists (see Appendix F). For reference, the MELBA pulse in Figure 4.26 would be classified as type 3, while the MELBA pulse in Figure 4.27 would be classified type 2. However, the distinction appears irrelevant at these higher input microwave powers.

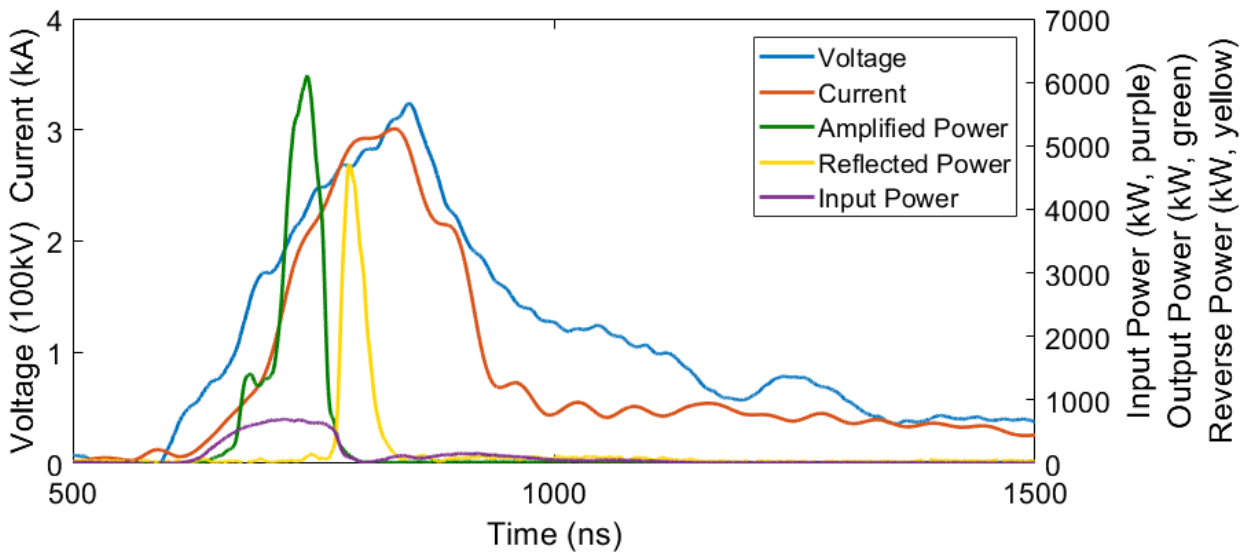

Figure 4.26: Shot 16817. MELBA current and voltage overlaid with the injected 633 kW at 3.0 GHz and 5.86 MW amplified power. Input power cuts off after amplified output breaks down the RPCFA and powerful reflected pulse induces RF breakdown in the circulator.

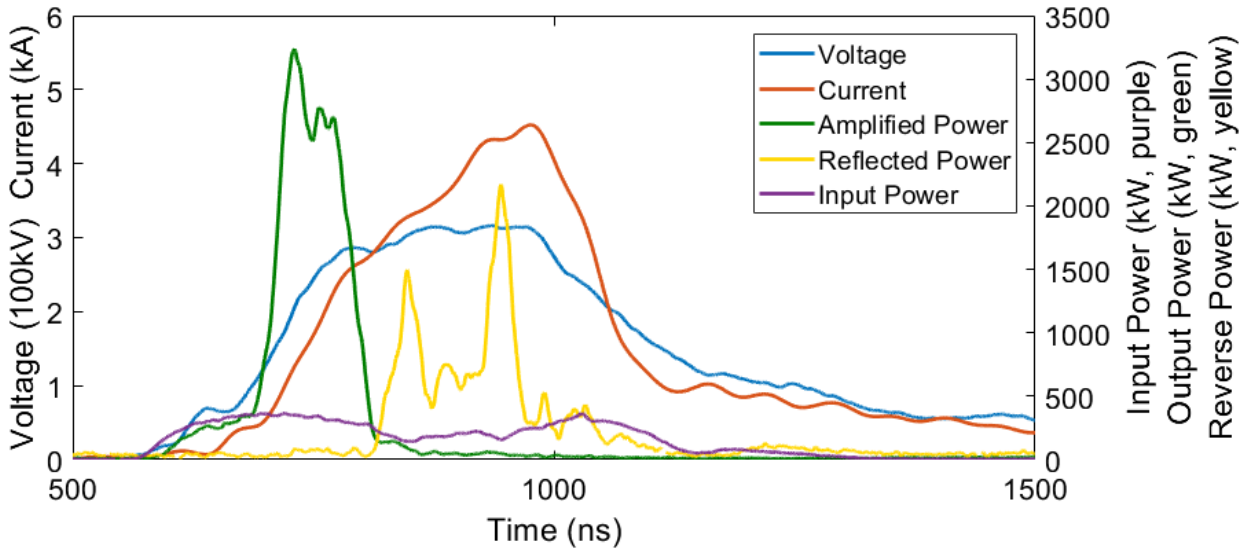

Figure 4.27: Shot 16829. MELBA current and voltage overlaid with the injected 340 kW at 3.0 GHz and 3.06 MW amplified power. Input power continues through the end of amplification despite RF breakdown at the SWS.

An additional RF output pulse shortening effect is also present due to the desynchronization of the Brillouin hub and the propagating wave at microwave power levels insufficient to induce RF breakdown at high microwave power drive. This effect is apparently related to the RF fields and can be demonstrated by a shot that reached a peak power greater than shot 15316 (Figure 4.5) but less than 16829 (Figure 4.27). Shot 16834 is an example of this, reaching just under 2 MW of peak output as shown in Figure 4.28. Peak power is reached early in the shot, consistent with both moderate and high-power operation. Like shot 15316, after peak power is reached, output power drops dramatically to a state of decreased amplification. While the reduced output power of shot 15316 remains nearly constant for the remainder of the MELBA pulse, shot 16834 decays further near transmission level microwave power, but more slowly as the weaker RF fields do not promote desynchronization as rapidly as they did at peak power. This suggests the RF fields play a significant role in promoting cathode plasma expansion and diode closure. Previous experiments using high power RPM oscillators which generated powers in excess of 5 MW on MELBA have demonstrated this behavior [43, 68]. In these RPM oscillator experiments, RF oscillation initiated at electrical fields lower than expected, and terminated prior to the reaching full voltage.

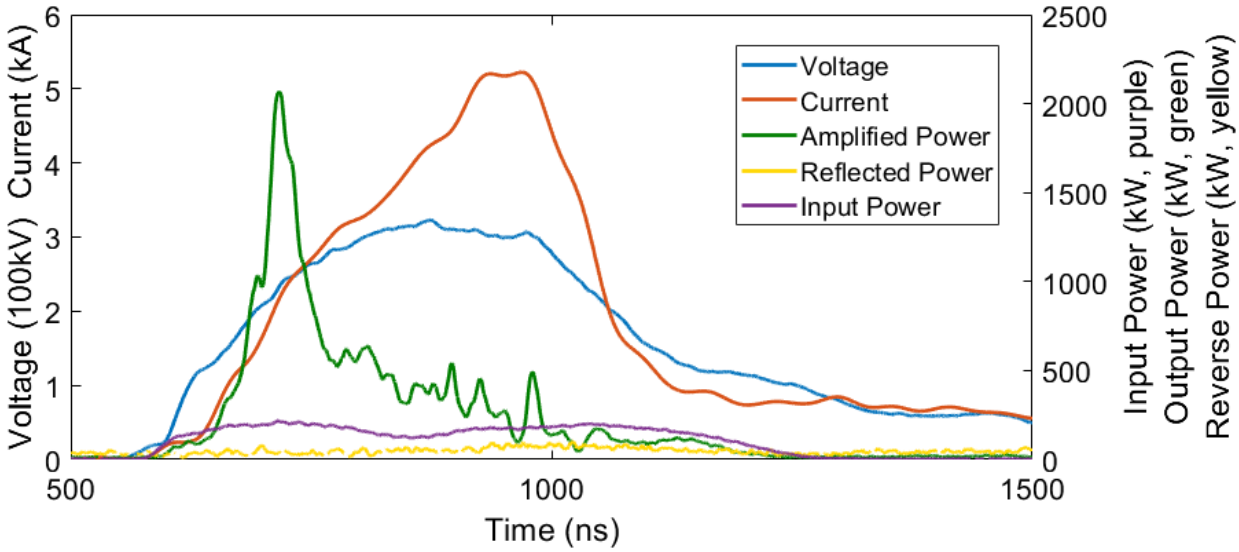

Figure 4.28: Shot 16834. Peak output power is reached during the rise of the MELBA pulse then decays rapidly. Slow, constantly decreasing gain is observed for much of the pulse. Reflected power never reaches significant levels in the absence of RF breakdown.

At these increased input drive levels (100s of kW), the RPCFA shows significantly increased mean gain and reduced variability. A plot of microwave output power versus input power for all shots near the design frequency where input power was varied, including those taken using the 40 kW MG5223F magnetron, illustrates this in Figure 4.29. Microwave output power versus input power still shows a positive correlation in the breakdown regime since the listed input power is the injected power at the moment of peak output. Breakdown occurs during the rise of the RF pulse, before peak input power is reached. Thus, while the peak output powers of these shots are determined by, and carry the variance of, the breakdown process, the gain is still in line with values measured at lower power. The mean gain for all 134 shots plotted in Figure 4.29 is 7.87 dB with a standard deviation of 2.74 dB. When the scope of the measurement is reduced to only the 50 shots with greater than 150 kW of input power, the mean gain is 8.71 dB with a standard deviation of 0.63 dB. This appears to represent a threshold above which the amplifier operates in a more consistent and effective manner.

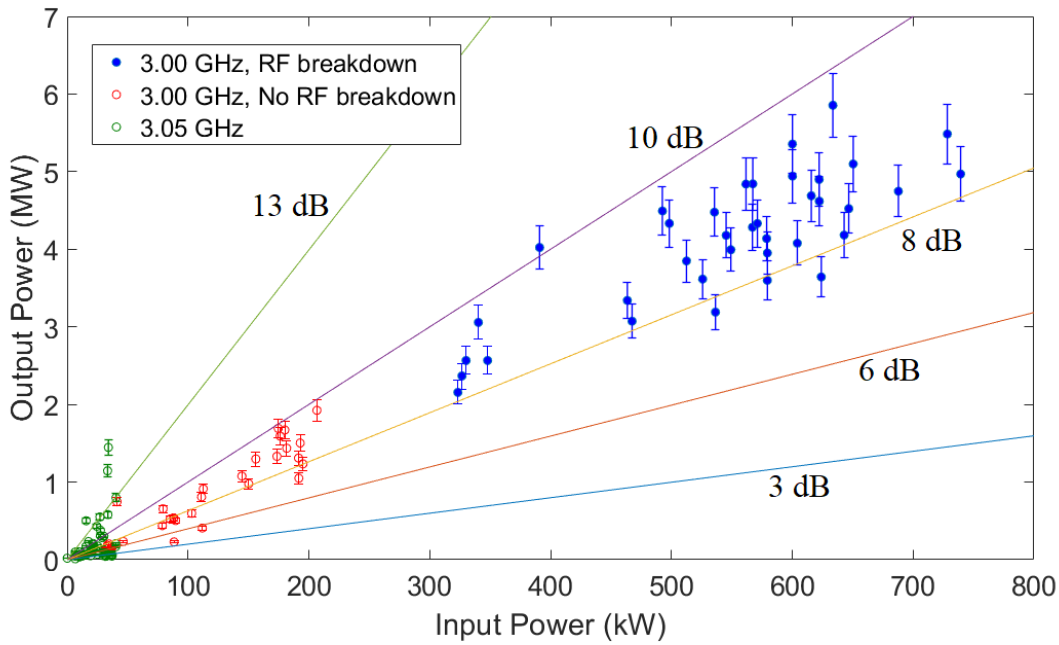

Figure 4.29: Peak output microwave power versus the simultaneous input power over the range of powers tested on the RPCFA.

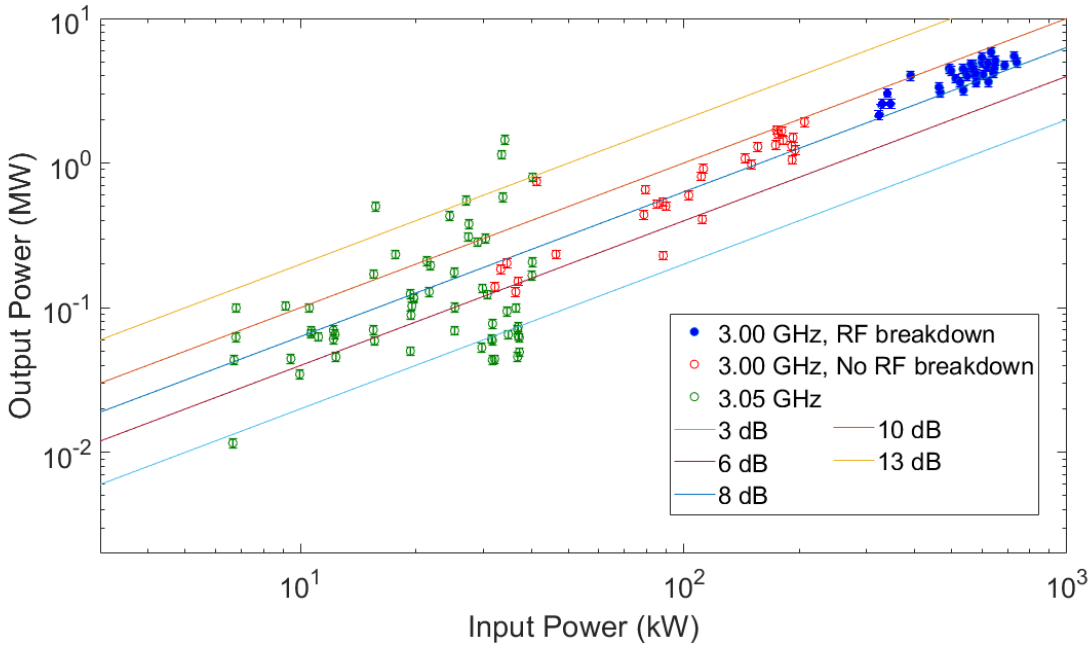

Figure 4.30: Peak output microwave power versus simultaneous input power plotted on a log scale. The transition to consistent amplification as the input power is increased to around 150 kW is apparent.

The impact of these high-power RF breakdown events is a concern for the durability of the design. Breakdown between vane tips leads to a decrease in the smoothness of the surface, which in turn increases the propensity for breakdown to occur. By this reasoning, the maximum output power achievable on the RPCFA should decline as the number of RF breakdown incidents increases. Plotting the peak power for shots that experienced RF breakdown versus the number of times RF breakdown was induced is presented in Figure 4.31 where this weak but predictable trend is apparent.

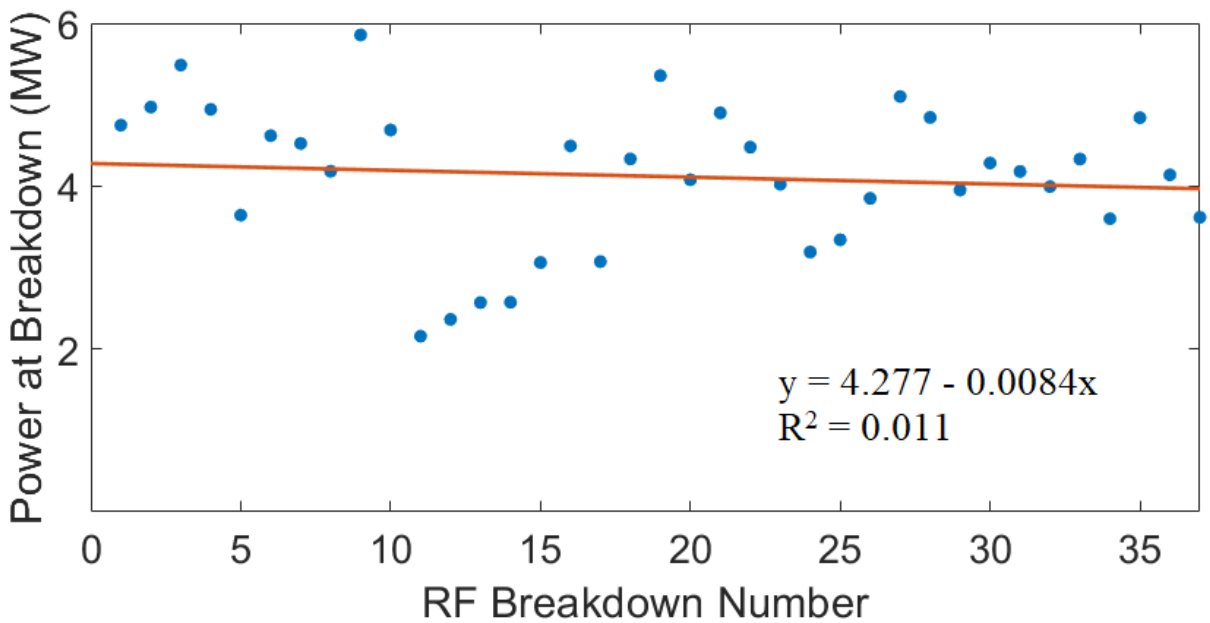

Figure 4.31: Peak microwave output power versus cumulative the number of times RF breakdown was induced for the 32 shots in which this occurred.

The improvement of both the mean gain and reproducibility can be attributed to the increased strength of the fringing RF fields in the SWS which consistently draw particles from the beam into a synchronous interaction. This result is not surprising and adds to the viability of the RPCFA as an HPM amplifier. A design with more consideration for reducing the strength of the fields to prevent breakdown, or improving the quality of the vacuum, are both means to extend lifetime as well as the maximum output power obtainable by this device. Reducing transmission loss with more precise construction and better

electrical connections, to reduce RF contact resistance, would likely increase gain without altering the operational characteristics established in these experiments.

4.7: Phase Analysis at High Power RF Drive

The increased consistency in RPCFA performance at high power permits a more detailed investigation into the phase shift between the injected and amplified RF signals. In section 4.2, analysis of the phase shift between the input and amplified signals was used to verify the amplifying nature of the output power as well as identify oscillatory operation in a minority of shots. The employment of CFAs in phased arrays necessitates precise control of the phase of the output signal. Compared to the magnitude of S_{21}, the phase shift is an extremely sensitive parameter and varies greatly in response to changes in drive frequency and RF circuit parameters, which in turn are sensitive to conditions in the experiment. The most consistent and reproducible environment for measuring the phase shift is transmission at constant frequency. Figure 4.32 plots the phase shift over time of the transmission of 30 kW of RF at 3.05 GHz from the MG5223F magnetron with no MELBA beam.

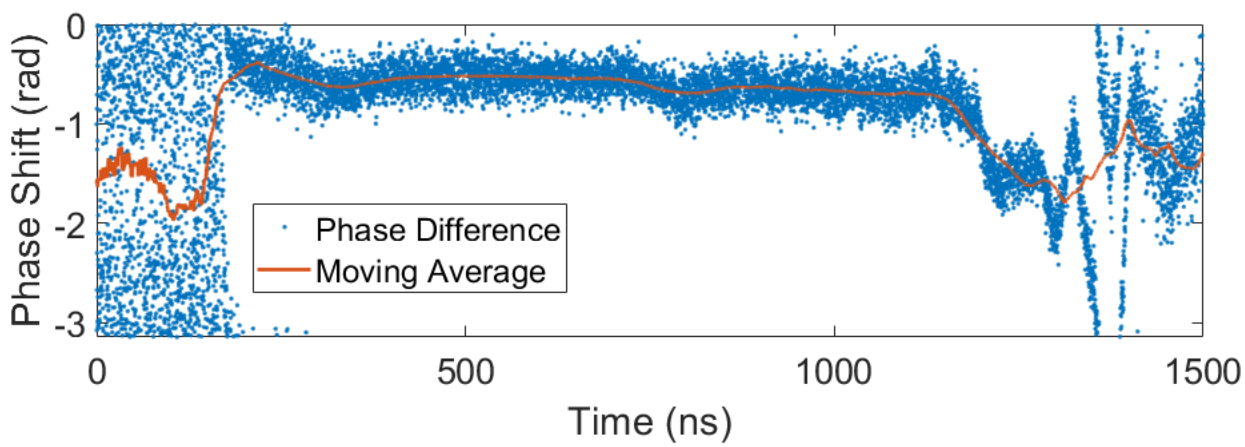

Figure 4.32: Phase shift over the transmission of 30 kW of RF input at 3.05 GHz with no MELBA beam. The microwave pulse begins around 200 ns.

It was shown in Figure 4.9b that the presence of hub currents or cathode/anode plasmas generated during RPCFA operation near the SWS can lead to a drift in the phase shift. In the absence of these currents, as seen in Figure 4.32, the phase shift is nearly as stable as predicted in MAGIC simulation, shown in Figure 4.7. Uncertainty in the phase shift measurement is due primarily to the fact that the signals measured are a significant fraction of the Nyquist frequency of the oscilloscope (6 GHz). This stability cannot be reproduced at high power due to the short duration and instability of XLB PFN pulses. The PFN did not produce the true voltage/current flat-top the MG5193 magnetron needed to produce a stable frequency and, consequently, a constant phase shift. The phase shift over a transmission of approximately 700 kW with no MELBA beam is shown in Figure 4.33 for comparison.

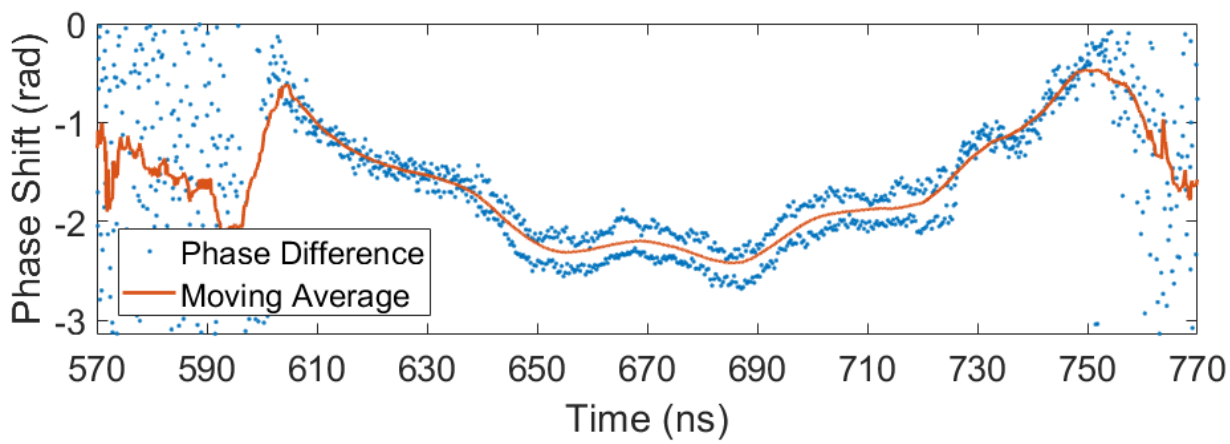

Figure 4.33: Phase shift over the transmission of approximately 700 kW of RF input at 3.0 GHz with no MELBA beam.

For both commercial off the shelf (COTS) magnetrons, the most rapid changes in phase shift occur near the ends of the pulse as the magnetron is entering and exiting stable operation in response to the driver pulse, undergoing slight shifts in frequency. Between the ends, the phase shift of the transmission of the high-power signal shows significantly greater variation over a much shorter length of time. This can be attributed to variation in the drive frequencies of the two magnetrons, shown in Figures 4.34a and 4.34b. Small variation in the drive frequencies are magnified over the length of the SWS and lead to relatively large variation in total phase shifts.

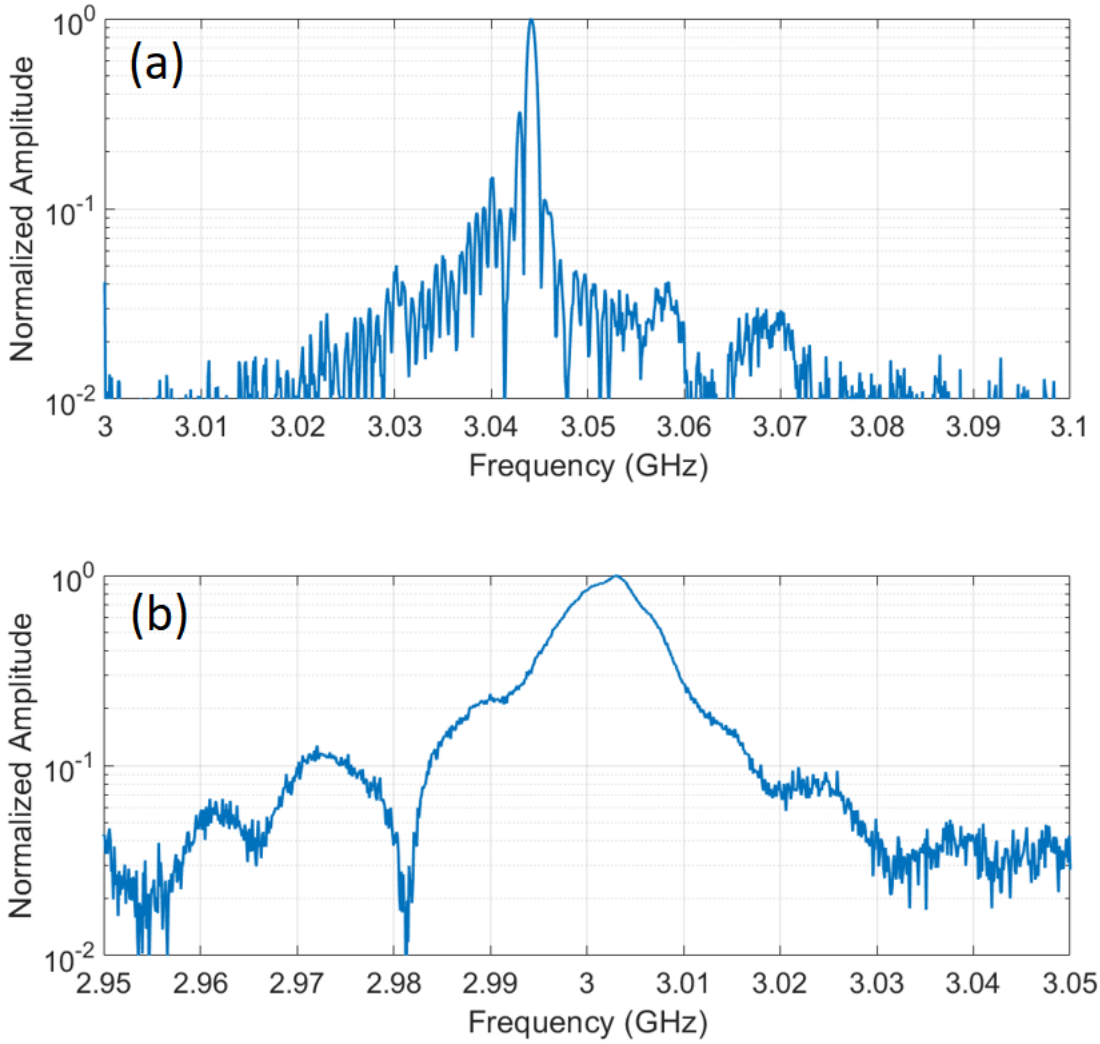

Figure 4.34a (top): Log plot of the integrated spectrum for the MG5223F magnetron driven by the Stanford Modulator.

Figure 4.34b (bottom): Log plot of the integrated spectrum for the MG5193 magnetron driven by the XLB PFN.

Recognizing this instability of the phase shift at high power drive, it is still possible to make a determination of the phase shift over the course of a shot series. Shots 16840-16893 were the final shot series at high power and showed the most consistent gain and output power. The mean phase shift was measured from a local average of phase shift data points ($\sigma \sim 0.4$ rad) 30ns after initial gain was recorded. This point generally corresponded to near peak power, early in the shot before the varying strength of the

RF fields and varying MELBA pulse currents obscured the phase measurement. A histogram showing the mean phase shift at this time for all 54 shots with the centroid identified is given in Figure 4.35.

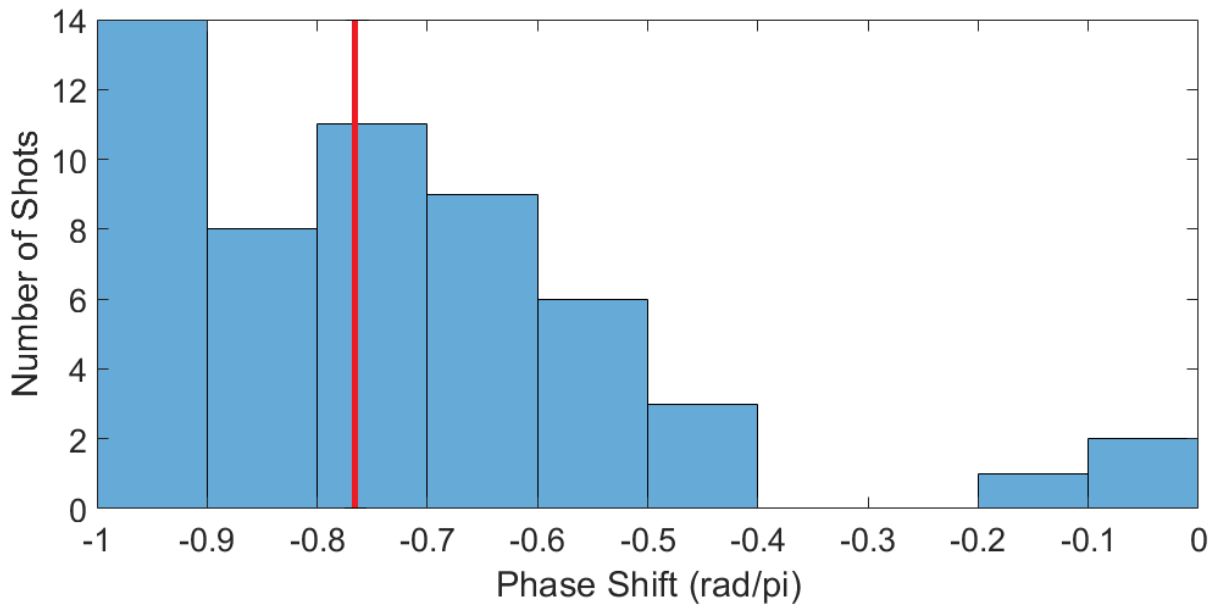

Figure 4.35: Histogram comparing the phase shift for 54 shots. The centroid is given by the red line, calculated by identifying phase shift values of zero with phase shift values of π to obtain a continuous distribution.

Figure 4.35 shows there exists clear anisotropy in the measurement of phase when the variables that may obscure this measurement are accounted for. This anisotropy suggests phase stability exists to some degree in the RPCFA. Extending this to phase measurements averaged over the length of the pulse, as well as decreasing the width of the distribution of phase measurements will require much greater consistency in both the RF and pulsed power sources. Greater control over the output phase will be required for application of the RPCFA in phased arrays.

CHAPTER 5

Summary and Conclusion

This chapter summarizes the significant computational and experimental results of the Recirculating Planar Crossed-Field Amplifier studies. The results are compared to commercially available devices, and suggestions for future work are provided.

5.1 Summary of Results

This dissertation catalogues the development of a novel high-power microwave amplifier, the RPCFA, from its fundamental design, to simulation, and finally to the fabrication and test of a prototype. This section will briefly summarize the key results detailed in previous chapters.

A transmission line circuit model was used to analyze potential circuit parameters for the RPCFA SWS. It was found that by varying 4 distinct parameters, a low loss SWS could be designed in either forward or backward wave configuration. A forward wave design was developed in Ansys HFSS, which showed circuit parameters in reasonable agreement with the model. The HFSS design also slowed the phase velocity of an injected 3 GHz RF signal to 0.3c, a speed which could be synchronized to a Brillouin hub generated in an experiment. At the design frequency (3 GHz), the scattering parameter that defines transmission across the SWS, S_{21}, was calculated in HFSS simulation found to be -0.6 dB. Acceptable transmission was observed over the range of frequencies 2.8 to 3.1 GHz with no high-Q oscillatory modes detected.

Using MAGIC PIC simulation, the SWS was embedded into a recirculating planar housing with a cathode and RF waveports for injecting and extracting RF power. The expected experimental parameters

were applied to this hot tube simulation: a voltage of 330 kV DC, a magnetic field of 0.23 T, and an input microwave drive power of 1.3 MW at 3 GHz. The result of this simulation predicted 29 MW of RF power extracted, a gain of 13.5 dB, and a total current draw of 540 A, giving an efficiency of 15.5%. This simulation, however, did not include the factors which limit the output of the device in experiment, primarily plasma diode closure and RF breakdown of the SWS. MAGIC simulation predicted the RPCFA to be stable under zero RF drive and possess a bandwidth slightly greater than 10%.

A prototype RPCFA was constructed. The intricate SWS was fabricated using the "lost wax" additive manufacturing technique. Additional components were fabricated using traditional machining techniques to secure the structure and facilitate microwave power flow into and out of the device. Pulsed power was provided to the RPCFA by MELBA, and RF drive was delivered by four different sources. A hard tube modulator was used to drive moderate power magnetrons, and a 2.8 MW pulse forming network was constructed to drive the high power, MG5193 magnetron. Various cathodes were used over the course of these RPCFA experiments, with limited improvements in performance.

With the prototype RPCFA, the results of simulation could be tested experimentally. Cold tests showed the device qualitatively reproduced transmission over the same range of frequencies, though with additional losses. Zero-drive stability was demonstrated experimentally, and amplification over a bandwidth of approximately 15% was observed. A wide range of RF input power was injected into the RPCFA with typical gains of 8.71 ± 0.63 dB for input powers greater than 150 kW. The results are summarized in Table 5.1. The maximum peak output power obtainable on this experiment (5 - 6 MW) was limited due to RF breakdown in the SWS. This limit tended to decrease as the number of RF breakdown incidents accumulated. Finally, the phase stability of the RPCFA was analyzed at input powers of > 150 kW. The device showed evidence of phase stability early in the shot, though this was lost as the pulse continued and the MELBA current increased.

RF Injected Input Power	0 – 100 W	100 W – 150 kW	150 kW – 350 kW	> 350 kW
Regime	Zero – drive	Irreproducible Amplification	Reproducible Amplification	RF Breakdown
dB Gain (mean ± 1σ)	N/A	7.87 ± 2.74	8.86 ± 0.69	8.76 ± 0.57
Description	Output power is low and no drive frequency is present in the output spectrum.	Output power is highly inconsistent but output frequency is equal to the drive frequency and the spectrum is pure	Output power is predictable and proportional to the input RF power. Spectrum is pure.	Output power is proportional to the input until RF breakdown limits the peak output power.

Table 5.1: Summary of RPCFA response to various levels of injected RF power.

5.2 Comparison to existing CFAs

The ultimate goal of this investigation was to demonstrate that the innovative geometry of the RPCFA could possibly produce a higher power than is obtainable in currently available CFAs. When compared to commercial S-band CFAs, as shown in Figure 5.1, the RPCFA shows increased peak power capabilities (see Appendix I for further details) [52]. However, experimental S-band CFAs have reached peak powers exceeding 30 MW at gains of nearly 8 dB [70].

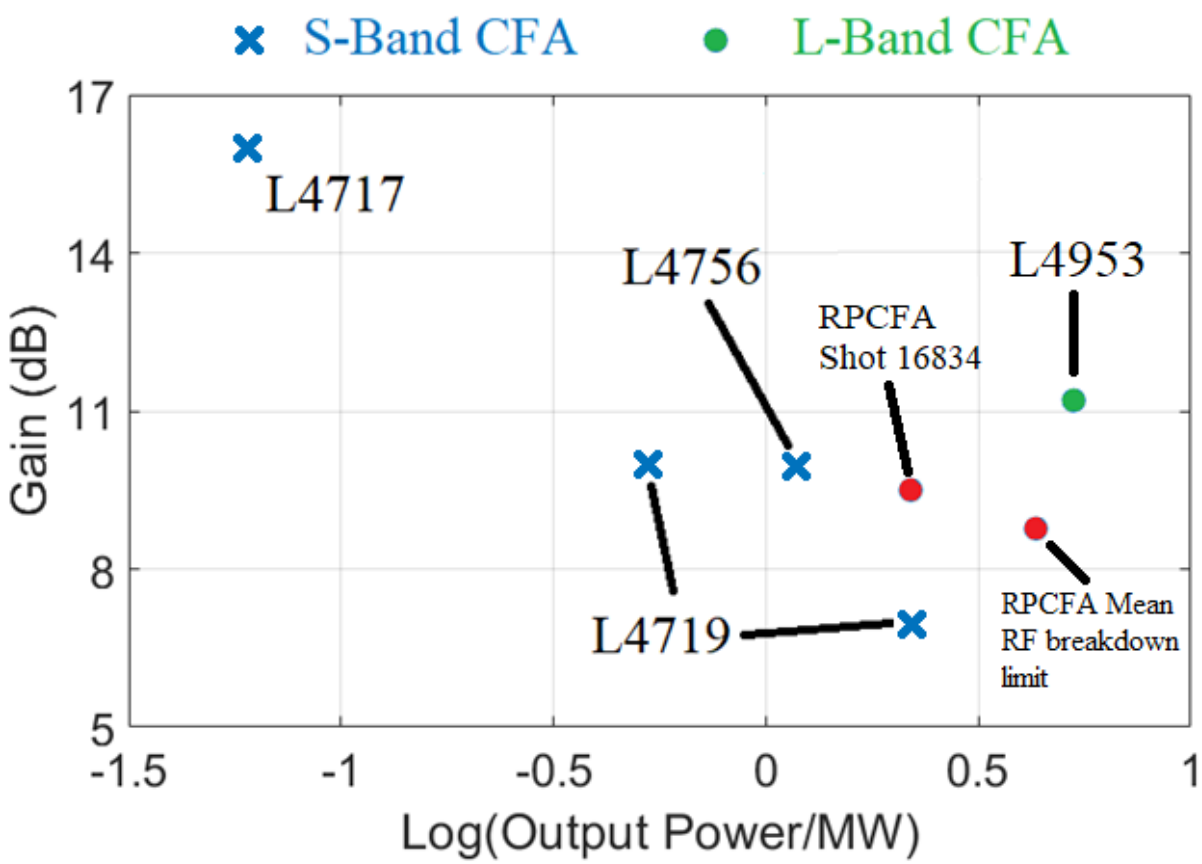

Figure 5.1: Comparison of the RPCFA, operated safely below RF breakdown (shot 16834) and at mean RF breakdown levels, with existing commercial CFAs.

This increased peak power comes at the expense of efficiency. The S-band CFAs listed in Figure 5.1 are typically greater than 50% efficient. Operating the RPCFA at -300 kV and 4 kA with 4 MW of output power, typical parameters for the high-power shot series, gives a peak total efficiency of 0.33%. Electron end loss current is likely a major contributor to this low efficiency (see appendix G). This may be mitigated by the addition of non-emitting endhats to the cathode [61]. An aluminum endhat was added to Cathode A in order to create a component of the pulsed electric field that would contain electrons within the interaction region. This did not significantly decrease the current drawn nor increase the gain of the RPCFA, suggesting the aluminum endhat is ineffective at preventing end loss. MAGIC simulations suggested that the addition of an endhat that is not permitted to emit would decrease the current drawn by approximately a factor of 6. In MAGIC simulations where end loss is not significant, the efficiency is as

high as 15.5%. This efficiency is still significantly lower than values expected from commercial CFAs (~50%). Investigation into an RPCFA that can operate at reduced operating voltages and currents with overall peak powers on the order of the expected amplified output may show improved efficiency.

Another issue that existing CFAs address that the RPCFA did not test is heat management. At a nominal duty cycle of 0.001, and a 15.5% interaction efficiency determining the total power dissipated into the interaction space, the RPCFA would need to exchange 29 kW of heat with flowing water to operate at 4.5 MW peak output. This is not an unreasonable value as the L4719 CFA operating at 2.2 MW peak output and 1.25% duty cycle, and assuming 50% efficiency, must exchange 55 kW with its cooling system. Some 20 kW/cm^2 of heat dissipation has been demonstrated in CFAs [71]. Flowing water lines would have to be cut through the meander line of the SWS, which is not a trivial addition to the fabrication process.

Phase coherency and control are another defining feature of CFAs. The RPCFA in its current experimental configuration demonstrated a limited ability to accomplish this. Managing plasma formation in the device, and maintaining stable pulsed currents may assist in resolving this. A modulator/high-power driver with improved regulation that can reduce the spread of injected frequencies into the RPCFA would be expected to improve phase control.

5.3 Recommendations for Future Work

While the RPCFA has a number of shortcomings compared to existing devices listed in the previous section, the primary purpose of this device is the demonstration of amplification of high-power microwaves. Reducing the transmission loss of the RPCFA is an obvious method for improving the overall gain of the device. Transmission losses are assumed to be resistive in nature, reducing the RF power flow in the circuit, though not introducing a reflected wave or dispersive effects. Because of this, eliminating these losses may directly increase the gain by the same amount. It is not unreasonable to suggest that the 8.8 dB amplification of the RPCFA with 3 dB of transmission loss can be improved to an 11 dB amplifier with much of those

losses removed. An improved coupling at the puck couplers is the most immediate upgrade, though higher precision additive manufacturing of the SWS should also be explored. RF contact resistance is believed to represent a large loss. If these modifications can be made, and assuming RF breakdown is not a concern at L-band, 11 dB amplification of a 5 MW L-band input drive would yield 63 MW of peak output RF power. This would be approximately 5.3% efficient with MELBA's present operating parameters, but would represent a much higher peak power than existing CFAs.

Exceeding the limit imposed by RF breakdown can be approached in a number of ways. Attempting to significantly improve the vacuum of the experiment may prove difficult with its current arrangement. Commercial high-power vacuum tubes typically operate on the scale of 10^{-8} to 10^{-9} Torr. The SWS may be modified to admit greater spacing between cells, reducing the strength of RF fields. This may also require the average phase shift per cell to be reduced, as maintaining the $\pi/2$ phase shift per cell with larger cells would increase the phase velocity beyond 0.3c. At increased beam speeds, it becomes difficult to synchronize the electron beam while maintaining magnetic insulation. Increased beam speeds also reduce the efficiency, though that is less of a concern on this experiment.

Rescaling the device to lower frequency, such as L-band, would easily admit a decrease in the RF field strength, which would increase the RF breakdown limit substantially (potentially by a factor of 4). A commercial L-band CFA is plotted in Figure 5.1 for reference. An L-band CFA would also require a high-power L-band source and potentially another driver, which are commercially available.

Utilization of the harmonic content available in the Brillouin hub (see appendix D) is also a means of extracting additional power from the device. There has been interest in generating harmonic frequencies in crossed-field and linear beam amplifying devices [46,72 - 76]. A CFA that extracted significant RF power at harmonic frequencies would represent a novel development.

Finally, the author is not aware of any analytic theory of crossed-field amplifiers whose realistic equilibrium state is the Brillouin flow. For example, even the gain parameter called “C” in Pierce classical theory of TWT, has not been calculated. The dispersion relation for a realistic CFA does not exist.

Appendix A

Estimating the Performance of the RPCFA

The theoretical framework established in chapter 2 is sufficient for making a computational prediction of the performance of the RPCFA. This calculation, developed by the author, is accomplished by mapping the particles in the Brillouin hub through their trajectory from interactions with the electric and magnetic fields. A number of approximations will be made for this calculation, many of which were also made in the derivations in previous sections. An unperturbed Brillouin hub as specified in section 2.2 is the initial condition from which particles are created. Particle dynamics are evaluated relativistically though the self-magnetic field is ignored, as in section 2.3. The precise geometry of RPCFA slow wave structure is unnecessary for the calculation though the guided wavelength of the RF excitation and the phase velocity of such an excitation is required for an accurate assessment of the device. For reference, the RPCFA is designed to operate at 300 kV DC bias, a magnetic field of 0.2267 T and an RF drive of 1.3 MW at 3.0 GHz. The justification for these operating points will be discussed in chapter 3. In addition, the AK gap width is 15 mm, the Brillouin hub width is 2.4 mm, and the period of the slow wave structure is 7.5 mm, as shown in Figure A.1.

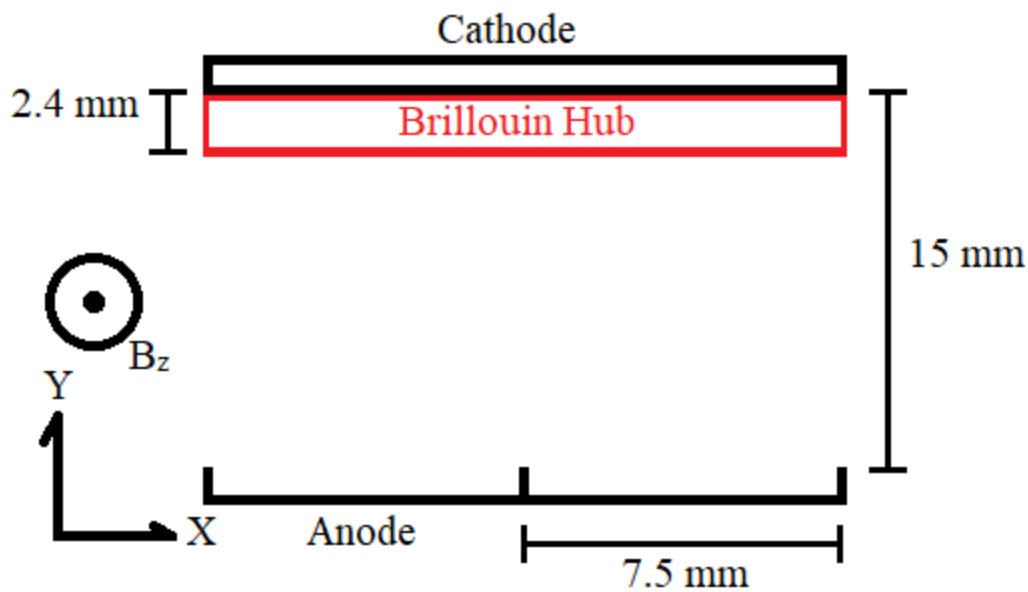

Figure A.1: Geometry over two SWS periods used in this estimation of RPCFA performance.

For this investigation, the SWS is now oriented such that the direction of propagation is along $+\hat{x}$, the DC electric field points along $+\hat{y}$, requiring the magnetic field to be directed along $+\hat{z}$. (This is not the same convention in Fig. 2.1) The problem is assumed to be constant in z for simplicity, though this assumption is easily contested as the axial dimensions of the SWS are not large compared to the length of cells nor the A-K gap. Applying this geometry gives the equations for the components of particles momentum, $\vec{P}$, and position, $\vec{x}$.

$$\frac{dP_x}{dt} = q\frac{dV}{dx} - \Omega_c P_y \qquad \text{(A1.1a)}$$

$$\frac{dx}{dt} = P_x/m\gamma \qquad \text{(A1.1b)}$$

$$\frac{dP_y}{dt} = q\frac{dV}{dy} + \Omega_c P_x \qquad \text{(A1.1c)}$$

$$\frac{dy}{dt} = P_y/m\gamma \qquad \text{(A1.1d)}$$

Here, $\Omega_c = qB/m\gamma$ and γ is the Lorentz factor.

Using equations A1.1a through A1.1d and the model for evaluating the electrical potential at a given point in space and time, the trajectory of a particle can be evaluated over time through standard finite differencing methods. The first time step is evaluated using a forward differencing scheme, $f_{n+1} = f_n +$

$\Delta t \frac{df_n}{dt}$ and subsequent time steps are evaluated using the leap-frog method, $f_{n+1} = f_{n-1} + 2\Delta t \frac{df_n}{dt}$. This leap frog method was chosen for its stability in approximating oscillating systems. Equations A1.1a through A1.1d can be verified using a simple example. Setting the potential in the system zero and giving some initial velocity recovers the expected cyclotron orbits shown in Figure A1.2.

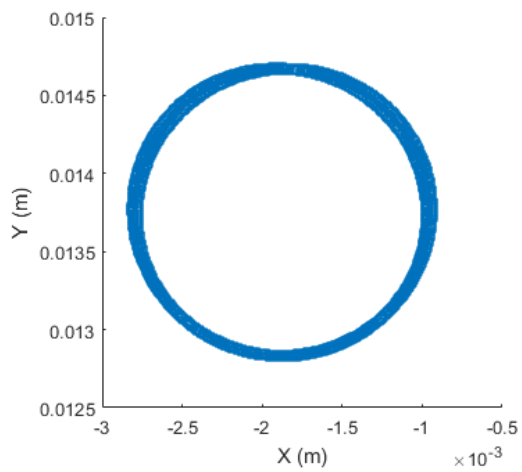

Figure A.2: Cyclotron orbit. Particle position in (x,y) space is traced over time for the case with no electric potential.

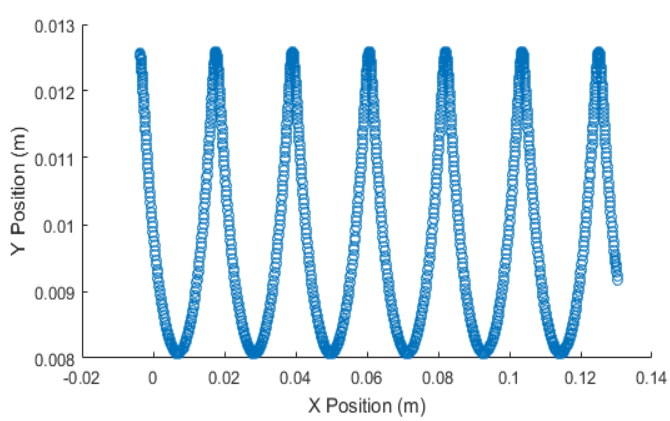

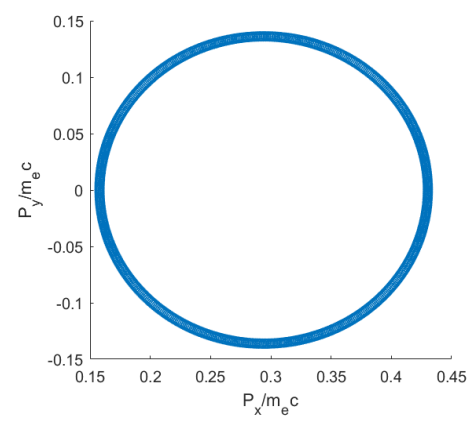

Figure A.3a (left): Cycloidal path traced by a particle in a static electric and magnetic field. In this figure, the cathode surface is located at y = 0.0125 m and the top of the single particle cycloidal orbit is at y = 0.008 m.

Figure A.3b (right): Normalized momentum trace for the same particle.

A dc electric field can be applied and the expected cycloidal orbits can be demonstrated. The momentum and position traces are shown in Figures A1.3a and A1.3b. The SWS of the RPCFA is designed such that the input signal propagates at a constant phase velocity without modulation. In the lab frame, the potential shown in Figure 2.4b propagates along the SWS at a constant phase velocity. Taking the transform:

$$x' = x - v_{phase}t, \tag{A1.2}$$

where v_{phase} is the phase velocity of this wave, the field appears static. In this Lagrangian frame, a particle initiated at the surface of the hub has zero initial velocity. Particles between the surface of the cathode and the surface of the hub are initiated at varying negative initial velocities depending on their position.

By imagining a 2-cell resonator of the SWS, shown in Figure A1.4a, the shape of the RF field can be approximated by artificial charges imposed at the vane tips. The interaction space bounded by the anode and cathode in $\hat{y}$, (the cathode is located at y = 15 mm, the anode tip is located at y = 0 mm) and the width of a cell in $\hat{x}$, is divided into a 16x16 grid. The cathode is taken to be a perfect conducting boundary condition. The pi-mode geometry suggests that 4 artificial charges of equal magnitude arranged in quadrupole configuration with two charges positioned at the anode vane tips gives a good approximation of the RF potential in the interaction space. The magnitude of the charges is a function of the input drive and the specific geometry of the SWS is determined from MAGIC simulation. The total RF potential in the interaction space is composed of repeated, alternating potentials generated from this quadrupole arrangement an example of which is shown in Figure A1.3b. If the trajectory of the particle takes it out of the frame shown in Figure A1.4b, the result is that the particle is transferred to the opposite side and the sign of the potential is reversed, indicating the particle has moved into the adjacent frame.

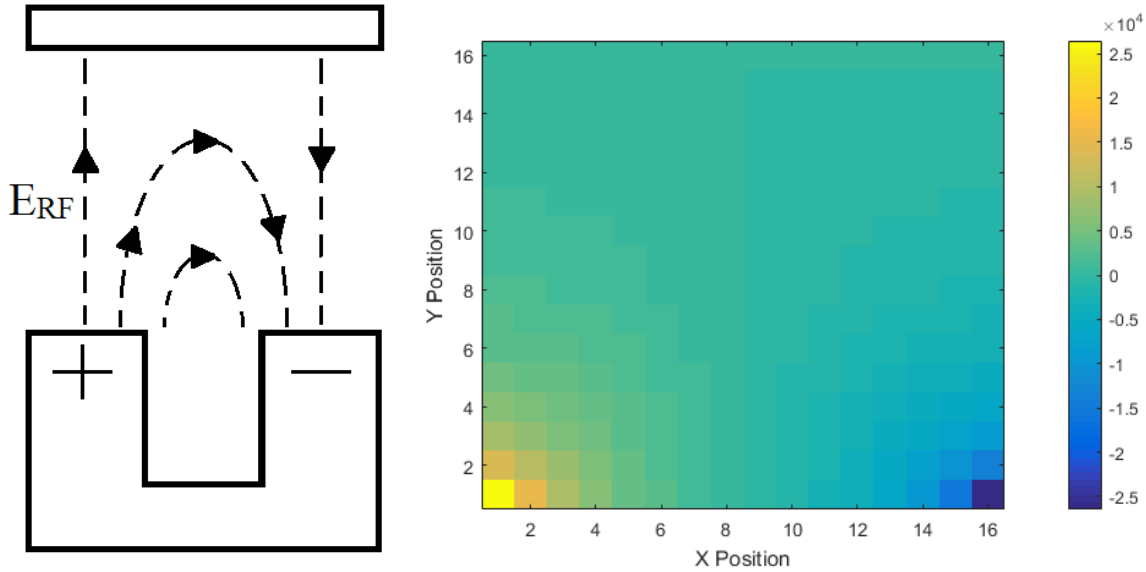

Figure A.4a: A section of an arbitrary SWS with the RF field drawn. For the 180º phase shift in RF field as shown this represents 2 cells of the RPCFA SWS. In this figure, the cathode is located at y = 15 mm and the anode vane tip is located at y = 0 mm. The x-coordinate at the middle of the cavity is x = 7.5 mm. Figure A.4b: The RF potential in the interaction space in V for a 1.3 MW RF excitation. The x, y coordinates of this figure illustrate the numerical grid. Each cell represents a square in physical space with a side length of 15/16 mm.

The Brillouin hub is divided into 10 layers starting from the cathode surface to the edge of the hub, and 32 columns spanning the length of a full wavelength. A two cell wide focusing frame, as shown in Figure A1.4b, and a two cell wide defocusing frame, which features potentials opposite those shown in Figure A1.4b, defines each unique starting point for a particle in the hub. This divides the Brillouin hub into 320 unique components. Each component's position and momentum are tracked for a length of time up to 3 RF cycles, the time required for the wave travelling at v_{phase} to traverse the SWS, or until it is collected by either electrode. The trace of a particle initiated at the edge of the hub, and drawn to the anode, is shown in Figure A1.5. The conditions for Figures A1.5 through A1.8 are near the expected experimental values, 300 kV DC bias, a magnetic field of 0.2267 T and an RF drive of 1.3 MW at 3.0 GHz, in which case the x-component of the RF electric field at the top of the Brillouin hub is 29.4 kV/m.

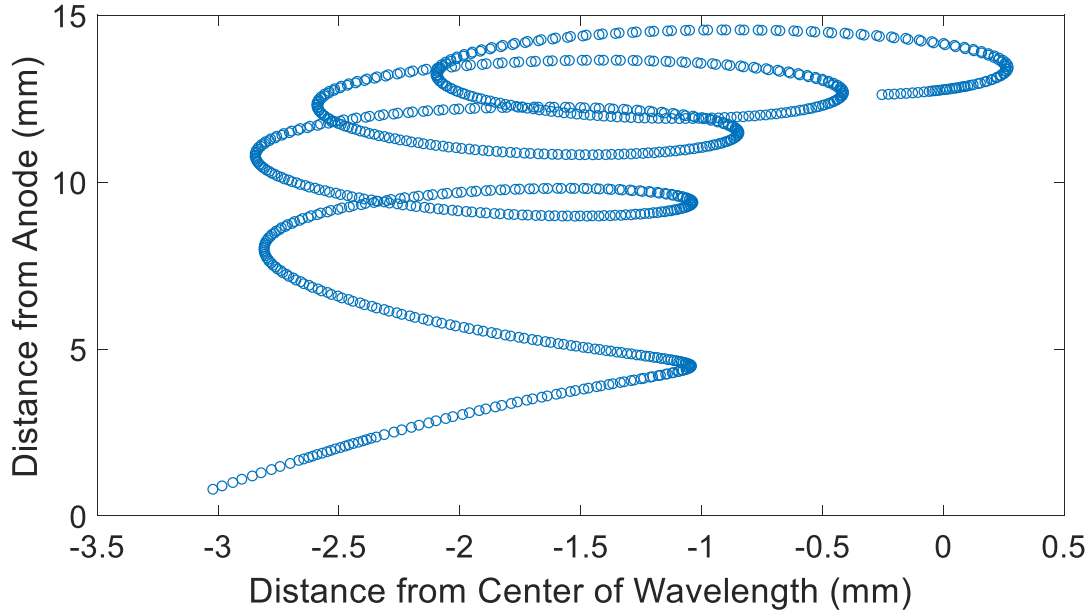

Figure A.5: Sample trajectory of a particle (in the Lagrangian frame) initiated at the center of the focusing field frame and the edge of the Brillouin hub. This particle's trajectory ends at the anode. In this figure, the initial y-coordinate (tip of Brillouin hub) is 12 mm from the anode.

The RF gain due to this particle is calculated by integrating $\overrightarrow{v_1} \cdot \overrightarrow{E_{rf}}$ along the particles trajectory and scaling according to the Brillouin hub density as instructed by equation 2.9 to get the $\overrightarrow{J_1} \cdot \overrightarrow{E_{rf}}$ source which is responsible for amplification as dictated by equation 2.18. The total gain is found by summing the integrated $\overrightarrow{J_1} \cdot \overrightarrow{E_{rf}}$ for all particles in 1 full wavelength of the hub. The individual contribution to the RF gain for each component of the Brillouin hub is shown in Figure A1.6. The individual contributions are additionally weighted by the rate at which they cross the A-K gap, and summed to give the total RF gain. This makes the assumption that the cathode is capable of quickly repopulating the Brillouin hub for particles that cross the diode. The total efficiency can be evaluated by the ratio of the total increase in power of the RF divided by the total power available due to particles crossing the A-K gap. A map of the end condition of components of the hub is shown in Figure A1.7.

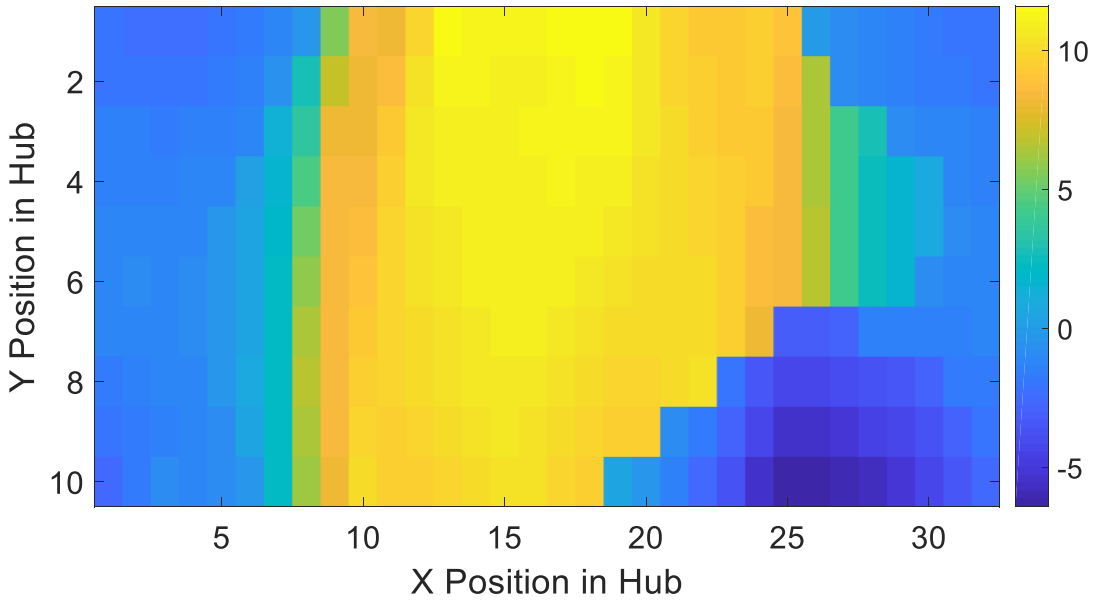

Figure A.6: Each of 320 components individual contribution to RF gain in units of 10 kW.

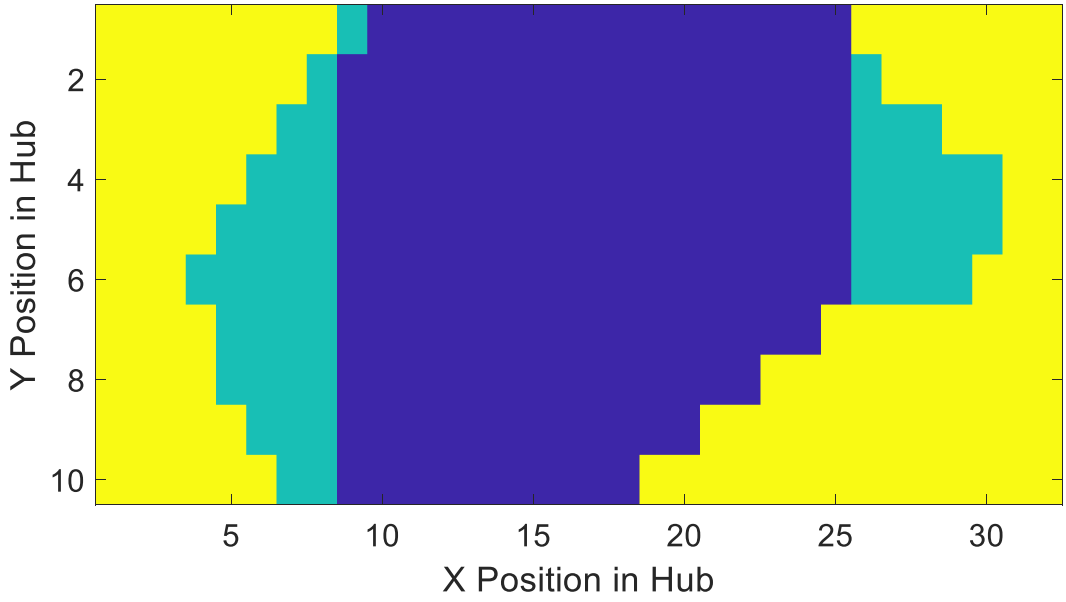

Figure A.7: Map of the end conditions for components of the Brillouin hub. Blue indicates the particle is drawn to the anode; green indicates it remains in the interaction space after a time of 3 RF periods. Yellow indicates the particle is returned to the cathode and does not contribute to the overall current draw.

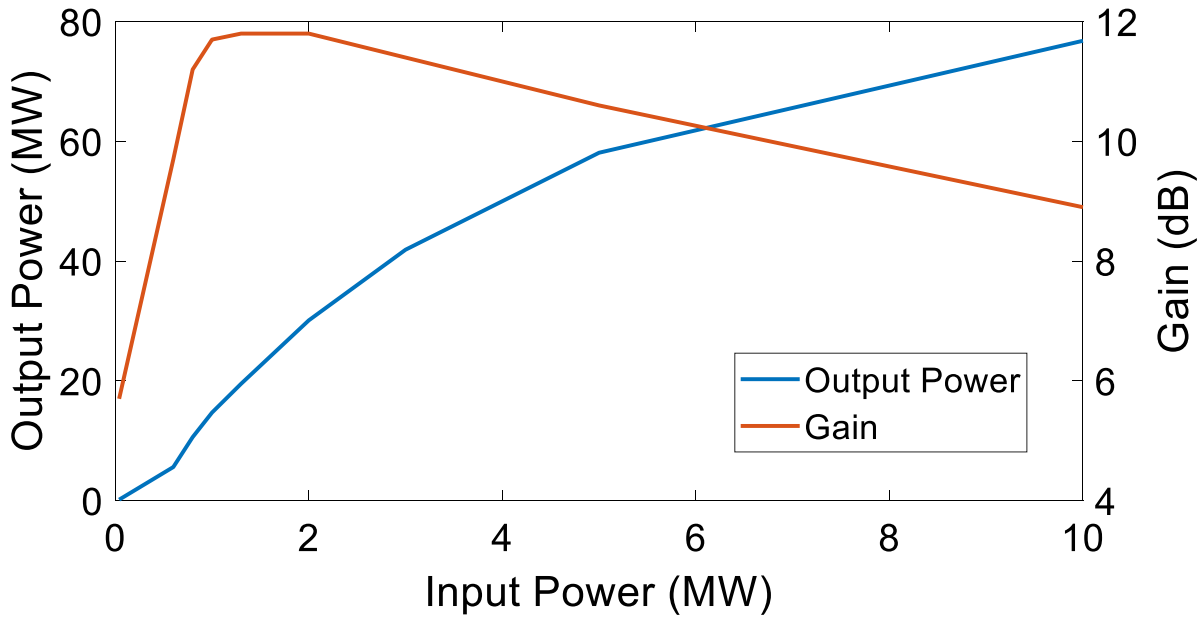

Figure A.8: Output Power and gain from the RPCFA for various levels of input drive.

For reference, the algorithm presented here predicts that for 1.3 MW of RF drive, the RPCFA should draw 780 A and generate 19.5 MW of RF power, giving a gain of 11.8 dB, at an efficiency of 7.8%. The input power can be varied to predict the response of the RPCFA. 11.8 dB is only slightly less than the 13.5 dB predicted by MAGIC simulation. The low efficiency is cause for concern especially since a characteristic feature of cross-field devices is their high efficiencies. This is due to the level of RF drive compared to the total power dissipated in the diode, $P_{Total} = I_{Total}V_{DC}$. Operating at higher RF drive can increase the efficiency to a limited extent. Greater RF drive leads to high powers generated, but also to much higher currents drawn, decreasing the efficiency. Additionally, the model developed in this investigation breaks down at higher current. At high current, the presence of space charge in the diode become significant, a factor which is completely ignored in the model as each component of the hub is treated individually. Lowering the DC voltage may provide higher efficiencies, though this parameter is fixed experimentally.

Appendix B

A Description of Devices used to Drive RF sources

The Stanford Modulator Model No. 344M, is a conventional hard-tube pulse modulator. The machine features two outputs, one for AC filament heating and the other for pulsed high-voltage. The high-voltage output must be connected to a high impedance (~2000 Ω) external path to ground for safe operation. This path must also be capable of dissipating the mean power output of the modulator, copper sulfate resistors were used in this experiment. The Stanford Modulator is rated for peak outputs of 40 kV and 30 A, a peak output power of 1.2 MW. The filament heater provides up to 25 V, 3 A at 60 Hz AC, suitable for all three magnetrons used in this investigation. Pulse lengths can be continuously varied from 0.1 to 5.0 μs, the repetition rate variable from 10 to 2000 Hz and a maximum duty cycle of 0.002.

When driving loads with impedances similar to the magnetrons used in this experiment (~ 450 Ω) the modulator was unable to maintain high voltage, reaching only 12.5 kV and delivering around 350 kW (28 A) peak power. Thus, this modulator was unable to drive the higher power magnetrons used in this investigation. Additionally, the external trigger of the modulator did not appear to not be functional. The sync-out monitor worked properly so the pulse waiting triggering method pictured in Figure 3.23 was used to synchronize the experiment to the modulator. The Stanford Modulator is pictured in Figure B.1.

Figure B.1: Stanford Modulator Model No. 344M.

A driver capable of reaching higher peak voltages and currents than the Stanford Modulator was required to drive the MG5193. For this purpose, the Extra Large Brass pulse forming network (XLB PFN) was designed, shown in Figure B.2. The PFN is type E network with 5 capacitor stages of 1 nF each. These capacitor stages are connected to a single long 480 μH air core inductor at points along the length of the inductor chosen to optimize the flatness of output pulses. An L-3 model 40264 spark gap switch connects the PFN to the load. The switches, capacitors and inductor are stored inside a large, brass (plated) SF_6 filled chamber held near 1 atm. The interior circuity can be seen in Figure B.3.

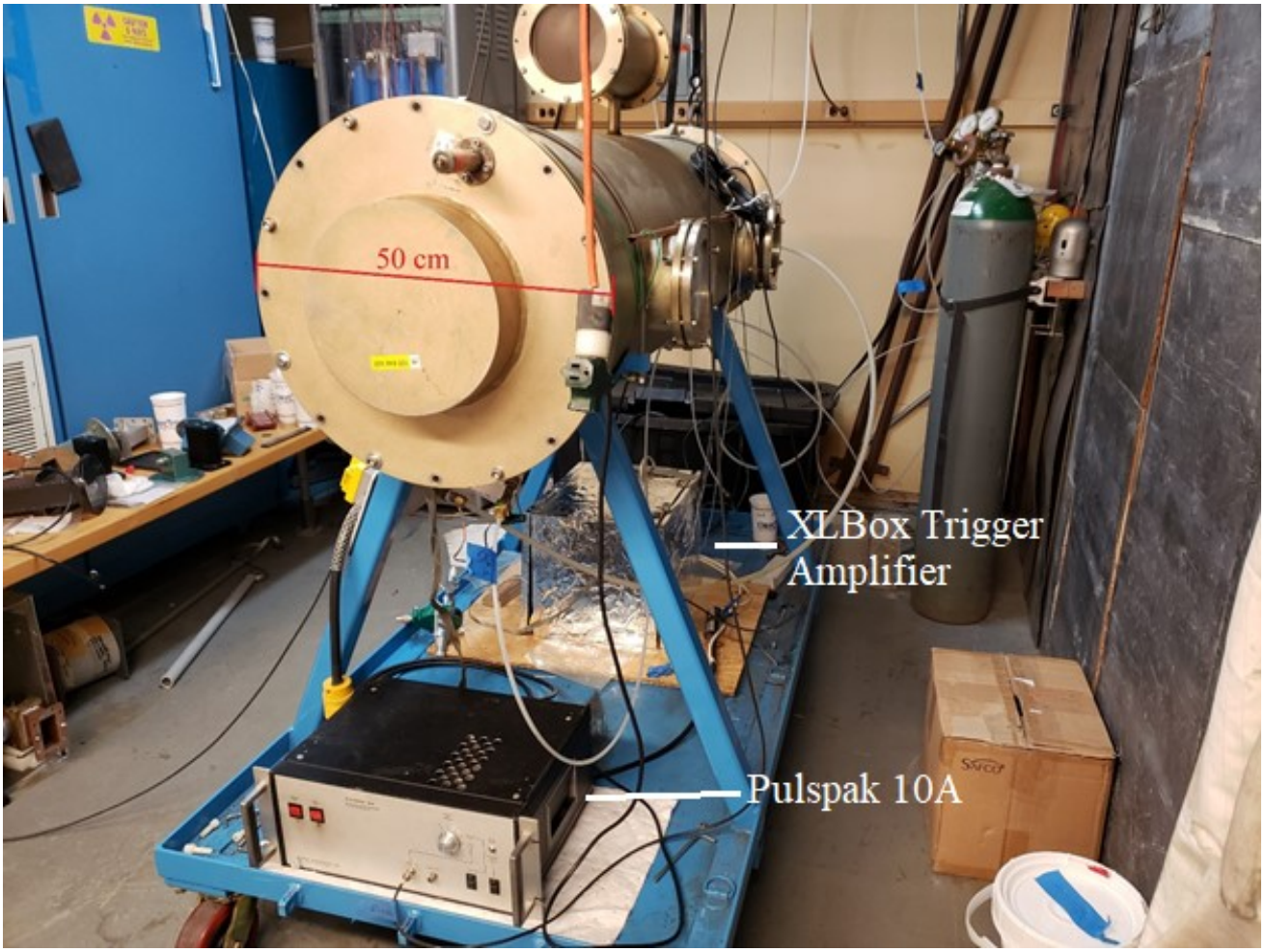

Figure B.2: XLB PFN with XLBox trigger amplifier and Pulspak 10A trigger generator.

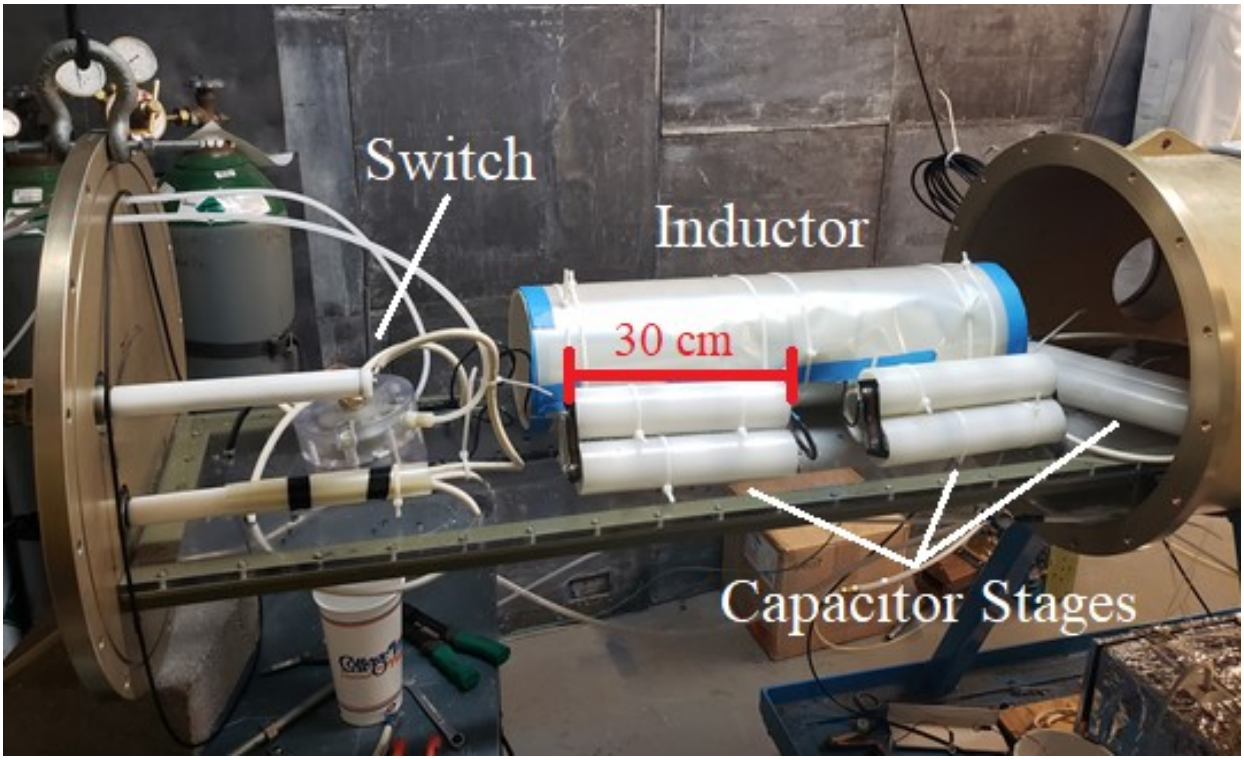

Figure B.3: XLB PFN with interior circuitry extracted. 2 additional capacitor stages are mounted below the breadboard and are not visible.

The XLB PFN is charged using a Glassman High Voltage DC power supply through a 1 Megaohm charging resistor. The PFN is fired from same the delay generator as MELBA. The delay generator sends a low voltage trigger to the Pulspak 10A, which then sends a 10 kV trigger to the XLBox trigger amplifier. The XLBox contains a PT-55 trigger generator which must be charged to +7 kV prior to firing. This PT-55 sends a capacitively coupled 40 kV pulse to breakdown the spark gap switch in the PFN. In addition to the magnetron, the output of the PFN is connected to a 1 kΩ parallel resistance, to protect the experiment from rapid impedance swings, and a 2 nF capacitor for filtering high frequency noise. A circuit diagram for the system is shown in Figure B.4.

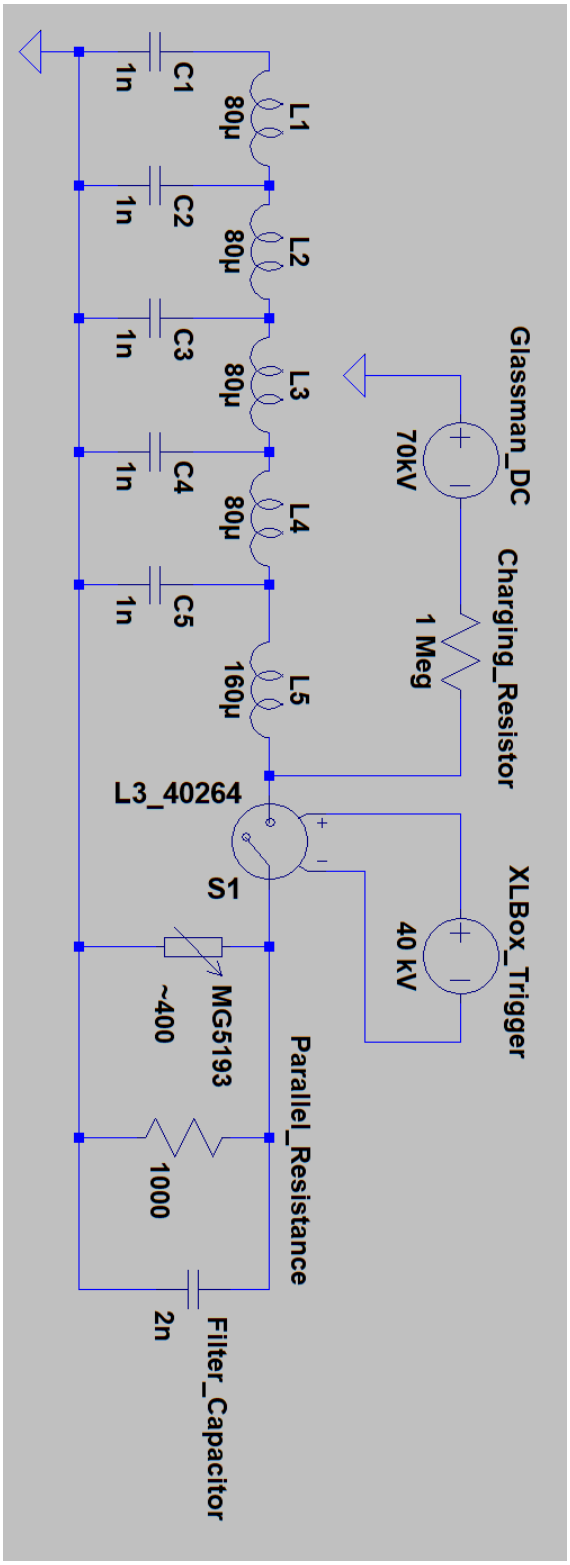

Figure B.4: Circuit diagram generated in LT SPICE for the XLB PFN with charging, triggering, and load architecture included.

An example pulse at 70 kV charge into a 400 Ω resistive load is shown in Figure B.5. Voltage is measured with a Northstar high-voltage probe. The peak voltage of -35 kV corresponds to approximately 88 A. Nearly 2 µs of useable flat-top voltage is available for running the MG5193 magnetron. The 400 Ω resistive load was replaced by the MG5193 magnetron to generate HPM.

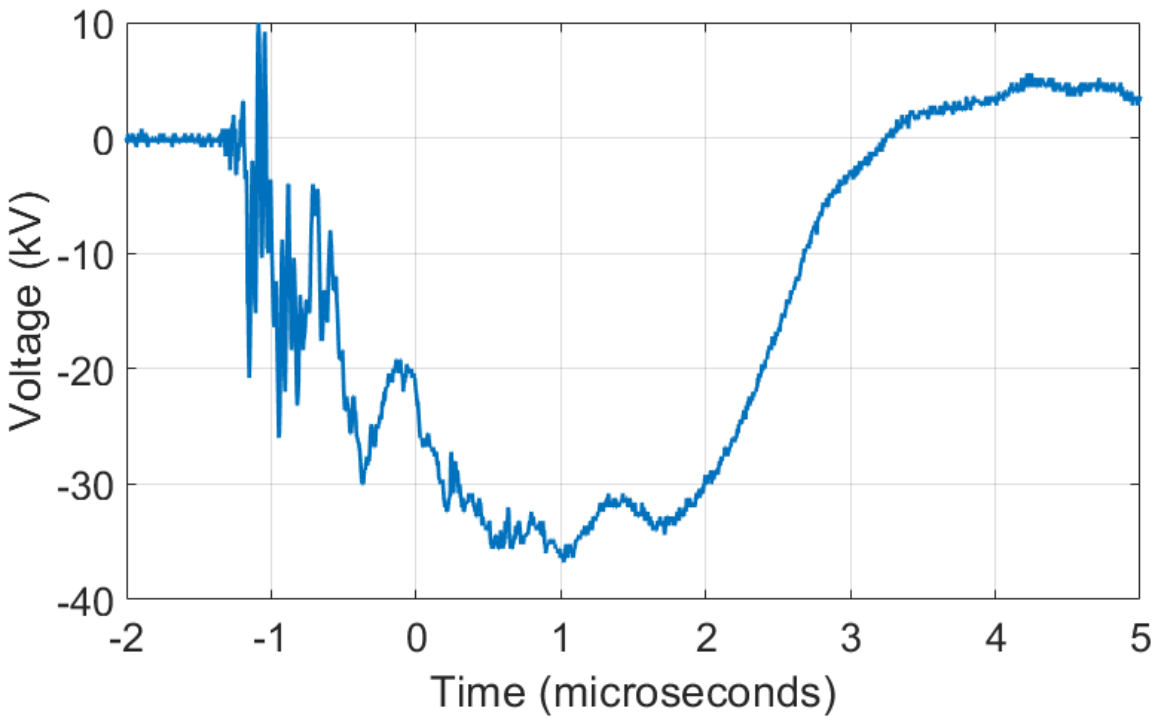

Figure B.5: Voltage trace of the XLB PFN at 70 kV charge firing into a resistive 400 Ω load.

Appendix C

Detail Drawings

This section presents detail drawings for fabricating the components used in the preceding RPCFA experiments in the following order:

1. RPCFA SWS
2. SWS Substrate
3. Cylindrical Ends
4. Smooth Bore Planar Section
5. Locking Back Wheel
6. Input/Output Waveguides
7. RPCFA Puck Couplers
8. Cathode Components
9. End Plate
10. Vacuum Interface
11. 4J32 Puck Coupler

O-ring grooves were designed in accordance with the Parker O-ring Handbook section 4.3 and design chart 4-3 [78]. The full SWS assembly was additively manufactured as a single piece. All other components were machined from 6061 Aluminum.

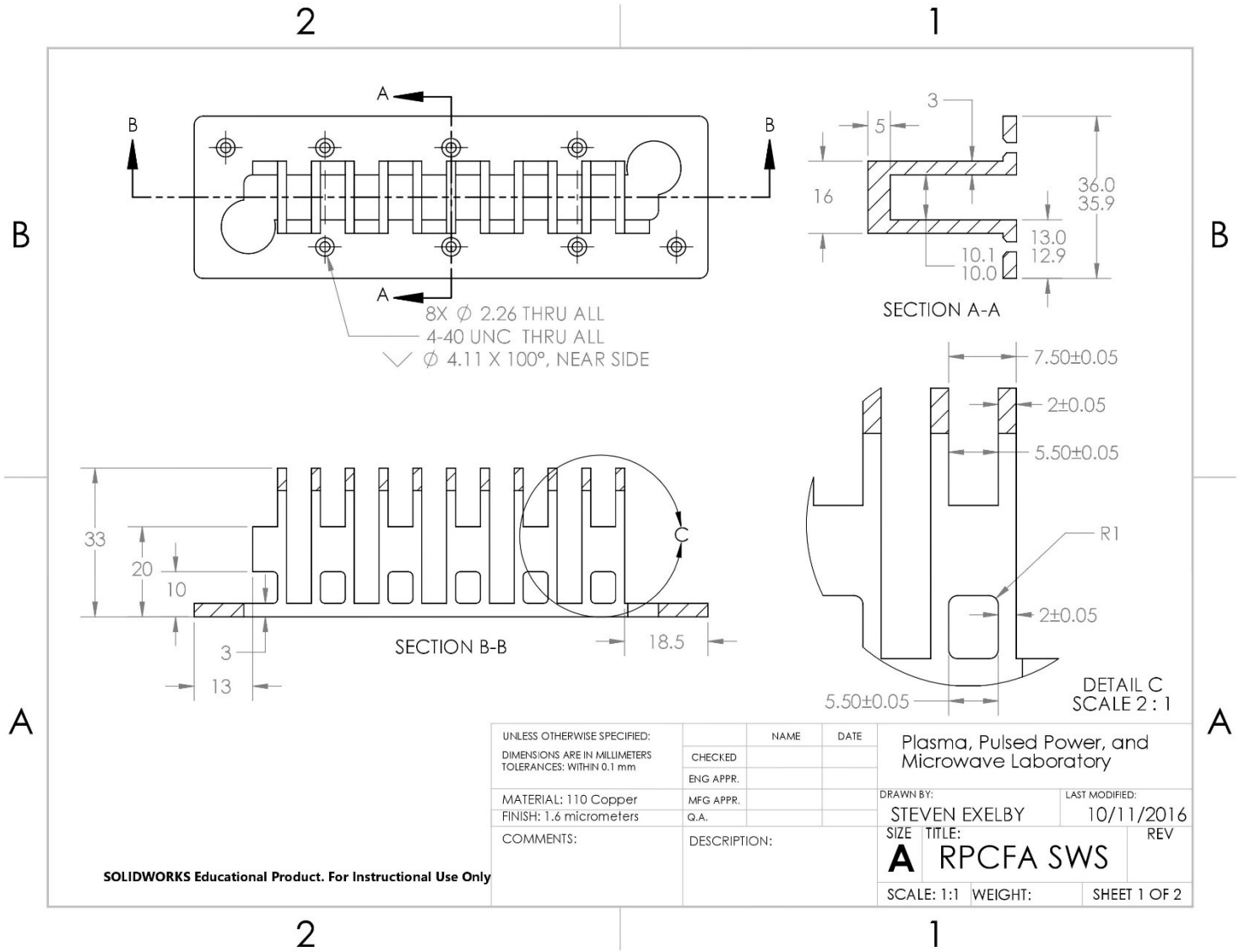

Figure C.1a: RPCFA Slow wave structure, page 1.

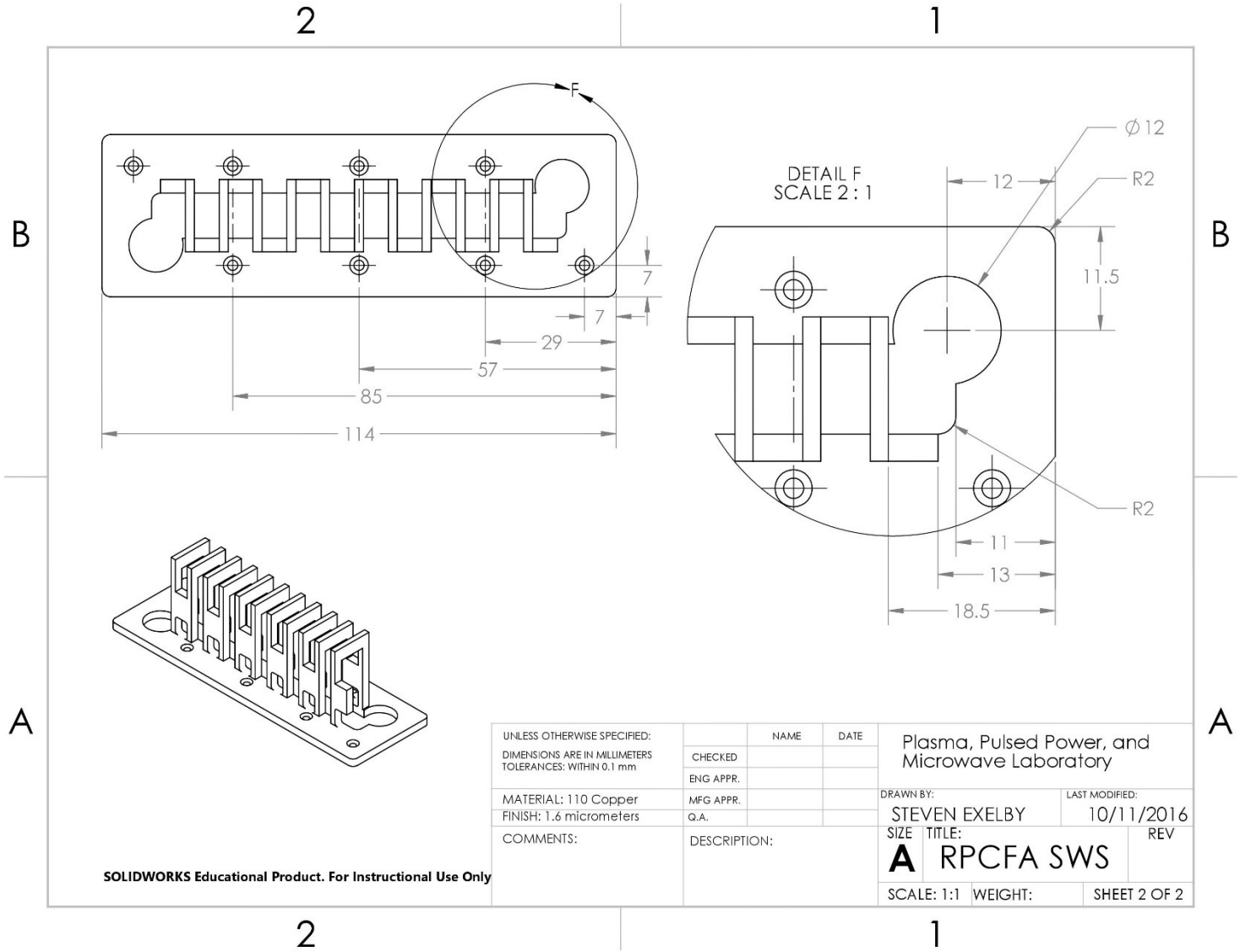

Figure C.1b: RPCFA slow wave structure, page 2.

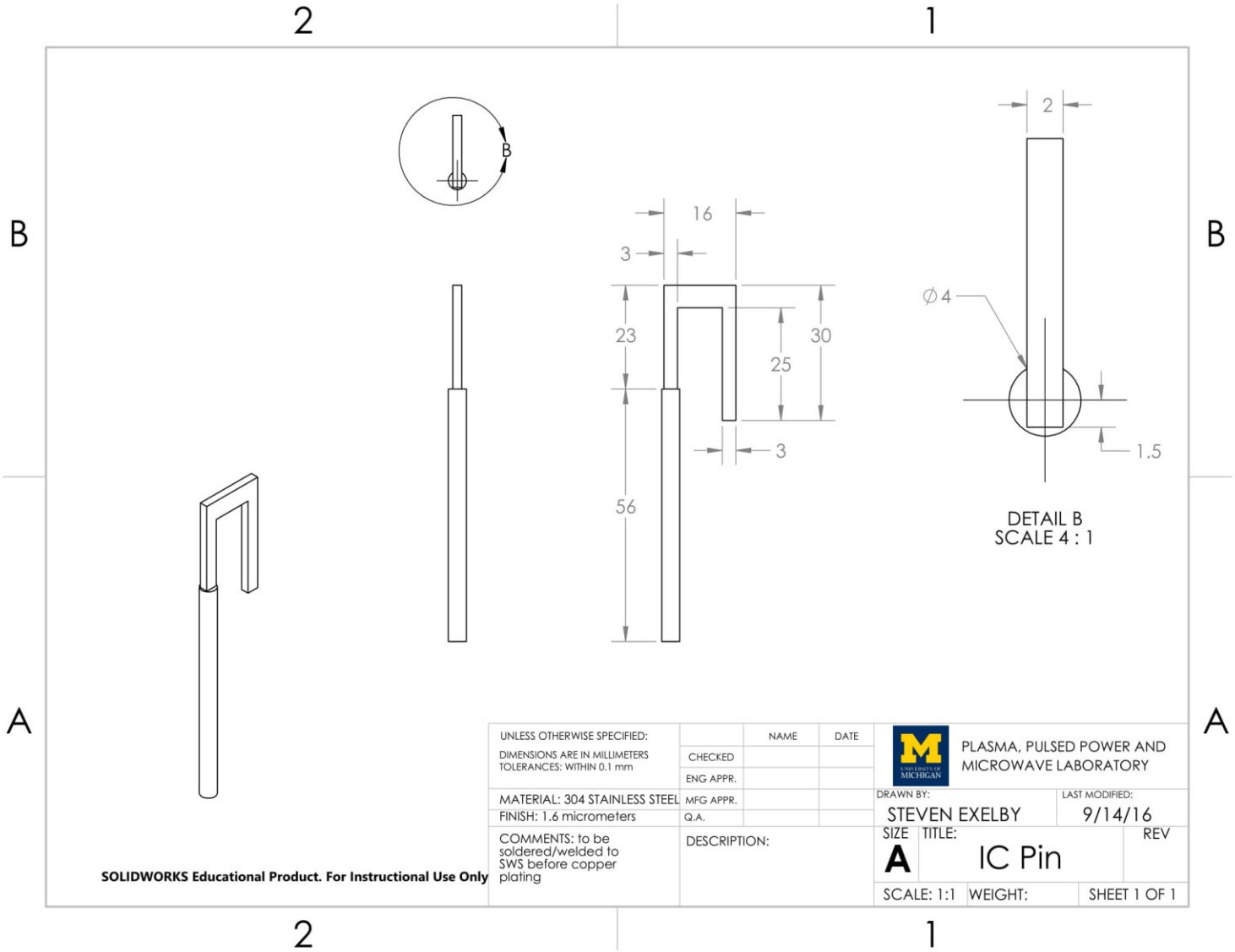

Figure C.1c: Inner conducting pin, connects the SWS into the puck couplers. Two of these plus the SWS form the assembly that was additively manufactured for the prototype RPCFA.

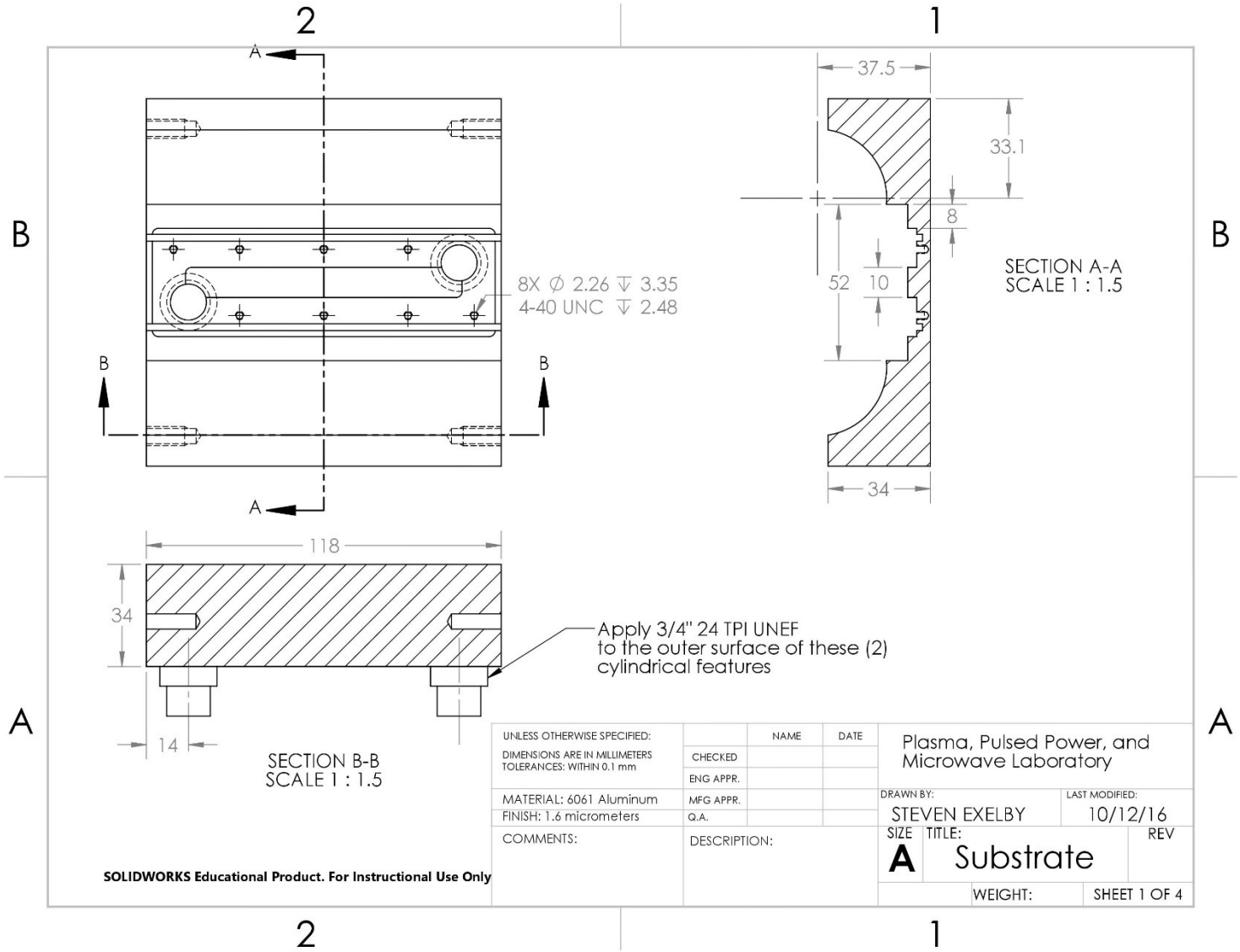

Figure C.2a: The RPCFA slow wave structure substrate, page 1.

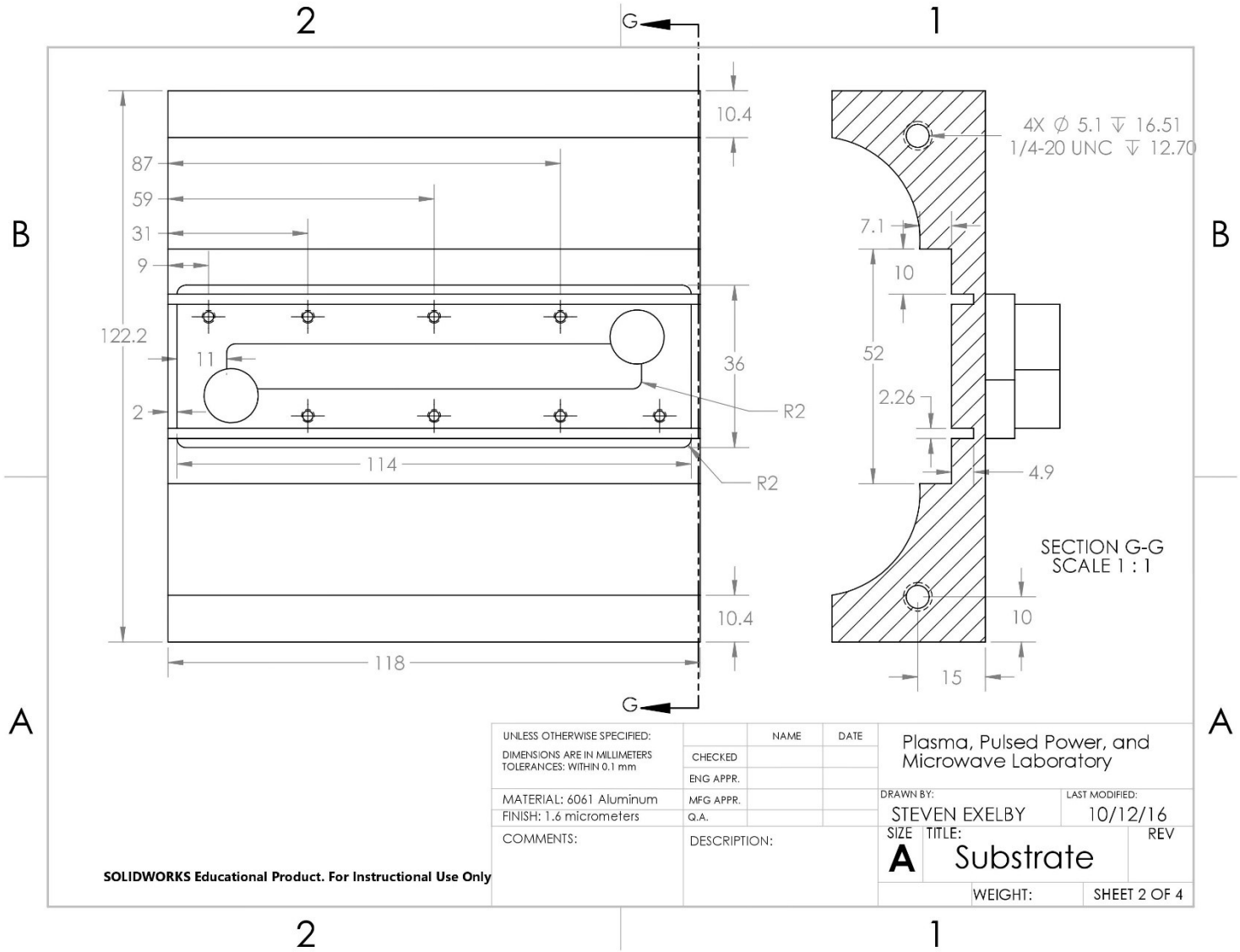

Figure C.2b: The RPCFA slow wave structure substrate, page 2.

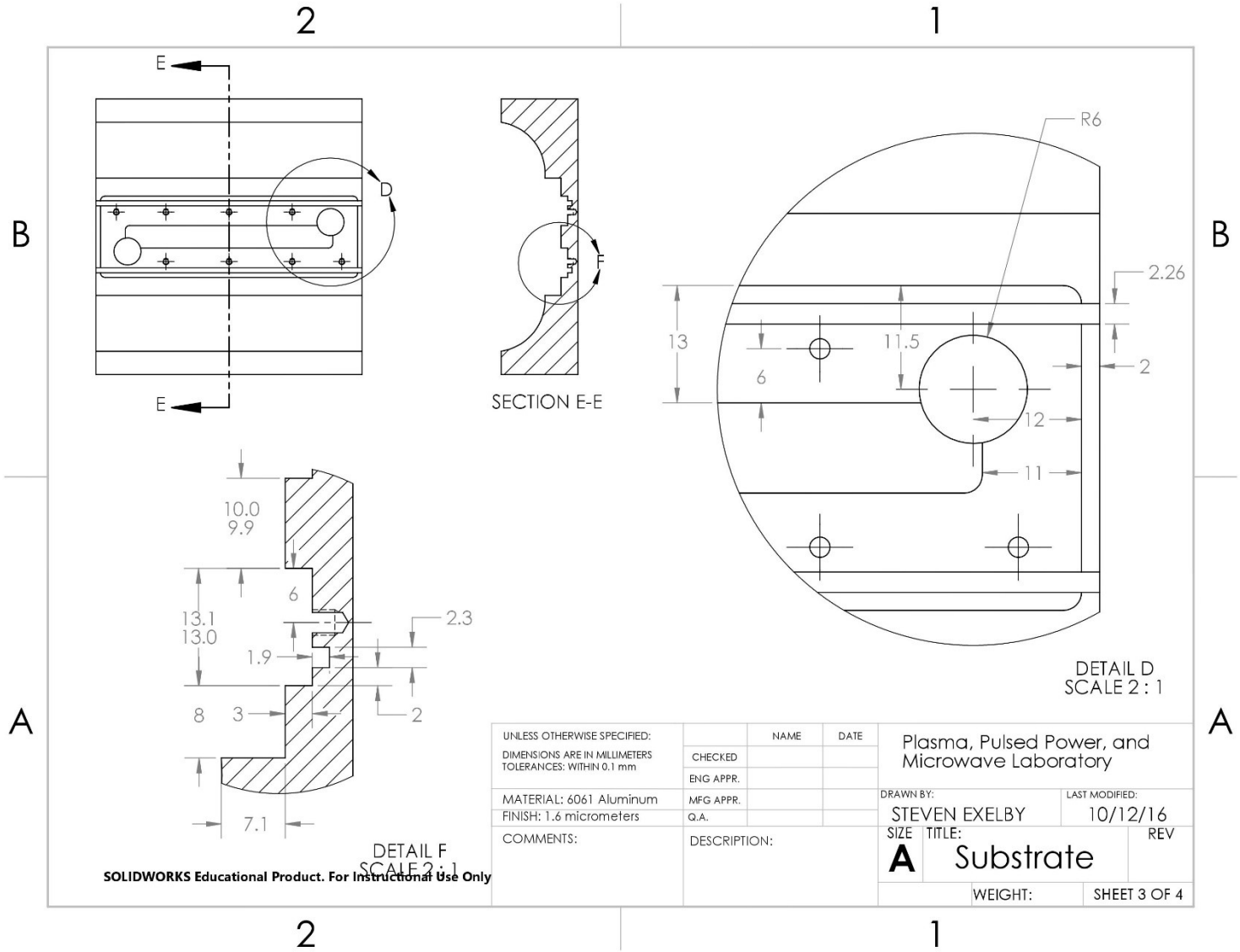

Figure C.2c: The RPCFA slow wave structure substrate, page 3.

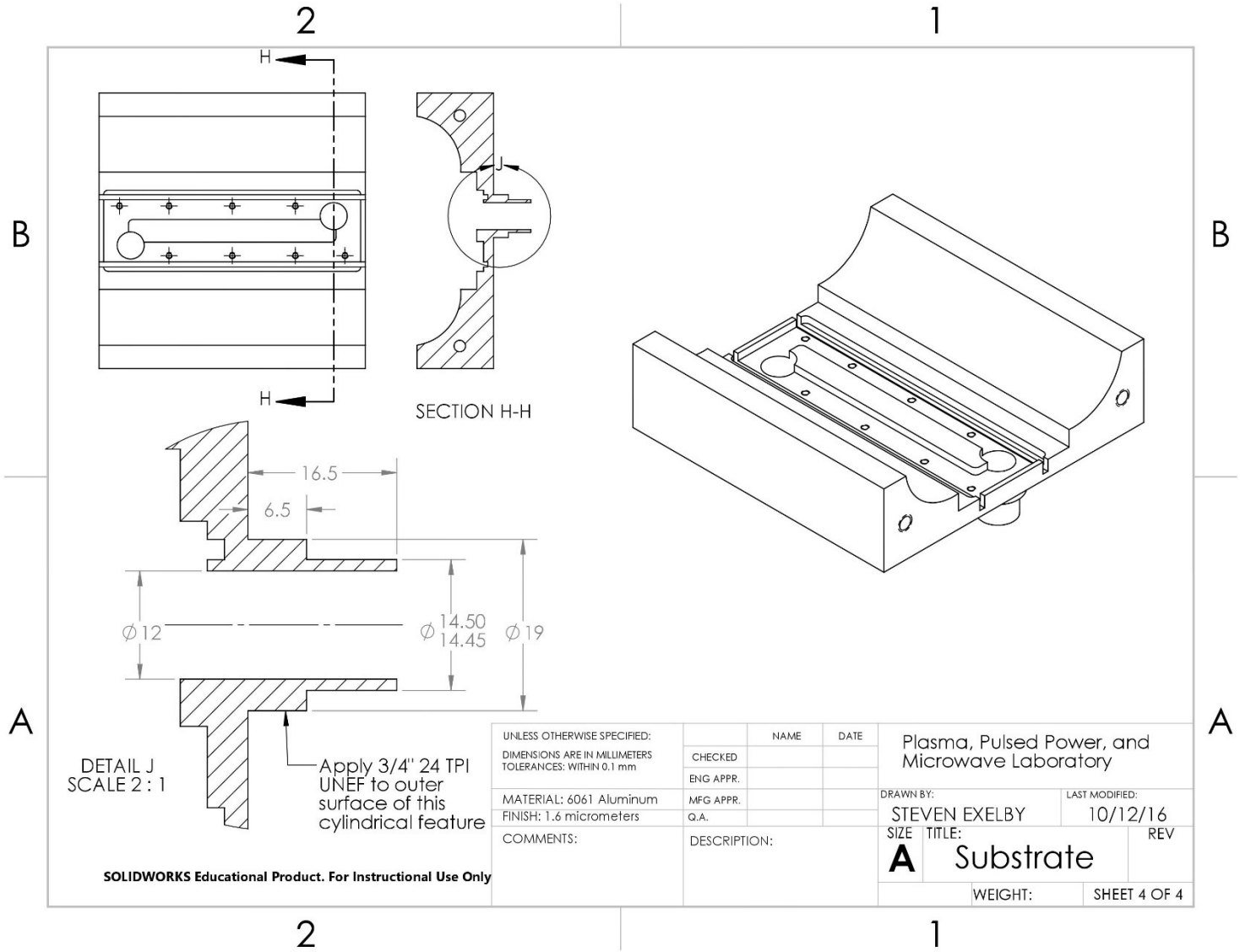

Figure C.2d: The RPCFA slow wave structure substrate, page 4.

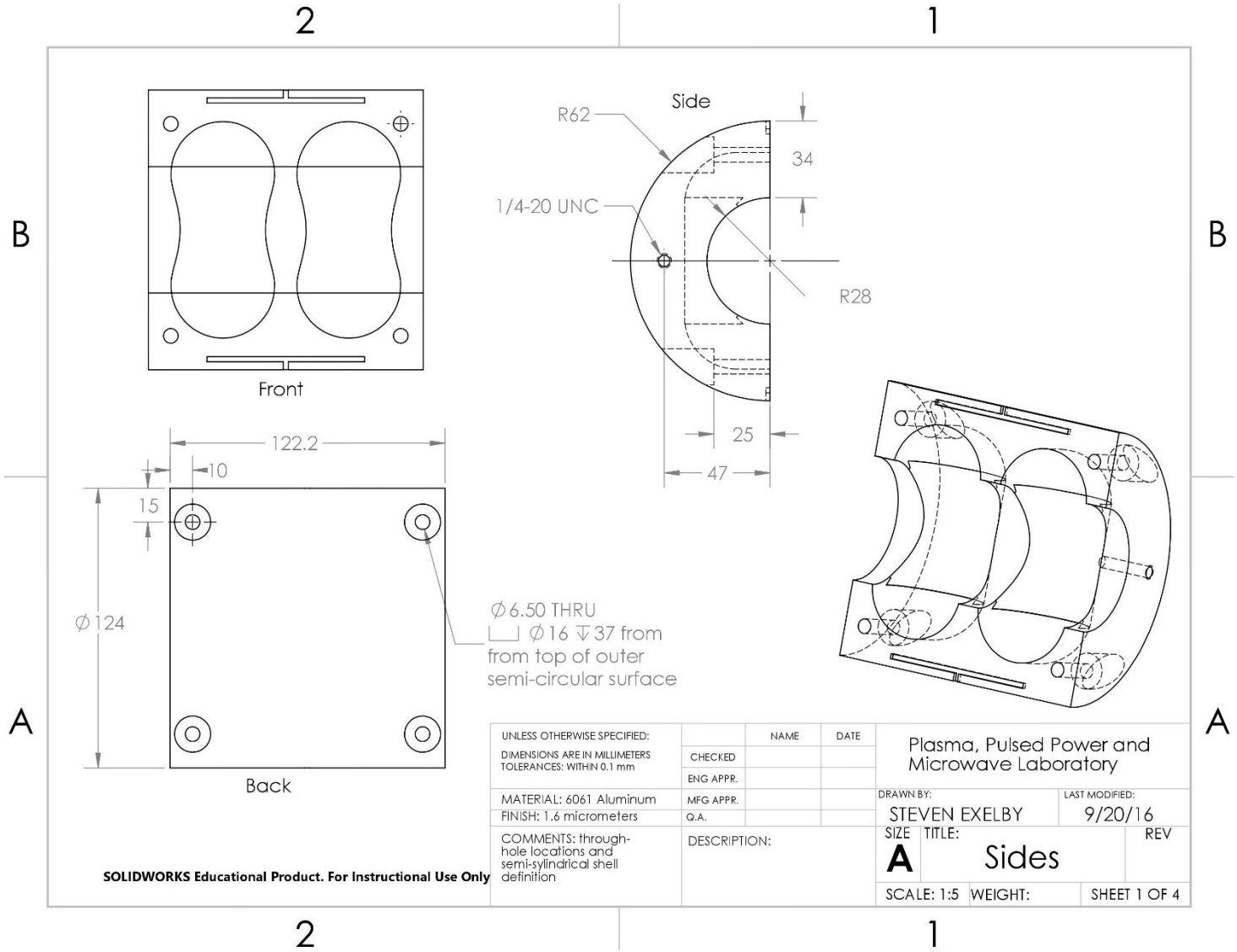

Figure C.3a: Cylindrical side pieces of the RPCFA inner housing, page 1.

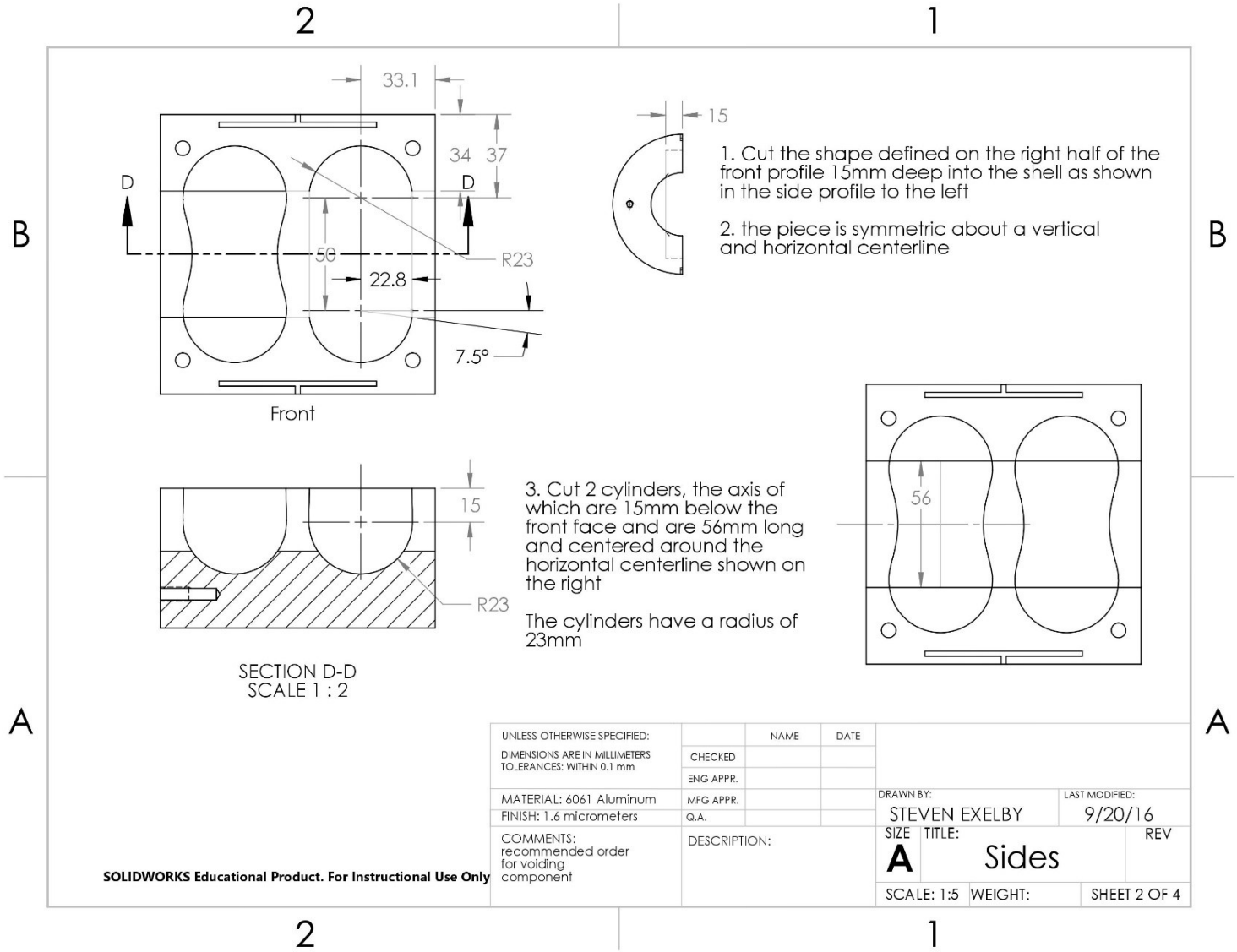

Figure C.3b: Cylindrical side pieces of the RPCFA inner housing, page 2.

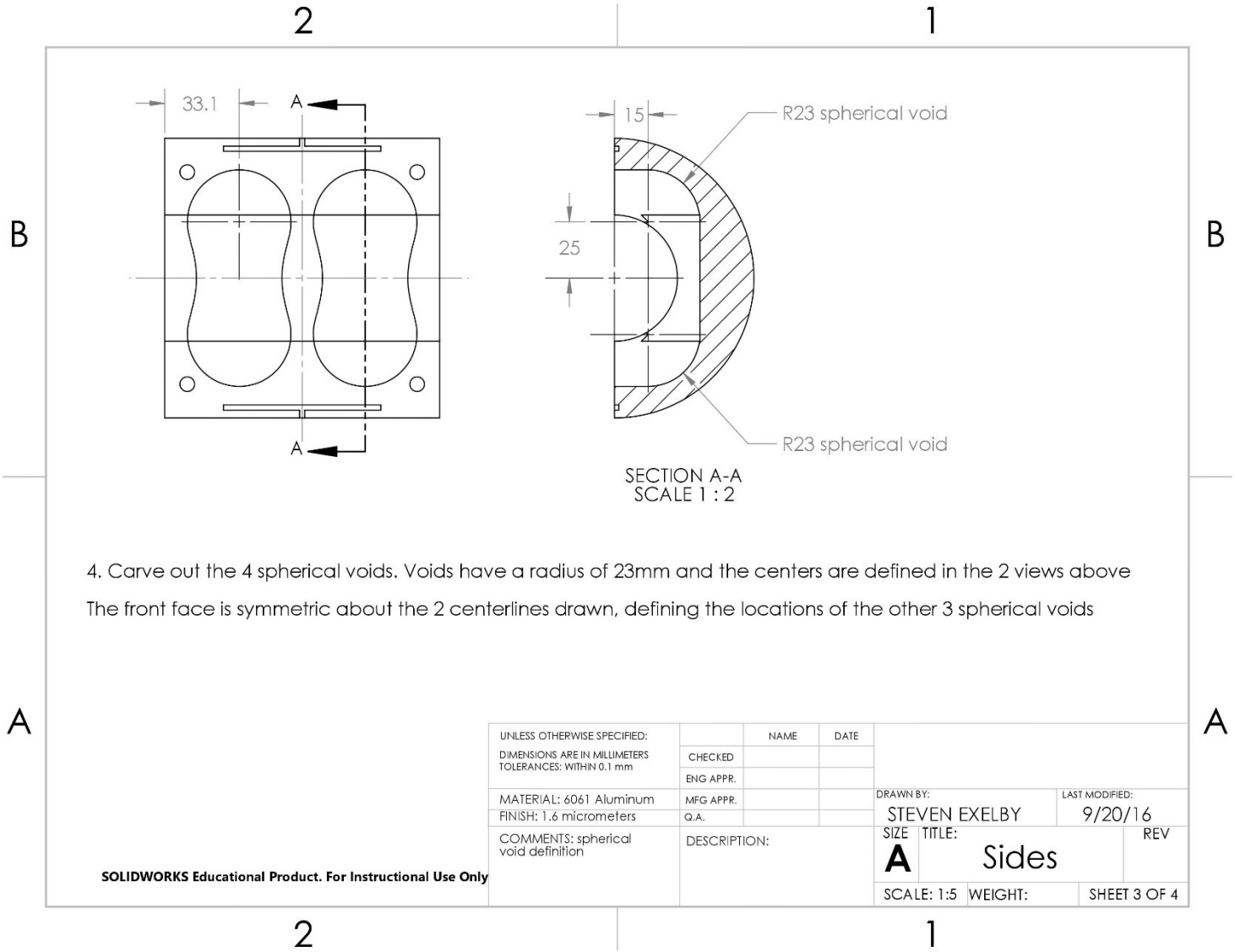

Figure C.3c: Cylindrical side pieces of the RPCFA inner housing, page 3.

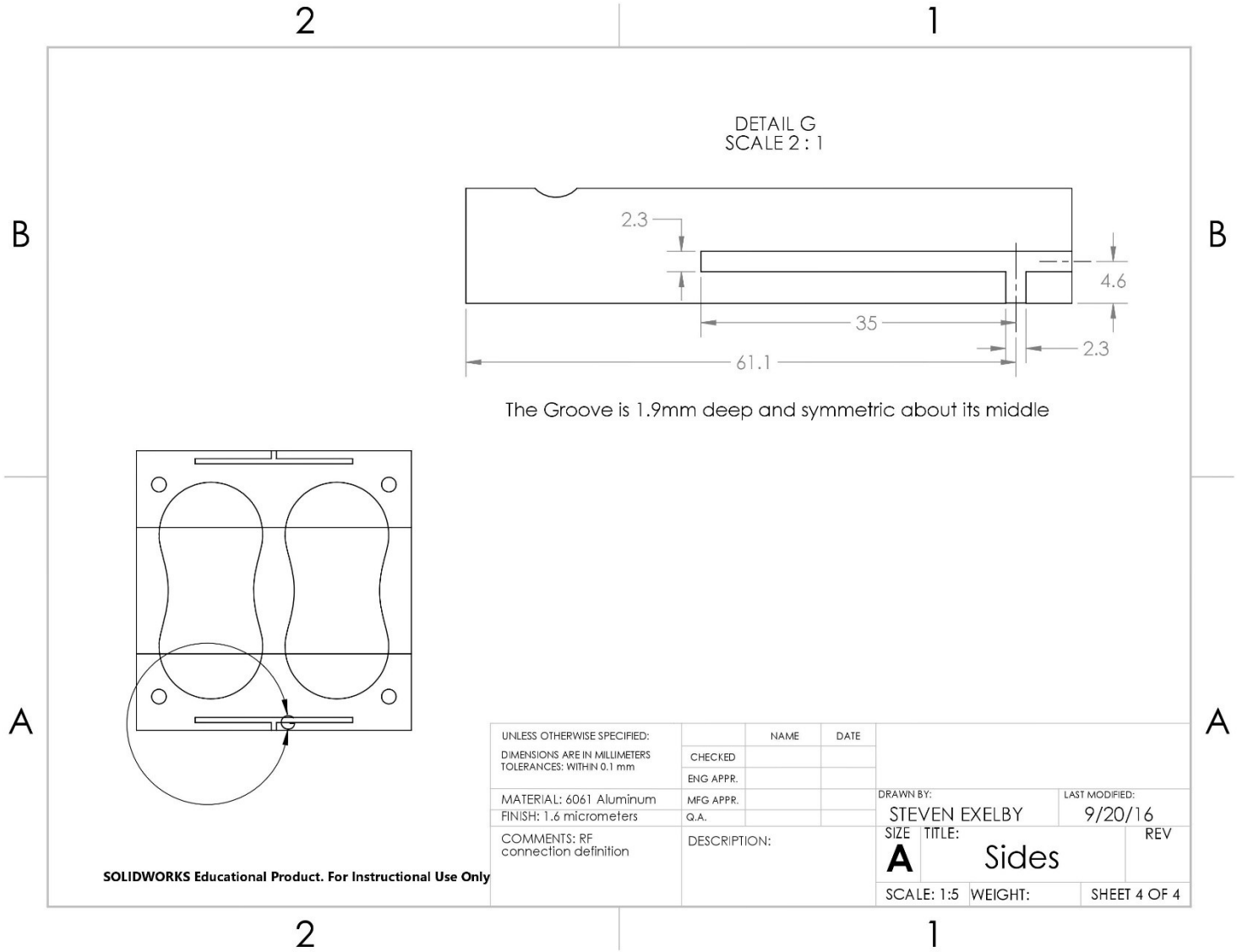

Figure C.3d: Cylindrical side pieces of the RPCFA inner housing, page 4.

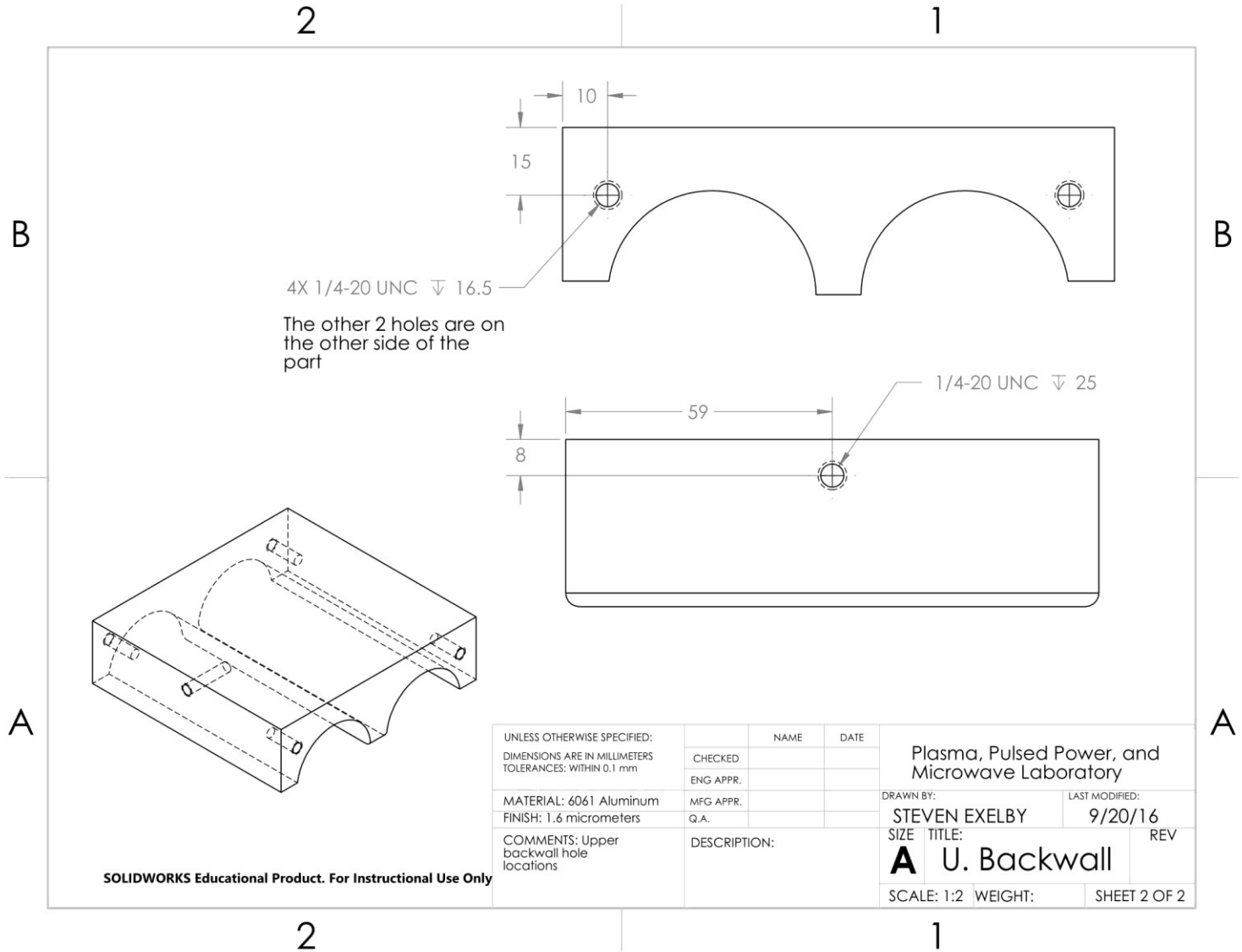

Figure C.4a: Smooth bore planar section of RPCFA inner housing, page 1.

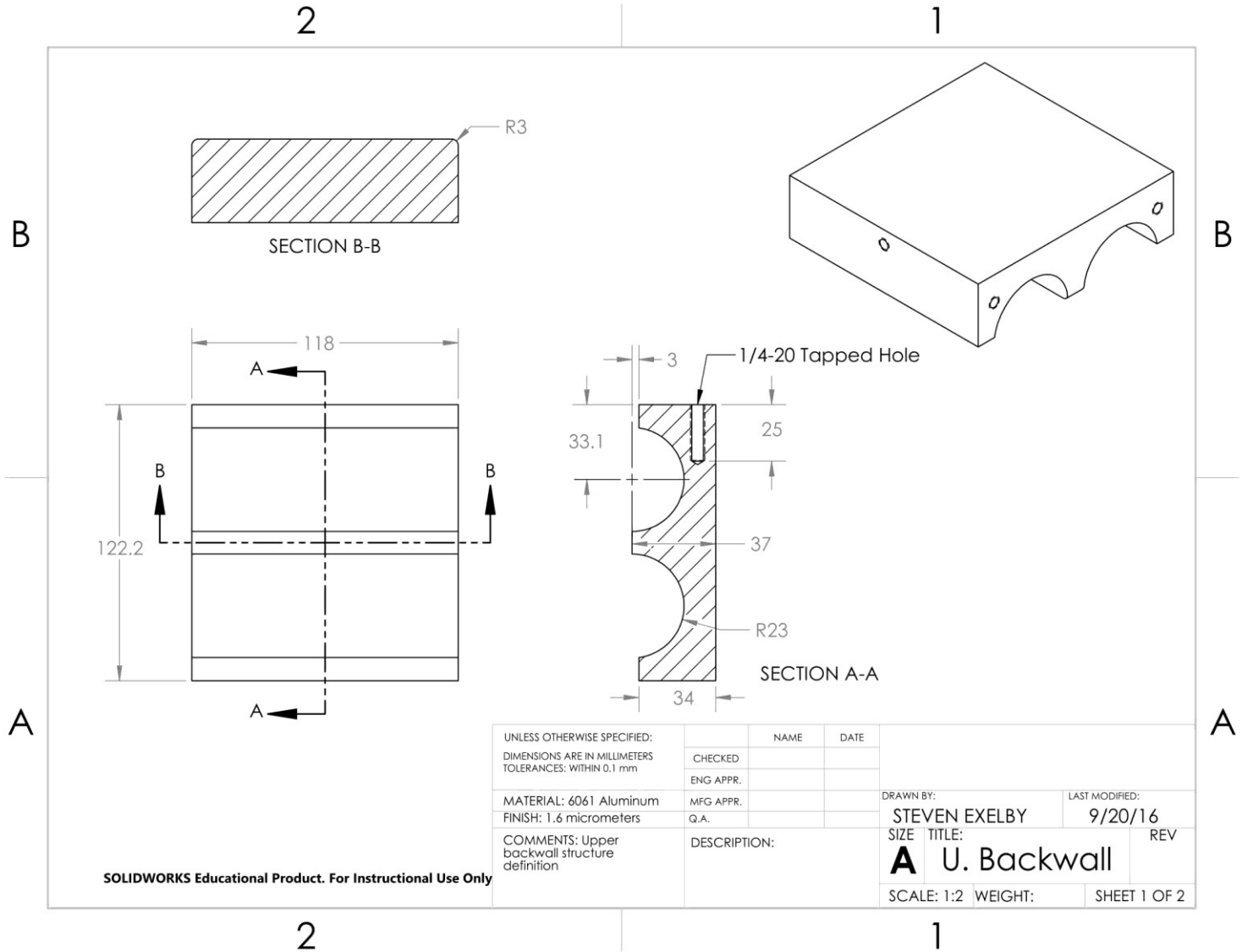

Figure C.4b: Smooth bore planar section of RPCFA inner housing, page 2.

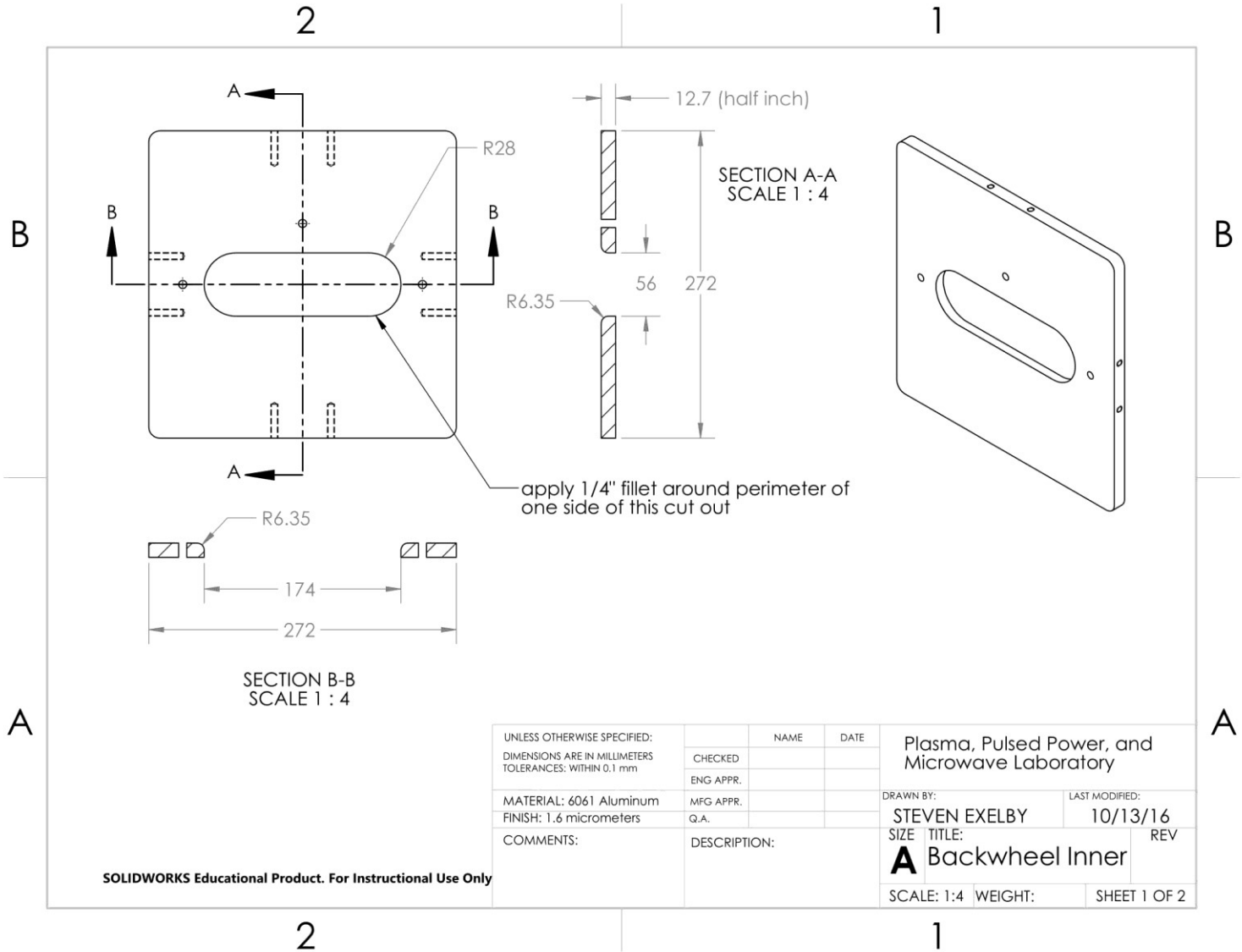

Figure C.5a: Center piece of the back wheel that locks the inner housing into position, page 1.

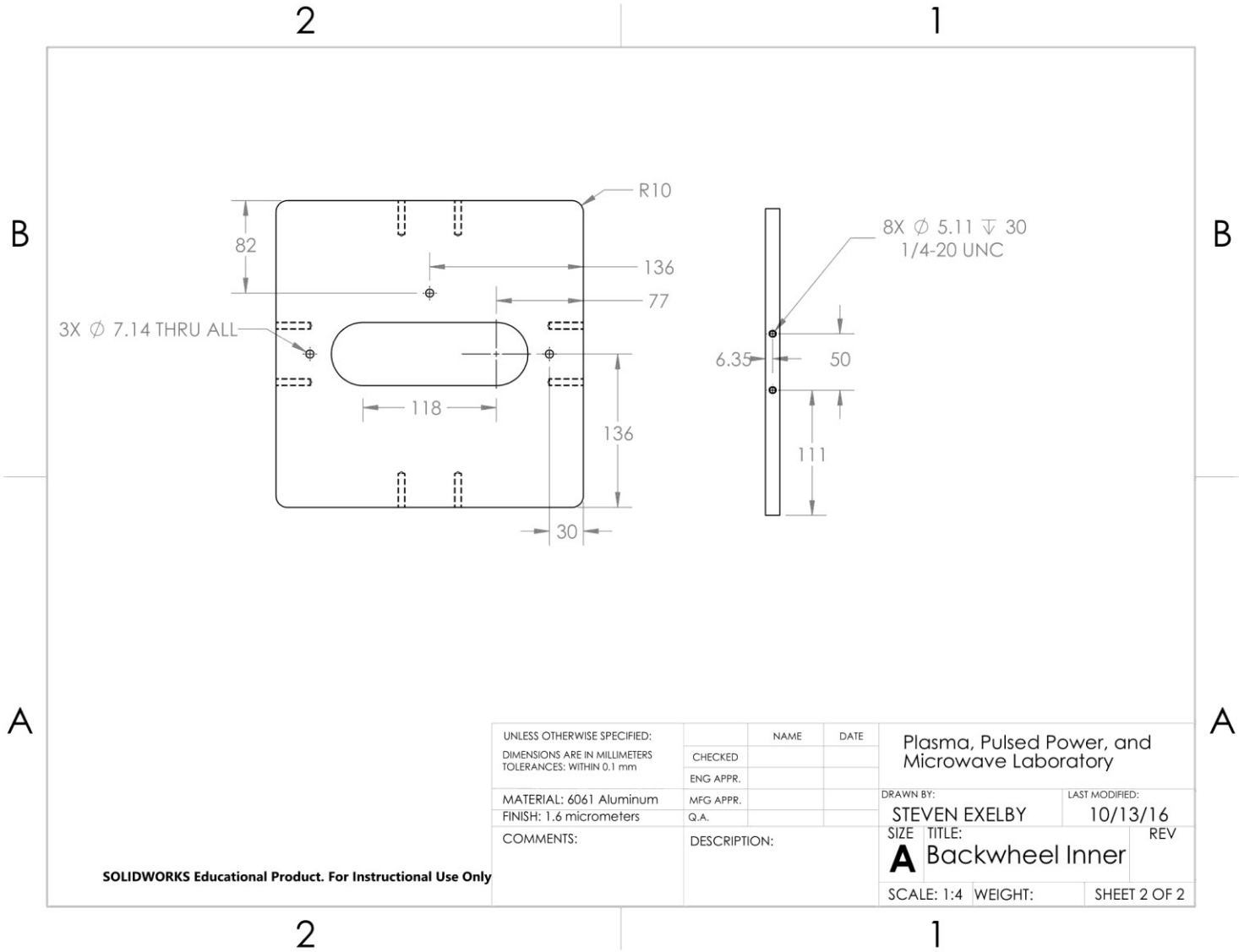

Figure C.5b: Center piece of the back wheel that locks the inner housing into position, page 2.

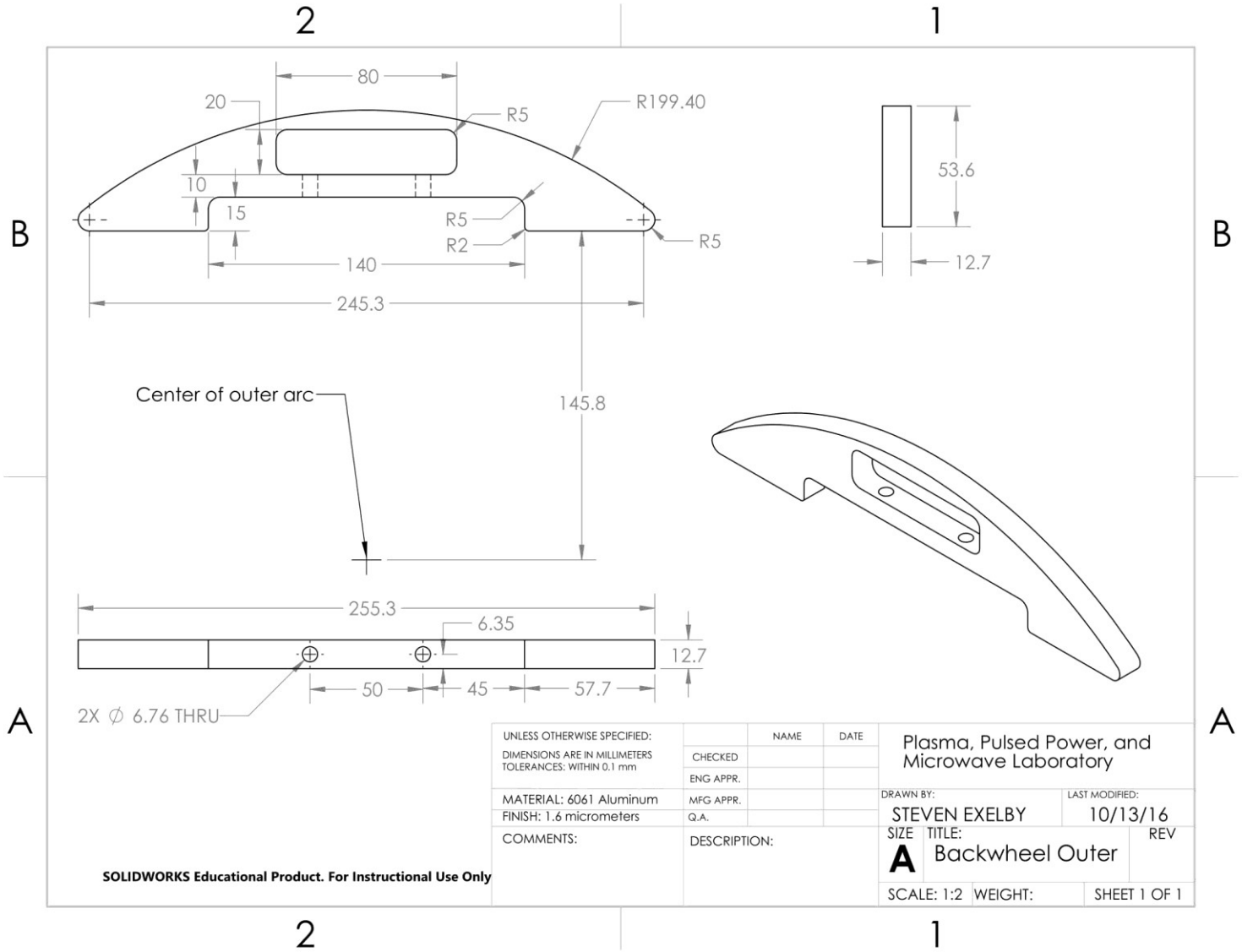

Figure C.6: Outer piece of the back wheel. Four of these surround the center piece on threaded ¼” rods lock the RPCFA into position.

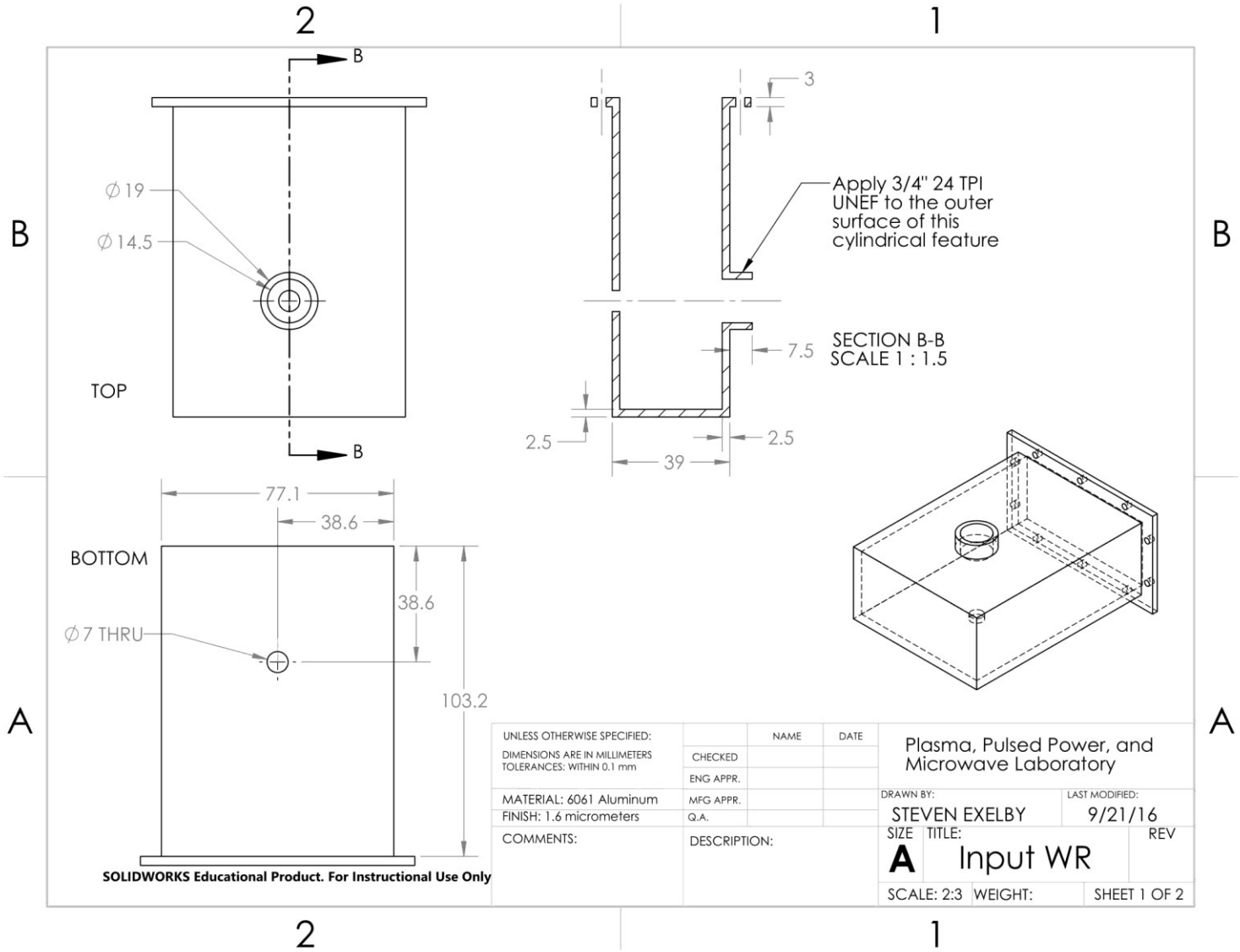

Figure C.7a: Input side waveguide to RPCFA adaptor. A puck coupler is bolted through the small hole in the bottom, page 1.

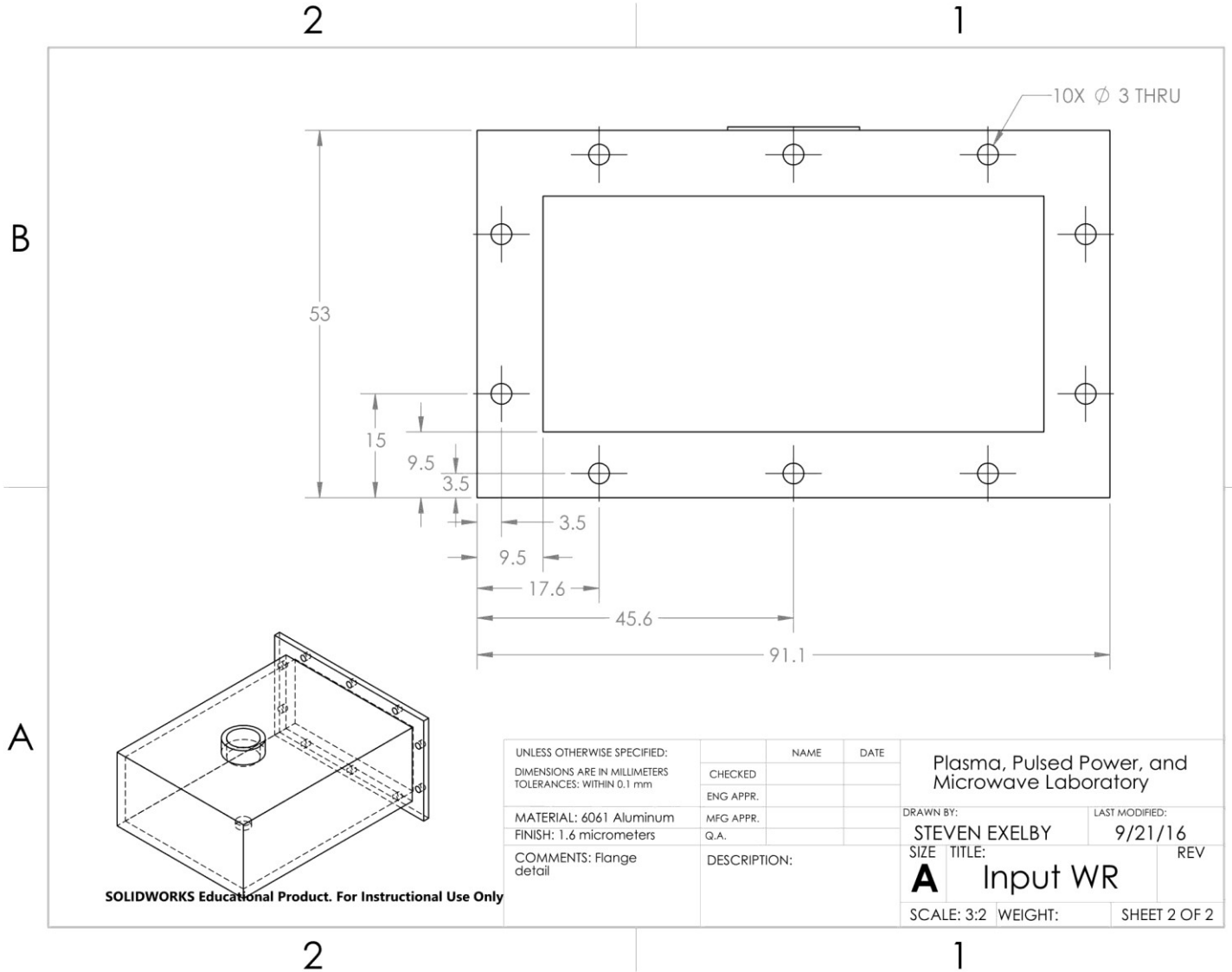

Figure C.7b: Input side waveguide to RPCFA adaptor. A puck coupler is bolted through the small hole in the bottom, page 2.

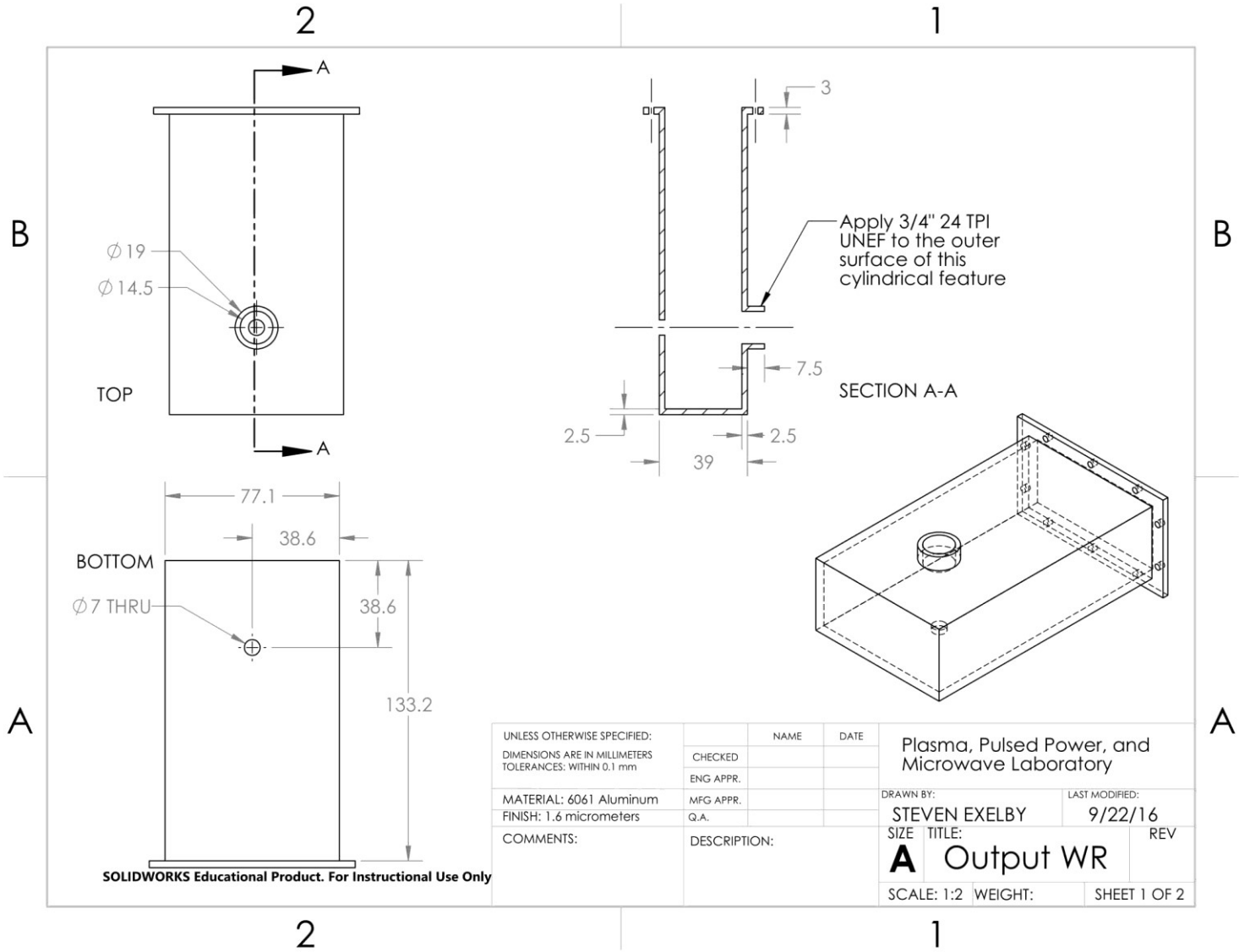

Figure C.8a: Output side waveguide to RPCFA adaptor. A puck coupler is bolted through the small hole in the bottom, page 1.

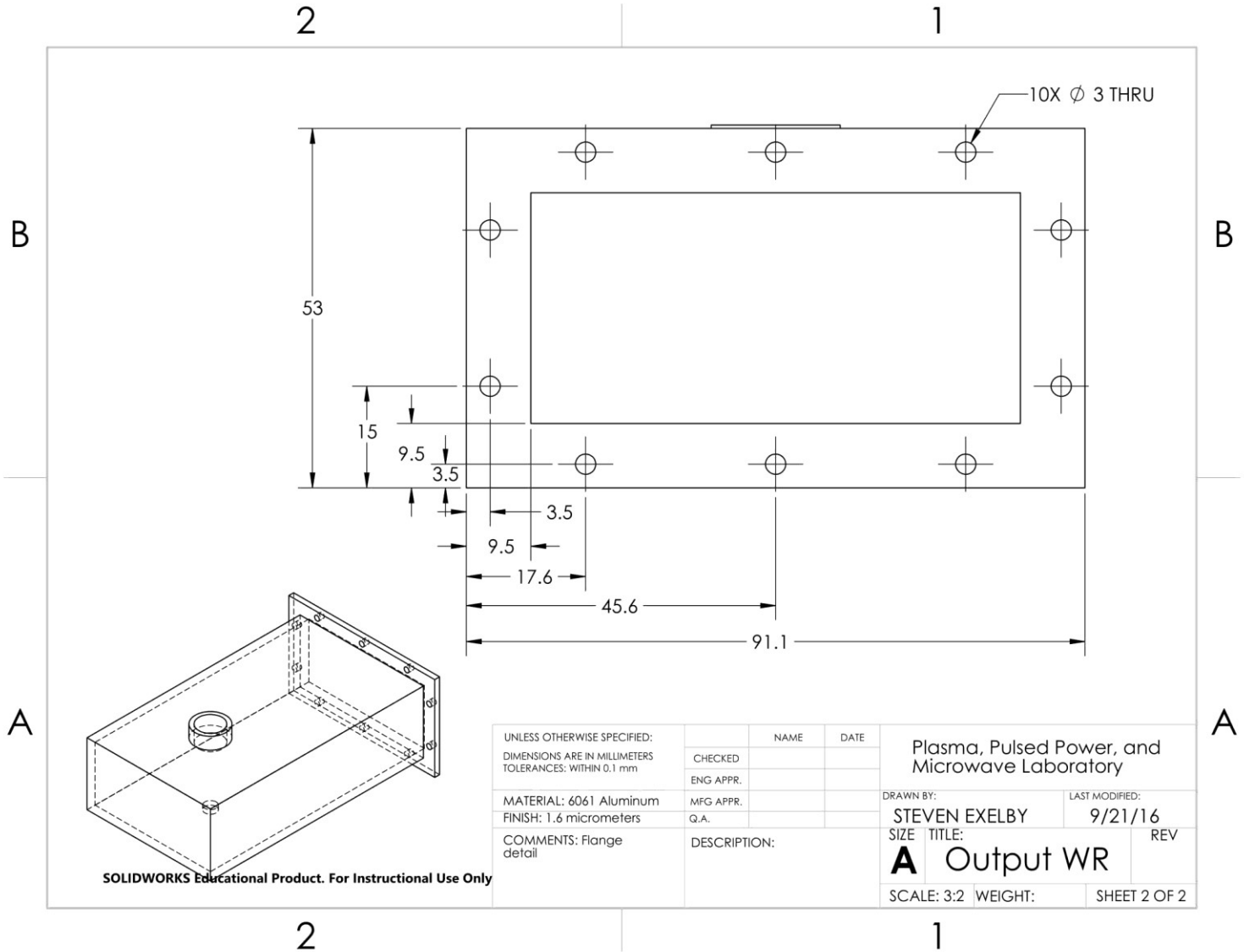

Figure C.8b: Input side waveguide to RPCFA adaptor. A puck coupler is bolted through the small hole in the bottom, page 2.

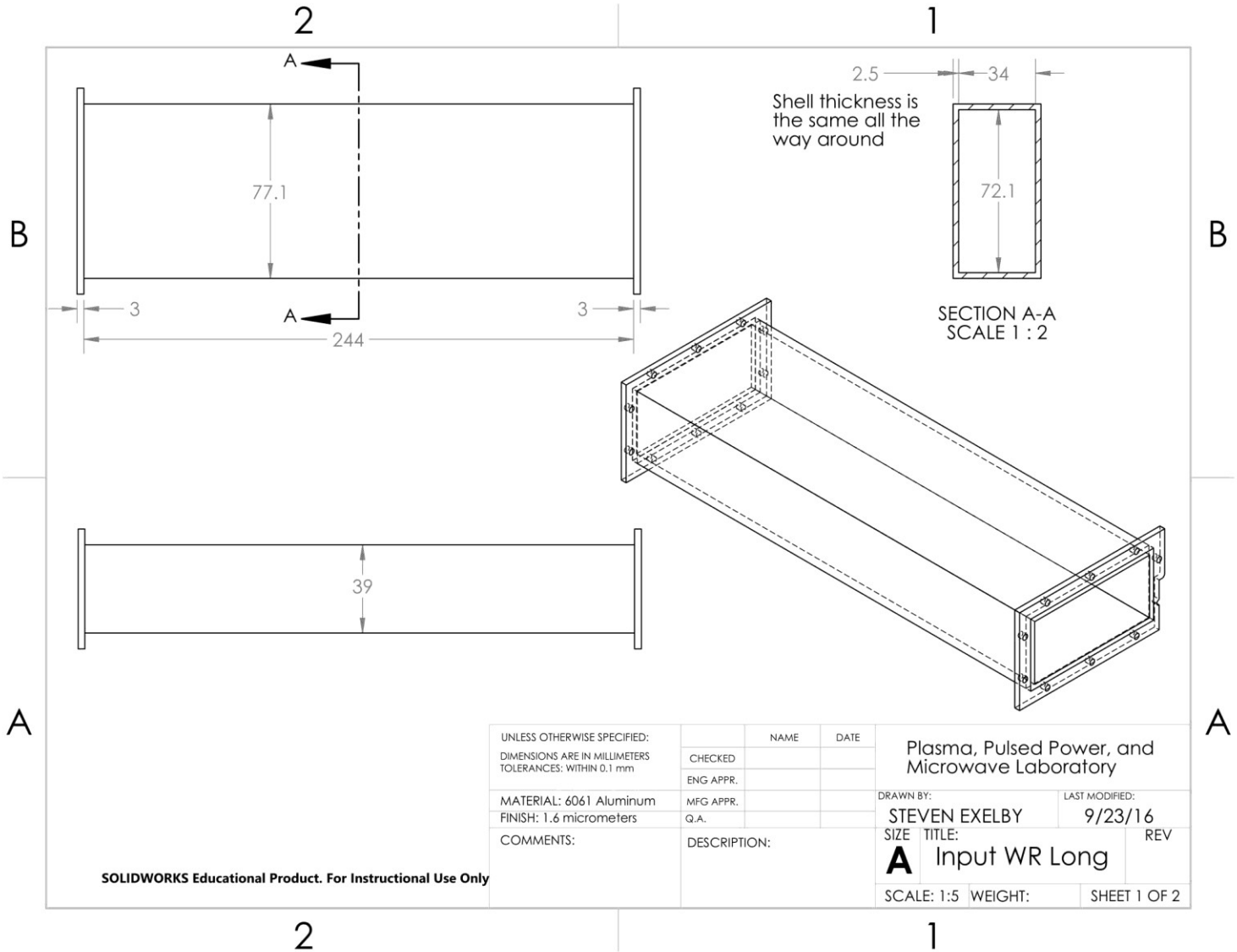

Figure C.9a: Input side waveguide (WR-284) with customized compact flange, page 1.

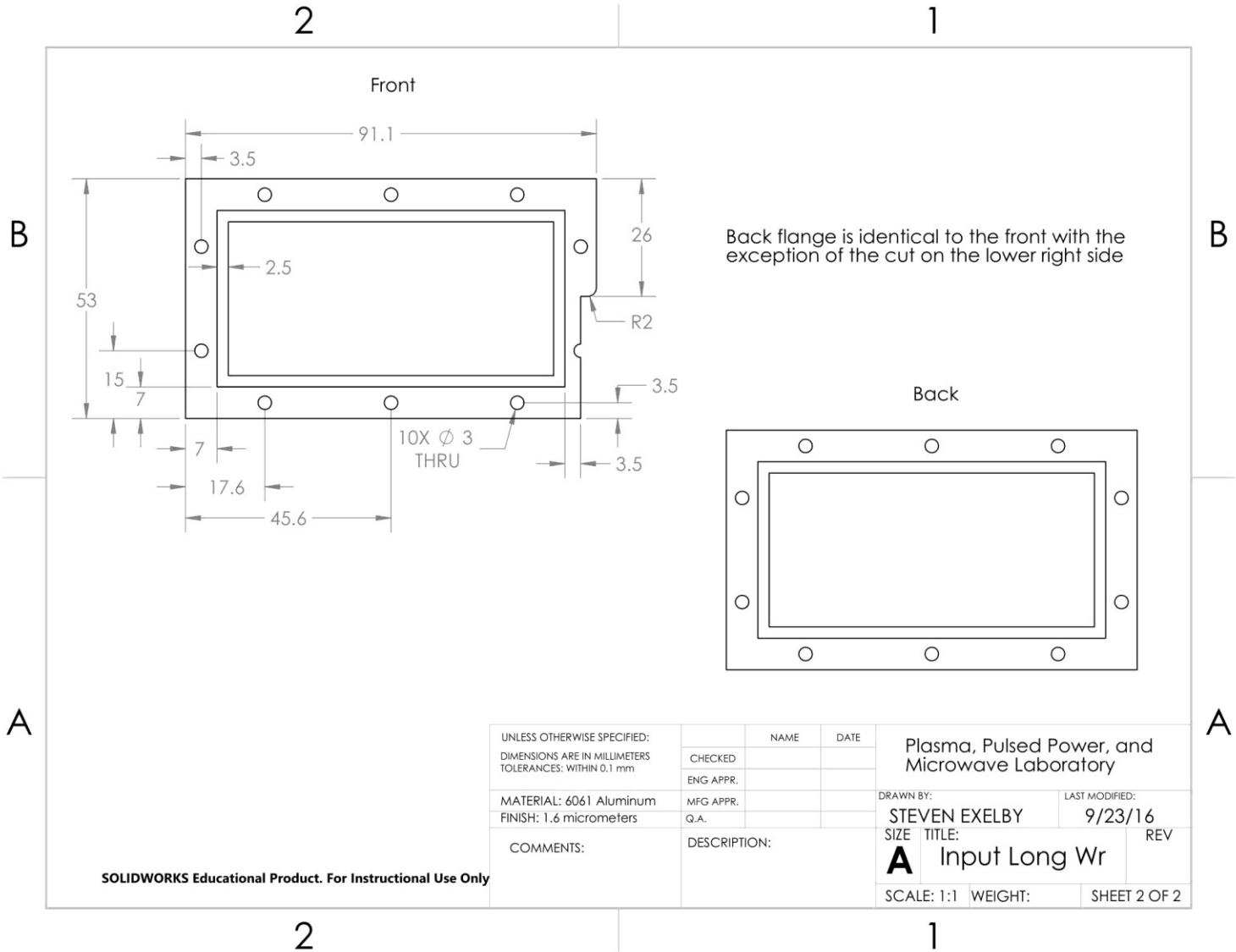

Figure C.9b: Input side waveguide (WR-284) with customized compact flange, page 2.

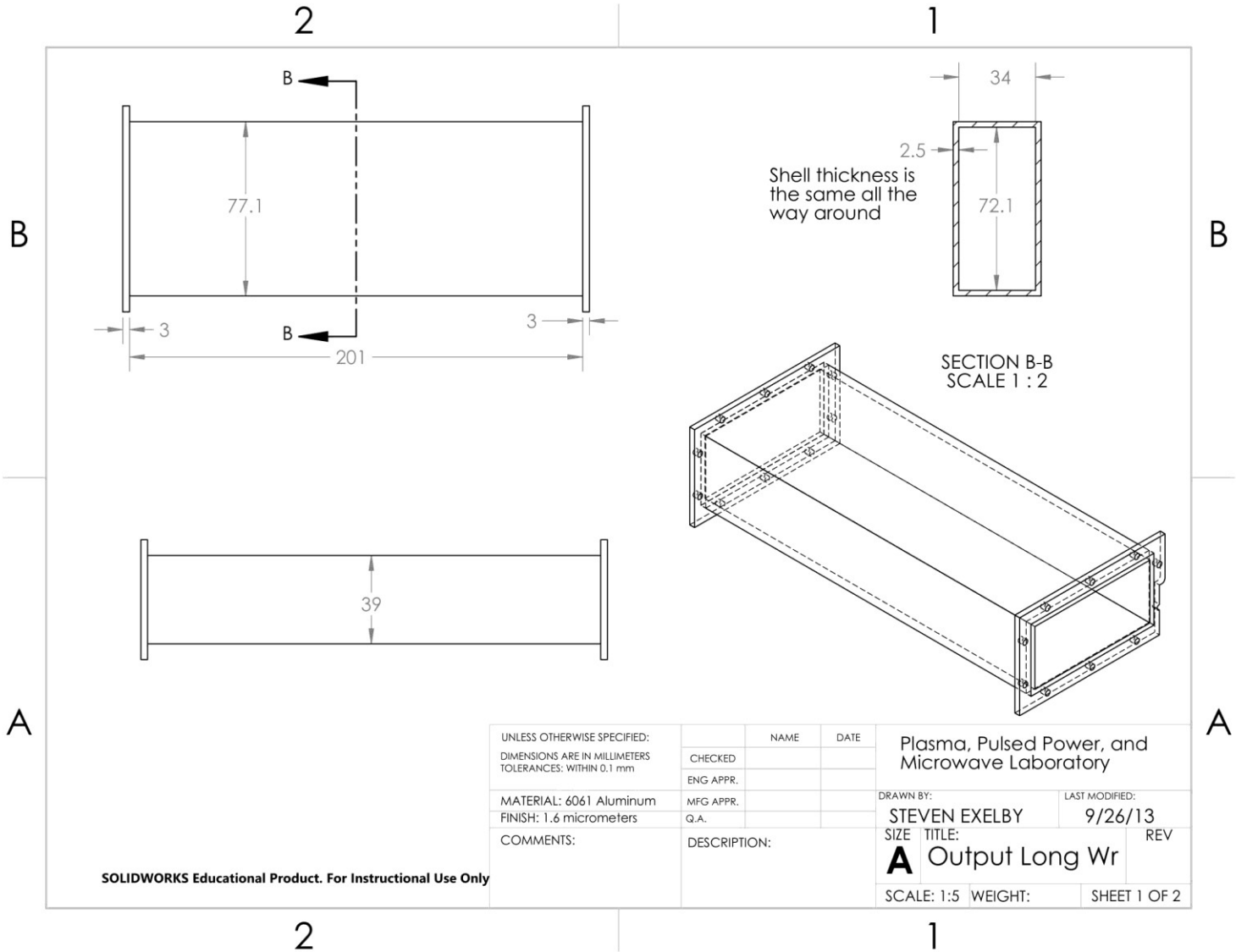

Figure C.10a: Output side waveguide (WR-284) with customized compact flange, page 1.

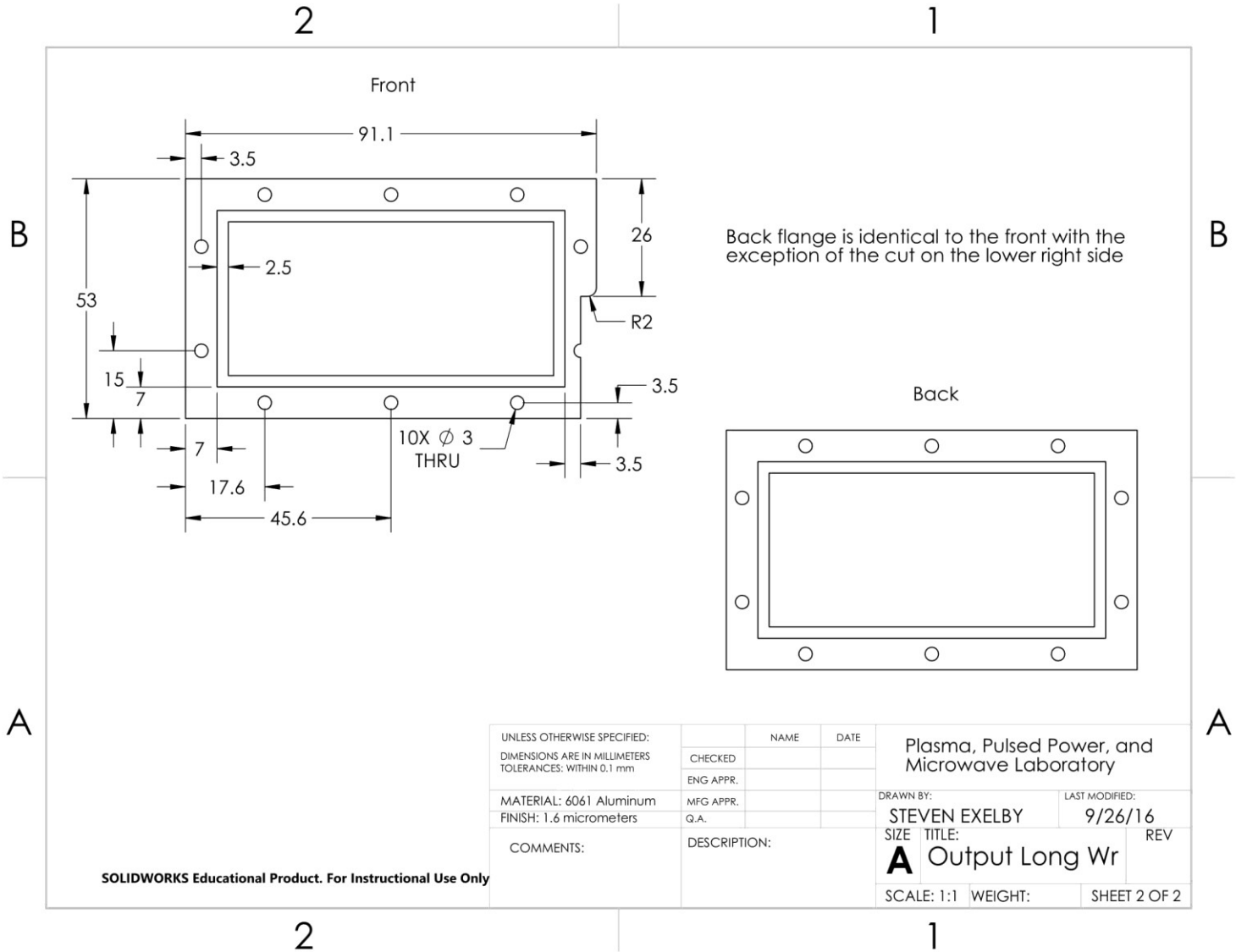

Figure C.10b: Output side waveguide (WR-284) with customized compact flange, page 2.

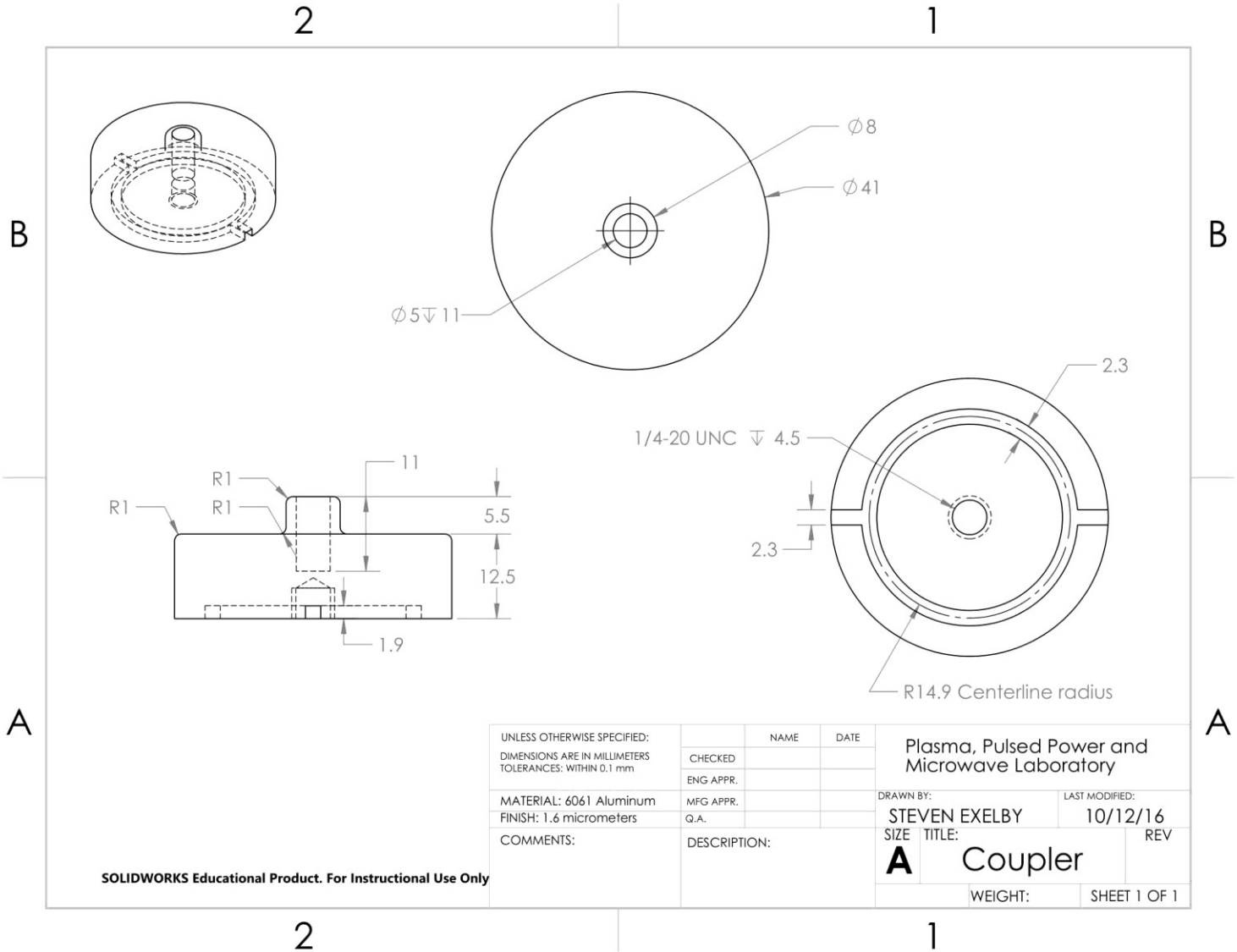

Figure C.11: Puck coupler.

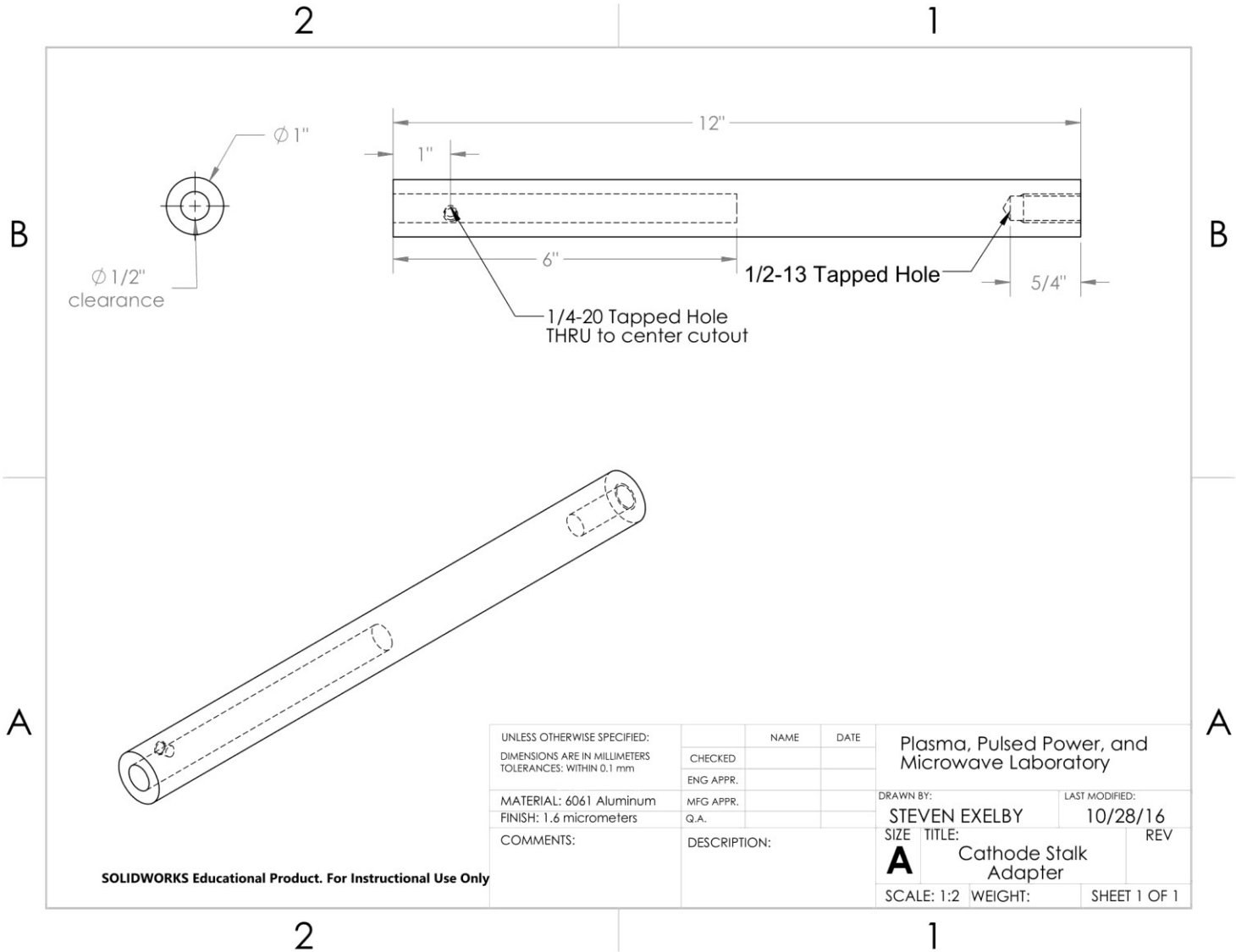

Figure C.12: Cathode stalk adaptor. Connects the MELBA cathode stalk to a ½" rod for mounting a cathode with variable z-axis positioning.

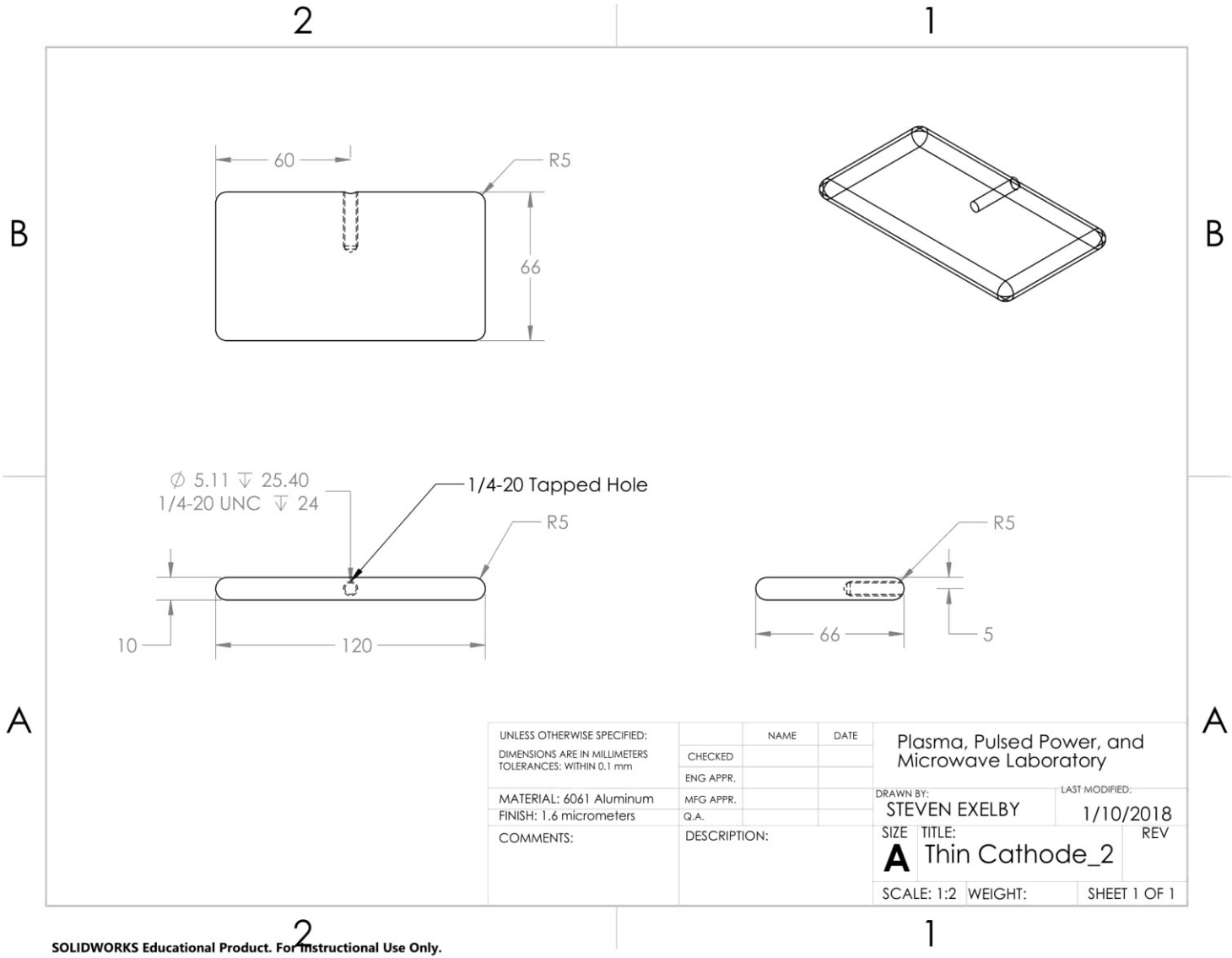

Figure C.13: Planar cathode. Fundamental shape used for all experiments.

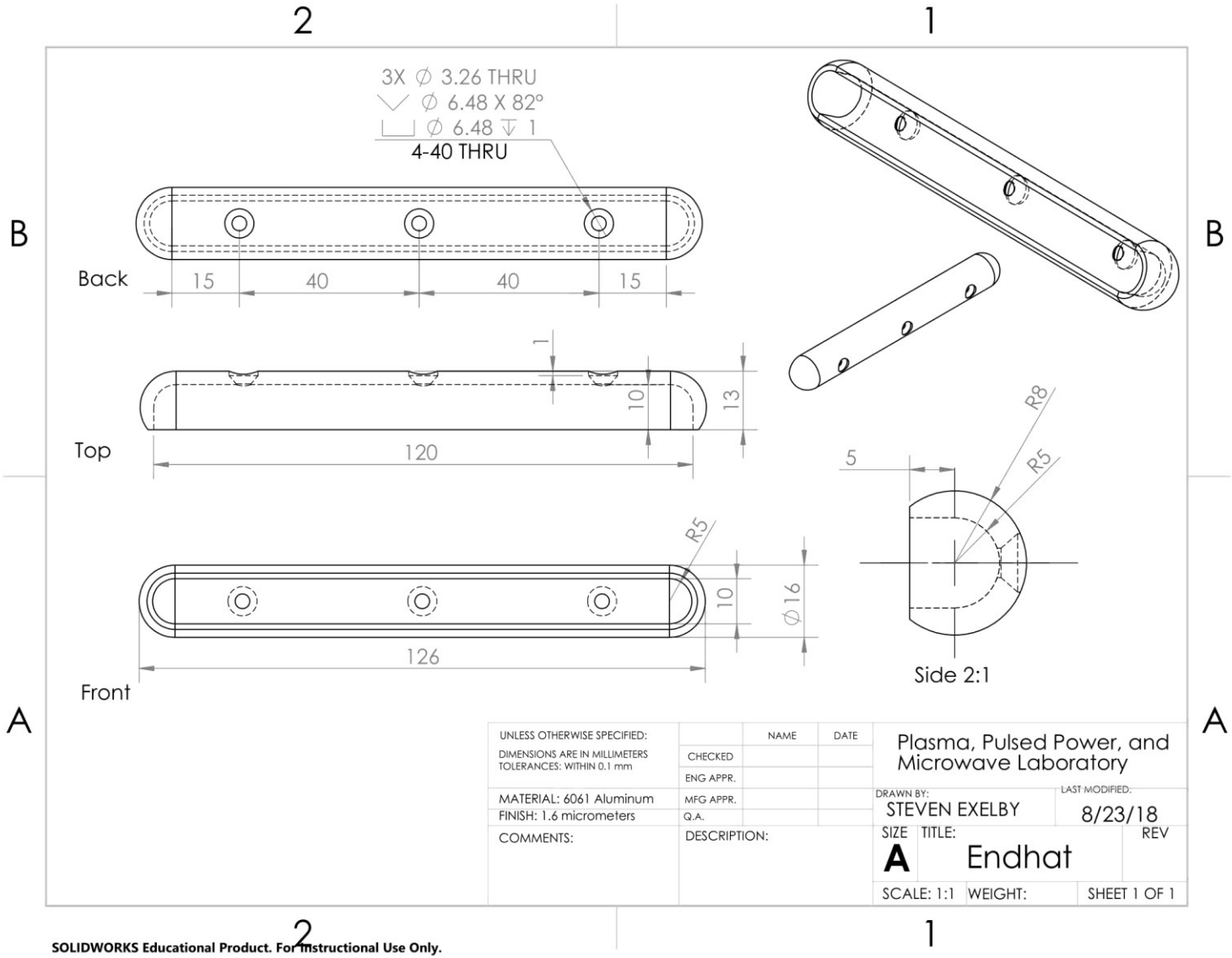

Figure C.14: Cathode endhat, mounted to front of planar cathode.

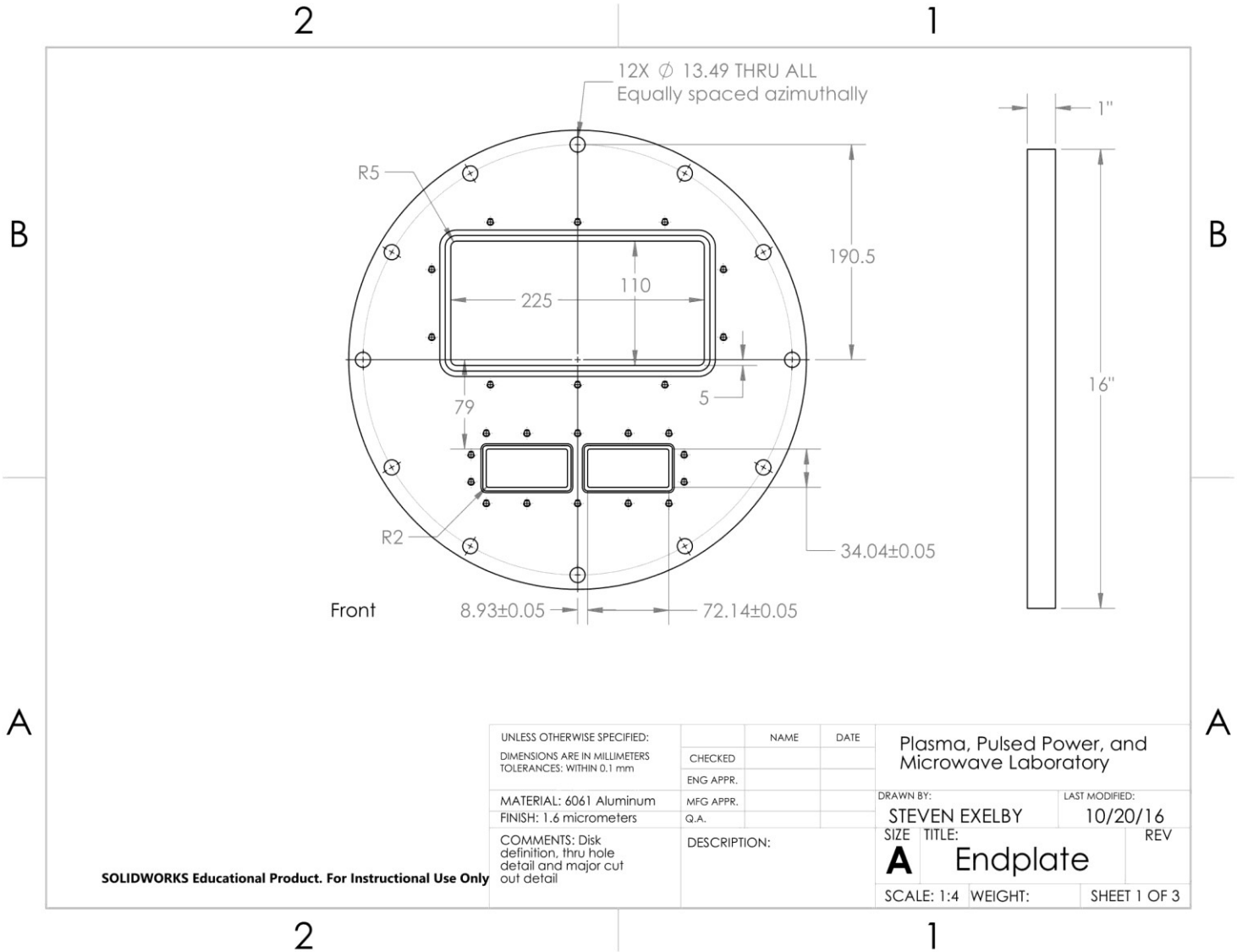

Figure C.15a: Endplate. Connects the interior vacuum waveguide to the exterior RF circuitry, page 1.

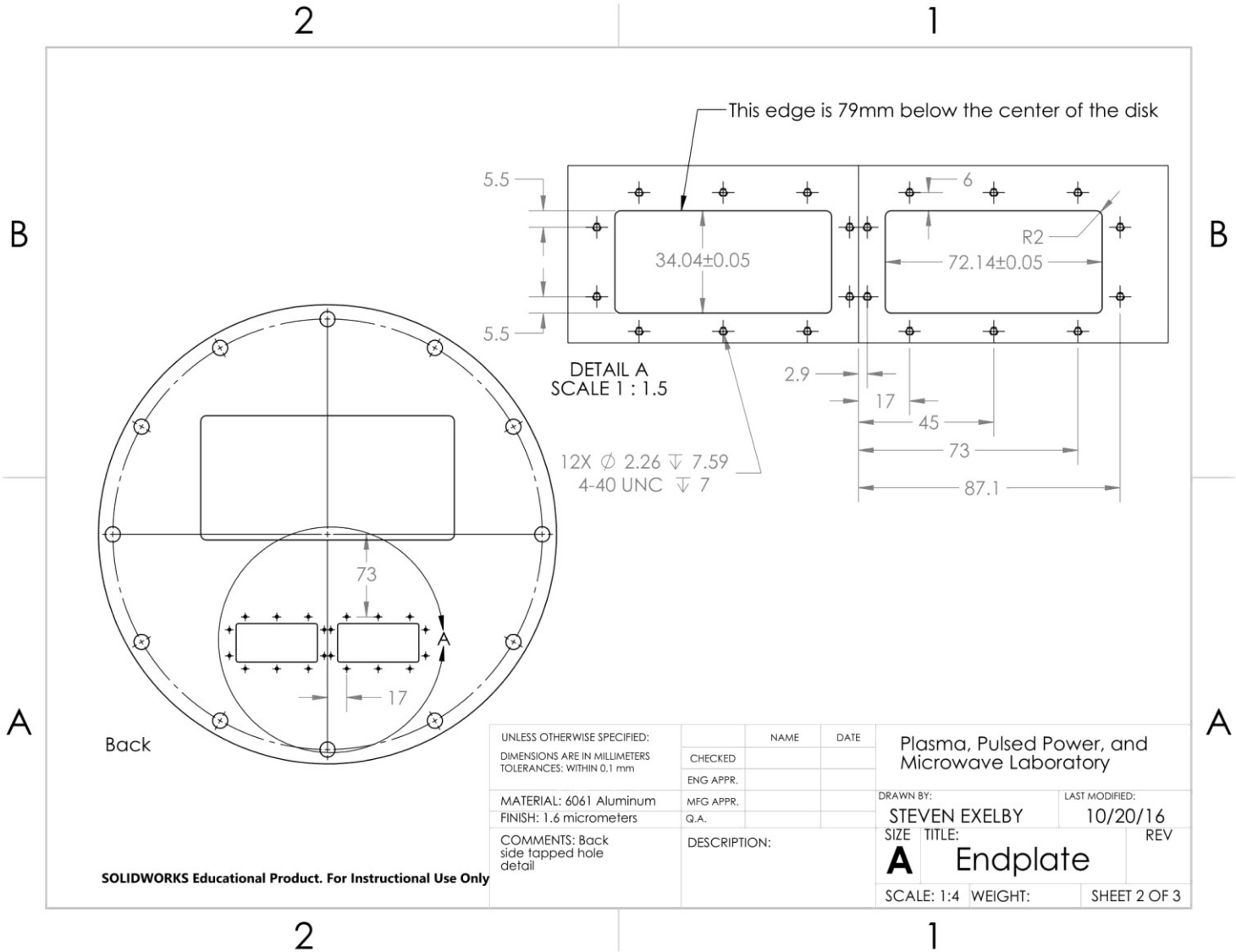

Figure C.15b: Endplate. Connects the interior vacuum waveguide to the exterior RF circuitry, page 2.

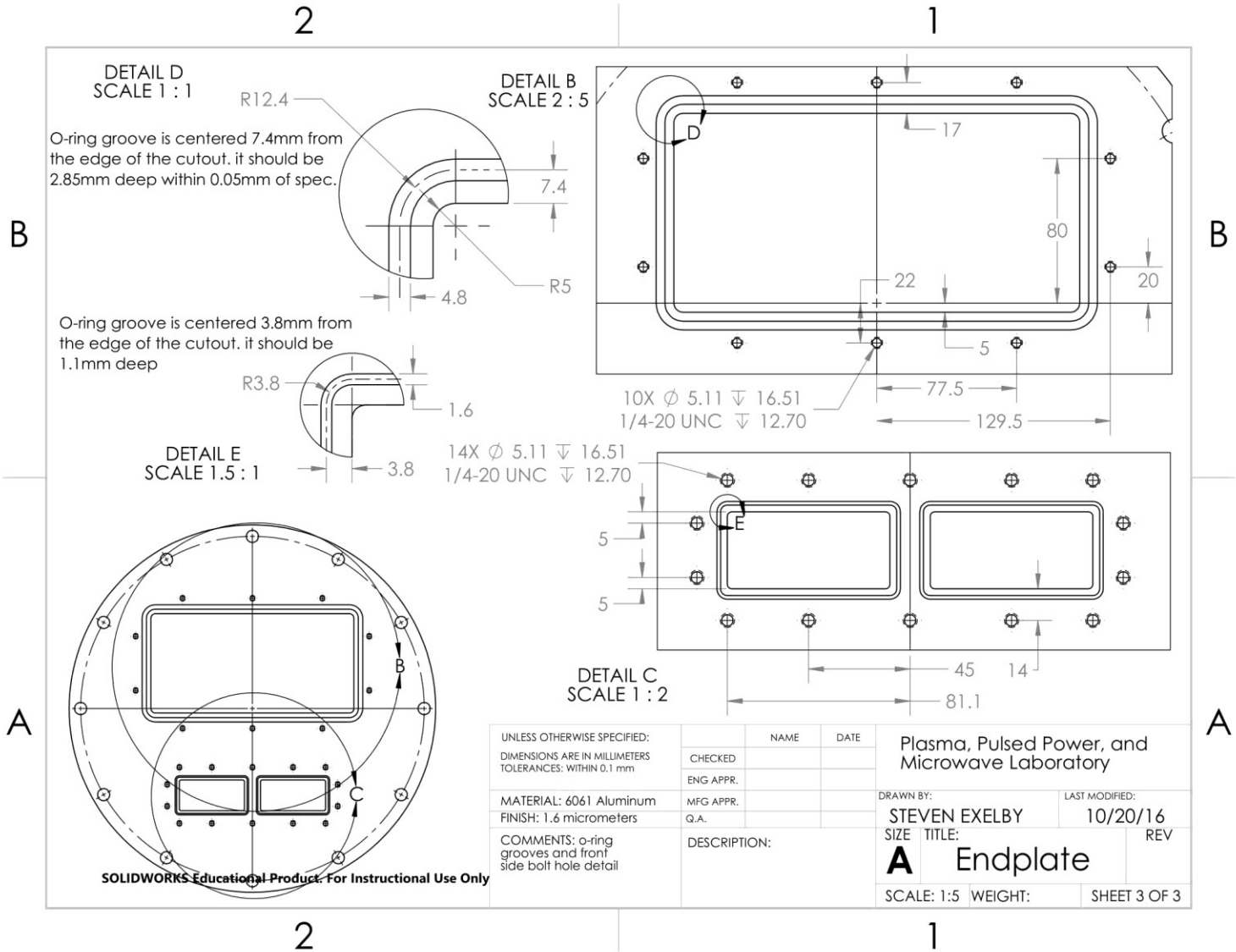

Figure C.15c: Endplate. Connects the interior vacuum waveguide to the exterior RF circuitry, page 3.

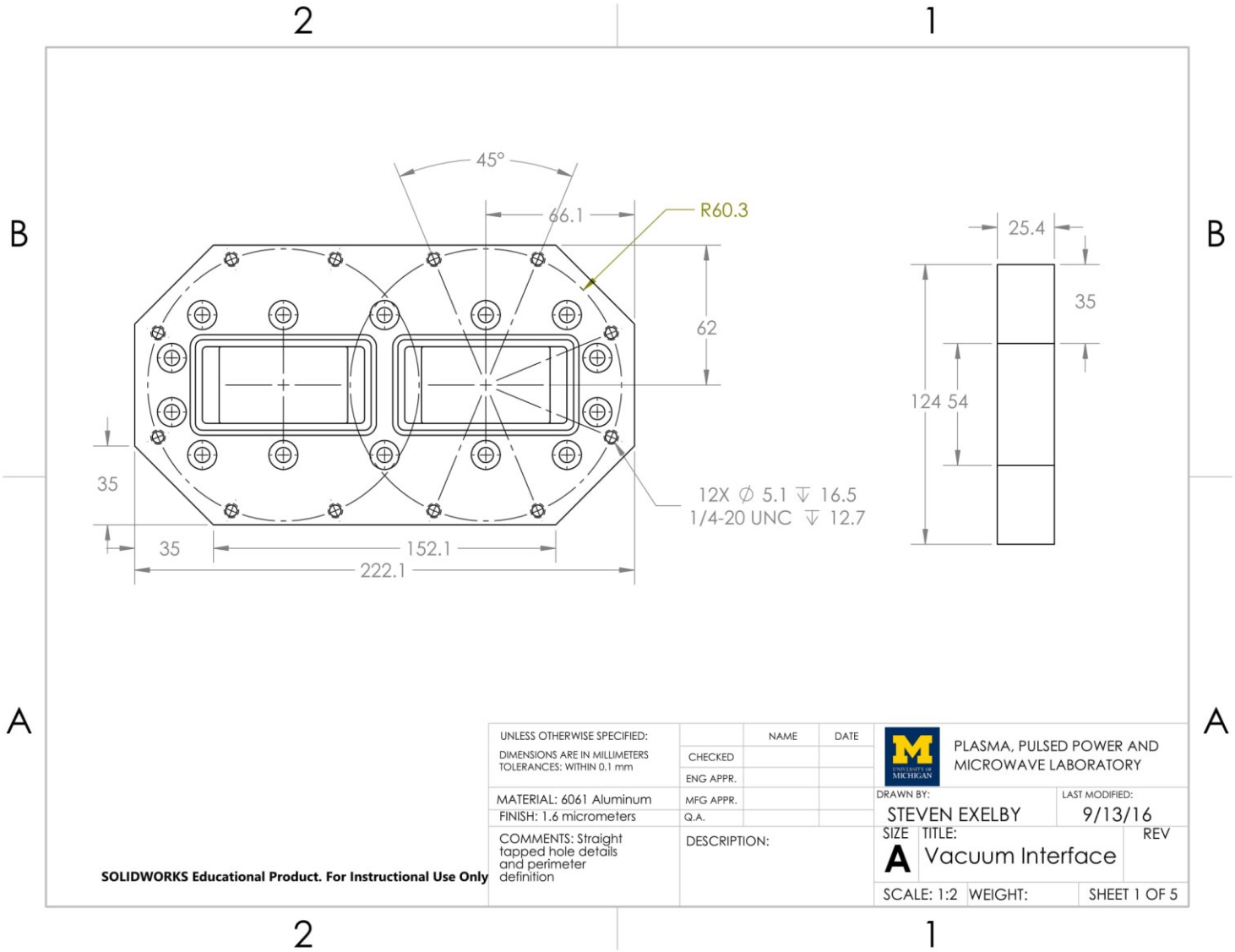

Figure C.16a: Vacuum interface, a 2mm thick lexan window is mounted between this piece and the endplate to make the vacuum window. Page 1.

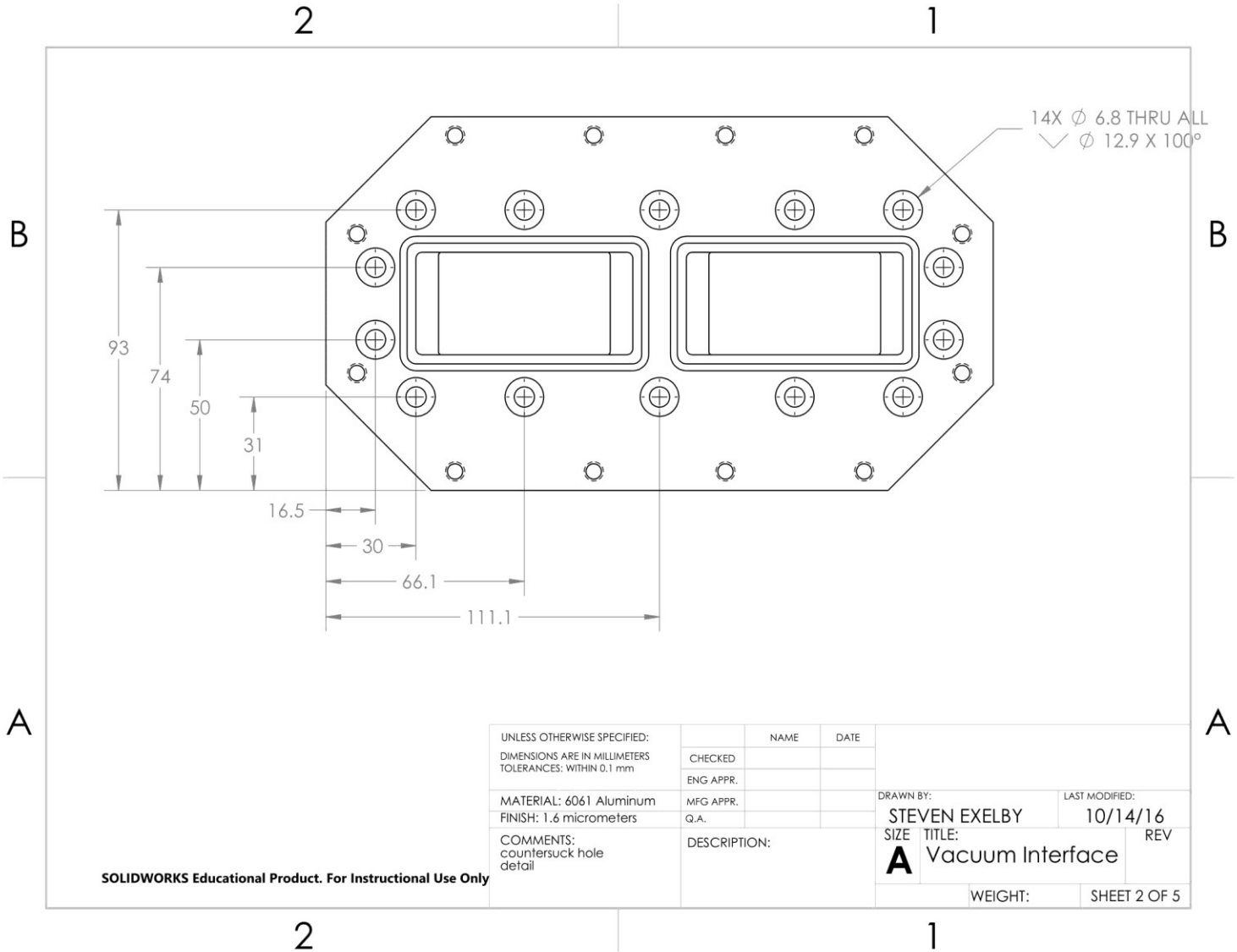

Figure C.16b: Vacuum interface, a 2mm thick lexan window is mounted between this piece and the endplate to make the vacuum window. Page 2.

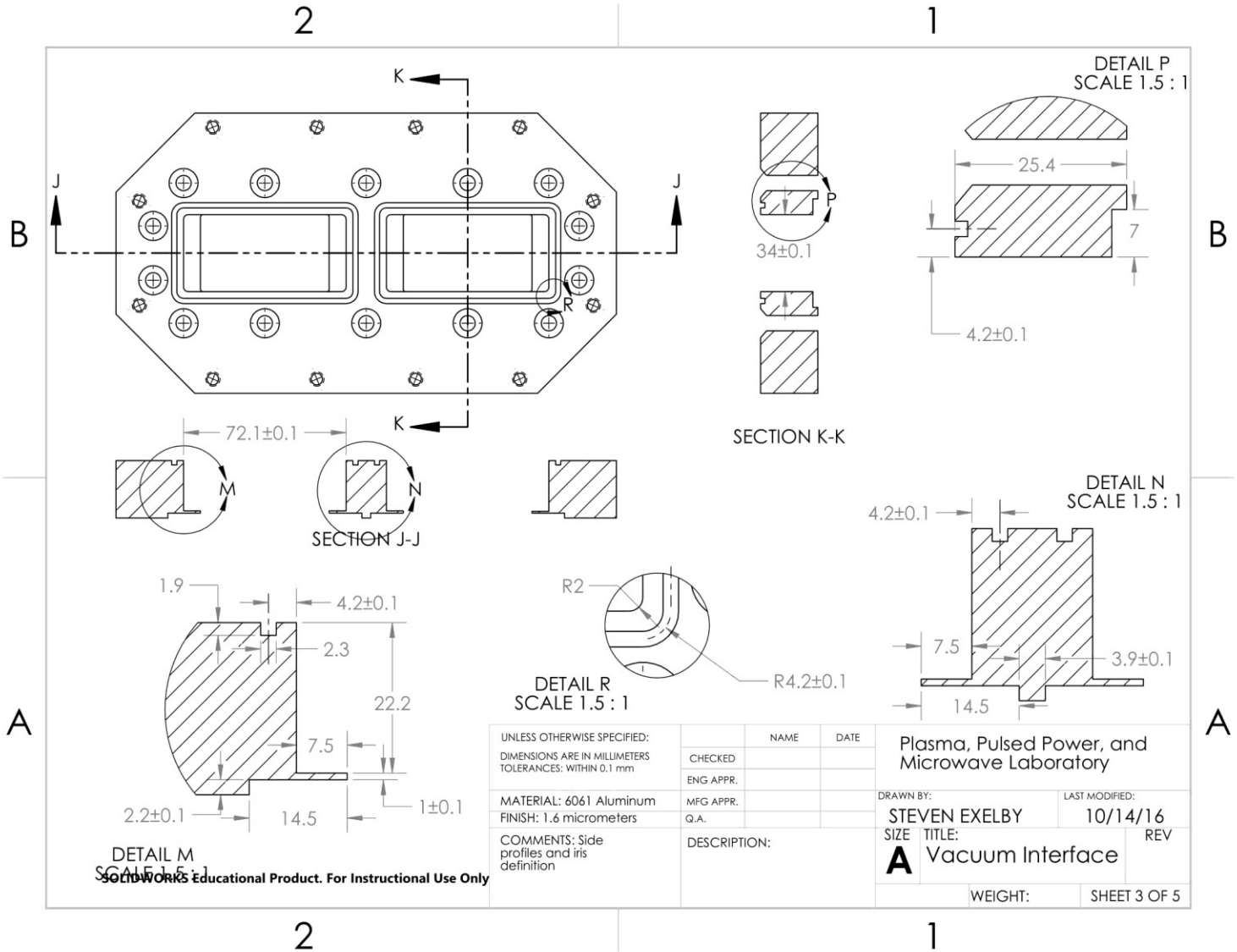

Figure C.16c: Vacuum interface, a 2mm thick lexan window is mounted between this piece and the endplate to make the vacuum window. Page 3.

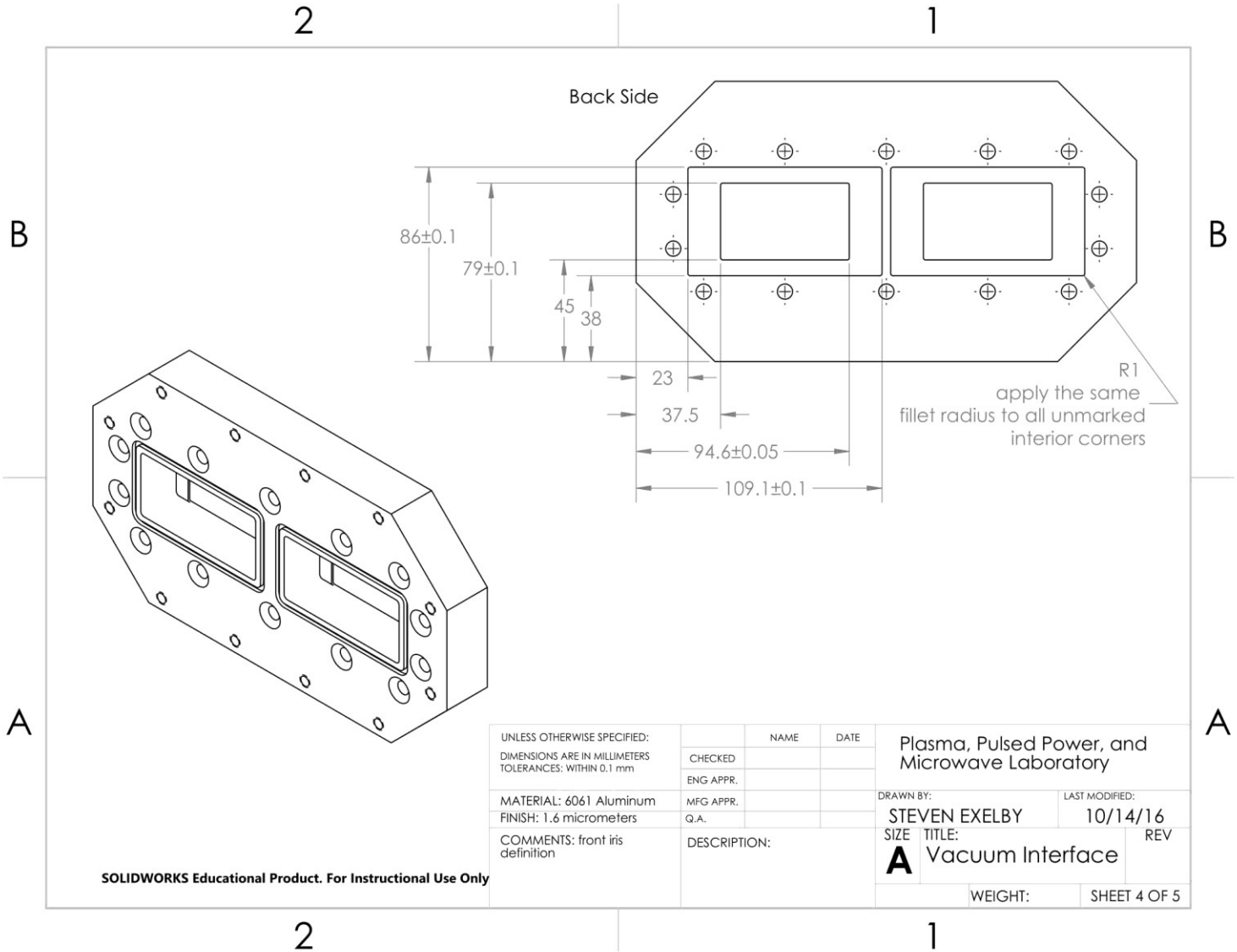

Figure C.16d: Vacuum interface, a 2mm thick lexan window is mounted between this piece and the endplate to make the vacuum window. Page 4.

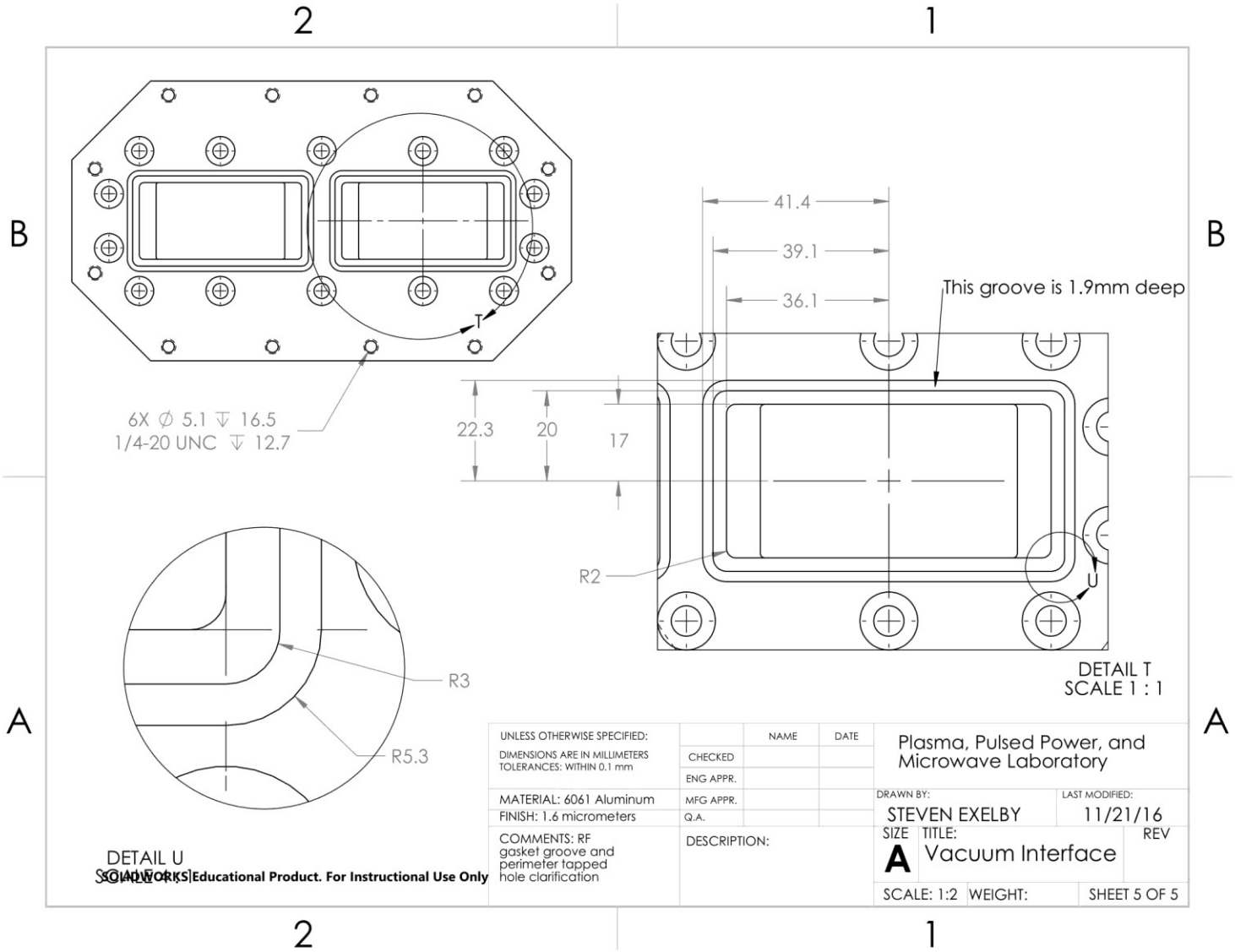

Figure C.16e: Vacuum interface, a 2mm thick lexan window is mounted between this piece and the endplate to make the vacuum window. Page 5.

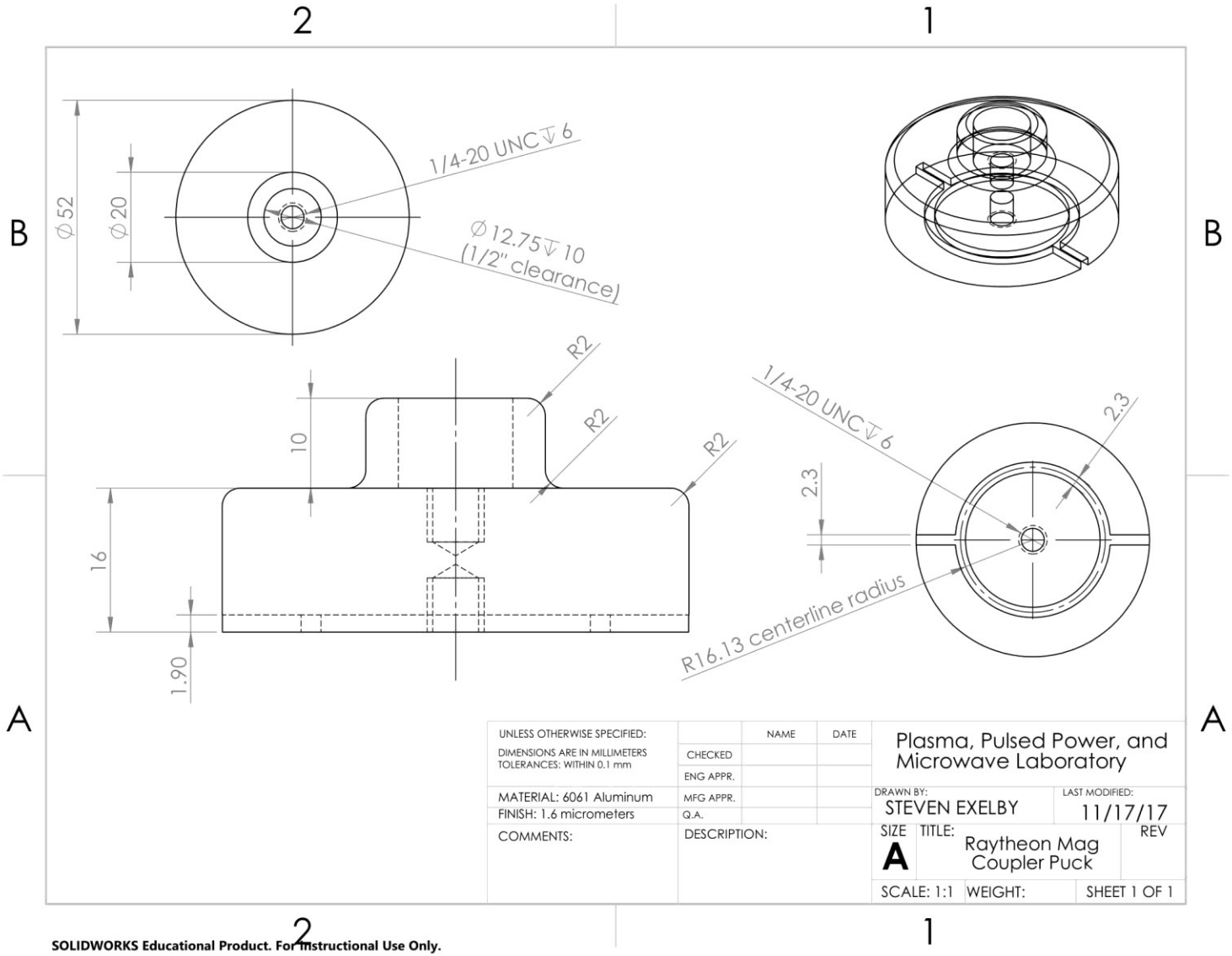

Figure C.17: Coupler puck used to extract power from the Raytheon 4J32 magnetron.

Appendix D

Analysis of Demodulation and Harmonic Beam Content

A measurement of the current passing perpendicular to the DC electric field was made in 3 points around the interaction space to observe the RF content of Brillouin hub and the effectiveness of the device in demodulating it. Rectangular loops were drawn normal to the x-direction in Figure D.1. These loops are the height of the A-K gap (in y) and the depth of the cathode (in z), thus collecting all particles travelling in the x-direction at the marked locations in the interaction space. By measuring the current over time through these loops, the claim that the recirculating bends effectively demodulate the hub can be verified. The currents measured through loops 1, 2, and 3 are given in Figures D.2a, D.2b, and D.2c respectively. Fourier transforms of these current traces are presented in Figures D.3a, D.3b, and D.3c respectively.

Figures D.2a through D.2c give further insight into the operation of the RPCFA. The current entering the amplification region at location 1 is, on average, higher than the current exiting the amplification region. This suggests the SWS is pulling current from the Brillouin hub faster than the cathode can repopulate it, a mechanism leading the device to saturation, explaining why decreased gain is observed at increased input drive. The average current at location 2, is significantly lower than either location 1 or 3. The increased current at the locations near the SWS can be attributted to the effect of the RF electric fields drawing current from the Brillouin hub into the interaction space. Additional current is emitted to repopulate the hub. For an unperturbed Brillouin hub with the voltage and magnetic fields applied in this simulation, the expected hub current can be calculated using equations 2.10, 2.11, and 2.12. This method predicts an average current of 150 A, approximately three times the average current measured at location 2 and well below the average currents measured at locations 1 and 3. The cause of this discrepancy is likely the endhats

on the cathode which are permitted to absorb particles and force a zero electric field condition at their surface.

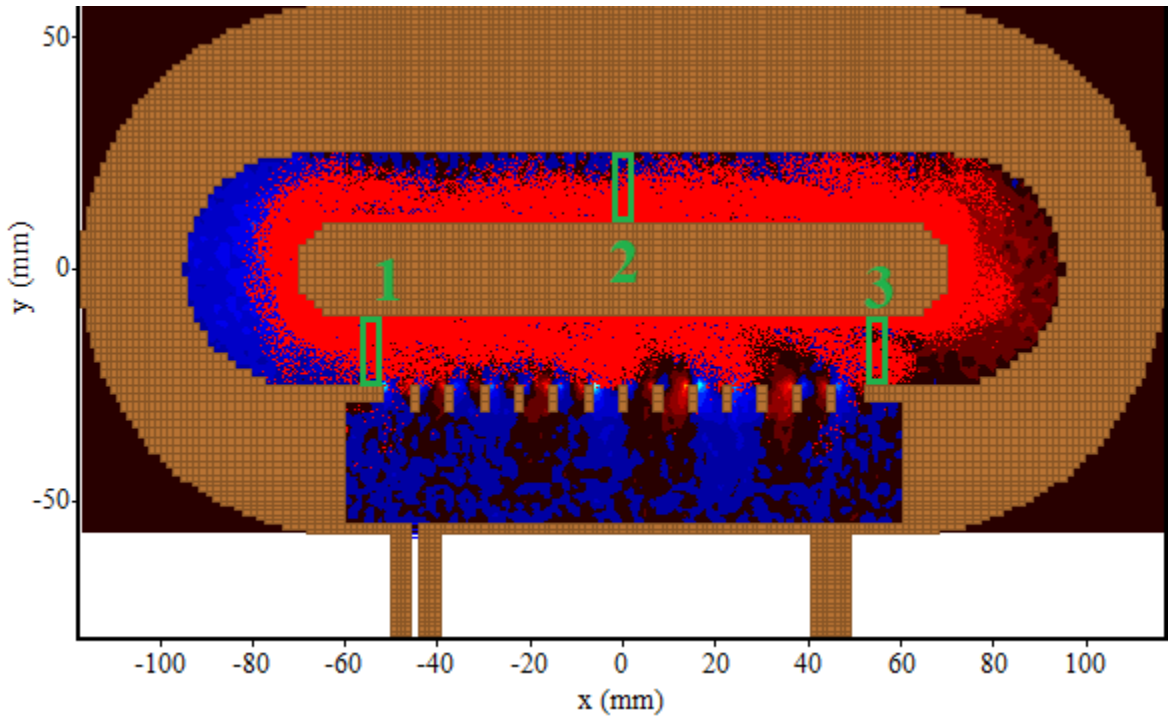

Figure D.1: Current measuring loops with surfaces perpendicular to x, the direction of $E_{rf} \times B$ drift. Electrons recirculate counter-clockwise in this figure. Location 1 measures the current flowing into the SWS, location 2 measures the current leaving the SWS, and location 2 measures current in the center of the planar drift region.

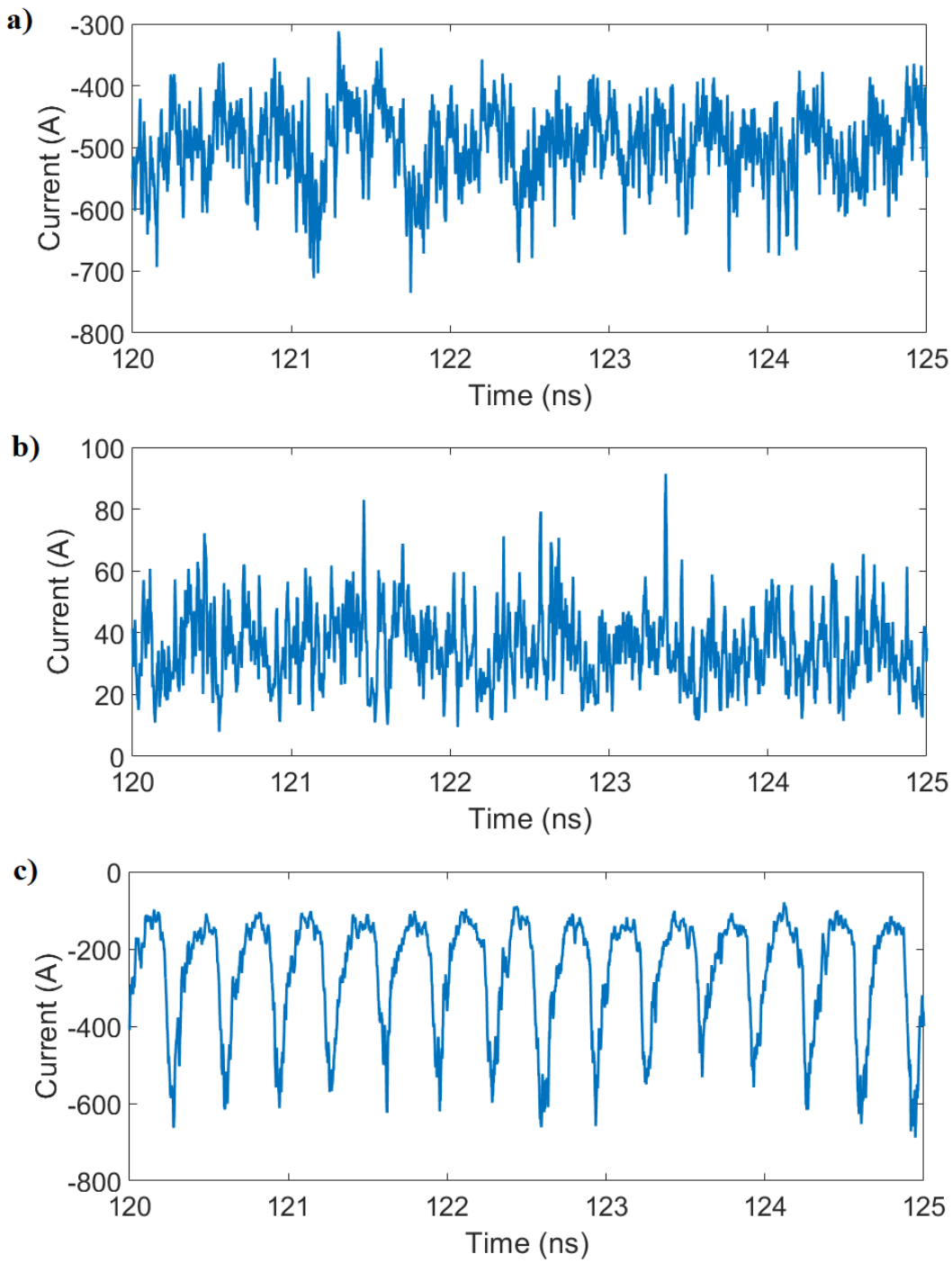

Figure D.2a (top): Current passing through loop 1, approaching the SWS.
Figure D.2b (middle): Current passing through loop 2, in the planar drift region. Unlike the other two locations, current is positive as electrons are travelling in the -x direction at this point.
Figure D.2c (bottom): Current passing through loop 3, leaving the SWS.

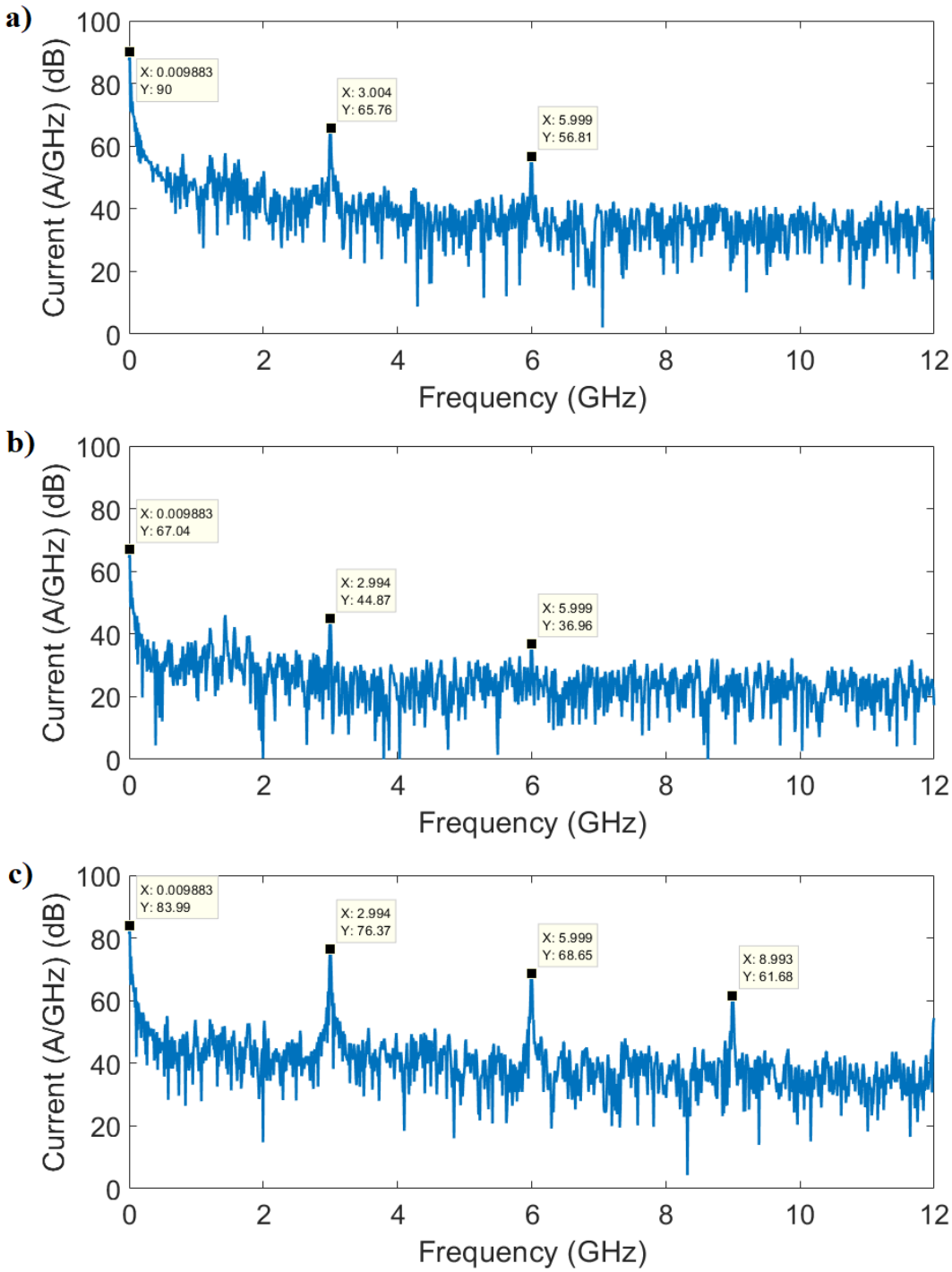

Figure D.3a (top): Frequency spectrum of the current passing through the loop at location 1. Peaks at the RF drive frequency and first harmonic can be observed.
Figure D.3b (middle): Frequency spectrum of current passing through the loop at location 2. Small peaks at the RF drive frequency and first harmonic can be observed.
Figure D.3c (bottom): Frequency spectrum of the current passing through the loop at location 3. The peaks at the fundamental RF frequency as well as the first and second harmonic are observed.

Figures D.2a and D.2b show significant noise but minimal modulation, but plotting the FFT on a log scale, as in Figures D.3a and D.3b, reveals that RF components exits to limited degree in the current trace. Figure D.2c shows the expected modulation at the drive frequency. The current is periodic however the result of the focusing RF fields is to arrange the Brillouin hub into a shape that is not sinusoidal. This deviation from a sinusoidal current trace gives rise to the harmonic content at octaves above the drive frequency. These can be observed when measuring the hub current but is not present in the output power spectrum as the RPCFA is not designed to extract at the harmonic frequency.

The magnitude of these components of the hub current can be evaluated by integrating the (linear) FFT around the peaks at a given frequency. Doing so at 4 frequencies: DC, the fundamental 3 GHz, the first harmonic 6 GHz, and the second harmonic 9 GHz, for the currents at the 3 locations gives insight into the capacity for demodulation of the RPCFA and the evolution of harmonic frequencies. The data is shown in Table D.1. As expected, the greatest RF currents are present at location 3, with nearly none present at location 2. At 1.3 MW input drive, the 278 A of 3 GHz current at location 3 is reduced to 8 A at location 2, a reduction of 15 dB. The maximum gain achievable before feedback overcomes the input drive is likely significantly higher than 16 dB as a full recirculating bend and half of the planar drift region exists between location 2 and location 1. The RF content content present at location 1 is due to its proximity to the RF fields at the input, affecting the trajectory of particles before they enter the amplifying section of the interaction space. This is verified by reducing the strength of the input power, which indeed reduces the relative modulation at location 1. The relative RF and higher order harmonic content is significantly lower than at location 3 as expected. Additionally, it can be seen from Table D.1 that increaseing the RF input drive decreases the average hub current passing through location 3 while also increasing the relative fraction of the AC current. This is further evidence that saturation is respondsible for the reduced gain at these input drive levels.

325 kW Input	DC (0 GHz)	3 GHz	6 GHz	9 GHz
Location 1	671	44	9	6
Location 2	47	2	2	1
Location 3	394	209	50	11

1.3 MW Input	DC (0 GHz)	3 GHz	6 GHz	9 GHz
Location 1	655	76	28	4
Location 2	47	8	3	1
Location 3	342	278	115	57

Table D.1: Frequency content of the Brillouin hub at three marked locations for two different magnitudes of input RF drive power.

Appendix E

Matlab Post-Processing Software

A flowchart describing the data analysis software written to process data acquired in RPCFA experiments. Is presented in Figure E.1. The primary scripts that perform these operations is provided in the following section.

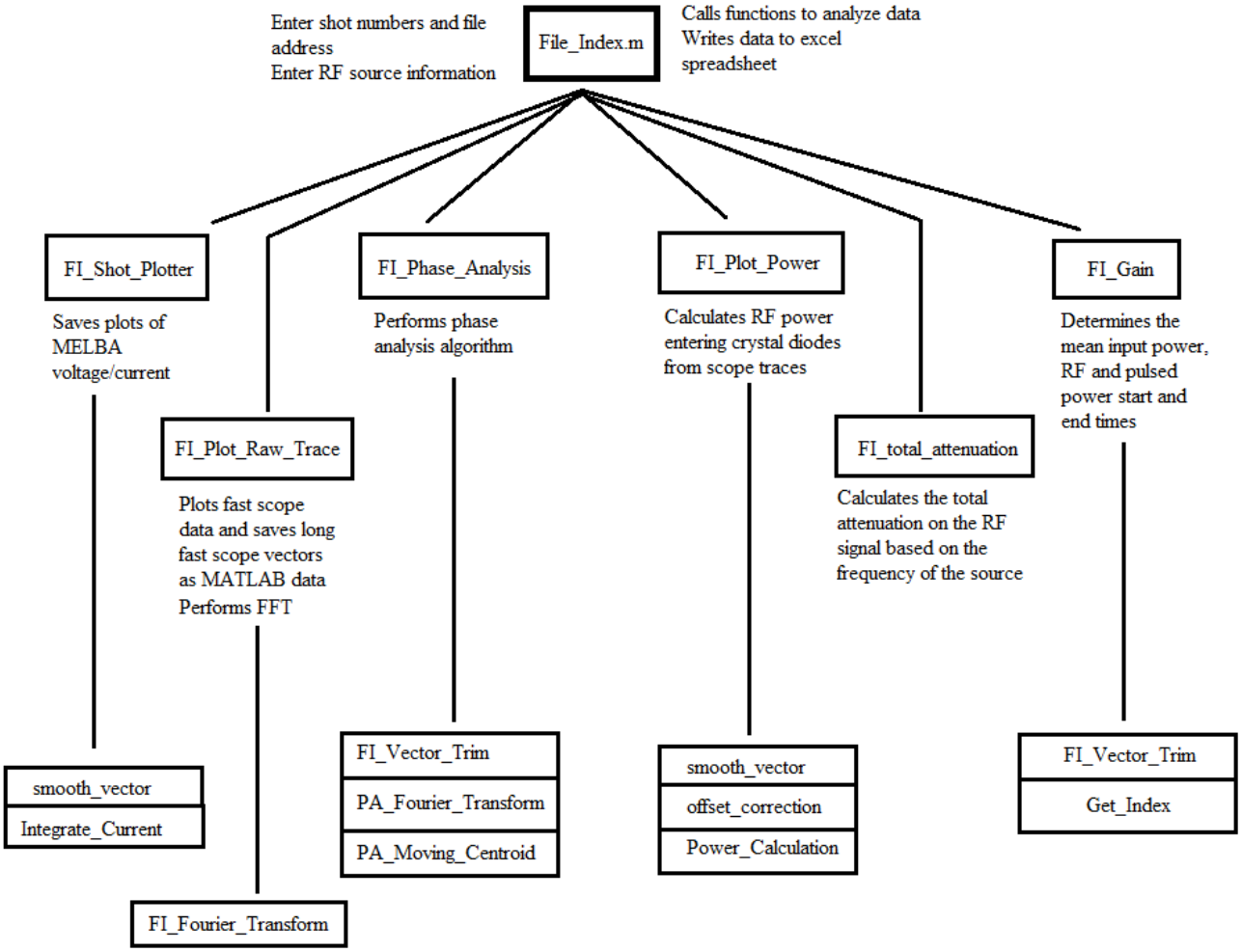

Figure E.1: Data processing software flowchart

File_Index.m

```
%Enters folders and extracts data
%stores experiment configuration
start = 10003; %first shot number with given attenuations
file_end = 10003; %last shot number with given attenuations
address = 'Y:\RPCFA\MG5193 test shot'; %address of parent folder

%===================================
C1_inline = 22;
C2_inline = 27;
C3_inline = 34;
C4_inline = 32.5;
%===================================
magnetron_number = 3;
%1 = MG5223F. 3.05 GHz, around 40 kW
%2 = 4J32. 2.84 GHz, also around 40 kW
%3 = MG5193. 3.0 GHz run with short pulse PFN
```

```
%4 = EPSCO generator tunable up to 2.7 GHz and ~1kW


%aggregate stats
vec_peak_gain = [];
vec_peak_output = [];
vec_mean_input = [];
vec_peak_width = [];
vec_amp_time = [];
vec_mean_reverse = [];
vec_peak_reverse = [];
vec_peak_reentrant = [];
vec_FIPA = [];
vec_transmission = [];
%=====================================

%% shot analysis
for shot_num = start:file_end

    str = int2str(shot_num);
    folder = strcat(address,'\',str,'\traces\');

    input_pwr = strcat(folder,str,'_002_001_Power1.txt');
    output_pwr = strcat(folder,str,'_002_002_Power2.txt');
    rev_in = strcat(folder,str,'_002_003_Power3.txt');
    rev_out = strcat(folder,str,'_002_004_Power4.txt');

    FI_Shot_Plotter(shot_num,address);
    freq = FI_Phase_Analysis(magnetron_number,shot_num,address);
    [c1_TA, c2_TA, c3_TA, c4_TA] =
FI_total_attenuation(magnetron_number,C1_inline,C2_inline,C3_inline,C4_inline
,freq);
    [PP, time ,smooth_input, smooth_output, rev_in, rev_out] =
FI_Plot_Power(shot_num,address,c1_TA,c2_TA,c3_TA,c4_TA);
    [mean_input, peak_output, peak_time, peak_width, amp_time, mean_rev,
peak_rev, peak_reentrant, transmission] =
FI_Gain(magnetron_number,time,smooth_input,smooth_output,rev_in,rev_out);

    FI_Plot_Raw_Trace(shot_num,address);
    peak_gain = peak_output/mean_input;
    FIPA = FI_Phase_Analysis(magnetron_number,shot_num,address);


    %% aggregate stats
    shot_list = start:shot_num;
    vec_peak_gain = [vec_peak_gain peak_gain];
    vec_peak_output = [vec_peak_output peak_output];
    vec_mean_input = [vec_mean_input mean_input];
    vec_peak_width = [vec_peak_width peak_width];
    vec_amp_time = [vec_amp_time amp_time];
    vec_mean_reverse = [vec_mean_reverse mean_rev];
    vec_peak_reverse = [vec_peak_reverse peak_rev];
    vec_peak_reentrant = [vec_peak_reentrant peak_reentrant];
    vec_FIPA = [vec_FIPA FIPA];
    vec_transmission = [vec_transmission transmission];
```

```
end
  %%
  %write to excel spreadsheet
    header_mat = {'Shot number', 'Mean Input', 'Peak Output', 'Peak Gain',
'Peak Width', 'Amplification Time', 'Mean reverse', 'Peak Reverse', 'Peak
Reentrant','oscillation parameter','transmission'};
    summary_mat = [shot_list', vec_mean_input', vec_peak_output',
vec_peak_gain', vec_peak_width', vec_amp_time', vec_mean_reverse',
vec_peak_reverse',vec_peak_reentrant',vec_FIPA',vec_transmission'];
    xlsaddress = strcat(address,'\','Shot_summary3.xls');
    xlswrite(xlsaddress,header_mat,1,'C3')
    xlswrite(xlsaddress,summary_mat,1,'C4')
    FI_Shot_Analysis(start,file_end,address);
```

FI_Shot_Plotter.m

```
function SP = Shot_Plotter(shot_num,address)
%saves a figure of the MELBA voltage and current
%address = 'Y:\RPCFA\15281-15413'; %set within File_index.m
str = int2str(shot_num);
folder = strcat(address,'\',str,'\traces\');

volm = strcat(folder,str,'_001_002_VOLN.txt');
entc = strcat(folder,str,'_001_003_MEC2.txt');

o = load(volm);
time = 1e9*o(:,1);
Voltage = o(:,2);

o = load(entc);
raw_signal = o(:,2);
smooth_signal = smooth_vector(raw_signal,100);
smooth_current = 1e-3*Integrate_Current(o(:,1),smooth_signal);
Current = smooth_current;
plot(o(:,1),smooth_signal)

%
plot(time,-Voltage,time,smooth_current,'LineWidth',2)
set(gca,'FontSize', 16)%sets fontsize for everything
ylabel('Voltage (100 kV) Current (kA)','FontSize', 20)
legend('Voltage','Current')
xlabel('Time (ns)','FontSize',20)
title(str)
%}


plot_name = strcat(folder,str,'_MELBA_Current_and_Voltage');
savefig(plot_name);
%close;
workspace = strcat(folder,str,'_MELBA_IV');
save(workspace,'Voltage','Current');
%}
```

FI_Plot_Raw_Trace.m

```
function RT = FI_Plot_Raw_Trace(shot_num,address)
%saves a figure of all raw traces from fast scopes and saves them as a .mat
%file
%address = 'Y:\RPCFA\15414-15458'; %set within File_index.m
str = int2str(shot_num);
folder = strcat(address,'\',str,'\traces\');

for_in = strcat(folder,str,'_GPIB06_001_Signal1.txt');
for_out = strcat(folder,str,'_GPIB06_002_Signal2.txt');
%rev_in = strcat(folder,str,'_GPIB06_003_Signal3.txt');
%rev_out = strcat(folder,str,'_GPIB06_004_Signal4.txt');

n = load(for_in);
time = 1e9*n(:,1);
forward_input_signal = n(:,2);
[f,FT] = FI_Fourier_Transform(time,forward_input_signal);
plot(f,FT);
axis([0 6 0 1]);
fwd_in_plot_name = strcat(folder,str,'_for_in_FFT.fig');
savefig(fwd_in_plot_name);
close;

n = load(for_out);
forward_output_signal = n(:,2);
[f,FT] = FI_Fourier_Transform(time,forward_output_signal);
plot(f,FT);
axis([0 6 0 1]);
fwd_out_plot_name = strcat(folder,str,'_for_out_FFT.fig');
savefig(fwd_out_plot_name);
close;

%{
n = load(rev_in);
reverse_input_signal = n(:,2);
[f,FT] = FI_Fourier_Transform(time,reverse_input_signal);
plot(f,FT);
axis([0 6 0 1]);
rev_in_plot_name = strcat(folder,str,'_rev_in_FFT.fig');
savefig(rev_in_plot_name);
close;

n = load(rev_out);
reverse_output_signal = n(:,2);
[f,FT] = FI_Fourier_Transform(time,reverse_output_signal);
plot(f,FT);
axis([0 6 0 1]);
rev_out_plot_name = strcat(folder,str,'_rev_out_FFT.fig');
savefig(rev_out_plot_name);
close;
%}

plot(time,forward_input_signal,time,forward_output_signal);
```

```
fwd_pwr_plot_name = strcat(folder,str,'_forward_signals.fig');
savefig(fwd_pwr_plot_name);
close;
workspace = strcat(folder,str,'_workspace');
save(workspace,'time','forward_input_signal','forward_output_signal');%,'reve
rse_input_signal','reverse_output_signal');
```

FI_Phase_Analysis.m

```
function [FIPA] = FI_Phase_Analysis(magnetron_number,shot_num,address)

% performs an analysis of the relative phase shifts of 2 signals of the
% same length. frequencies should be close and the forward input signal is
% taken to be the baseline
%recommended start times:
%for 4j32 (magnetron code 2): start = 500, end = 1100
%for MG5223F  (magnetron code 1): start = 250, end = 1000
%for epsco generator (magnetron code 4)
%for mg5193 with short pulse pfn 700 to 1100 (magnetron code 3)

%% initial conditions for shot analysis

%shot_num = 15442;
%address = 'Y:\RPCFA\15414-15458'; %set within File_index.m

str = int2str(shot_num);
folder = strcat(address,'\',str,'\traces\');
for_in = strcat(folder,str,'_GPIB06_001_Signal1.txt');
for_out = strcat(folder,str,'_GPIB06_002_Signal2.txt');

n = load(for_in);
time1_long = n(:,1);
forward_input_signal_long = n(:,2);

m = load(for_out);
time2_long = m(:,1);
forward_output_signal_long = m(:,2);

if (magnetron_number == 2)
    start_time = 500*1e-9;
    end_time = 1500*1e-9;
elseif (magnetron_number == 1)
    start_time = 300*1e-9;
    end_time = 1700*1e-9;
else
    start_time = 500*1e-9;
    end_time = 1000*1e-9;
end

[time1,forward_output_signal,forward_input_signal] =
FI_vector_trim(time1_long,start_time,end_time,forward_input_signal_long,
forward_output_signal_long);
time2=time1;
```

```
%%
k = length(time1);

format long
[f,FT] = PA_Fourier_Transform(time1,forward_input_signal,1,6);
FIPA = cumtrapz(f);
logic = (FT == max(FT));
if (sum(logic) ~= 1)
    warning('multiple dominant frequencies found!');
end

dominant_f = logic*f;
FIPA = dominant_f*1e-9;
zerolist1 = []; %list of times at which the signal value is zero
for i = 1:k-1
    if (forward_input_signal(i)*forward_input_signal(i+1) <= 0)
        zerolist1 = [zerolist1
get_zero(time1(i),forward_input_signal(i),time1(i+1),forward_input_signal(i+1
))];
    elseif (forward_input_signal(i) ==0)
        zerolist1 = [zerolist1 time1(i)];
    end

end


zerolist2 = []; %list of times at which the signal value is zero
for i = 1:k-1
    cross = forward_output_signal(i)*forward_output_signal(i+1);
    if (cross < 0 )
        zerolist2 = [zerolist2
get_zero(time2(i),forward_output_signal(i),time2(i+1),forward_output_signal(i
+1))];
    elseif (forward_output_signal(i) ==0)
        zerolist2 = [zerolist2 time2(i)];
    end
end

t = length(zerolist2);
phase_shift = zeros(1,t);
for k = 1:t
    s = min(abs(zerolist1 - zerolist2(k)));
    for j = 1:length(zerolist1)
        jj = zerolist1(j)-zerolist2(k);
        if (abs(jj) == s)
            sign = jj/s;
        end
    end
    phase_shift(k) = sign*s*2*pi*dominant_f;
end
%%
%sets the window for possible values. if turned off, range is -pi/2 to
%pi/2
```

```
%reccommended on for the MG5223F and off for the 4J32


for i = 1:length(phase_shift)
    if (phase_shift(i)> 0)
        phase_shift(i) = phase_shift(i)-pi;
    end
end

%avg = movmean(phase_shift,0.02*length(phase_shift));
avg = PA_moving_centroid(phase_shift,0.02*length(phase_shift));

%% reduces the number of points plotted by a given ratio
plot_ratio = 0.25; %must be (0,1]
rand_vec = rand([1,length(phase_shift)]);
select = rand_vec < plot_ratio;
reduced_phase_shift = zeros(1,sum(select));
reduced_time = zeros(1,sum(select));
j=1;
for i = 1:length(phase_shift)
    if (select(i)== 1)
        reduced_phase_shift(j)=phase_shift(i);
        reduced_time(j) = zerolist2(i);
        j = j+1;
    end
end

figure
scatter(reduced_time*1e+9,reduced_phase_shift, '.')
hold on
plot(zerolist2*1e+9, avg)
title(shot_num);
xlabel('Time (ns)');
ylabel('Phase Shift (rad)');
axis([1e9*start_time 1e9*end_time -pi 0])
filename = strcat(folder,'PhaseAnalysis.fig');
savefig(filename)
close;
```

FI_Plot_Power.m

```
function [PP, time, input_power, output_power, rev_in, rev_out]  =
FI_Plot_Power(shot_num,address,c1_TA,c2_TA,c3_TA,c4_TA)
%function [PP, time, input_power, output_power]  =
FI_Plot_Power(shot_num,address,c1_TA,c2_TA,c3_TA,c4_TA)
%takes the shot number as an int and the the shot series folder address as
%a string and saves plots of the output and input power. for mean input and
%peak output analysis use FI_Gain.m
%{
C1_inline = 3;
C2_inline = 12;
c3_inline = 6;
C4_inline = 3;
%}
```

```
%address = 'Y:\RPCFA\15281-15413'; %set within File_Index.m
str = int2str(shot_num);
folder = strcat(address,'\',str,'\traces\');
input_pwr = strcat(folder,str,'_002_001_Power1.txt');
output_pwr = strcat(folder,str,'_002_002_Power2.txt');
in_rev = strcat(folder,str,'_002_003_Power3.txt');
out_rev = strcat(folder,str,'_002_004_Power4.txt');

    m = load(input_pwr);
    time = 1E9*m(:,1); %time in nanoseconds
    volts_out = 1E3*m(:,2);%volts in mV
    smoothing_step = floor(length(time)/1000);
    smooth_input = smooth_vector(volts_out,smoothing_step);
    smooth_input = offset_correction(smooth_input,0);
    rectified_input_voltage = abs(smooth_input);
    input_power = Power_Calculation(rectified_input_voltage,2,c1_TA);
    PP = plot(time,input_power);
    hold on

    m = load(output_pwr);
    time = 1E9*m(:,1); %time in nanoseconds
    volts_out = 1E3*m(:,2);%volts in mV
    smoothing_step = floor(length(time)/1000);
    smooth_output = smooth_vector(volts_out,smoothing_step);
    smooth_output = offset_correction(smooth_output,0);
    rectified_input_voltage = abs(smooth_output);
    output_power = Power_Calculation(rectified_input_voltage,4,c2_TA);
    PP = plot(time,output_power);

    m = load(in_rev);
    time = 1E9*m(:,1); %time in nanoseconds
    volts_out = 1E3*m(:,2);%volts in mV
    smoothing_step = floor(length(time)/1000);
    rev_in_raw = smooth_vector(volts_out,smoothing_step);
    rev_in_raw = offset_correction(rev_in_raw,0);
    rectified_input_voltage = abs(rev_in_raw);
    rev_in = Power_Calculation(rectified_input_voltage,1,c3_TA);

    m = load(out_rev);
    time = 1E9*m(:,1); %time in nanoseconds
    volts_out = 1E3*m(:,2);%volts in mV
    smoothing_step = floor(length(time)/1000);
    rev_out_raw = smooth_vector(volts_out,smoothing_step);
    rev_out_raw = offset_correction(rev_out_raw,0);
    rectified_input_voltage = abs(rev_out_raw);
    rev_out = Power_Calculation(rectified_input_voltage,4,c4_TA);

    output_pwr_plot_name = strcat(folder,str,'output_power.png');
    output_pwr_fig_name = strcat(folder,str,'output_power.fig');
    print(output_pwr_plot_name,'-dpng','-r600');
    savefig(output_pwr_fig_name);
    close;
```

FI_total_attenuation.m

```
function [c1_TA, c2_TA, c3_TA, c4_TA] =
FI_total_attenuation(magnetron_number,C1_inline,C2_inline,C3_inline,C4_inline
,frequency)
%returns the total attenuation into each channel
cable_A_3ghz = 9.75;
cable_B_3ghz = 10.25;
cable_C_3ghz = 9.55;
cable_D_3ghz = 12.75;
cable_E_3ghz = 14.25;
cable_A_2_85ghz = 9.35;
cable_B_2_85ghz = 9.45;
cable_C_2_85ghz = 9.15;
cable_D_2_85ghz = 12.65;
cable_E_2_85ghz = 13.35;

if (magnetron_number == 1 || magnetron_number == 3)
    c1_TA = 39+cable_A_3ghz+3.1+C1_inline;
    c2_TA = 39.6+cable_B_3ghz+3.1+C2_inline;
    c3_TA = 33.2+cable_E_3ghz+3.1+C3_inline;
    c4_TA = 33.6+cable_C_3ghz+3.1+C4_inline;
elseif (magnetron_number == 2)
    c1_TA = 39+cable_A_2_85ghz+3.1+C1_inline;
    c2_TA = 39.6+cable_B_2_85ghz+3.1+C2_inline;
    c3_TA = 33.2+cable_E_2_85ghz+3.1+C3_inline;
    c4_TA = 33.6+cable_C_2_85ghz+3.1+C4_inline;
elseif (magnetron_number==4)
    cableA = (0.7/0.45)*frequency+4.92;
    cableB = 2*frequency+3.75;
    cableC = (0.7/0.45)*frequency+4.72;
    cableD = (2.1/0.45)*frequency-0.65;
    cableE = (3/0.45)*frequency-5.65;

    c1_TA = 39+cableA+3.1+C1_inline;
    c2_TA = 39.6+cableB+3.1+C2_inline;
    c3_TA = 33.2+cableD+3.1+C3_inline;
    c4_TA = 33.6+cableC+3.1+C4_inline;


else
    warning('magnetron number not found!')
end
```

FI_Gain.m

```
function [mean_input peak_output peak_time peak_width amp_time, mean_rev,
peak_rev, peak_reentrant,transmission] =
FI_Gain(magnetron_number,time,smooth_input,smooth_output, rev_in, rev_out)
%function [mean_input peak_output peak_time peak_width amp_time] =
FI_Gain(magnetron_number,time,smooth_input,smooth_output)
%give the magnetron number and the vectors for the input and output powers.
```

```
%the magnetron number determines the time (in ns) to average the mean input
%power
%peak width is the FWHM of the peak gain
%amp width is the length of time in which the output power exceeds the
%input power
if magnetron_number == 1
    start_time = 500;
    end_time = 1000;
    T_window_start = 0;
    T_window_end = T_window_start + 250; %may need to update if used
elseif magnetron_number ==2
    start_time = 500;
    end_time = 1250;
    T_window_start = 0;
    T_window_end = T_window_start + 250; %may need to update if used
elseif magnetron_number == 3
    j = 1;
    i=0;
    while i == 0
        T_window_start = time(j);
        if smooth_input(j) < max(smooth_input)/10
            j = j+1;
        else
            i = i+1;
        end
    end
    T_window_end = T_window_start+200;
    start_time = 500;
    end_time = 1250;

else
    start_time = 500;
    end_time = 1000;
    T_window_start = 0;
    T_window_end = T_window_start + 250;
end

for i = 1:length(time)
    if time(i)<T_window_end
        T_end_index = i;
    end
end
for i = linspace(length(time),1,length(time))
    if time(i)> T_window_start
        T_start_index = i;
    end
end


    mean_input = 0;
    mean_rev = 0;
    j = 0;
    for i = 1:length(time)
        if (time(i) > start_time && time(i) < end_time)
            j = j+1;
            mean_input = mean_input + smooth_input(i);
```

```
            mean_rev = mean_rev + rev_in(i);
        end
    end
    mean_input = mean_input/j;%~~~
    mean_output = mean(smooth_output(T_start_index:T_end_index));
    transmission = mean_output/mean_input;
    mean_rev = mean_rev/j; %~~~
    peak_output = max(smooth_output);%~~~
    peak_index = Get_Index(smooth_output,peak_output);
    if magnetron_number ==3
        mean_input = smooth_input(peak_index);
    end
    peak_time = time(peak_index);%~~~
    peak_rev = max(rev_in);%~~~
    peak_reentrant = max(rev_out);%~~~
    [cut_time cut_output cut_input] = FI_vector_trim(time, start_time,
end_time, smooth_input, smooth_output);


    if sum(cut_output > cut_input)>=1 %if there is gain

        max_time = Get_Index(smooth_output,peak_output);
        peak_start = max_time;
        peak_end = max_time;
        lim = 0;

        while (smooth_output(peak_start)> peak_output/2 && lim ==0)
        peak_start = peak_start - 1;
            if (peak_start ==0)
            lim = 1;
            end
        end
        while (smooth_output(peak_end)> peak_output/2)
        peak_end = peak_end + 1;
            if (peak_end == length(smooth_output))
                lim = 1;
            end
        end
        peak_width = time(peak_end)-time(peak_start);%~~~
        amp_time = 0;
        for i = 2:length(time)
        if (smooth_output(i)>smooth_input(i) && time(i)>500 && time(i)<1250)
            amp_time = amp_time + time(i)-time(i-1);
        end
        end
    else %if there is no gain
        peak_width = 0;
        amp_time = 0;
    end
```

Appendix F

Determination of RF Breakdown

The determination of RF breakdown can be made by observing the magnitude of reflected RF power. RF breakdown leads to a short circuit of the slow wave structure causing the amplified wave to be reflected. This reflected signal is attenuated as it travels backwards across the SWS. If the reflected signal is of sufficient magnitude, as shown in Figure F.1, it can induce RF breakdown in the circulator, leading to a termination of the input microwave signal. At slightly lower magnitudes of input microwave power, RF breakdown can be induced where a reflected wave does not lead to a breakdown in the circulator, as shown in Figure F.2. In either case, RF breakdown causes a rapid termination of the amplified output, not seen in Figure F.3 where RF breakdown does not occur.

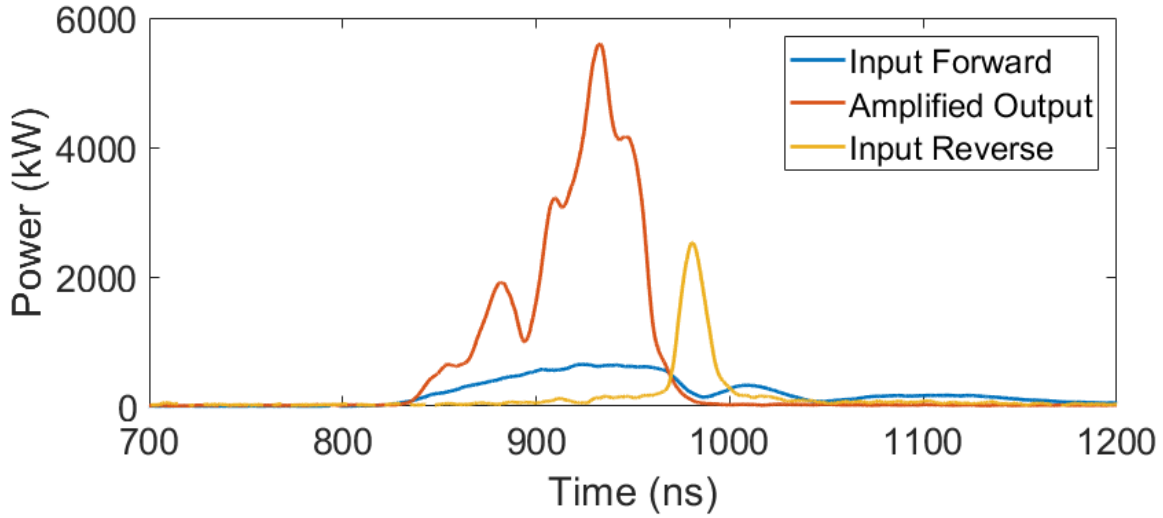

Figure F.1: Shot #16868, showing high power amplification sufficient to cause both RF breakdown in the SWS, and again when the reflected amplified signal reaches the circulator, terminating the input pulse.

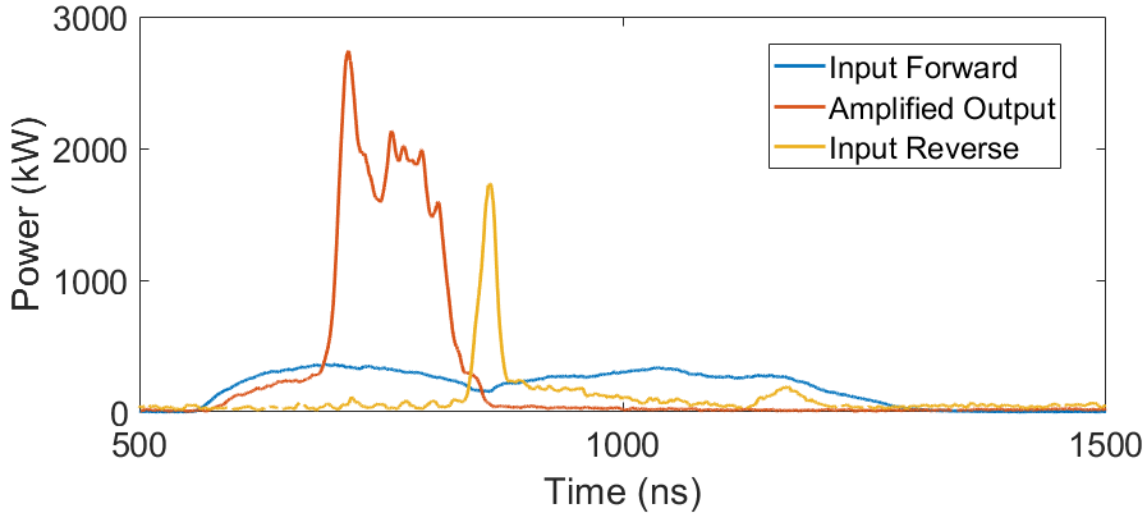

Figure F.2: Shot #16819, showing high power amplification sufficient to cause RF breakdown in the SWS, but insufficient to induce breakdown when the reflected amplified signal reaches the circulator, not terminating the input pulse.

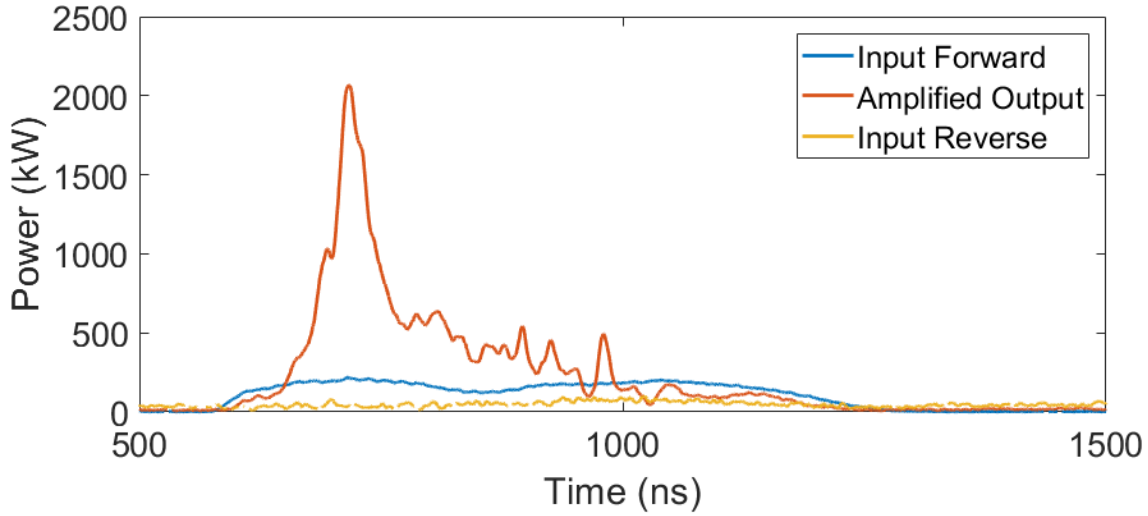

Figure F.3: Shot #16834, showing high power amplification insufficient to cause RF breakdown in the SWS. Amplified output power decays gradually as the wave desynchronizes from the beam.

Appendix G

A Discussion of Endloss and Electronic Efficiency

A measurement of endloss current in the RPCFA is necessary in order to accurately evaluate the efficiency of the device. Endloss current is current emitted from the cathode that does not cross the magnetically insulated A-K gap but instead flows parallel to the magnetic field lines and is ejected out the ends of the device. This current is measured entering the RPCFA though it does not contribute to the crossed-field interaction that generates microwave gain. Thus, this endloss leads to a potentially significant discrepancy between the total efficiency, the ratio of microwave power generated to the total electronic power consumed, and the electronic efficiency, the ratio of the microwave power generated to the electronic power required to perform the crossed-field interaction described in chapter 2. In experiment, endloss is especially difficult to evaluate on the RPCFA due to the logistical limitations of placing a current collecting plate inside the vacuum chamber in a way that does not perturb the experiment. For this reason, MAGIC simulation is used to estimate the electronic efficiency of the RPCFA.

The simulations presented in chapter 2 represent an idealized version of the RPCFA. Large endhats and a reduced A-K gap contain the emitted particles in the interaction space, as seen in Figure G.1. This leads to both reduced total current draw and essentially no endloss. In experiment, it was found that both these features were arc hazards and the A-K gap was increased from 1.5 cm to 2.0 cm and the front endhat was reduced to the modest size shown in figure 3.15d, with the rear endhat being removed altogether. A simulation was run with these modifications included, additionally, the inner housing was placed in a large chamber to simulate the MELBA vacuum chamber. As shown in figure G.2, endloss has increased substantially with much of the endloss being lost to the rear of the chamber where no endhat is present.

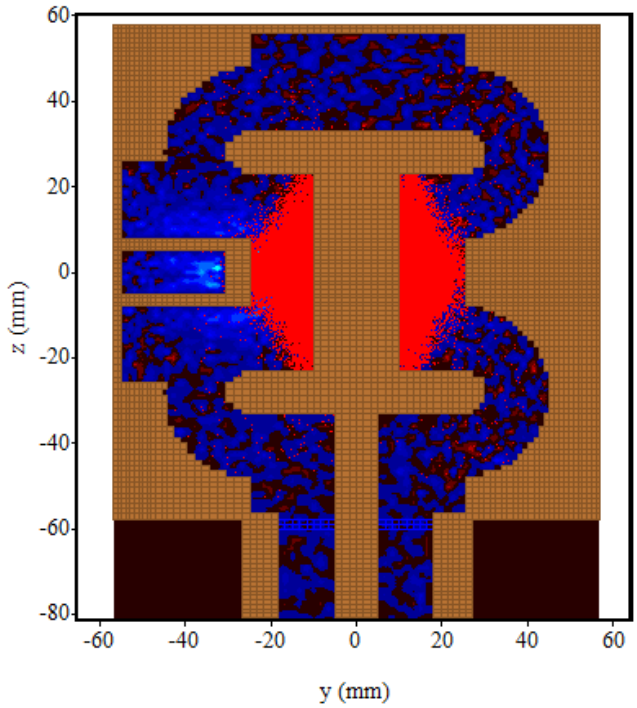

Figure G.1: Cross section of MAGIC simulation showing cathode with large endhats and a reduced A-K gap spacing that effectively inhibits endloss current.

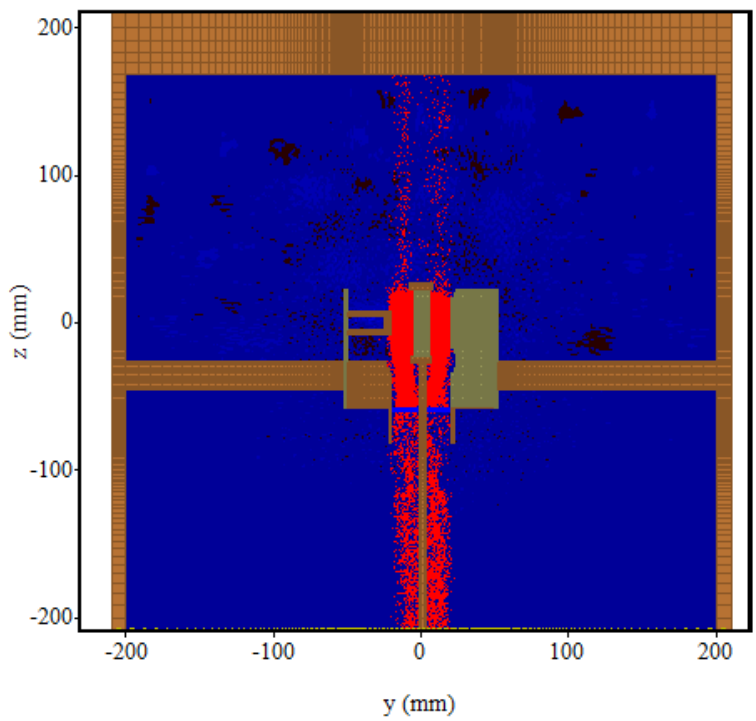

Figure G.2: Realistic simulation of RPCFA in MELBA chamber with modest endhats and increased A-K gap spacing. Significant endloss is apparent.

The currents measured from the realistic MAGIC simulation are summarized in Figure G.3. Approximately 840 A of total current are drawn at steady state with around 375 A of that current being endloss (360 A to the back of the chamber toward -z and the remaining 15 A to the front) and 325 A are collected at the SWS. The remaining 140 A is collected elsewhere in the simulation, such as at the inner housing or on the cathode stalk. This simulation calculated the amplification of a 0.95 MW input microwave signal to around 12 MW of output power, thus around 11 MW of RF was generated by the RPCFA. From the 330 kV gap voltage and the total current draw this gives a total efficiency of 4%. Using the current collected by the SWS this gives an electronic efficiency of 10%.

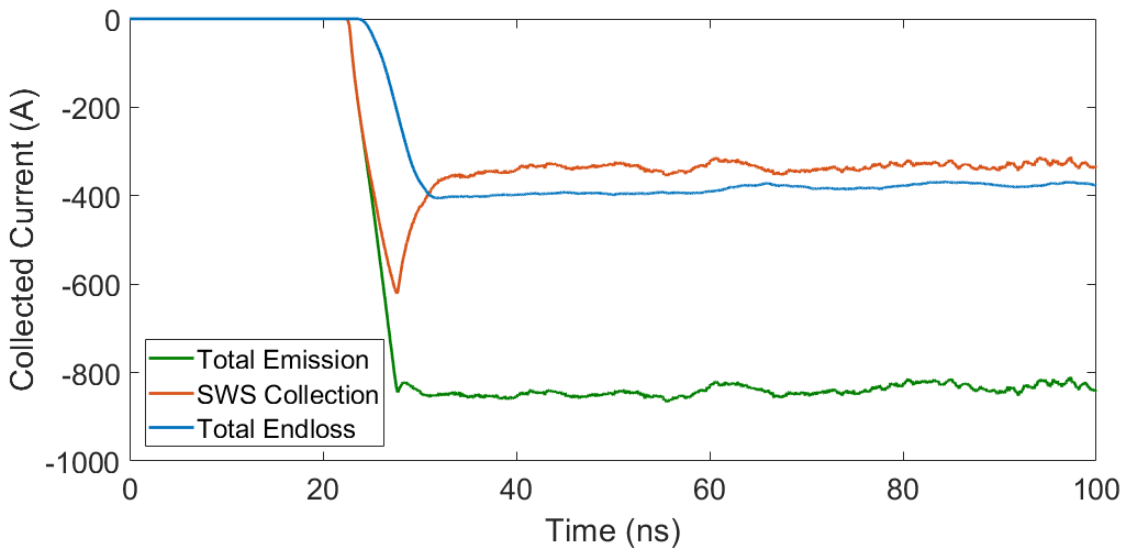

Figure G.3: Collected currents from a realistic simulation of the RPCFA.

The total current emitted in this simulation is still significantly lower than the currents measured in experiment. The discrepancy is likely due to the idealized emission model used in this simulation. Here emission is only permitted from the emitter located on the body of the cathode. In reality, all conducting surfaces pulsed to high voltage, including the endhat, are potential sources of electron emission, which is

likely extremely significant as the emitting region of the cathode constitutes only a small fraction of the potential emitting surface area. Emission from regions other than the cathode body was omitted from simulation as the introduction of such a large non-conformally shaped emitting region would substantially increase the runtime of the simulation, without introducing physics that significantly affect the RPCFA. It is the author's opinion that the 10% electronic efficiency is an accurate figure as MAGIC is a well-tested PIC code that can be expected to faithfully predict the interaction of electrons and electromagnetic fields in the RPCFA. Applying this to nominal metrics obtained experimentally: 5 MW output power generated at 300 kV, gives an estimated 170 A collected by the SWS. This 170 A is a small fraction of the typical 3 kA drawn during amplification of high power microwave signals, but likely representative of the fraction of the current emitted at the designated emitter of the cathode compared to the total potential emitting surface.

Appendix H

X-ray Photoelectron Spectroscopy

X-ray photoelectron spectroscopy (XPS) is a technique used for measuring the elemental composition of the surface of a material. XPS is capable of measuring the types of bond an element is making at the surface of a material and can therefore be used to evaluate the chemical state of the material being analyzed. This technique was applied to the slow wave structure of the RPCFA to determine the surface chemistry that occurs during shots. A small (0.5cm x 0.5 cm) patch of the SWS was removed from the front vane tip, facing the incoming electron beam, and a similarly sized patch was removed from the surface that is bolted to the substrate, representing an unperturbed surface. The SWS had been subjected to ~120 shots, fired using the Cathode A with endhat at moderate microwave power input drive. The XPS spectrum for the unperturbed patch is shown in figure H.1 and the patch taken from the exposed vane tip is shown in figure H.2

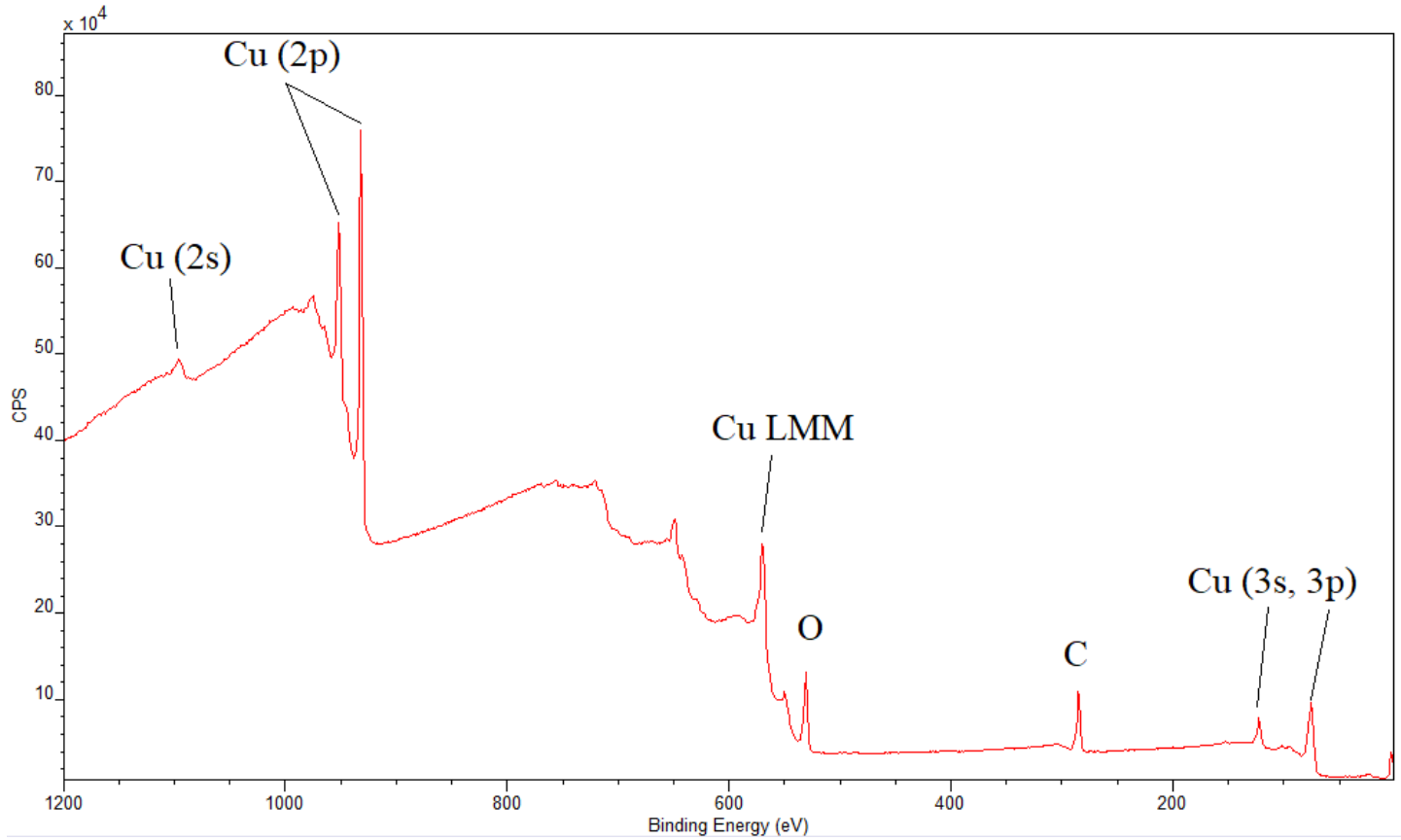

Figure H.1: XPS spectrum from the unperturbed patch of the SWS. Copper is the dominant element, as expected, but oxygen and carbon can be seen in small amounts.

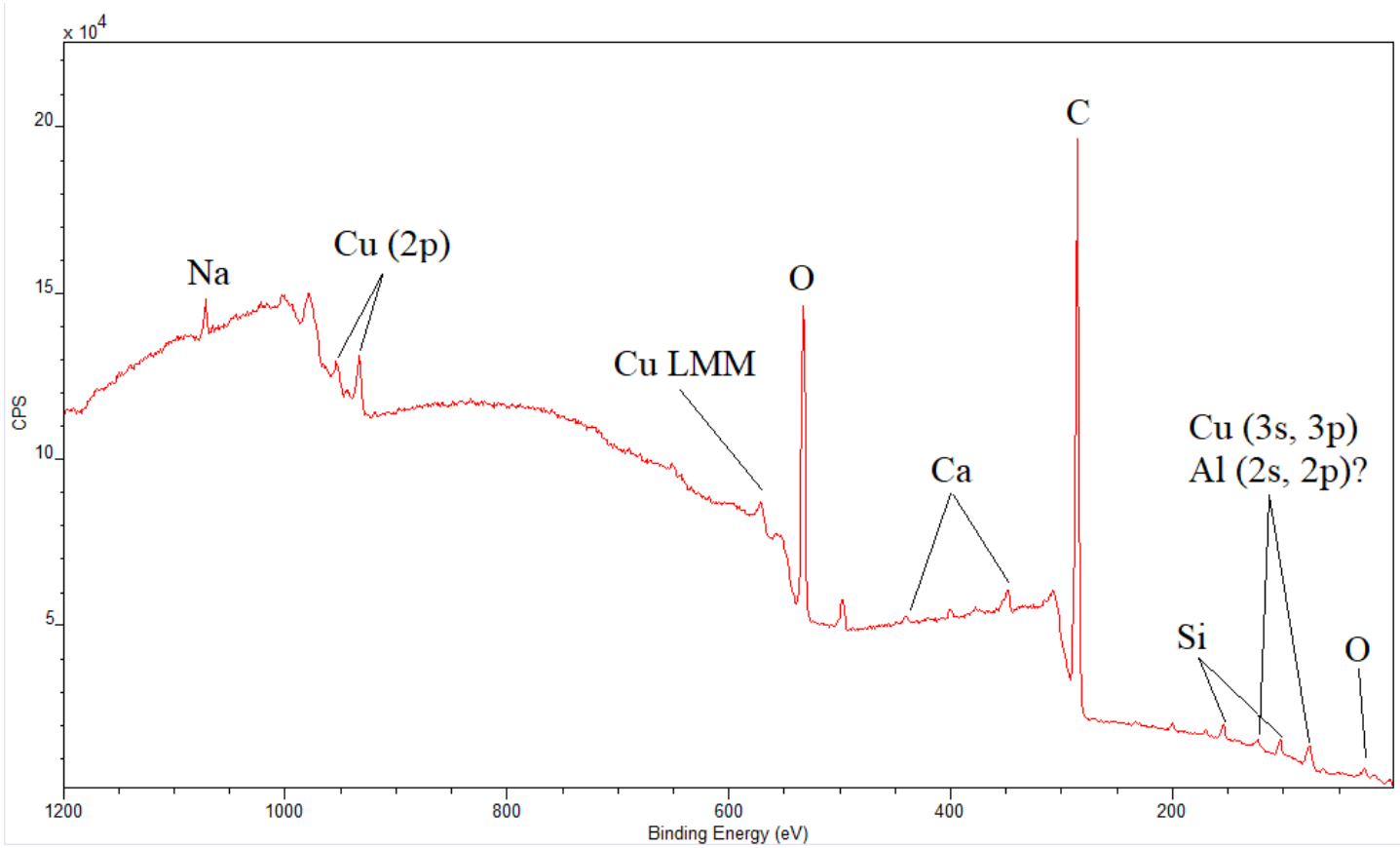

Figure H.2: XPS spectrum from the exposed section of the SWS vane tip. Additional elements not seen in the unperturbed spectrum include sodium, calcium, and silicon.

The differences in these spectra give insight into the surface chemistry occurring in the RPCFA. The most significant difference is the increase in the size of the carbon peak. This is most likely due to two factors. The structure may have been inadvertently contacted during assembly or between shot series during cleaning. The structure was rinsed using methanol prior to installation to remove biological deposits though this may have been an incomplete removal (explaining the sodium and calcium presence) and may have additionally led to the deposition of more carbon and oxygen. Hydrogen (and helium) are not detected due to a physical limitation of the XPS process. The other significant source of carbon is the carbon emitter of Cathode A. Material ablated in the emission process or due to back bombardment of the electrons may have easily liberated carbon and deposited it on the SWS. The presence of silicon is likely due to the light sanding (using SiC sandpaper) applied to the SWS to remove excessive deposition between shot series.

It should be noted that iron is not present on the spectrum indicating material from the body of Cathode A is not ablated in the process. The presence of aluminum is ambiguous as the spectral lines are very close to the Cu 3s and 3p lines. This is surprising as the majority of the material surrounding the SWS is aluminum. Stronger peaks at these locations would be confirm the presence of significant quantities of aluminum.

Appendix I

Table of Commercially Available Crossed-Field Amplifiers

Tube Type	Frequency Range (GHz)	Min. Peak Power (MW)	Duty Cycle (%)	Nominal Gain (dB)	Pulse Width (μ)	Raytheon Equivalent
L4806	1.25 to 1.35	0.1	3.2	13.5	40	QKS-1319
L4939/4940	1.25 to 1.35	0.55	1.24	N/A	3	QK-629/QK-630
L4953	1.28 to 1.35	5.3	0.1	11.2	2	QK-653
L4153	1.28 to 1.35	20	0.03	10	2	N/A
L4253	1.525 to 1.625	17.5	0.03	10	2	N/A
L4717	2.9 to 3.1	.06	2.8	16	35	QKS-1629
L4719	2.9 to 3.1	0.525/2.2	2.5/1.25	10/7	28	QKS-2071
L4756	3.09 to 3.51	1.2	2.5	10	110	QKS-2064
L4822	5.4 to 5.9	0.630/1.25	1.0/0.56	10.2/7.0	37/35	QKS-1343
L4764	9.5 to 10.0	0.5	0.11	12	2	QKS-1721

Table I.1: List of commercially available crossed-field amplifiers at the time of publication [52].

BIBLIOGRAPHY

[1] T. A. Spencer, "Current HPM source research," in *Proc. 6th Workshop High Energy Density High Power RF*, Berkeley Springs, WV, USA, 2003, p. 46.

[2] J. A. Benford, J. A. Swegle, and E. Schamiloglu, *High Power Microwaves*. Boca Raton, FL, USA: CRC Press, 2007.

[3] R. M. Gilgenbach, Y. Y. Lau, H. McDowell, K. L. Cartwright, and T. A. Spencer, "Crossed-Field Devices," in *Modern Microwave and Millimeter-Wave Power Electronics,* 1st ed*.,* R. J. Barker, N. C. Luhmann, J. H. Booske, and G. S. Nusinovich, Eds. Piscataway, NJ, USA: IEEE Press, 2004.

[4] A. S. Gilmour, Klystrons, Traveling Wave Tubes, Magnetrons, Crossed-Field Amplifiers, and Gyrotrons. Norwood, MA, USA: Artech House, 2011, pp. 543–581.

[5] R. M. Gilgenbach, M. E. Read, K. E. Hackett, R. Lucey, B. Hui, V. L. Granatstein, K. R. Chu, A. C. England, C. M. Loring, O. C. Eldridge, H. C. Howe, A. G. Kulchar, E. Lazarus, M. Murakami, and J. B. Wilgen, "Heating at the Electron Cyclotron Frequency in the ISX-B Tokamak," Phys. Rev. Lett., vol. 44, no 10, pp. 647-650, Mar. 1980 [Online]. Available: https://doi.org/10.1103/PhysRevLett.44.647

[6] N. Friedman, *The Naval Institute Guide to World Naval Weapon Systems*, 5th ed. Naval Institute Press, 2006.

[7] W. C. Brown, "Description and Operating Characteristics of the Platinotron, a new Microwave Tube Device," *Proceedings of the IRE*, Vol. 45, No. 9, pp. 1209 – 1222, Sept. 1957

[8] W. C. Brown, "Design and development of the Platinotron, Amplitron, and Stabilotron, Final Report." Signal Corps contract No. DA-36-039-sc-56644, Signal Corps Project No. 322A, Dept. of the Army Project No. 3-19-03-021. August 1, 1953 – December 31, 1955.

[9] G. K. Farney, "Crossed-Field Microwave Devices," Technology Service Corporation/Crane Division Naval Surface Warfare Center, 1995.

[10] R. R. Warnecke et al., "Magnetron-type Travelling Wave Amplifier Tube," *Proc. IRE*, Vol. 38, No. 5, May 1950, pp. 330-336.

[11] A.W. Hull, "The Effect of A Uniform Magnetic Field on the Motion of Electrons Between Coaxial Cylinders," Phys. Review, Vol. 18, No. 1, pp. 31 – 57, July 1921.

[12] Erich Habann: "Eine neue Generatorröhre," Zeitschrift für Hochfrequenztechnik. Jahrbuch der drahtlosen Telegraphie und Telephonie. Bd. 24, 1924, ZDB-ID 1011026-4, S. 115–120, 135–141, (zugleich: Jena, Universität, Dissertation, 1924).

[13] J. Goerth, “Early magnetron development especially in Germany,” 2010 International Conference on the Origins and Evolution of the Cavity Magnetron (CAVMAG), pp. 17-22, 2010.

[14] Y. Blanchard, G. Galati, P. van Genderen, “The Cavity Magnetron: Not Just a British Invention,” in *IEEE Antennas and Propagation Magazine*, Vol 55, No. 5, October 2013.

[15] E. G. Bowen, *Radar Days*, Briston, UK, Adam Hilger (Institute of Physics Publishing), 1987.

[16] S. Phelps, *The Tizard Mission: The Top Secret Operation that Changed the Course of World War II*, Yardley, PA, Westholme Publishing, 2010.

[17] Kaiser, W. (1994). "The Development of Electron Tubes and of Radar technology: The Relationship of Science and Technology". In Blumtritt, O.; Petzold, H.; Aspray, W. (eds.). Tracking the History of Radar. Piscataway, NJ, USA: IEEE. pp. 217–236.

[18] W.C. Brown, “The History of the Reentrant Beam Crossed-Field Amplifier with Emphasis on Noise Comparison with the Magnetron” in *Proc. First International Workshop on Crossed-Field Devices*, Ann Arbor, MI, USA, 1995, p. 9.

[19] W. C. Brown, “The Platinotron: Amplitron and Stabilotron,” in E. Okress, G. Mourier, J. Feinstein, E. Kettlewell, and G. R. Feaster, Eds., *Crossed-Field Microwave Devices*, Vol. 2, pp. 165-209. New York, NY: Academic Press, Inc., 1961.

[20] J. F. Skowron, “The Continuous Cathode (Emitting Sole) Crossed-field Amplifier,” *Proc. IEEE*, Vol. 61, No. 3, March 1973, pp. 330-336.

[21] F. F. Chen, *Introduction to Plasma Physics and Controlled Fusion.* Springer, Jan. 1984.

[22] L. Brillouin, “A theorem of Larmor and its importance for electrons in magnetic fields,” *Physical Review,* Vol. 67, pp. 260-266, Apr. 1945.

[23] E. Ott and R. Lovelace, “Magnetic insulation and microwave generation.” *Applied Physics Letters*, Vol. 27, pp. 378 – 380, Oct. 1975.

[24] D. H. Simon, Y. Y. Lau, G. Greening, P. Wong, B. W. Hoff, and R. M. Gilgenbach, “Stability of Brillouin flow in planar, conventional, and inverted magnetrons,” *Physics of Plasmas*, vol. 22, No. 8, p. 082104, Aug. 2015.

[25] R. V. Lovelace and T. F. T. Young, “Relativistic Hartree condition for magnetrons: Theory and comparison with experiments,” *Physics of Fluids*, Vol. 28, pp. 2450-2452, Aug. 1985.

[26] Y. Y. Lau, J. Luginsland, K. L. Cartwright, D. H. Simon, W. Tang, B. W. Hoff, and R. M. Gilgenbach, “A re-examination of the Buneman-Hartree condition in a cylindrical smooth-bore relativistic magnetron,” *Physics of Plasmas,* Vol. 17, p. 033102, Mar. 2010.

[27] Y. Y. Lau, “Theory of Crossed-Field Devices,” in High-Power Microwave Sources, V. L. Granatstein and I. Alexeff, Eds. Norwood, MA: Artech House, 1987, pp. 309–349.

[28] W. L. Menninger et al., “70% efficient Ku-band and C-band TWTs for satellite downlinks,” *IEEE Trans. Electron Devices*, Vol. 52, No. 5, May 2005, pp. 679 – 684.

[29] P. Ehret et al., “L-band TWTAs for navigation satellites,” *IEEE Trans. Electron Devices*, Vol. 52, No. 5, May 2005, pp. 650 - 652.

[30] D. Sprehn, R. M. Phillips, and G. Caryotakis, “The design and performance of 150-MW S-band klystrons,” SLAC-PUB-6677, Stanford Linear Accelerator Center, September 1994.

[31] G. Caryotakis, “High-power microwave tubes: in the laboratory and on-line,” *IEEE Trans. Plasma Science*, Vol. 22, No. 5, October 1994, pp. 683 – 691.

[32] CPI, “VGB-8194, gyrotron amplifier,” CPI Microwave Power Products, 811 Hansen Way, Palo Alto, CA 94303-0750.

[33] R.M. Gilgenbach, Y.Y. Lau, D.M. French, B.W. Hoff, J. Luginsland, and M.A. Franzi, “Crossed field device,” U.S. Patent US 8 841 867 B2, Sep. 23, 2014

[34] M. A. Franzi, “Relativistic Recirculating Planar Magnetrons,” Ph.D. dissertation, University of Michigan, Ann Arbor, MI, USA, 2014.

[35] R. M. Gilgenbach, Y. Y. Lau, D. M. French, B. W. Hoff, M. A. Franzi, and J. Luginsland, “Recirculating Planar Magnetrons for High-Power High-Frequency Radiation Generation,” *IEEE Trans. Plasma Science,* Vol. 39, No. 4, pp. 980 – 987, Apr. 2011. [Online]. Available: https://doi.org/10.1109/TPS.2010.2099670.

[36] G. E. Pokorny, A. E. Kushnick, and J. F. Hull, “The DEMATRON – a new crossed-field amplifier,” *IRE Trans. Electron Devices*, Vol. 9, No. 4, pp. 337 – 345, July 1962.

[37] A. H. McCurdy, “Modification of Electron Cyclotron Maser Operation by Application of an Externl Signal,” Ph. D. dissertation, Yale University, New Haven, CT, USA, 1987.

[38] R. Adler, “A study of locking phenomena in oscillators,” Proceedings of the IEEE, vol. 61, no. 10, pp. 1380–1385, Oct. 1973. [Online]. Available: http://dx.doi.org/10.1109/PROC.1973.9292

[39] J. W. Gewartowski and H. A. Watson, *Principles of Electron Tubes*. Princeton, NJ: D. Van Nostrand, 1965.

[40] G. Mourier and E. Okress, *Crossed Field Devices.* Vol. 1, pp. 1-15. New York, NY: Academic Press, Inc., 1961.

[41] G. B. Collins, *Microwave Magnetrons*. New York, NY, USA: McGraw-Hill, 1948.

[42] ANSYS, Inc., https://www.ansys.com/products/electronics , *Maxwell*, v.16 ed.

[43] ANSYS, Inc., https://www.ansys.com/products/electronics , *High Frequency Structure Simulator*, v.16 ed.

[44] MAGIC Electromagnetic-PIC Software, Alliant Techsyst. (ATK), Newington, VA, USA, 2014.

[45] S. C. Exelby, G. B. Greening, N. M. Jordan, D. A. Packard, D. H. Simon, Y. Y. Lau, B. W. Hoff, R. M. Gilgenbach, "High-Power Recirculating Planar Crossed-Field Amplifier Design and Development," in IEEE Transactions on Electron Devices, vol. 65, no. 6, pp. 2361-2365, June 2018. [Online] Available: https://doi.org/10.1109/TED.2018.2790802

[46] G. B. Greening, “Multi-Frequency Recirculating Planar Magnetrons,” Ph. D. dissertation, University of Michigan, Ann Arbor, MI, USA, 2017.

[47] D. M. Pozar, Microwave Engineering, 4th ed. Hoboken, NJ: John Wiley & Sons, Inc., 2012.

[48] W. V. Smith, “Coupled Circuit Tuning,” pp. 576 – 591. *Microwave Magnetrons Radiation Laboratory Series*, Vol. 6, McGraw-Hill, New York, 1948.

[49] Vaughan, “A model for calculation of magnetron performance," *IEEE Transactions on Electron Devices*, Vol. 20, pp. 818-826, Sept. 1973.

[50] M. I. Fuks and E. Schamiloglu, “70% efficient relativistic magnetron with axial extraction of radiation through a horn antenna,” *IEEE Trans. Plasma Sci*., vol. 38, no. 6, pp. 1302–1312, Jun. 2010.

[51] J. Benford, H. Sze, W. Woo, R. R. Smith, and B. Harteneck, “Phase locking of relativistic magnetrons,” *Phys. Rev. Lett*., vol. 62, no. 8, pp. 969–971, Feb. 1989.

[52] L-3 Communications Holdings, Inc. (2015). Crossed-Field Amplifiers. [Online]. Available: http://www2.l-3com.com/edd/products/r_cfas.htm

[53] C. Waters, “Current Transformers Provide Accurate, Isolated Measurements,” Dec. 1986.

[54] M. C. Jones, “Cathode Priming of a Relativistic Magnetron Using Multi-Emission Zones on Projection Ablation Lithography Cathodes,” Ph.D. dissertation, University of Michigan, Ann Arbor, MI, USA, 2005.

[55] Materialise NV. (2017). Lost Wax Printing and Casting. [Online]. Available: https://i.materialise.com/3d-printing-technologies/lost-waxprinting-casting

[56] M. R. Gomez, D. M. French, W. Tang, P. Zhang, Y. Y. Lau, and R. M. Gilgenbach, “Experimental validation of a higher dimensional theory of electrical contact resistance,” Appl. Phys. Lett., vol. 95, no. 7, p. 072103, Aug. 2009. [Online]. Available: http://dx.doi.org/10.1063/1.3205116

[57] P. Zhang, Y. Y. Lau, and R. M. Gilgenbach, “Thin film contact resistance with dissimilar materials,” Journal of Applied Physics, vol. 109, no. 12, p. 124910, Jun. 2011. [Online]. Available: http://dx.doi.org/10.1063/1.3596759

[58] M. D. Haworth, G. Baca, J. Benford, T. Englert, K. Hackett, K. J. Hendricks, D. Henley, M. LaCour, R. W. Lemke, D. Price, D. Ralph, M. Sena, D. Shiffler, and T. A. Spencer, “Significant pulse-lengthening in a multigigawatt magnetically insulated transmission line oscillator,” IEEE Transactions on Plasma Science, vol. 26, no. 3, pp. 312–319, Jun. 1998. [Online]. Available: http://dx.doi.org/10.1109/27.700759

[59] Y. M. Saveliev, S. N. Spark, B. A. Kerr, M. I. Harbour, S. C. Douglas, and W. Sibbet, “Effect of cathode end caps and a cathode emissive surface on relativistic magnetron operation,” Plasma Science, IEEE Transactions on, vol. 28, no. 3, pp. 478–484, 2000. [Online]. Available: https://doi.org/10.1109/27.887651

[60] M. Lopez, R. Gilgenbach, D. Jordan, S. Anderson, M. Johnston, M. Keyser, H. Miyake, C. Peters, M. Jones, V. Neculaes, Yue Ying Lau, T. Spencer, J. Luginsland, M. Haworth, R. Lemke, and D. Price, "Cathode effects on a relativistic magnetron driven by a microsecond e-beam accelerator," IEEE Transactions on Plasma Science, vol. 30, no. 3, pp. 947–955, Jun. 2002. [Online]. Available: https://doi.org/10.1109/TPS.2002.801543

[61] C. Leach, S. Prasad, M. I. Fuks, and E. Schamiloglu, "Suppression of Leakage Current in a Relativistic Magnetron Using a Novel Design Cathode Endcap," IEEE Transactions on Plasma Science, vol. 40, no. 8, pp. 2089–2093, Aug. 2012. [Online]. Available: http://doi.org/10.1109/TPS.2012.2199136

[62] E. A. Abramyan, E. N. Efimov, and G. D. Kuleshov, "Energy recovery and power stabilization of pulsed electron beams in Marx generator circuits," in Proceedings of the 2nd International Topical Conference on High Power Electron and Ion Beam Research and Technology, vol. 2, Oct. 1977, pp. 755–760.

[63] Electron Beam Accelerator. Pulse Sciences Inc., Aug. 1983.

[64] R. M. Gilgenbach, L. D. Horton, R. F. Lucey Jr, S. Bidwell, M. Cuneo, J. Miller, and L. Smutek, "Microsecond Electron Beam Diode Closure Experiments," in Proc. IEEE Pulsed Power Conf., 1985, pp. 126–132.

[65] R. F. Lucey, Jr., "Long-Pulse Relativistic Electron Beam Generation and Propagation In Gases And In Ultraviolet Laser Ionized Channels," Ph.D. dissertation, University of Michigan, Ann Arbor, MI, USA, 1988.

[66] T. A. Treado, R. S. Smith, C. S. Shaughnessy, and G. E. Thomas, "Temporal study of long-pulse relativistic magnetron operation," IEEE Transactions on Plasma Science, vol. 18, no. 3, pp. 594–602, Jun. 1990. [Online]. Available: http://dx.doi.org/10.1109/27.55932

[67] D. A. Shiffler, J. W. Luginsland, R. J. Umstattd, A. LaCour, K. Golby, M. D. Haworth, M. Ruebush, D. Zagar, A. Gibbs, and T. A. Spencer, "Effects of anode materials on the performance of explosive field emission diodes," IEEE Transactions on Plasma Science, vol. 30, no. 3, pp. 1232–1237, Jun. 2002. [Online]. Available: http://dx.doi.org/10.1109/TPS.2002.802146

[68] N.M. Jordan, G.B. Greening, S.C. Exelby, D.A. Packard, Y.Y. Lau, R.M. Gilgenbach, "Pulse Shortening in Recirculating Planar Magnetrons", IEEE Transactions on Electron Devices, accepted for publication.

[69] N. M. Jordan, G. B. Greening, B. W. Hoff, S. S. Maestas, S. C. Exelby, and R. M. Gilgenbach, "Additively Manufactured High Power Microwave Anodes," IEEE Trans. Plasma Sci., vol. 44, no. 8, pp. 1258–1264, Aug. 2016. [Online]. Available: http://dx.doi.org/10.1109/TPS.2016.2565261

[70] J. Skowron, Raytheon Co., Workshop on High-Power, Space-Based Microwave Systems, Los Alamos NM, March 1985.

[71] Raytheon Company, "Ultra high-power amplitron," Vol. 1, CW Amplitron Development, Rome Air Development Center, Griffiss Air Force Base, NY, Technical Report No. RADC-TDR 64-389, May 1965.

[72] D. A. Packard, G. B. Greening, N. M. Jordan, S. C. Exelby, Y. Y. Lau, R. M. Gilgenbach, B. W. Hoff, and J. F. Hammond, "A study of harmonic locking between oscillators in a dual frequency magnetron," in 2019 *IEEE International Vacuum Electronics Conference (IVEC),* Apr. 2019.

[73] N. J. Dionne, "Harmonic generation in octave bandwidth traveling-wave tubes," IEEE Transactions on Electron Devices, vol. 17, no. 4, pp. 365–372, Apr. 1970. [Online]. Available: http://doi.org/10.1109/T-ED.1970.16981

[74] C. F. Dong, P. Zhang, D. Chernin, Y. Y. Lau, B. W. Hoff, D. H. Simon, P. Wong, G. B. Greening, and R. M. Gilgenbach, "Harmonic Content in the Beam Current in a Traveling-Wave Tube," IEEE Trans. Electron Dev., vol. 62, no. 12, pp. 4285–4292, Dec. 2015. [Online]. Available: http://dx.doi.org/10.1109/TED.2015.2490584

[75] J. Cai, X. Wu, and J. Feng, "Travelling-wave tube harmonic amplifier in terahertz and experimental demonstration," IEEE Trans. Electron Dev., vol. 62, no. 2, pp. 648–651, Feb. 2015. [Online]. Available: http://dx.doi.org/10.1109/TED.2014.2377914

[76] P. Y. Wong, "A Contemporary Study in the Theory of Travelling-Wave Tubes," Ph.D. dissertation, University of Michigan, Ann Arbor, MI, USA, 2018.

[77] B. W. Hoff, S. Beeson, W. Tang, A. Sayir, "IMPROVED FIELD EMISSION CATHODE," United States Patent pending (filed 2018 as US Patent Application Number 62741892).

[78] "Parker O-Ring Handbook (ORD 5700)," 2007.

[79] F. Antoulinakis, Y.Y. Lau, "A Theory of AC Contact Resistance", ICOPS 2019, Orlando, FL, June 2019.